Università degli Studi di Genova

Istituto Italiano di Tecnologia

PhD School in Sciences and Technologies of Chemistry and Materials - Curriculum Nanochemistry

-XXXII Cycle-

Metallic Nanoparticles and their Application in Heterogeneous Catalysis for Environmental Sciences

by

Cansunur DEMIRCI

A thesis submitted for the degree of

DOCTOR OF PHILOSOPHY

Supervisors: Prof. Liberato MANNA

Dr. Massimo COLOMBO

Dr. Dipak SHINDE

Tutor: Prof. Simona DELSANTE

Genoa, September 2020

Abstract of the Thesis

This thesis provides a comprehensive concept on how catalysis can tackle climate change and global warming by reducing greenhouse gases using three different approaches. In a first approach, gold nanoparticles were synthesized by means of a colloidal synthesis method and subsequently transformed to 3D gold structures, which allowed for the selective oxidative coupling of methanol to methyl formate and by this, reducing the emission of carbon dioxide (CO_2) as a side-product. In a second approach, the wetness incipient impregnation method was utilized to obtain a palladium catalyst supported on aluminum oxide, which was investigated for its activity in the lean methane oxidation at elevated pressures and temperatures. Elevated pressures allowed overall higher combustion rates of methane to CO_2, which is, in perspective, less harmful as a greenhouse gas than methane. The last approach tackled the reduction of CO_2, using this greenhouse gas as a feedstock to reduce it electrochemically over nanoparticulate copper and gold catalyst, which were synthesized using the chemical solution deposition method followed by an in-situ electrochemical reduction. The final products of this reaction can be hydrocarbons, which can be utilized as fuels or chemicals. All in all, the idea was to find catalysts and methods to contribute to the reduction of potential greenhouse gases and finally closing the carbon cycle for a more sustainable and greener future of planet Earth.

List of Publications

First authorship publications

1. Demirci, C., Marras, S., Prato, M., Pasquale, L., Manna, L. Massimo, C., Design of catalytically active porous gold structures from a bottom-up method: The role of metal traces in CO oxidation and oxidative coupling of methanol, J. Catal., 2019, 375, 279-286. https://doi.org/10.1016/j.jcat.2019.06.016.
2. Co-First authorship: Florén, C.-R., Demirci, C., Carlsson, P.-A., Creaser, D., Skoglundh, M., Total oxidation of methane over Pd/Al_2O_3 at pressures from 1 to 10 atm, Catal. Sci. Technol., 2020, https://doi.org/10.1039/D0CY00813C.

Other publications

1. Bellani, S., Martín-García, B., Oropesa-Nuñez, R., Romano, V., Najafi, L., Demirci., C., Prato, M., Del Rio Castillo, A. E., Marasco, L., Mantero, L., D'Angelo, G., Bonaccorso, F., "Ion sliding" on graphene: a novel concept to boost supercapacitor performance, Nanoscale Horiz., 2019, 4, 1077-1091. https://doi.org/10.1039/C8NH00446C
2. Campagnolo, L., Morselli, D., Magrì, D., Scarpellini, A., Demirci, C., Colombo, M., Athanassiou, A., Fragouli, D., Silk Fibroin/Orange Peel Foam: An Efficient Biocomposite for Water Remediation, Adv. Sustainable Syst. 2019, 3, 1800097. https://doi.org/10.1002/adsu.201800097

List of Communications at Conferences

Poster Communications

1. Tailored design of ultralight unsupported heterogeneous catalysts through a bottom-up approach, presented at Catalysis Fundamentals and Practice Summer School, Liverpool (United Kingdom) 17-21 July 2017
2. Bottom-up design of heterogeneous catalysts through ice-templated nanoparticles assembly, presented at Faraday Discussion: Designing Nanoparticle Systems for Catalysis, London (United Kingdom), 16-18 May 2018
3. The role of metal traces in bottom-up porous gold structures in oxidative catalysis, presented at International Meeting on Nanoalloys, Genova (Italy), 4-7 June 2019
4. Bottom-up design of heterogeneous gold catalysts for the oxidative coupling of methanol, presented at EuropaCat: Catalysis without Borders, Aachen (Germany), 18-23 August 2019

Oral Communications

1. Bottom-up design of heterogeneous catalysts through ice-templated nanoparticles assembly, presented for a Lightning Session at Faraday Discussion: Designing Nanoparticle Systems for Catalysis, London (United Kingdom), 16-18 May 2018
2. Bottom-up design of heterogeneous gold catalysts for the oxidative coupling of methanol, presented as invited speaker to DFG meeting (FOR 2213) Oldenburg (Germany), 17-18 September 2018

Table of Contents

Chapter I: Introduction

Abstract

This chapter covers the impact of the so-called greenhouse gases on climate change and global warming and on how to reduce the amount of greenhouse gases in the atmosphere by means of catalysis. A major focus will be set on the reduction of potential greenhouse gases, in particular carbon dioxide (CO_2) and methane (CH_4), by using metallic nanoparticles via thermal gas-phase catalysis but also via electrocatalysis. Furthermore, three different catalytic approaches will be presented, which were used in this thesis on a more fundamental level to target overall greenhouse gas reduction. The main objective of this introduction is to show the reader the following aspects: i) how greenhouse gases can potentially damage our climate, due to increased global surface temperatures causing climate change; ii) where these greenhouse gases are generate; iii) how catalysis can tackle this problem by means of different catalytic approaches. All these aspects have the same aim in common: the reduction of greenhouse gases for a greener and more sustainable future.

1. The Climate

Natural environment, global warming and climate change are three important topics inevitably linked to each other[1,2]. *Global warming* is an expression that is used to describe the increase of the global mean surface temperature (GMST) of lands and oceans in comparison to pre-industrial (around 1880) values[2,3]. The term *climate change* refers to the changes of the atmosphere, such as the altering composition of the global atmosphere, partially due to anthropogenic impact and partly to natural processes[1–3]. Comparing the data of GMST to pre-industrial times, a consistent increase of the mean surface temperature has been identified (see **Figure 1.1**)[2,4]. It is estimated that the anthropogenic global warming increases at the moment with 0.2°C per decade due to present but also past emissions[2].

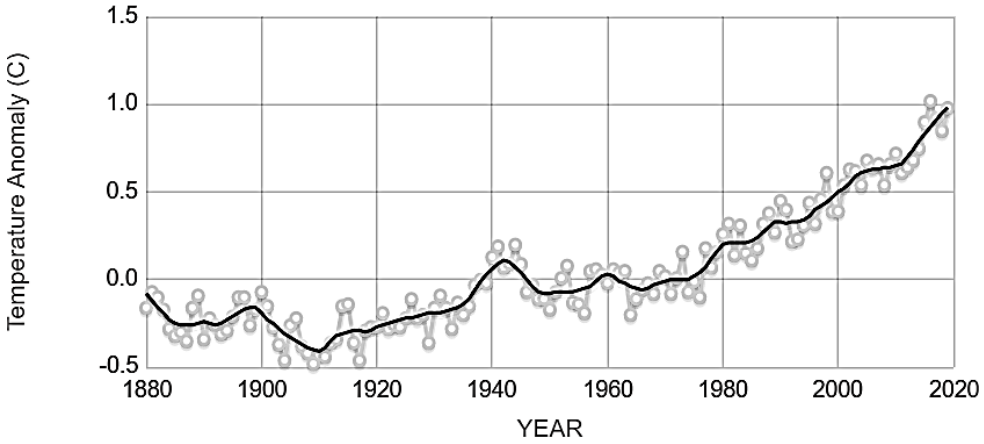

Figure 1.1 The change of global surface temperature relative to 1951-1980 average temperatures by NASA's Goddard Institute for Space Studies. Grey dots: annual mean temperature; Black line: Lowess smoothing.[4]

The onset of the industrial revolution caused an increase of the overall global mean surface temperature of around 0.98°C[2,5,6] until today. The limit of 1.5°C is a very frequently observable value and at the same time a critical threshold, indicated by scientists, for politicians, policymakers and stakeholders worldwide. It is a boundary past which there is no return to the values from where it all started[2], after which extreme climate events can be expected to occur with severe consequences[2,7]. With the current rate, the value of 1.5°C for the GMST will be reached between 2030 and 2052[2]. The Intergovernmental Panel on Climate Change (IPCC) projected heavy precipitations events and flood risks, droughts and larger dry land areas, reduction of water supplies stored in glaciers, the extinction of entire ecosystems (which are crucial for the natural carbon reduction), coastal erosions and coral bleaching due to increased sea-surface temperatures (and many more effects caused by the above mentioned events)[2,8]. The change of the GMST can have an impact on climate change, whereas climate change can have a back-impact on global warming[1,2] by additionally increasing the surface temperature. Nowadays, natural catastrophes have become more frequent than before, extreme temperatures are more common[7], and ecosystems recede in various areas of the planet[9,10]. Hence, it is not only the task of the governments worldwide to take action and prevent this critical value from being reached. It is also the objective of scientists worldwide to find new technologies and methods to prevent the unpredictable from occurring.

This thesis deals with my contribution to efforts to reduction of emissions on a smaller scale. The overall scope of the thesis is to gain insight into the mechanism of certain catalytic reactions, with the long term goal of decreasing the impact of the chemical industries and fossil fuel combustion

on global warming and climate change. In the next sections the mechanisms underlying climate change and global warming will be explained in more detail. Furthermore, a discussion on how catalysis can help to reduce but also to capture chemicals involved in global warming will be presented.

1.1. The Greenhouse-Effect

The term *greenhouse-effect* derives from the function of a greenhouse: A greenhouse is usually built in countries where the temperatures are too cold or it is too rainy to grow certain crops. The function of a greenhouse is to keep the heat coming from sunlight inside the house, as the sunlight can enter the house and partially heat up the plant matter and soil. While one part of the radiation exits from the glass walls of the house, another part is retained inside, causing the greenhouse to warm up, thus contributing to a warm and protected condition to grow certain plants. The very same effect can be found on a much grander scale with the Earth[11]: Firstly, the solar radiation reaches the atmosphere, and part of it is reflected back into space. The remaining part is absorbed by the land and the ocean, which causes the warm temperatures of planet Earth. A fraction of this radiation exits the atmosphere back into space, whereas the other part is retained in the atmosphere by natural greenhouse gases, which ultimately keep the Earth warm enough to sustain life. However, besides naturally generated greenhouse gases, the presence of other greenhouse gases of anthropogenic nature can trap additional heat in the atmosphere, which causes an additional, man-made greenhouse effect, and global warming on a longer run. The following image illustrates the greenhouse-effect:

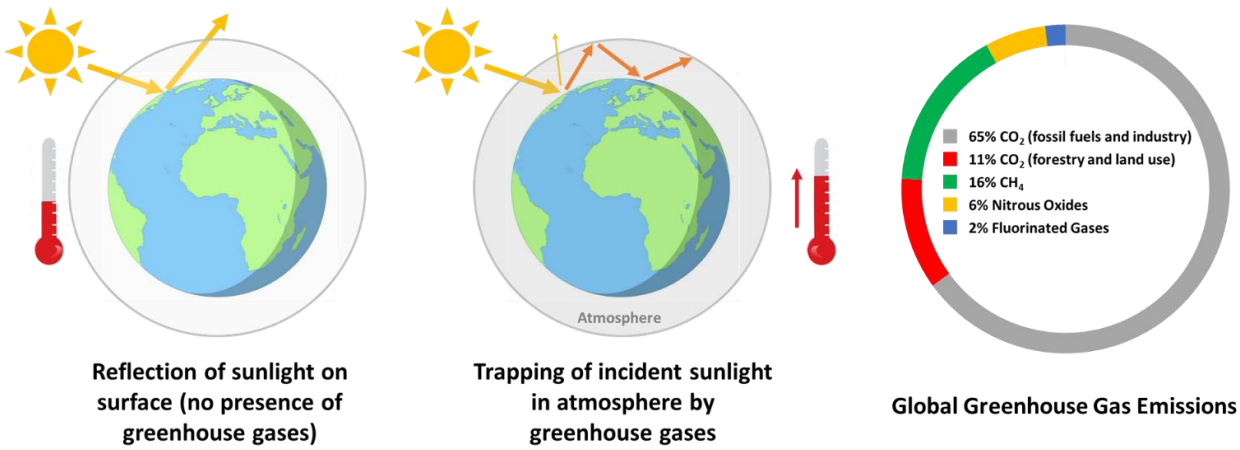

Figure 1.2 Illustration of the greenhouse-effect: Earth at preindustrial temperatures with less greenhouse gases in atmosphere (left) and Earth nowadays, with high amount of greenhouse gases in atmosphere causing increased surface temperatures (center). Global emissions of main greenhouse gases worldwide (right)[11].

As mentioned before, these gases that cause the atmosphere to heat up are called *greenhouse gases* and different gases have different impacts on global warming. They can be of natural but also anthropogenic nature and are part of Earth's atmosphere. Their capability of absorbing and emitting radiation of specific wavelengths within the spectrum of radiation generated by the terrestrial surface, the atmosphere and by clouds[3] can lead to increased temperatures. Prior to the repercussions associated with man-made climate change, naturally occurring greenhouse gases were responsible for sustainable temperatures on planet Earth. Primary greenhouse gases in the atmosphere are carbon dioxide (CO_2), water vapor, nitrous oxide (N_2O), methane (CH_4) and ozone (O_3)[1,3]. Some of these greenhouse gases are naturally transformed and absorbed by different ecosystems, thus returning the carbon or nitrogen back into the energetic cycle, whereas other gases remain longer in the atmosphere and constantly contribute to the increase of the global surface temperature of our planet[6,11]. In addition to the previously mentioned greenhouse gases, halocarbons and other halogen-containing substances are released to the atmosphere entirely due to human activity[3]. The most commonly known and accepted greenhouse gas is CO_2[12], which is principally formed during the combustion of fossil fuels. As the quantities of this gas that are emitted are large, it is used as a standard unit of measurement against which the global warming potential (GWP) of other gases are compared[1,11]. However, a diverse range of so-called trace gases can contribute with a higher impact to global warming, due to their higher capability, compared to CO_2, of storing the infrared radiation and also due to their longer lifetime[1,5,12–14]. Among those trace gases, a very crucial greenhouse gas is methane (CH_4) which can be largely found in the agricultural sector and in waste management. The GWP of methane relative to CO_2 is around 28-36 over 100 years[11]. Nitrous oxides can be formed in the usage of agricultural fertilizers and have a GWP of around 265-298 over 100 years[11], and halogenated gases can have thousands or even tens of thousands higher GWP compared to CO_2[11]. These gases are released in industrial processes, they are used for refrigeration and are present in different consumer products (such as deodorants)[11]. Between 1970 and 2004 CO_2 made up 77% of the most emitted anthropogenic greenhouse gases[1], as such it is crucial to understand where the major emission lies. In the next section this will be analyzed in more detailed, in particular with a deeper insight into the chemical process industry.

1.2. Greenhouse gas emission

Around 65% of the global emission of greenhouse gases due to anthropogenic events are attributed to CO_2, in particular to the use of fossil fuels[8,11]. With a focus on the chemical process industry

(like the bulk chemical[15–17] industry, the life sciences industry[18,19] and the fine chemical industry[1]), fossil fuels are required to power energy-intensive manufacturing processes but are also significant as a raw material in the production lines[1]. The majority of the emissions in the chemical industry derive, according to the International Council of Chemical Associations, from the production of chemicals, whereas another part derives from the extraction phase of the feedstock and fuel material used in the production lines and the final disposal of the produced chemicals[1,20]. Of the production of the chemicals, around 75% of the emissions are linked to the consumption of fossil fuels to power the manufacturing process[1,21]. To generate this energy, different energy sources are used, of which 36% percent are dedicated to the use of petroleum, 27% to coal, 23% to natural gas, 12% to electricity, and around 2% to others, which might involve the application of renewable energies[1].

Besides the energy consumption in the chemical industry, a part of the greenhouse gas emission derives from the chemical production itself, which can be considered as a non-energy industrial source of CO_2 emissions but also a source for the emission of trace greenhouse gases[22]. The employment of CO_2 emission-rich feedstocks (petroleum and natural gas) is one of the main causes. The emission of a range of greenhouse gases can be found in the production of ammonia (CO_2 emission)[17,22], nitric acid (N_2O emission)[15,22], titanium dioxide (CO_2 emission)[22–24], soda ash (CO_2 emission)[22,25], carbon black[22,23] and in the petrochemical production (CO_2 emission)[22,26,27]. Taking the Haber-Bosch process for ammonia synthesis as an example[17,22], which involves the reaction of hydrogen and nitrogen in a 3:1 ratio at high temperatures and pressures, the generation of hydrogen for the reaction is the main CO_2 emission factor. It requires the steam reforming method[28,29], which is the reaction of methane with water gas to obtain hydrogen and CO_2. Furthermore, nitrogen is usually obtained by a secondary air reforming process, which results in the formation of carbon monoxide as a side-product. This carbon monoxide is in a second step (the water-gas shift reaction[29]) oxidized in presence of water to CO_2.

In addition to the chemical process industry, the consumption of fossil fuels can be found at a consumer level, namely in the operation of heat engine driven vehicles (trucks, cars and aircrafts)[30–33]. Heat engines convert the heat energy obtained by fuel combustion to mechanical energy. The largest part of the emission during this process is CO_2, followed by water vapor, carbon monoxide, hydrocarbons, nitrogen oxides and particulate matter such as soot[30,33,34]. Water vapor and CO_2 are released during the combustion of fuel (higher chained hydrocarbons)[30]. Carbon monoxide, hydrocarbons (including methane) and soot are the result of an incomplete combustion. Since an

internal combustion engine requires the presence of air next to the fuel, the nitrogen in air can get oxidized to nitrous gases[35].

To tackle the emission of greenhouse gases, many different areas, both in industry but also at a consumer level need a radical change and the help of science. In the following section, different possibilities where catalysis can play a key role, with a view on the scope of this thesis, will be presented and explained in further detail.

1.3. Catalysis for the reduction of greenhouse gas emissions

To remain below the indicated limit of overall global surface temperature increase of 1.5°C, different actions can be taken. One very simple and straightforward way to do so is to reduce, or better to avoid, the emission of greenhouse gases. It is no secret that burning fossil fuels has the greatest impact on the emission of greenhouse gases (CO_2 but also CH_4)[11,30,32,33]. But, also in industrial processes CO_2 can be found as a side-product of different reactions for bulk chemical synthesis[36]. Taking as an example, methyl formate is usually produced by oxidatively coupling two methanol molecules to form the final product[37,38]. One side-product during this reaction is CO_2. Hence, a requirement here would be to design a catalyst in such a way that the selectivity of the reaction is shifted towards the more desired methyl formate, in order to reduce CO_2 emission. This reaction in particular was investigated over an unsupported gold catalyst in the first project of this thesis and will be further discussed in the introduction of Chapter II.

As methane has a higher GWP compared to CO_2, its emission has to be drastically reduced. In the transportation sector, where fossil fuels (especially natural gas) are used to generate energy for vehicles, the slip of uncombusted methane into the atmosphere is possible[30,39,40]. A catalyst in these sectors is required to reduce the methane slip by decreasing the activation energy of the combustion reaction and obtain the less harmful CO_2[11]. This parameter was investigated in the second project of this thesis, where the total pressure and temperature influence of the methane combustion was studied over a palladium catalyst. Further details related to this topic can be found in Chapter III.

Another approach is to capture the CO_2 formed during industrial processes and use it as a carbon source to synthesize useful chemicals, which can be used again as a fuel or to further obtain fine chemicals[41–44]. To name a few, the production of urea[45], methanol[46,47] and salicylic acid[47] require the usage of CO_2, of which 94% is dedicated to the production of urea. However, the emission of CO_2 in the urea production is higher than the consumed CO_2, due to the utilization of ammonia,

which is a CO_2-emission intensive process[17]. In the chemical industry, high CO_2-emissions are commonly generated by the necessity of high energy-inputs, which often implement the employment of fossil fuels to power these processes (as previously stated). Considering that green energy (energy which does not emit CO_2, for example from renewable energy sources) is used to power the reaction, a closed circle of CO_2 capture and emission can be obtained[41]. By this method, net CO_2 emissions can finally be reduced to zero. The third and last project (Chapter IV) tries to tackle this task by electrochemically reducing CO_2 over a copper and gold catalysts to form C1 (hydrocarbon containing one carbon atom) to C3 (hydrocarbon containing three carbon atoms) hydrocarbons.

The following scheme shows the relations between the three different projects, which close the circle of CO_2 production and consumption by catalytic oxidation and reduction reactions over different metal catalysts using heterogeneous catalysis (gas-phase and electrocatalysis).

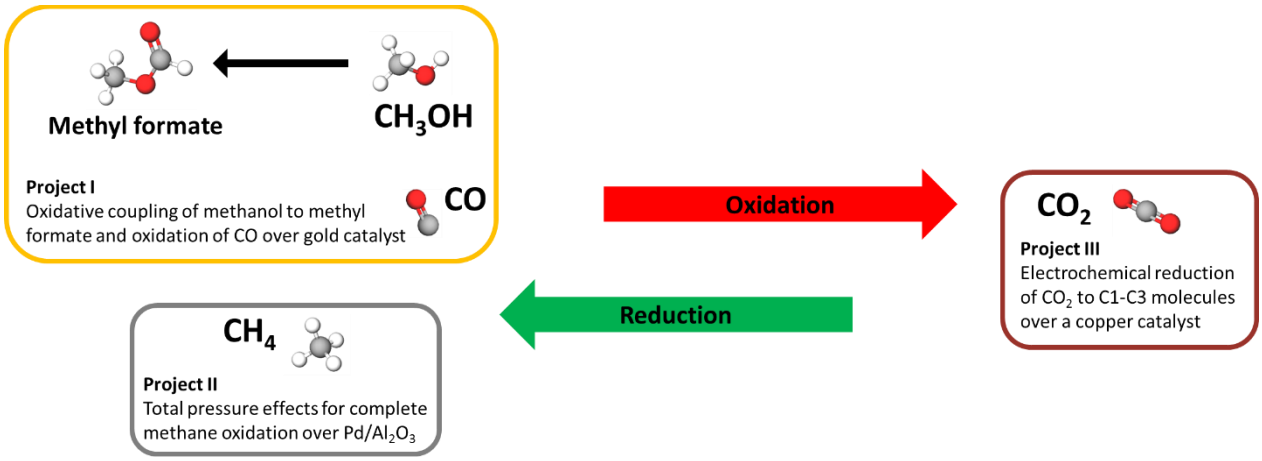

Figure 1.3 Summary and relation of the three topics of heterogenous catalysis investigated in this thesis.

In the following three chapters these topics in catalysis will be further discussed on different materials and reactions to underline how interdependent these reactions are to reach a net zero CO_2 emission. Each chapter will describe in detail the basic idea of the catalytic reaction involved in the project, the state-of-the-art methods and the aim of each project on how to improve these catalysts and reactions. Finally, conclusions and perspectives for each chapter will be highlighted in the last chapter.

2. References

(1) Leimkühler, H.-J. *Managing CO2 Emissions in the Chemical Industry*; Wiley-VCH Verlag GmbH & Co. KGaA, 2010.

(2) Masson-Delmotte, V.; Zhai, P.; Pörtner, H.-O.; Roberts, D.; Skea, J.; Shukla, P. R.; Pirani, A.; Moufouma-Okia, W.; Péan, C.; Pidcock, R.; et al. *Global Warming of 1.5 ^{o}C*; Geneva, Switzerland, 2018.

(3) Masson-Delmotte, V.; Zhai, P.; Pörtner, H.-O.; Roberts, D.; Skea, J.; Shukla, P. R.; Pirani, A.; Moufouma-Okia, W.; Péan, C.; Pidcock, R.; et al. IPCC, 2018: Annex I: Glossary https://www.ipcc.ch/sr15/chapter/glossary/ (accessed Apr 6, 2020).

(4) NASA. Global Temperature https://climate.nasa.gov/vital-signs/global-temperature/ (accessed Apr 6, 2020).

(5) Lacis, A.; Hansen, J.; Lee, P.; Mitchell, T.; Lebedeff, S. Greenhouse Effect of Trace Gases, 1970-1980. *Geophys. Res. Lett.* **1981**, *8* (10), 1035–1038. https://doi.org/10.1029/GL008i010p01035.

(6) NASA. GISS Surface Temperature Analysis (GISTEMP v4) https://data.giss.nasa.gov/gistemp/ (accessed Apr 6, 2020).

(7) Power, S. B.; Delage, F. P. D. Setting and Smashing Extreme Temperature Records over the Coming Century. *Nat. Clim. Chang.* **2019**, *9* (7), 529–534. https://doi.org/10.1038/s41558-019-0498-5.

(8) Pachauri, R. K.; Reisinger, A. *Climate Change 2007: IPCC Synthesis Report to the Fourth Assessment Report*; Geneva, Switzerland, 2007.

(9) Jones, N. The Polar Bear Struggle. *Nat. Clim. Chang.* **2011**, *1* (9), 433. https://doi.org/10.1038/nclimate1306.

(10) McClanahan, T. R.; Darling, E. S.; Maina, J. M.; Muthiga, N. A.; 'agata, S. D.; Jupiter, S. D.; Arthur, R.; Wilson, S. K.; Mangubhai, S.; Nand, Y.; et al. Temperature Patterns and Mechanisms Influencing Coral Bleaching during the 2016 El Niño. *Nat. Clim. Chang.* **2019**. https://doi.org/10.1038/s41558-019-0576-8.

(11) United States Environmental Protection Agency. Overview of Greenhouse Gases https://www.epa.gov/ghgemissions/overview-greenhouse-gases#main-content (accessed Oct 10, 2019).

(12) Lashof, D. A.; Ahuja, D. R. Relative Contributions of Greenhouse Gas Emissions to Global Warming. *Nature* **1990**, *344* (6266), 529–531. https://doi.org/10.1038/344529a0.

(13) Hansen, J.; Fung, I.; Lacis, A.; Rind, D.; Lebedeff, S.; Ruedy, R.; Russell, G.; Stone, P. Global Climate Changes as Forecast by Goddard Institute for Space Studies Three-Dimensional Model. *J. Geophys. Res. Atmos.* **1988**, *93* (D8), 9341–9364. https://doi.org/10.1029/JD093iD08p09341.

(14) Ramanathan, V.; Cicerone, R. J.; Singh, H. B.; Kiehl, J. T. Trace Gas Trends and Their Potential Role in Climate Change. *J. Geophys. Res. Atmos.* **1985**, *90* (D3), 5547–5566. https://doi.org/10.1029/JD090iD03p05547.

(15) Sadykov, V. .; Isupova, L. .; Zolotarskii, I. .; Bobrova, L. .; Noskov, A. .; Parmon, V. .; Brushtein, E. .; Telyatnikova, T. .; Chernyshev, V. .; Lunin, V. . Oxide Catalysts for Ammonia Oxidation in Nitric Acid Production: Properties and Perspectives. *Appl. Catal. A Gen.* **2000**, *204* (1), 59–87. https://doi.org/10.1016/S0926-860X(00)00506-8.

(16) W., W. The Manufacture of Sulphuric Acid (Contact Process). *Nature* **1925**, *116* (2915), 385–386. https://doi.org/10.1038/116385a0.

(17) Appl, M. Ammonia, 2. Production Processes. *Ullmann's Encyclopedia of Industrial Chemistry*. October 15, 2011. https://doi.org/doi:10.1002/14356007.o02_o11.

(18) Bamoharram, F. F.; Heravi, M. M.; Roshani, M.; Gharib, A.; Jahangir, M. Catalytic Method for Synthesis of Aspirin by a Green, Efficient and Recyclable Solid Acid Catalyst (Preyssler's Anion) at Room Temperature. *J. Chinese Chem. Soc.* **2007**, *54* (4), 1017–1020. https://doi.org/10.1002/jccs.200700146.

(19) Murphy, M. A. Early Industrial Roots of Green Chemistry and the History of the BHC Ibuprofen Process Invention and Its Quality Connection. *Found. Chem.* **2018**, *20* (2), 121–165. https://doi.org/10.1007/s10698-017-9300-9.

(20) The International Council of Chemical Associations (ICAA). *Innovations for Greenhouse Gas Reductions-A Life Cycle Quantification of Carbon Abatement Solutions Enabled by the Chemical Industry*; 2009.

(21) McKinsey&Company. *Pathways to a Low-Carbon Economy: Version 2 of the Global Greenhouse Gas Abatement Cost Curve*; 2013.

(22) Harnisch, J.; Jubb, C.; Nakhutin, A.; Sena Cianci, V. C.; Lanza, R.; Martinsen, T.; Mohammad, A. K. W.; Santos, M. M. O.; McCulloch, A.; Mader, B. T.; et al. *2006 IPCC Guidelines for National Greenhouse Gas Inventories - Volume 3: Industrial Processes and Product Use*; 2006.

(23) Kirk-Othmer. *Concise Encyclopedia of Chemical Technology*, Fifth Edit.; Wiley-VCH Verlag GmbH & Co. KGaA, 2007.

(24) Chemlink. Titanium Dioxide and Titanium Dioxide pigment http://www.chemlink.com.au/titanium.htm (accessed Apr 6, 2020).

(25) Thieme, C. Sodium Carbonates. *Ullmann's Encyclopedia of Industrial Chemistry*. June 15, 2000. https://doi.org/doi:10.1002/14356007.a24_299.

(26) Sadeghbeigi, R.; Sadeghbeigi, R. FCC Catalysts. *Fluid Catal. Crack. Handb.* **2000**, 84–124. https://doi.org/10.1016/B978-088415289-7/50004-4.

(27) Nikitin, A. V; Dmitruk, A. S.; Arutyunov, V. S. Effect of Pressure on the Oxidative Cracking of C2—C4 Alkanes. *Russ. Chem. Bull.* **2016**, *65* (10), 2405–2410. https://doi.org/10.1007/s11172-016-1597-3.

(28) Ali, S.; Zagho, M. M.; Arafat, Y. I.; Khader, M. M. Development of Nickel-Based Catalysts for Methane Steam Reforming. *Proc. 4th Int. Gas Process. Symp.* **2015**, 111–116. https://doi.org/10.1016/B978-0-444-63461-0.50011-0.

(29) Vozniuk, O.; Tanchoux, N.; Millet, J.-M.; Di Renzo, F.; Cavani, F. Spinel Mixed Oxides for Chemical-Loop Reforming: From Solid State to Potential Application. *Stud. Surf. Sci. Catal.* **2019**, *178*, 281–302. https://doi.org/10.1016/B978-0-444-64127-4.00014-8.

(30) Thakur, P.; Thakur, P. Diesel Exhaust Control. *Adv. Mine Vent.* **2019**, 157–187. https://doi.org/10.1016/B978-0-08-100457-9.00011-0.

(31) Ericson, C.; Westerberg, B.; Odenbrand, I. A State-Space Simplified SCR Catalyst Model for Real Time Applications. SAE International 2008. https://doi.org/10.4271/2008-01-0616.

(32) Friedl, R. R. AVIATION METEOROLOGY | Aircraft Emissions. *Encycl. Atmos. Sci.* **2015**, 153–159. https://doi.org/10.1016/B978-0-12-382225-3.00061-X.

(33) Graham, L. A.; Rideout, G.; Rosenblatt, D.; Hendren, J. Greenhouse Gas Emissions from Heavy-Duty Vehicles. *Atmos. Environ.* **2008**, *42* (19), 4665–4681. https://doi.org/10.1016/J.ATMOSENV.2008.01.049.

(34) Kuhns, H. D.; Mazzoleni, C.; Moosmüller, H.; Nikolic, D.; Keislar, R. E.; Barber, P. W.; Li, Z.; Etyemezian, V.; Watson, J. G. Remote Sensing of PM, NO, CO and HC Emission Factors for on-Road Gasoline and Diesel Engine Vehicles in Las Vegas, NV. *Sci. Total Environ.* **2004**, *322* (1–3), 123–137. https://doi.org/10.1016/J.SCITOTENV.2003.09.013.

(35) Hanson, T.; Egerton, A. C. Nitrogen Oxides in Internal Combustion Engine Gases. *Proc. R. Soc. London. Ser. A-Mathematical Phys. Sci.* **1937**, *163* (912), 90–100.

(36) Speight, J. G.; Speight, J. G. Hydrocarbons from Synthesis Gas. *Handb. Ind. Hydrocarb. Process.* **2011**, 281–323. https://doi.org/10.1016/B978-0-7506-8632-7.10008-8.

(37) Rao, V. M.; Shankar, V. High Activity Copper Catalyst for One-Step Conversion of Methanol to Methyl Formate at Low Temperature. *J. Chem. Technol. Biotechnol.* **1988**, *42* (3), 183–196. https://doi.org/10.1002/jctb.280420303.

(38) Wittstock, A.; Zielasek, V.; Biener, J.; Friend, C. M.; Bäumer, M. Nanoporous Gold Catalysts for Selective Gas-Phase Oxidative Coupling of Methanol at Low Temperature. *Science (80-.).* **2010**, *327* (5963), 319 LP – 322. https://doi.org/10.1126/science.1183591.

(39) Schlatter, J. C.; Taylor, K. C. Platinum and Palladium Addition to Supported Rhodium Catalysts for Automotive Emission Control. *J. Catal.* **1977**, *49* (1), 42–50. https://doi.org/10.1016/0021-9517(77)90238-X.

(40) Cohn, J. G. Catalytic Converters for Exhaust Emission Control of Commercial Equipment Powered by Internal Combustion Engines. *Environ. Health Perspect.* **1975**, *10*, 159–164. https://doi.org/10.1289/ehp.7510159.

(41) Morales-Guio, C. G.; Cave, E. R.; Nitopi, S. A.; Feaster, J. T.; Wang, L.; Kuhl, K. P.; Jackson, A.; Johnson, N. C.; Abram, D. N.; Hatsukade, T.; et al. Improved CO2 Reduction Activity towards C2+ Alcohols on a Tandem Gold on Copper Electrocatalyst. *Nat. Catal.* **2018**, *1* (10), 764–771. https://doi.org/10.1038/s41929-018-0139-9.

(42) Clark, E. L.; Hahn, C.; Jaramillo, T. F.; Bell, A. T. Electrochemical CO2 Reduction over Compressively Strained CuAg Surface Alloys with Enhanced Multi-Carbon Oxygenate Selectivity. *J. Am. Chem. Soc.* **2017**, *139* (44), 15848–15857. https://doi.org/10.1021/jacs.7b08607.

(43) Zhuang, T.-T.; Pang, Y.; Liang, Z.-Q.; Wang, Z.; Li, Y.; Tan, C.-S.; Li, J.; Dinh, C. T.; De Luna, P.; Hsieh, P.-L.; et al. Copper Nanocavities Confine Intermediates for Efficient Electrosynthesis of C3 Alcohol Fuels from Carbon Monoxide. *Nat. Catal.* **2018**, *1* (12), 946–951. https://doi.org/10.1038/s41929-018-0168-4.

(44) Otto, A.; Grube, T.; Schiebahn, S.; Stolten, D. Closing the Loop: Captured CO2 as a Feedstock in the Chemical Industry. *Energy Environ. Sci.* **2015**, *8* (11), 3283–3297. https://doi.org/10.1039/C5EE02591E.

(45) Meessen, J. H. Urea. *Ullmann's Encyclopedia of Industrial Chemistry*. October 15, 2010. https://doi.org/doi:10.1002/14356007.a27_333.pub2.

(46) Aresta, M.; Dibenedetto, A. Utilisation of CO2 as a Chemical Feedstock: Opportunities and Challenges. *Dalt. Trans.* **2007**, No. 28, 2975–2992. https://doi.org/10.1039/B700658F.

(47) Quadrelli, E. A.; Centi, G.; Duplan, J.-L.; Perathoner, S. Carbon Dioxide Recycling: Emerging Large-Scale Technologies with Industrial Potential. *ChemSusChem* **2011**, *4* (9), 1194–1215. https://doi.org/10.1002/cssc.201100473.

Chapter II: Porous Gold Catalysts from a Bottom-Up Approach for Oxidation Reactions

This chapter of the thesis is subdivided into two parts, namely the "Mixed Gold Systems" (Part A) and the "Pure Gold Systems" (Part B). In both cases porous gold structures are obtained through the assembly of gold nanoparticles to form a 3D-network. For further investigation, added metal traces (Part A) and remaining impurities (Part B) will be analyzed and interpreted with regards to the activity of the samples in the oxidation of carbon monoxide and the selective oxidative coupling of methanol. In part A, a major focus will be put on the role of different metal traces in the porous gold structure and how these can influence the activity and selectivity in above mentioned reactions. In contrast, part B of this chapter focuses on the trapped sodium impurities of supposedly pure porous gold samples and how their presence (or absence) can influence the activity of the catalyst in the selective oxidative methanol coupling reaction.

Chapter II, Part A: Mixed Gold Systems

Abstract

Nanoporous gold (NPG) is a novel catalyst with a high variety of chemical, physical and mechanical characteristics in different reactions. The synthesis of these materials has two major drawbacks, which include the impurity of the material after etching (metal traces remain) and the chemical composition of the product. For these reasons, in our work we chose to adopt a bottom-up approach, based on the ice-templated assembly of nanoscale units with the ice subsequently removed through freeze-drying (cryogelation). The cryogelation of Au NPs enabled us to synthesize on the one hand pure, self-standing, porous gold gels. On the other hand, we developed a procedure to eventually decorate the gold gels with different elements (Ag, Ce, Cu and Pd) to study the role of metal traces and to overcome the compositional restrictions of gold alloys. Through SEM-imaging we observed highly porous, non-ordered and interconnected networks of sheets and wires revealing macroscopic and microscopic changes after high temperature catalytic tests. The synthesized samples were used in reactions where the NPG is known to have exceptional activity and selectivity, hence focusing on CO oxidation and the gas-phase oxidative methanol coupling. In the case of CO oxidation, the pure gold sample exhibited almost no catalytic activity. When this sample was compared to the doped gels, the positive effect of the dopants resulted in higher CO conversion rates, with the extent of the promotion being a function of the dopant

element. The coupling of methanol neglected the positive influence of metal traces. Instead, the pure gold system manifested the highest activities and selectivity for the reaction to form methyl formate.

1. Introduction

In industrial processes, esterification plays a key role in the synthesis of essential compounds used in different areas of application such as in the field of fibers, films, adhesives, plastics and solvents[1]. The process of *esterification* mainly involves the reversible reaction of an alcohol and a carboxylic acid molecule to form an ester and condensate water. For this reason the removal of water, the by-product, during the industrial production in liquid phases is of crucial interest[1]. Natural sources of esters are fats and fatty oils and are formed in nature by enzymes, which act as a catalyst in the reaction[2]. Besides these natural reactions, different catalyst materials such as strong mineral acids (sulfuric acid, hydrogen chloride[3,4]) or ion exchangers[5] catalyze the synthesis of esters in industrial approaches. The drawback of these methods is the formation of environmentally harmful by-products (e.g. different types of acids, heavy metal compounds). Therefore, the usage of environment friendly materials in the synthesis is of high importance. Different metal catalysts can be used, which catalyze the reaction and avoid malign by-products at the same time. For this reason, the increasing interest in gold (Au) catalysts in the oxidative coupling reactions of alcohols has led to the development of new nanostructured materials in recent years[6]. One material established in the last few decades is the so-called nanoporous gold (NPG). This material is synthesized by the chemical or electrochemical etching of gold-alloys that were previously formed with different miscible metals (i. e. aluminum[7], silver[8] and copper[9]). The so-obtained porous structure, with small ligament sizes, capable of holding metal traces from the dealloying process, is able to catalyze different reactions (such as oxidative methanol coupling in liquid or gas phase[10] and the oxidation of carbon monoxide[11]) with enhanced activities at low temperatures compared to corresponding supported catalysts[12,13].

One model reaction, frequently used in the literature, is the oxidation of carbon monoxide (CO) to carbon dioxide (CO_2)[14–19]. This reaction is traceable in larger quantities in the emissions control of vehicles[20–22]. CO tends to be one of the main partially oxidized products after the fuel combustion in the engine, which gets further oxidized by the exhaust catalyst to release the rather less toxic CO_2 into the environment. This reaction would require very high temperatures or may not even be possible under certain working conditions, for which the catalyst is the solution to decrease the

working temperature necessary in the exhaust (with a catalyst temperature can be reduced to <300°C[23]). The following image shows a scheme of a simplified energy diagram for a reaction carried out in absence and presence of a catalyst, on the example of the CO-oxidation.

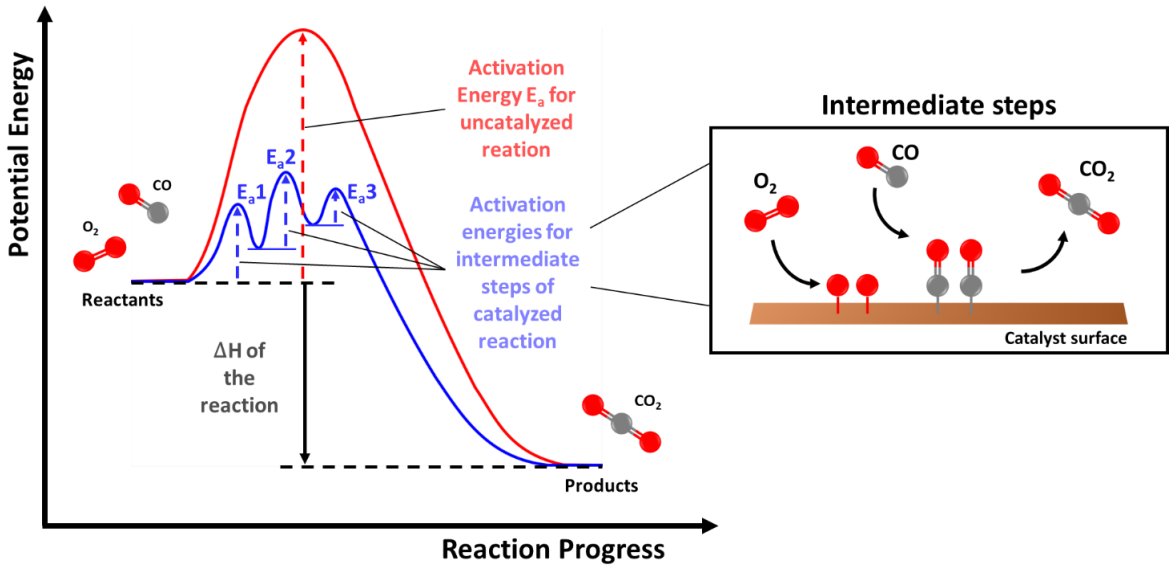

Figure 2A.1 Left: Energy diagram for uncatalyzed and catalyzed reaction as a simplified example on the oxidation of carbon monoxide. Right: Simplified intermediate steps involved in the oxidation of carbon monoxide on a catalyst surface[24–26].

This considerably simple reaction goes through a diverse number of intermediate steps –subdivided to adsorption, dissociation and reaction of the reactants with the final desorption of the product – which ultimately decrease the overall activation energy in comparison to the uncatalyzed reaction itself (see left part of **Figure 2A.1**).

Another reaction of interest for the nanoporous gold is the oxidative methanol coupling in the gas phase over the gold catalysts, in which two methanol molecules are coupled by using oxygen over the gold surface[27]. The following scheme adapted and modified from the work of Personick et al.[6] describes the mechanism of the oxidative methanol coupling on the gold surface and will be used to further explain the reaction.

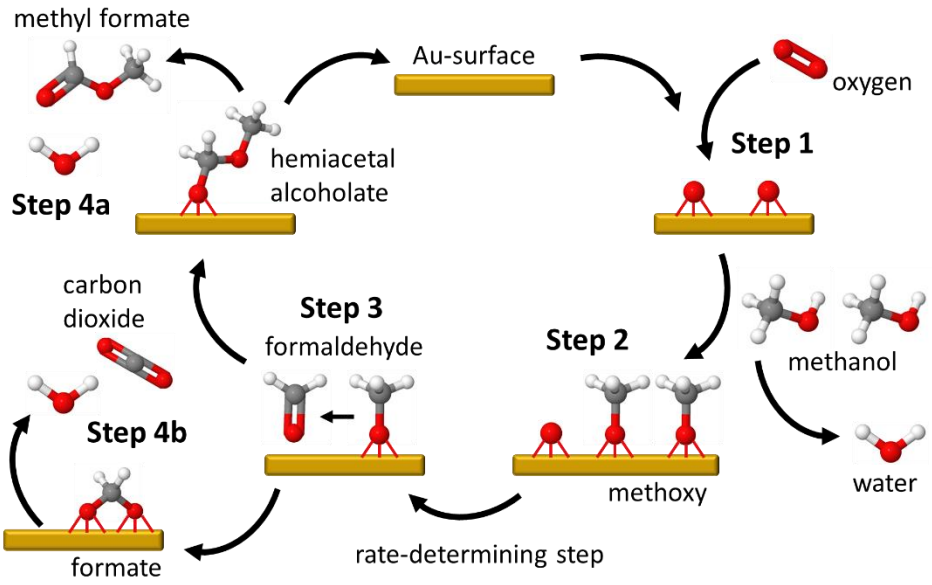

Figure 2A.2 Reaction mechanism of oxidative methanol coupling to methyl formate over a gold surface[6].

The initiating step of the oxidative methanol coupling (**Figure 2A.2**) is the adsorption of oxygen on the catalyst surface (Step 1) followed by the formation of methoxy groups from the methanol feed and the simultaneous condensation of water (Step 2). The rate-limiting step in this reaction is the β-H-elimination of the methoxy-group to form formaldehyde (Step 3). This formaldehyde can undergo two different reaction paths: Firstly, a formaldehyde molecule can react with other methoxy-species to become a hemiacetal alcoholate on the surface which finally desorbs to form the products methyl formate and water (Step 4a). Apart from this step, the formaldehyde can be further oxidized on the surface to formate, which finally combusts to carbon dioxide and water (Step 4b). This step occurs in the presence of higher oxygen concentrations in which CO_2 is an undesirable side-product[27]. Related to this, the selectivity for the coupling products appears to decrease with increasing metal trace content, as the metal traces can be present on the surface in an oxidized state, which are required in a moderate amount for the reaction to occur[28]. In the work of Wittstock et al. the ratio of higher concentrations of adsorbed oxygen compared to adsorbed methanol favored the combustion to CO_2 and, along with high O_2 pressures[29], were showing a similar behavior in the reaction. In other works of Lackmann et al.[10] low coordinated surface sites of gold were identified to be active for the coupling of methanol. This result was controversial, due to the previously mentioned influence of the metal trace content on the activity, and requires further investigation. Although a large number of studies clearly indicates that the presence of metal traces

are the reason for the high activity of these catalysts, low coordinated surface sites are not a negligible characteristics and can contribute to the activity[30,31].

Despite these fascinating catalytic functions, the synthesis method of these materials has many drawbacks, such as the limitation of the chemical composition of the final product or the restriction of control over pore sizes. Furthermore, no published work can explain if actual pure NPG structures are able to catalyze the reaction, to prove if the metal traces in the NPG synthesized by the top-bottom approach play a crucial role in the reactions. In addition, the reproducibility of this approach is not high, as the starting point of the alloy is not always homogenous and the formation of clusters during the dealloying process[32] leads to a poor distribution of the metal traces. For these reasons, it would be desirable to develop a new method for the synthesis of nanoporous structures by which it is possible to tune the composition and amount of metal trace in the system, in order to investigate in more detail these effects on the activity.

In our work, we chose a bottom-up approach to tackle this challenge, exploiting the self-assembly of nanoscale units (i.e. metallic nanoparticles) through the cryogelation method[33–35] to synthesize nanoporous materials. The colloidal synthesis of nanoparticles[36] can be briefly explained in three crucial steps. In a first step, the precursors for the formation of the particles are dissolved in a solvent until a critical supersaturation is reached, which leads to the second step of the process: the formation of nuclei from the monomers. Some of these nuclei go back to solution, but the ones which remain stable grow into the last stage of nanoparticles. The amount and type of precursor is crucial for the size control of the particles[37,38], as the formation of the nuclei depends on the presence of the precursor in solution which ultimately leads to the particles. As a rule of thumb, a small amount of precursor in solution will lead to no particles or to a large size distribution of formed particles, while large amount of precursor lead to a narrow size distribution[37]. This correlation is displayed by the LaMer diagram in the following **Figure 2A.3**.

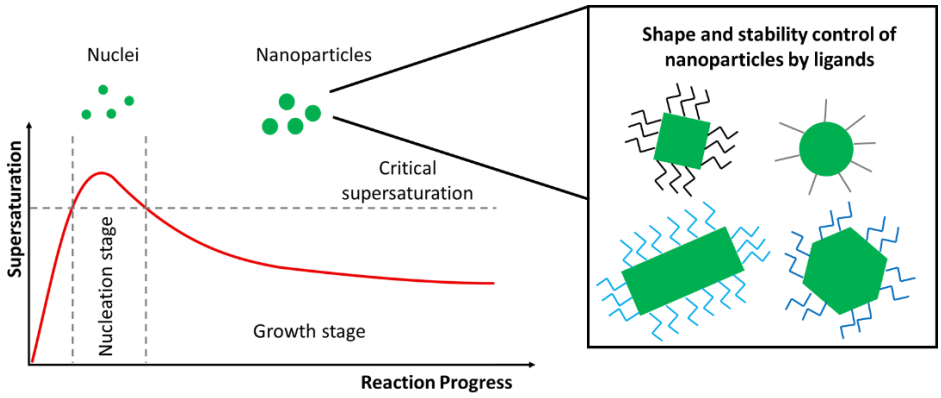

Figure 2A.3 LaMer diagram (left): After reaching critical supersaturation of precursor material, the nucleation stage is reached followed by the growth stage[39]. The choice of ligand can control the stability but also the size and shape of a nanoparticle (right).

The physicochemical properties depend on the chemical composition, shape and size of the particles and can range from large surface areas, optical activity and chemical reactivity. Whenever the formed particles aggregate, the properties they possessed can be partially lost. Hence, it is crucial to stabilize particles, which can be achieved using different methods[40,41]. The most common way of stabilization is the usage of ligands having long carbon chains to passivate the surface of the particles. The ligands do not only control the shape of a particle by attaching to certain crystal sites of a particle and blocking those in their growth[41,42]. They also stabilize the particle through steric hindrance: whenever two particles with surface ligands get close, the ligands hinder the possibility of aggregation. Furthermore, it enables the particle to be soluble in solvents which are in the same polarity range of the ligand itself. Another method to stabilize particles is to provide a charge on the particle surface[40,43], which leads to Coulomb repulsion whenever particles come too close to each other (as in case of citrate-capped particles)[44].

In catalysis, the synthesized nanoparticles can be deposited on high surface area oxides to perform catalytic reactions, as the interface between the oxide and the nanoparticle can enhance the catalytic activity[15,45]. Another possibility is to use the pure particles either by depositing them on a plane surface[46], or through a self-assembly method which leaves a 3D network of particles as a final material. The self-assembly of particles is obtained by a controlled destabilization[34]. Taking particles with a ligand, a destabilization agent can be added to the solution to destabilize the particles without aggregation. This destabilization agent can be a salt in case of particles with a surface charge or oxidizing agents for particles with long-chained ligands. The ions of a saline solution added to a nanoparticle with surface charge can destabilize the particle by a recombination

of charges resulting in an uncharged particle. Oxidizing agents instead can oxidize the ligands on the surface of a particle leading to partial destabilization[47,48]. Taking as an example, thiolate capped nanoparticles can be destabilized using hydrogen peroxide in a controlled manner[47]. Then the solvent can be dried by using the supercritical drying method, in which liquid CO_2 is used to exchange the solvent of the system, which then evaporates after reaching the supercritical point[33,34]. The so obtained structure has no volume loss and is called *aerogel*[33,34]. Another method[35] is to concentrate the particles to a certain level such that freezing the solution (as in case of water as a solvent) results in an ice-templated assembly of these particles. The subsequent freeze-drying step (temperatures below freezing point of water and application of vacuum environment) leads to the sublimation of the ice-template and results in a self-standing 3D-structure of particles. Hence, this method can be called *cryogelation*[35]. Freytag et al. showed in their work a simple method to build 3D disordered porous structures (i.e. cryogels) by freeze-drying of different metallic nanoparticles (NPs)[35].

The aim of this work is thus to obtain nanoporous metal structures with morphologically and chemically controlled properties as the building units, which is not achievable through the more established dealloying process (as in the case of NPG). With this approach, the role of the metal traces in the oxidative methanol coupling will be studied and clarified in further detail.

2. Experimental Methods

Synthesis of nanoparticles and gels

The aqueous Au NPs were prepared by a citrate reduction approach at room temperature[35] (gold(III) chloride hydrate, sodium borohydride, trisodium citrate dihydrate purchased from Sigma-Aldrich). Subsequently, the NPs were concentrated by using 10 kDa cellulose membranes (purchased from Sartorius for Vivacell® and centrifuge tubes purchased from Millipore) to the required volume ratio of 0.1% v/v[35]. The concentrated solution was injected in liquid nitrogen and subsequently freeze-dried (using a freeze-dryer model Lio 5P) to remove the ice templates and obtain a 3D self-standing nanoporous structures of pure gold (also called “gel”). In order to obtain nanoporous structures decorated with different metals (in a gold to metal ratio of 95:5 to aim for similar structures as in published works[9,28]), aqueous copper/silver/cerium/palladium (copper(II) nitrate trihydrate, silver nitrate, cerium(III) nitrate hexahydrate, tetraamminepalladium(II) chloride monohydrate purchased from Sigma-Aldrich) salt-solutions were added to the diluted Au NPs prior to concentration. The following scheme describes the procedure for the synthesis of the gels.

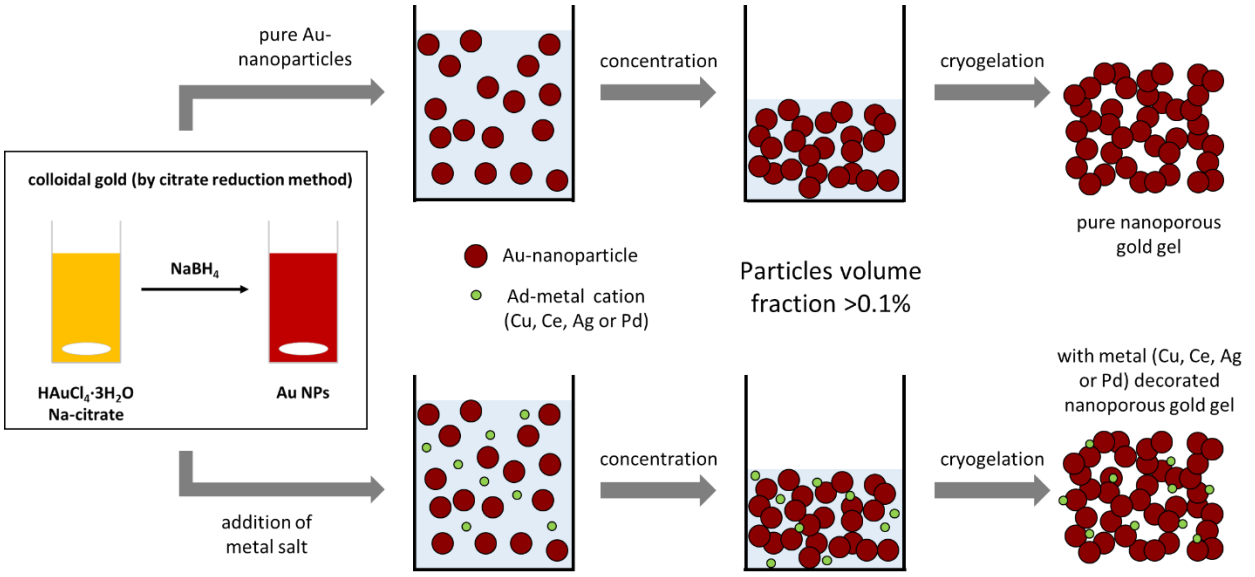

Figure 2A.4 Scheme of synthesis procedure for pure gold gel systems (upper part) and decorated gold gel systems (lower part).

Transmission electron microscopy (TEM)

To characterize the gold nanoparticles regarding size and shape, the sample solution was dropped on a copper-grid and dried in air. Afterwards, the sample was analyzed by transmission electron microscopy (TEM, Jeol JEM-1011 with a thermionic W source operated at 100 kV).

Elemental analysis

The concentration of the solution was analyzed before and after the concentration step, to verify if the necessary volume fraction of 0.1% v/v, which is the minimum concentration for a successful gelation, was achieved[35]. In addition, the amount of add-metal was determined before and after concentration. The term *add-metal* derives from the fact that metal salt solutions were added to the colloidal solution, which finally results in the presence of add-cations and after cryogelation the presence of add-metals on the surface of the catalyst. The characterization was carried out with an inductively coupled plasma-optical emission spectroscope (ICP-OES, iCAP 600 series by Thermo Scientific). The sample was dissolved in aqua regia (3:1 ratio of hydrochloric acid and nitric acid: Sigma-Aldrich, for analysis) and diluted 1:10 with water after letting it digest overnight. Then the solution was filtered (syringe filter, PTFE-membrane with 0.2 µm pore diameter) and analyzed.

Scanning electron microscope (SEM) and energy dispersive X-ray spectroscopy (EDX)

The gels were investigated for their microscopic structure and porosity. For this, the sample was fixed with an adhesive carbon tape on an aluminum stub and investigated with a scanning electron

microscope (SEM, Jeol JSM-6490LA with an embedded energy dispersive X-ray analyzer). Furthermore, the chemical composition of each gel was analyzed by energy dispersive X-ray spectroscopy (EDX) at three different areas of the material and compared to previously collected data by ICP-OES after concentrating the individual solutions.

X-ray Photoelectron Spectroscopy (XPS)

To further compare the concentrations of decorated metals to gold on the surfaces of the samples, X-ray Photoelectron Spectroscopy (XPS, Kratos Axis Ultra DLD spectrometer equipped with a monochromatic Al Kα source (15 kV, 20 mA)) was carried out on each sample before and after the catalytic tests. The samples were prepared as previously described for SEM investigations, creating a flat surface by pressing the sample on the tape.

High resolution scanning electron microscope (SEM) equipped with EDX

Backscattered electrons (BSE) images having compositional contrast were collected using a JEOL JSM-7500FA instrument, equipped with a cold field emission gun (single crystal <310> emitter), a 2-segment solid state annular BSE detector and operating at 10kV. The performed experiments were used to investigate the surface of the samples with add-metals.

High angle annular dark field (HAADF) scanning TEM (STEM) equipped with EDX

High angle annular dark field (HAADF) scanning TEM (STEM) images were collected using a FEI Tecnai G2 F20 TWIN TMP with a Schottky emitter operated at 200 kV. The EDX analyses have been acquired using a Bruker XFlash 6|T30 silicon-drift detector (SDD), with 30 mm^2 effective area. The samples were sonicated for 3 h in ethanol and dropped on a Nickel grid (previously cleaned with a plasma-beam) to let it dry in air. The information gathered by this method was used to verify surface species of add-metals.

Krypton physisorption measurements

Krypton physisorption measurements were carried out at 77 K using a gas sorption analyzer, model Autosorb-iQ (Quantachrome Instruments). The samples were initially degassed for 2 h at 120 °C under vacuum conditions to remove weakly adsorbed species. The specific surface areas were calculated using the multipoint Brunauer-Emmett-Teller (BET) model, considering 8-11 equally spaced points in the P/P_0 range from 0.05 to 0.3. P_0 is the vapour pressure of Kr at 77 K, corresponding to 2.63 Torr. A more detailed discussion on the specific surface area can be found in the appendix of this chapter.

CO oxidation

Besides these characterization techniques, two different catalytic tests were carried out on each sample. First, the conversion of carbon monoxide to carbon dioxide was analyzed, since this is a model reaction for catalysts[9]. The term *conversion* in gas-phase catalysis describes the amount of reactant transformed into products. The amount of the converted reactant depends on the catalyst properties. Following equation states the reaction for the oxidation of CO to CO_2:

$$2\,CO + O_2 \rightarrow 2\,CO_2 \qquad (2A.1)$$

In some reactions it is possible that not all of the CO is converted to CO_2, due to poor catalyst performance, low reaction temperatures and poisoning of the catalyst over time[49,50]. This would automatically lead to lower CO-conversions, which can be identified by the known concentration of CO fed into the system $[CO_{in}]$ and by analyzing the emitted CO after the catalytic reaction $[CO_{out}]$. Then the conversion (in %) of the reaction can be calculated according to the following Equation (2):

$$\text{Conversion}\% = \frac{[CO_{in}] - [CO_{out}]}{[CO_{in}]} \cdot 100 \qquad (2A.2)$$

The total concentration of the fed CO ($[CO_{in}]$) to the system subtracted the concentration of CO after catalytic reaction ($[CO_{out}]$) divided by the total initial CO concentration results in the final conversion of CO.

To obtain the required values, the samples were measured using a micro reactor system coupled with a gas analyzer (Advance Optima AO2020 Series Continuous Gas Analyzer) to detect the CO and CO_2 concentrations at the reactor outlet. The reaction was carried out using 1 vol-% CO and 10 vol-% O_2 balanced with He, at a flow rate of 60 Ncc/min. The outlet concentrations were screened while the temperature of the reactor was ramped to 300°C at 5°C/min ending in a dwell at this temperature for 1 h. After that, the cooling step on each system was initiated (cooling rate of 25°C/min).

Methanol coupling

Furthermore, the oxidative methanol (MeOH) coupling[28] reaction was carried out to form methyl formate (MeF). This reaction can be written as following:

$$2\,MeOH + O_2 \rightarrow MeF + H_2O \qquad (2A.3)$$

The *reaction rate* of a reaction describes the consumption of reactant per unit time or the formation of the product per unit time[51]. The reaction rate for the oxidative methanol coupling was calculated using the following two equations:

$$Q_m(CH_3OH) = \frac{Q(CH_3OH) \cdot Conversion(CH_3OH)}{V_m} \quad (2A.4)$$

$$r = \frac{Q_m}{m_{cat}} \quad (2A.5)$$

In the first equation the molar flow rate Q_m of methanol is calculated by using the volumetric flow rate Q of methanol, the conversion of methanol and the molar Volume V_m (which is 22.414 L mol^{-1}). In the second equation the molar flow rate is used to calculate the reaction rate r of a certain mass of catalyst m_{cat}. As the reaction rate can depend on the amount of catalyst used or on the specific surface area of the catalyst further considerations need to be carried out. To have a better comparability between different reactions/catalysts, the reaction rate can be normalized to the used mass of catalyst or specific surface area. To do so, the reaction rate is divided by the mass/specific surface area.

Some reactions can have multiple products after reaction, of which one is a more favored product[28]. Hence, it can be necessary to identify which catalyst is promoting the formation of the desired product with a higher selectivity. Taking the oxidative coupling of methanol as an example[28], the preferred product obtained during this reaction is methyl formate, which is formed over various intermediate steps on the catalyst surface. One of the intermediate steps can lead to carbon dioxide instead of continuing on the path for methyl formate, which is an undesired product. To calculate the selectivity of the reaction the following equation was applied to the obtained product concentrations:

$$S_P(MeF) = \frac{2 \cdot [MeF]}{2 \cdot [MeF] + [CO_2]} \quad (2A.6)$$

In this equation S_P represents the selectivity of the product (here methyl formate MeF), whereas the concentrations of the products methyl formate and carbon dioxide are represented by $[MeF]$ and $[CO_2]$, respectively.

To follow this reaction, a time-resolved Fourier-transform infrared spectroscope (FTIR) was used (Spectrum Two™ by Perkin Elmer). The flow rate was set to 40 Ncc/min containing around 2.3 vol-% methanol and 1.15 vol-% O2 balanced with He. The catalyst was tested in a steady-state

reaction at 50, 100, 150 and 200°C for 1 h. A saturator filled with methanol was prepared and cooled by using a chiller (~-8°C). To create a flow with methanol, helium and oxygen were sent to the saturator and switched to the reactor (see scheme in **Figure 2A.5**). The estimated methanol concentrations in the flow were calculated by applying the temperature of the ice bath on the Antoine-equation[52] (further explained in the appendix of this chapter).

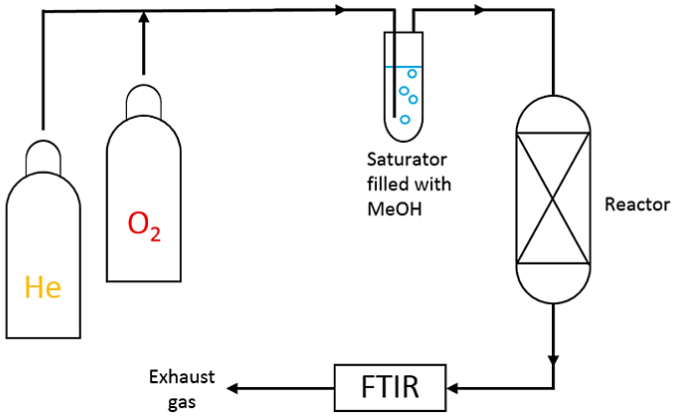

Figure 2A.5 Scheme of experimental setup: Oxygen balanced with Helium flows through a cooled saturator filled with methanol into the reactor. Out coming products are measured at the exit of the reactor by a FTIR.

The total flow of the reaction was 40 Ncc/min, all set temperatures and gas mixtures (in vol-% balanced with He) can be taken from **Figure 2A.6**.

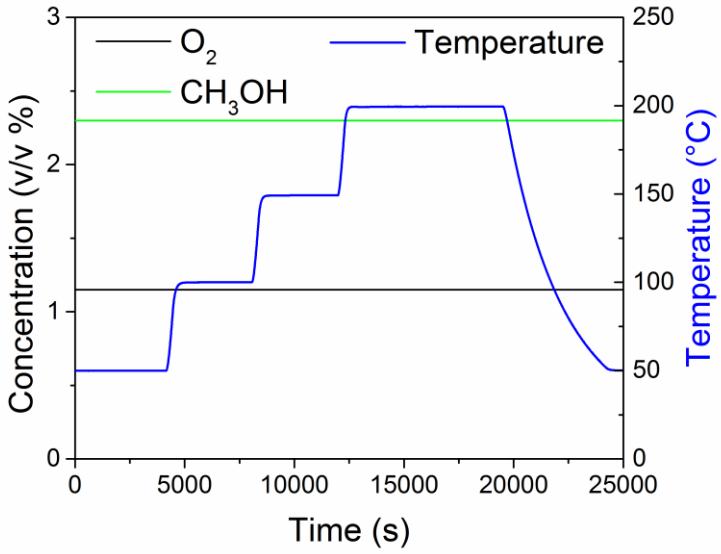

Figure 2A.6 Sequence of gases and temperature dwells for methanol coupling on synthesized catalysts.

3. Results and Discussion

Characterization of gels

The synthesized Au particles showed a non-spherical shape with a size distribution of 3.8 ± 1.1 nm, which was identified by TEM (see following figure).

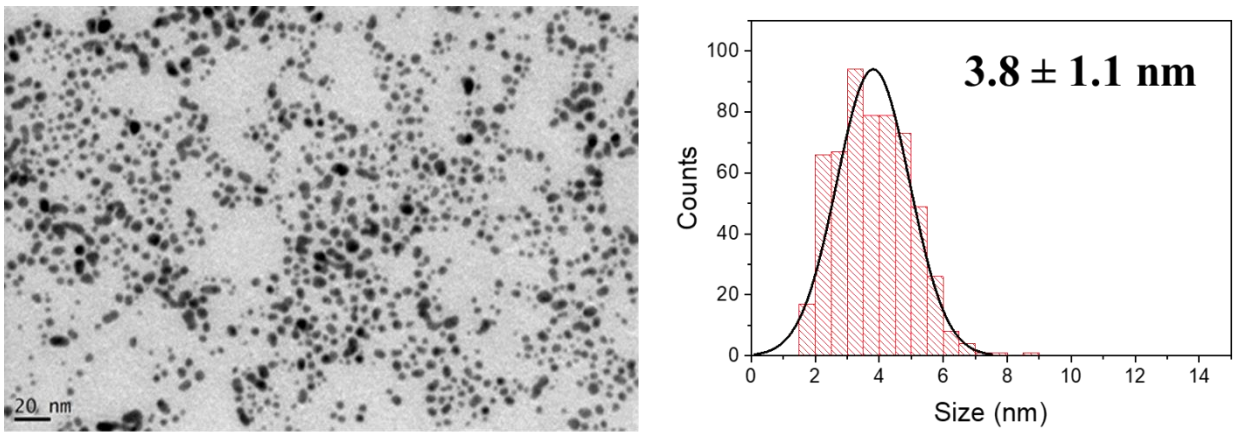

Figure 2A.7 TEM-image of synthesized Au NPs using citrate reduction method (left) and particle size distribution (right).

These particles were used for the synthesis of the gels. The dark red color of the particles is partially visible in the freshly synthesized gels (slightly darker or occasionally with a golden shimmer). The following figure is showing the change of the gels after the exposure to reaction conditions (at 300°C for 1 h in 1 vol-% CO and 10 vol-% O_2 atmosphere).

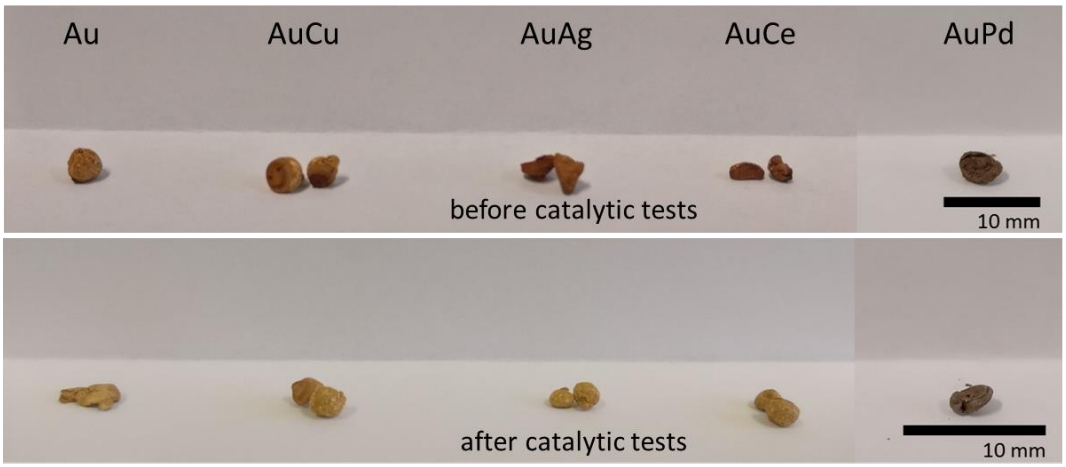

Figure 2A.8 Selection of gels: Pure (with Na+) and doped with different cations before (up) and after (bottom) catalytic tests (at 300°C for 1 h in 1 vol-% CO and 10 vol-% O_2 atmosphere).

Figure 2A.8 shows the change of the color of the gels after the tests: All samples were dark red with a slight golden shimmer when freshly synthesized. Only the sample containing Pd was moderately brown due to the presence of Pd. Independently from the doping cation, the gels appear brighter but also smaller (loss of volume) and more stable than the fresh gels after being exposed to reaction conditions. This can be explained by the high temperatures at which they have been exposed to in the reactors (~300°C), which on one hand "cleaned" the surface of the gels from organic ligands, but on the other hand lead to a shrinkage of the nanoporous network. This loss of volume can be detrimental for the activity of the catalyst, as a decreased surface area can be linked to the loss of volume. This behavior is similar to the coarsening effect occurring in case of the nanoporous gold, in which smaller ligaments can coarsen to ten times of their starting sizes[53]. Such an observation was characterized by SEM-imaging of the gels before and after exposure to high temperatures (at 300°C for 1 h in 1 vol-% CO and 10 vol-% O_2 atmosphere) and can be seen in the following images.

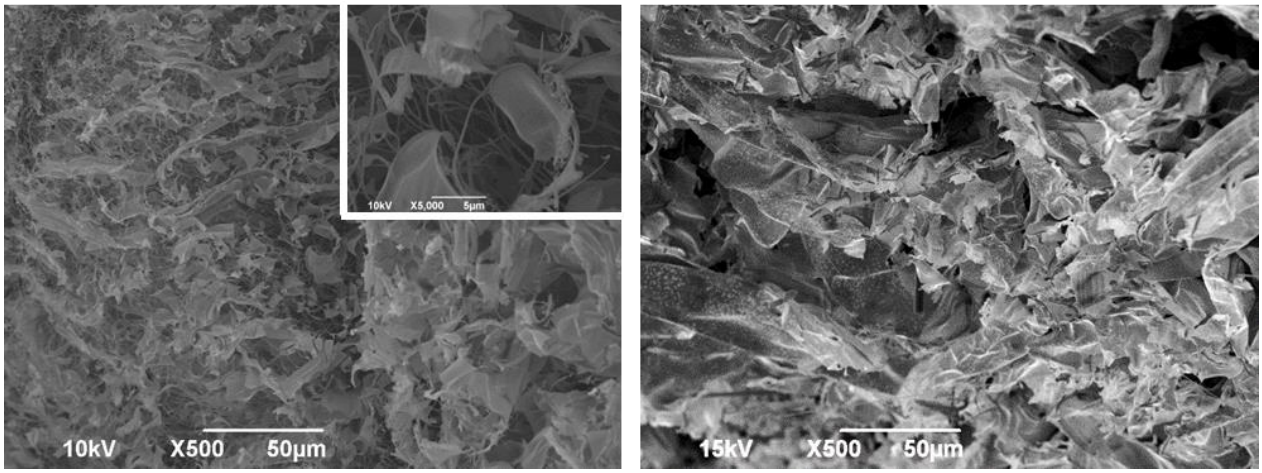

Figure 2A.9 Pure Au-gel (with Na+) before (left) and after (right) catalytic tests (at 300°C for 1 h in 1 vol-% CO and 10 vol-% O_2 atmosphere).

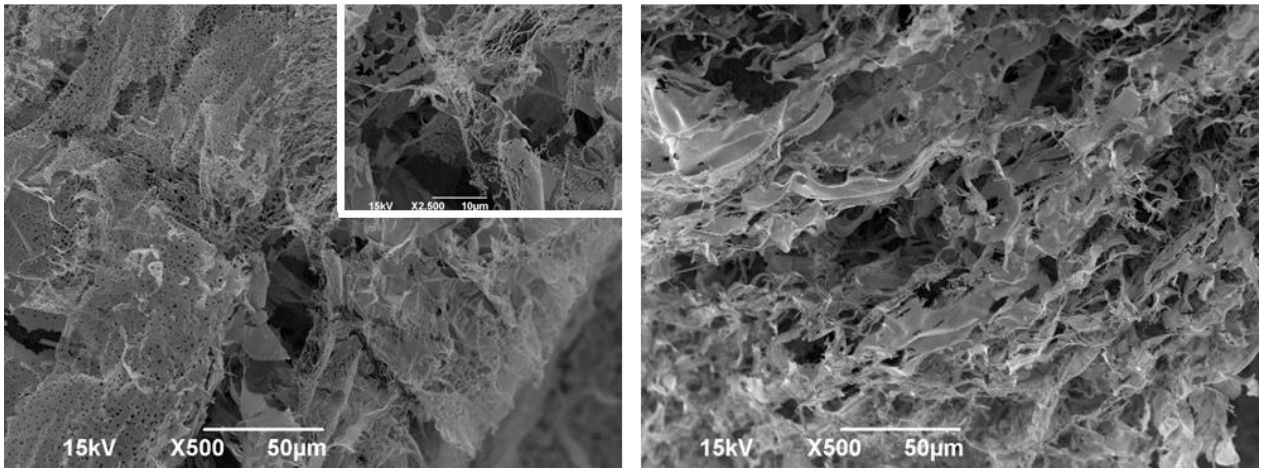

Figure 2A.10 AuCu-gel synthesized according second approach before (left) and after (right) catalytic tests (at 300°C for 1 h in 1 vol-% CO and 10 vol-% O_2 atmosphere).

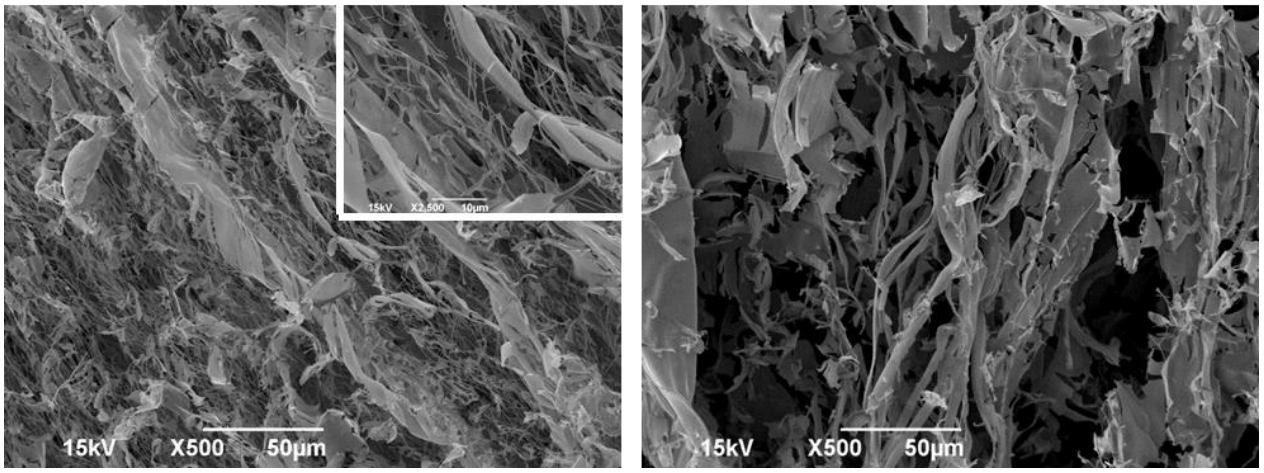

Figure 2A.11 AuCe-gel synthesized according second approach before (left) and after (right) catalytic tests (at 300°C for 1 h in 1 vol-% CO and 10 vol-% O_2 atmosphere).

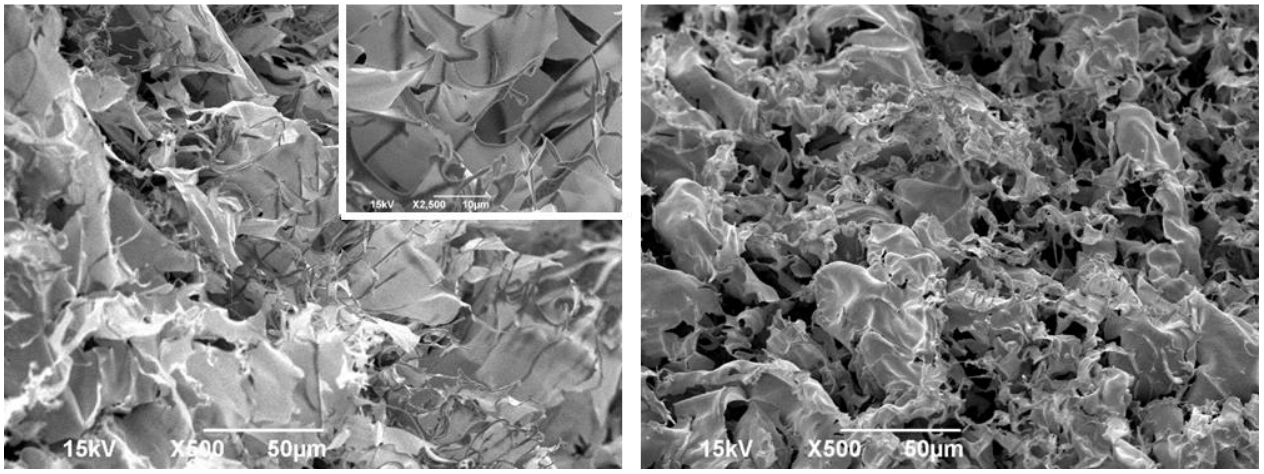

Figure 2A.12 AuAg-gel synthesized according second approach before (left) and after (right) catalytic tests (at 300°C for 1 h in 1 vol-% CO and 10 vol-% O_2 atmosphere).

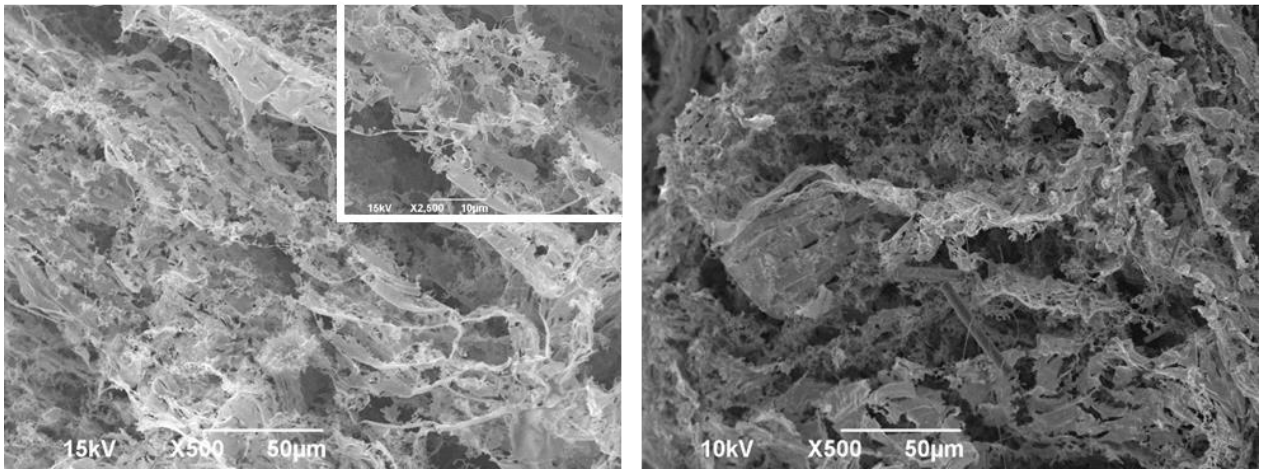

Figure 2A.13 AuPd-gel synthesized according second approach before (left) and after (right) catalytic tests (at 300°C for 1 h in 1 vol-% CO and 10 vol-% O_2 atmosphere).

In **Figure 2A.9-Figure 2A.13** SEM-images of different Au-gels with different add-metals before and after thermal treatment (at 300°C for 1 h in 1 vol-% CO and 10 vol-% O_2 atmosphere) are shown. Morphologically, there is no difference between the gels: Independent from the add-metal (or without) the samples show wire-like and flake-like porous structures at the beginning, which reduce once the catalyst was exposed to catalytic conditions. This type of coarsening can also be found for the nanoporous gold[53] whenever temperatures above 100°C are reached and can be explained by the low Tammann temperature[54] of gold (around 395°C). In comparison to the porous structures observed by SEM, the specific surface area (SSA) measured by Kr physisorption revealed low SSA of around 1 $m^2 g^{-1}$ (see isotherms in appendix). These results were comparable to NPG obtained by a top-down approach (2 to 5 $m^2 g^{-1}$)[11].

To further underline the change of the nanoparticular domains, XRD-experiments were performed to determine the crystallite sizes using the SCHERRER-equation (further explained in the appendix of this chapter). The following table presents the results of these experiments.

Table 2A.1 Crystallite sizes of synthesized Au-gels (with and without add-metals) before and after thermal treatments (at 300°C for 1 h in 1 vol-% CO and 10 vol-% O_2 atmosphere) determined by XRD.

Sample	Crystallite size before thermal treatment /nm	Crystallite size after thermal treatment /nm
Au-gel	**6.8 ± 0.6**	**20.9 ± 0.2**
AuCu-gel	**8.5 ± 1.7**	**22.2 ± 1.3**
AuCe-gel	**21.8 ± 0.7**	**19.9 ± 0.2**
AuAg-gel	**11.6 ± 1.2**	**21.2 ± 1.0**
AuPd-gel	**6.7 ± 0.7**	**20.2 ± 1.4**

As it can be seen in the comparisons of the crystallite size before and after thermal treatments, the crystallite domain grew double to three times compared to the starting value. Hence, the applied SCHERRER-equation on these patterns confirm the increased ligament sizes observed by SEM previously. The only exception can be found for AuCe-gel (marked in red) which shows a similar crystallite size before but also after the treatments. This observation can be explained by the possibility that the domain size for this sample is larger than for the other samples from the beginning, due to instability of the particles when the Ce-salt is added to the solution prior to concentration and gelation.

The synthesized Au NPs solutions were analyzed by ICP-OES before and after the concentration step not only to verify the presence of the doped metals in the correct ratio after concentration, but also to verify that the desired volume ratio of 0.1 vol-% was achieved. The gels obtained from these solutions were then analyzed by EDX and XPS, before and after catalytic tests to have a comparison. Furthermore, comparing EDX and XPS data could show differences between the bulk (EDX) and surface composition (XPS). The following table is showing the results of the measurements (in atomic %) before and after catalytic tests for each metal decoration.

Table 2A.2 Ratios of gold to doped metal determined (atomic %) by ICP-OES, EDX and XPS before and after catalytic tests (at 300°C for 1 h in 1 vol-% CO and 10 vol-% O_2 atmosphere).

Metals	Before catalytic tests			After catalytic tests		
	XPS	EDX	ICP	XPS	EDX	ICP
Au	98	99	99	99	99	-
Cu	2	1	1	1	1	-
Au	95	99	99	86	99	-
Ce	5	1	1	14	1	-
Au	85	97	96	85	97	-
Ag	15	3	4	15	3	-
Au	94	97	96	95	97	-
Pd	6	3	4	5	3	-

As it can be seen in **Table 2A.2**, the values before and after catalytic tests are comparable for AuCu and AuPd. This means that the surface concentration of the species corresponded to their bulk concentration. However, for the AuCe and AuAg gels, a different situation was observed (marked in red). In the case of AuCe-gel, the surface concentration of Ce was much higher after the catalytic tests. This can be explained by the formation of Ce-oxides on the surface of the gels. The Ce seems to migrate from the bulk of the sample to the surface to form oxides (presence verified by EDX-mapping, discussed later). For the AuAg-gel, the formation of AgCl-crystals (presence verified by EDX-mapping, discussed later) already in the fresh sample can be an explanation for the observed results. The usage of Gold (III) chloride trihydrate as a precursor to synthesize the Au NPs delivers chlorine ions in the solution, which lead to the growth of AgCl-crystals on the Au-gel surface as soon as the silver nitrate is added to the colloidal solution prior to gelation.

XPS was also identified as the best technique to understand the oxidation state of the decorated metals on the sample surface before and after exposure to catalytic atmospheres. The following image summarizes the oxidation states of the decorated metals before and after the tests.

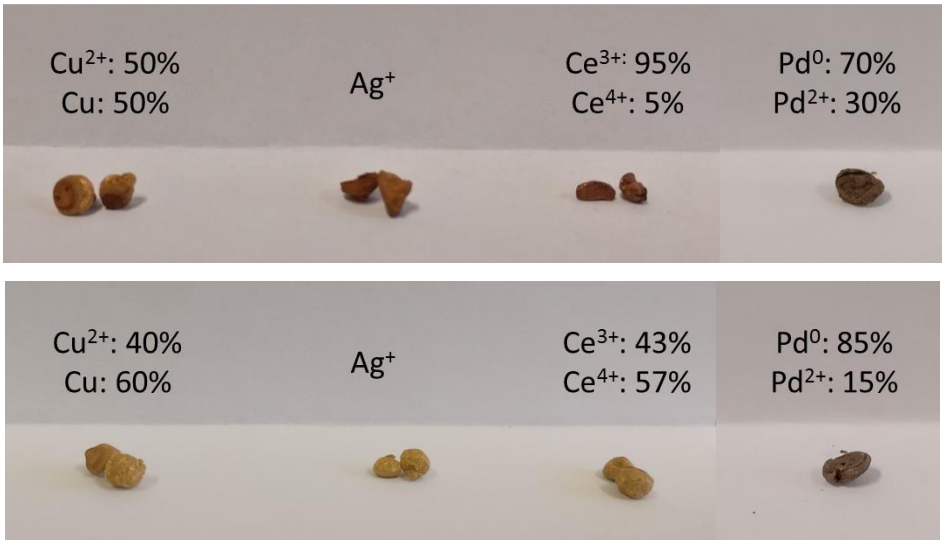

Figure 2A.14 Semi-Quantitative XPS-investigations on oxidation state before (top) and after (bottom) reaction conditions (at 300°C for 1 h in 1 vol-% CO and 10 vol-% O_2 atmosphere, followed by oxidative methanol coupling at 200°C for 1 h in 2.3 vol-% MeOH and 1.15 vol% O_2).

The presence of Ag^+ before and after the tests, displayed in **Figure 2A.14**, is explained by the formation of AgCl, which will be further underlined by EDX-mappings later in this chapter. Apparently, in the case of copper a reduction is taking place. However, to avoid misunderstandings it is important to mention that Cu^{2+} species can be reduced due to X-ray radiation[55]. Hence, the sample might have both oxidation states present, although Cu^{2+} is more likely, as a Cu^{2+}-salt was used during the synthesis. In case of AuCe-gel a transformation from Ce^{3+} to Ce^{4+} can be observed which is in agreement with other investigations such as EDX-mapping, which will be discussed later in the thesis. This observation can be an indication for the formation of oxides on the sample surface. The oxidation state of Pd was problematic to identify as the signals of Pd (3d peaks) were covered by Au (4d peaks) signals (same binding energy range). Nevertheless, the reduction of Pd can be due to a reductive atmosphere on the catalyst during the reaction (i. e. the methanol can reduce the surface). Furthermore, the explanation for the starting material with Pd being 70% in the reduced oxidation state can be due to the excess of the reducing agent (sodium borohydride) in the reaction solution of the synthesized nanoparticles.

To understand the distribution of the metal traces on the samples, the gels were investigated by EDX-mapping (HRSEM and STEM). The following images are showing the results on the AuAg-gel of these measurements.

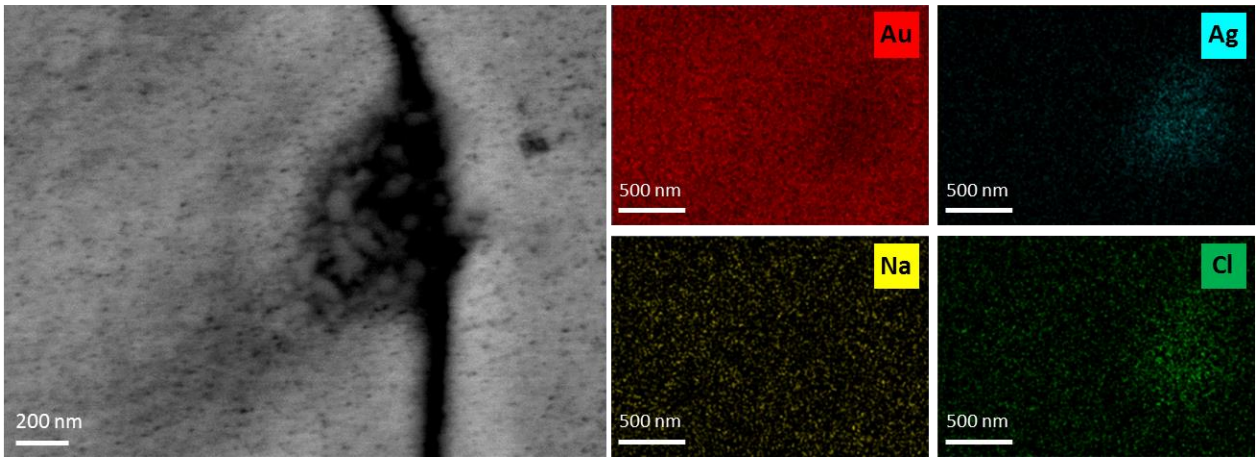

Figure 2A.15 HRSEM-EDX image on AuAg-gel before reaction conditions; left: Image used for mapping, right: Mapping with Au, Ag, Cl and Na.

In **Figure 2A.15** the mapping reveals presence of AgCl particles of a few hundred nm size, as the Ag and Cl-signals overlay, where Au-signals are lower. This can be seen as a clear identification of AgCl crystals distributed on the surface of the catalyst.

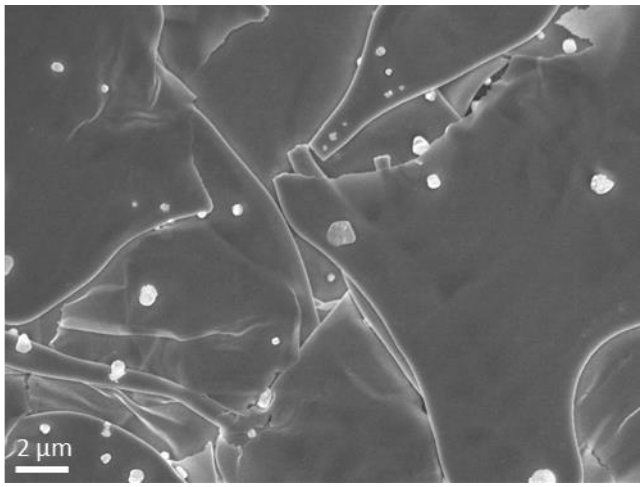

Figure 2A.16 SEM-image of AgCl-crystals on the gel before reaction conditions.

In **Figure 2A.16** the SEM-image shows little crystallites, which were identified as AgCl by EDX-mapping. Consequently, in this case the silver is not distributed on the catalyst surface but instead accumulated as AgCl. AgCl is a very stable composition, which can lead to inactivity during catalytic tests. Indeed, this was the case with this sample when CO-oxidation and the methanol coupling reactions were carried out (see later). In literature the enhancing effect of silver impurities

in NPG were reported[8]. Controversially to this, we obtained the poorest results for this sample in comparison with other samples for the CO-oxidation due to AgCl crystallization. Hence, this sample cannot be directly compared to NPG, as the Ag is not present as a metal trace, which can be oxidized on the surface to contribute to the activity of the catalyst.

The usage of the HAADF-STEM equipped with EDX was used to identify the distribution of the decorated metals Cu and Ce on smaller gel-fragments with a more precise method. In the following the results on both samples (AuCu- and AuCe-gel) will be discussed.

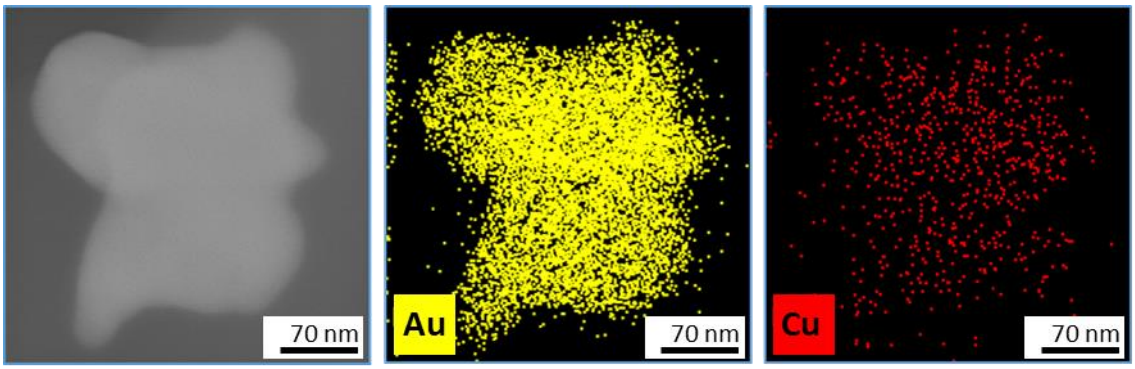

Figure 2A.17 HAADF-STEM-EDX image on AuCu-gel (left) and the correlated mapping of Au (center) and Cu (right) before reaction conditions.

Figure 2A.17 displays a fine distribution of copper on the gold fragments. No accumulations are visible which is useful for catalytic applications as more Au/Cu interfaces are available, which can increase the activity due to synergistic effects[56]. This sample is comparable to the NPG achieved by a top-bottom approach, whereas in this case the distribution of the metal trace seems to be all over the fragment, while in case clustering can occur due to the kinetics of the dealloying process[32]. The here synthesized porous gold samples were dissolved in ethanol for microscopic measurements. In general, the so formed fragments were rather large and thick, which makes a further analysis at a significantly higher magnification (for example by HR-TEM) impossible. Nevertheless, a further analysis of these samples at a slightly higher magnification can be useful to underline the state of a fine distribution of Cu on the porous gold structure.

Next, the AuCe-gels were investigated using the same technique and to clarify the results of the XPS analysis with regards to the oxidation state and Au:Ce ratio after catalytic treatments.

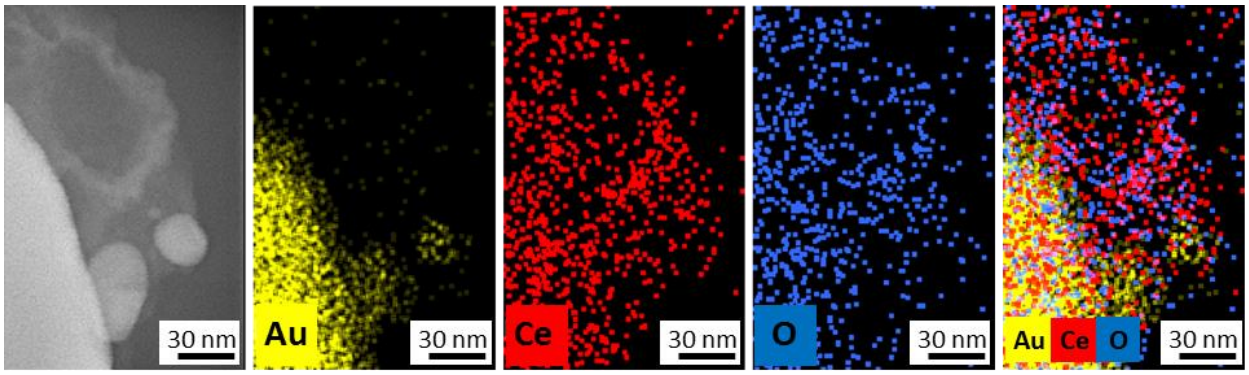

Figure 2A.18 HAADF-STEM-EDX image on AuCu-gel (left) and the correlated mapping of Au, Ce and O (center) and overlayed mapping (right) after reaction conditions (at 300°C for 1 h in 1 vol-% CO and 10 vol-% O_2 atmosphere).

In **Figure 2A.18** the formation of cerium oxide on the sample in the shape of around 100 nm islands can be identified. The mapping clearly shows cerium being located on oxygen. The usage of gold nanoparticles deposited on cerium oxide results in highly active catalysts due to the interface between the metal and the metal oxide[57]. However, the here found formation of cerium oxide islands on the surface of the porous gold can lead to inactivity during reactions, due to the reduced extent of the gold/oxide interface[56]. This result was indeed observed during the reproducibility experiments for the CO oxidation, explained at a later point.

AuPd-samples were used in HRSEM-EDX to map the distribution of Pd on the gold catalyst. The following images show the results of this experiment.

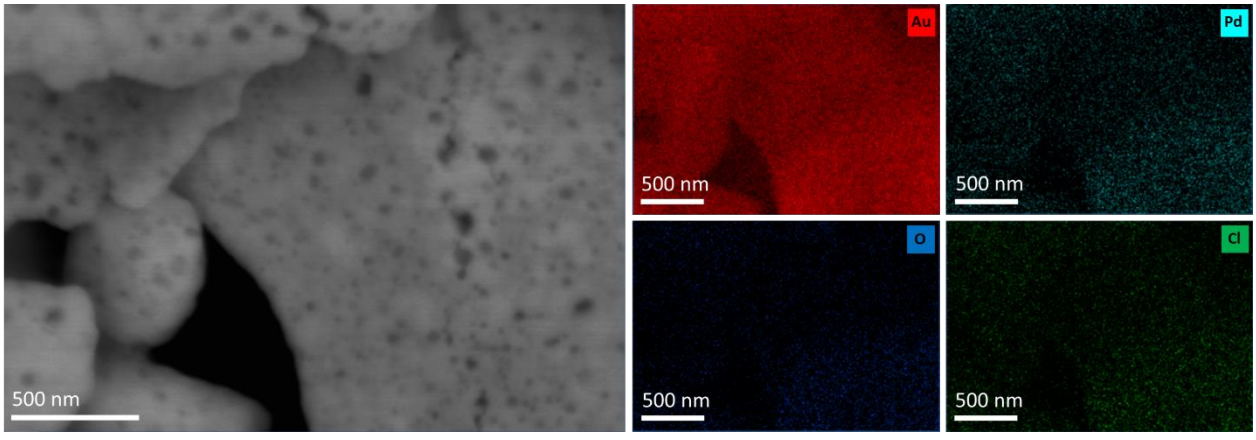

Figure 2A.19 HRSEM-EDX image on AuPd-gel before reaction conditions; left: Image used for mapping, right: Mapping with Au, Pd, O and Cl.

For AuPd-gel (see **Figure 2A.19**) a well distributed Pd-signal on the sample was found. Clustering of Pd would explain a poor activity of the catalyst due to reduced Au/Pd interfaces which are known to enhance activity of the catalyst for CO oxidation[58,59]. However, this experiment is not rich in detail and gives only an understanding on a larger scale. To see if the Pd is distributed comparable to Cu as previously shown, experiments using higher resolution techniques (such as STEM or HR-TEM) are required. Nevertheless, collecting the results of each experiment (ICP-OES, EDX and XPS) with regards to the chemical composition of the synthesized samples shows the expected gold/add-metal ratios and distribution, except in the case of AuAg-gel.

Catalytic tests: CO oxidation

To check the catalytic activity of the catalysts in CO oxidation, around 20 mg of the synthesized gels were transferred in a glass pipe filled with quartz wool. The comparison of all gels is displayed in **Figure 2A.20**.

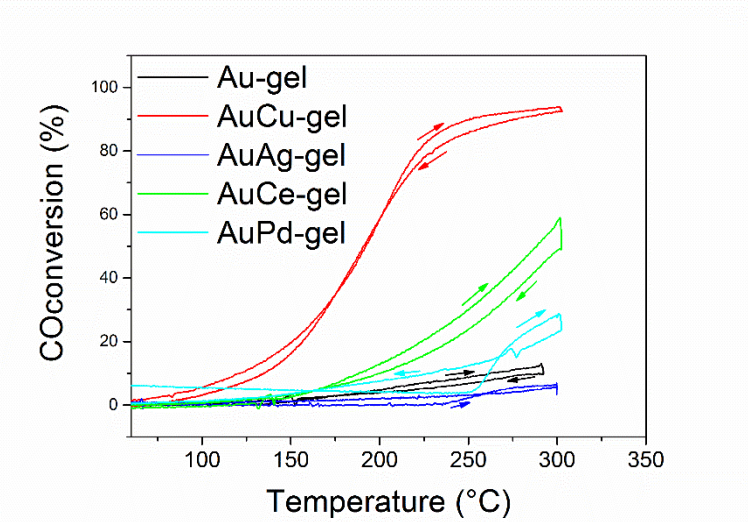

Figure 2A.20 CO-oxidation: Comparison on catalytic activity for all synthesized gels. The used sample weight in each case was 20 mg.

Figure 2A.20 reveals the effect of the different metal decorations on the porous gold system: While the AuCu-gel is active for the CO-oxidation, other dopants are showing less or no activity. The positive effect of the Cu-decoration can be due to the good distribution of the metal on the gold surface, which was investigated by HAADF-STEM-EDX. Comparing the results to NPG containing Cu as metal traces, the here shown sample has its ignition temperature at around 100°C,

while nanoporous gold is active at lower temperatures showing 100% conversion from room temperature up to 80°C at comparable catalyst weights and experimental conditions[7,9].

In case of the AuCe-gel a significant decrease of activity was detected with each cycle (see **Figure 2A.21**), explained by the development of oxides (Cerium (IV) oxide) on the surface reducing the gold/cerium oxide interface, verified by XPS and HAADF-STEM-EDX (see previous description).

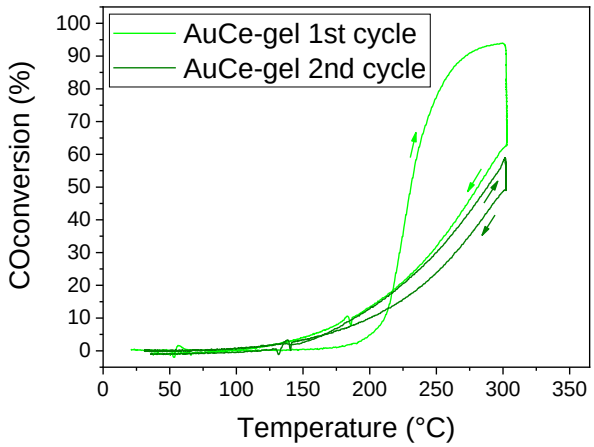

Figure 2A.21 CO-oxidation: Comparison on catalytic activity for AuCe-gel after two identical cycles.

The AuPd-gel shows a lower activity than previously mentioned samples, which is controversial given the high activities expected, due to the well distributed Pd on the sample (verified by EDX-mapping). On the other hand, it can have similar explanations to the AuCe-gel as Pd is prone to oxidize in oxidative atmospheres at high temperatures[60], which can contribute to the reduction of Au/Pd interfaces. For this reason, a more detailed study on this sample may be required, such as the mapping with higher resolution in particular before but also after the CO oxidation reaction.

Especially, the gels without any doping and with Ag show very low activity. For the AuAg-gel the presence of AgCl crystals was confirmed by HR-SEM-EDX and by XPS. The formation of those crystals prevents the catalyst from being active as they are too stable to form oxides. In addition, any pretreatment (oxidative or reductive) does not lead to changes in activity. The pure Au-gel is expected to be inactive in CO oxidation, due to missing metal traces which are known to enhance the activity of the catalyst like in case of nanoporous gold[29,61], which was confirmed by this experiment.

Catalytic tests: Oxidative coupling of methanol.

For the oxidative coupling of methanol, the previously mentioned sequence (see Experimental Methods section) was applied on each measurement, while the time and the methanol feed was differed slightly for each experiment, mainly due to different environment temperatures and consequently different methanol vapor concentrations (further explained in the Appendix of this chapter). Similarly, 20 mg of the catalyst was transferred in a quartz glass reactor and packed in between quartz wool.

To compare the activity of the catalyst to each other, the reaction rate normalized on the mass of the used catalyst was plotted against the temperature points (50, 100, 150 and 200°C) during the reaction. **Figure 2A.22** shows the results on this comparison but also the selectivity towards methyl formate of each catalyst at different temperatures.

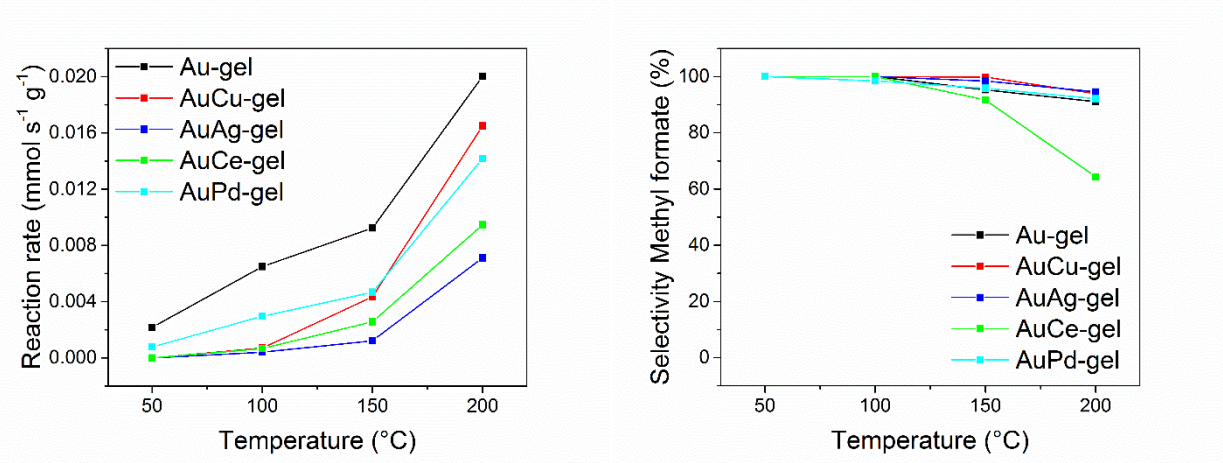

Figure 2A.22 Comparison of all catalyst for oxidative coupling of methanol; Left: Comparison on reaction rate, Right: Comparison on selectivity towards methyl formate.

Comparing the reaction rates of each catalyst, the surprising positive performance of the Au-gel is visible followed by AuPd at low temperatures (50 to 150°C) and AuCu at high temperatures (200°C). The lowest reaction rates can also be confirmed for AuAg-gel. In addition, the AuCe-gel is less active than the previously mentioned samples. Furthermore, the AuCe-sample shows lower selectivity compared to other samples. The reactivity of both samples can be affected by the formation of inactive species such as AgCl in case of AuAg-gel and CeO_2 in case of AuCe-gel, reducing the interface of Au to add-metal. Both compounds were verified by EDX-mapping and XPS. We compared the reactivity of the synthesized gels with literature values on nanoporous

gold[28]. The obtained reaction rate in case of the nanoporous gold at 80°C was 0.022 $mmol_{CH3OH}$ s^{-1} g_{cat}^{-1} while in the case of the synthesized sample the reaction rate was calculated to be 0.020 $mmol_{CH3OH}$ s^{-1} g_{cat}^{-1} (for the pure Au-gel) at 200°C. Although it is undeniable that the gels were less active than nanoporous gold, the former ensured a selectivity above 90% even at 200°C, while in the works of Wittstock et al.[28] the selectivity was decreasing already at lower temperatures. Similar selectivity was observed at similar reaction rates.

When the selectivity is compared for each gel sample, a tendency towards lower selectivity with increasing temperatures can be observed. AuCe-gel in particular shows a drop in selectivity at higher temperatures. Once again, this can be due to the formation of oxides on the surface, which can enhance the selectivity for CO_2 rather than methyl formate. This assumption was proven by the works of Wittstock et al.[28], which showed that higher adsorbed oxygen concentrations favor the combustion of the intermediate species formaldehyde to CO_2. Similar results were obtained by Xu et al.[29] claiming the higher the oxygen coverage the higher the combustion rate. Excluding this result, all samples show in general a high selectivity for methyl formate, which is comparable to published results[28].

In the works of Mahr et al.[32] the controversial activity of nanoporous gold regarding the metal trace content (formed by a gold-silver alloy) on the CO oxidation and the oxidative alcohol coupling was proven: a higher Ag content was beneficial for the CO oxidation and disadvantageous for the oxidative methanol coupling. This relation was proven for the oxidative coupling reaction independent from the phase (gas phase and liquid phase), which was resulting in combustion instead of coupling. Instead, for lower Ag contents the work of Mahr et al. signaled contradictory results. In our work, we are able to show the positive influence of the decoration with metals for the CO oxidation (see AuCu), while for the methanol coupling it seemed to be the pure Au-gel which was enhancing the activity for the coupling. Considering the published works, the general observation is the enhanced activity of the nanoporous gold in the presence of metal traces, due to their ability to dissociate oxygen and make it available for the coupling reaction. Hence, the pure NPG or in this case the pure Au-gel is expected to be inactive for the oxidative coupling of methanol, which is controversial to the here presented results. A deeper investigation on this case by means of XPS-analysis revealed the presence of sodium ions on the catalyst surface. These sodium ions can be found in the synthesis route of the nanoparticles (ligand and reducing agent contain sodium) used for the catalyst preparation. For a further understanding if and how these

sodium traces can influence the activity, further studies on this sample were performed and will be discussed in detail in the next part (Part B "Pure Gold Structures") of this chapter.

4. Conclusion

This work showed a simple method for the design of novel catalysts using nanoscaled units as building blocks to obtain 3D-networks. Here porous gold samples were synthesized using gold nanoparticles as building blocks and decorating the structures with a diverse range of added metals (Cu, Ce, Ag and Pd) to compare the materials to established nanoporous gold structures via top-down methods. The designed samples were compared to each other before and after catalytic tests using a diverse range of methods. The loss of wire-like structures and the shrinkage of the monoliths was identified by means of SEM-analysis after exposure to catalytic environments Different elemental composition analyses, such as ICP-OES, EDX and XPS, were used to understand the ratios of gold to decorated metal trace: When the results on AuCu- and AuPd-gels were compared for each technique, no major differences could be identified in the ratios. Instead, AuAg- and AuCe-gel had an enrichment of added cations on the surface, as verified by XPS-analysis. When the oxidation states were observed utilizing XPS, the Ce was oxidizing after thermal treatments in reactive atmosphere, emigrating from the bulk of the sample to the surface. In the case of AuAg the Ag was identified to be in oxidation state +1 which was underlined by HRSEM-EDX-mapping indicating the presence of AgCl crystallites. By using STEM-EDX-mapping the distribution of Cu all over the fragments was verified, while in the case of AuCe-gel the formation of CeO_2 islands were demonstrated and were in agreement with previously obtained XPS-results.

The results of the catalytic tests underlined the aforementioned characterization results: The AuCu-gel was active in the CO-oxidation but also in the methanol coupling, due to the presence of Au/Cu interfaces. Instead, the AuAg-gel showed very low to no activity in both reactions due to AgCl crystallites formed on the surface, which was proven by XPS and EDX, hindering the participation of Ag in the reaction. The AuCe-sample showed low activity in the methanol coupling and the lowest selectivity towards methyl formate amongst all samples. These observations, in addition to the fact that each cycle in the CO oxidation led to decreased conversion rates, were in good agreement with the results from the XPS and EDX-mapping: the Ce was forming larger CeO_2 islands on the surface resulting in fewer interfaces of gold and ceria, which consequently lead to lower activities in the CO-oxidation. Furthermore, the presence of cerium oxides on the surface

favored the combustion rather than the coupling of methanol and hence decreasing the selectivity of the catalyst in the methanol coupling reaction. As expected, the pure Au-gel was showing no activity in CO oxidation but displayed the highest activity during the methanol coupling reaction. Due to the controversially high activity of the pure Au-gel in the oxidative methanol coupling, an in-depth investigation of this system is required and was clarified in the next part of this chapter.

A perspective for this part of the work would be the in-depth investigation on the activity of the decorated Cu and Pd on the nanoporous structure. To do so, the sample can be washed and used in the CO-oxidation and the methanol coupling. This will clarify if the Cu- or Pd-ions on the sample surface are washable and if they play a key role in this system or if the add-metals are partially alloyed and cannot be washed of the surface (possible in the case of Pd but difficult to be identified with the presented techniques such as XRD and XPS). Furthermore, a direct comparison to actual nanoporous gold produced by a top-bottom approach can be carried out. As the pure Au-gel was expected to be inactive in both the CO oxidation and oxidative coupling of methanol, but showed controversial observations in the here presented results, the synthesized material will be discussed in further detail in the next part of this chapter.

In addition, new samples using different nano-units can be synthesized to test them in a reaction the nanoparticles are known to be active for (such as Pd-gels in the methane oxidation) and compare those to supported materials in a more mechanistical study. The method is simple and multifunctional and can pave a road for a broad range of catalysts.

5. Appendix

ANTOINE equation and calibration of the used FTIR for methanol, methyl formate and CO_2

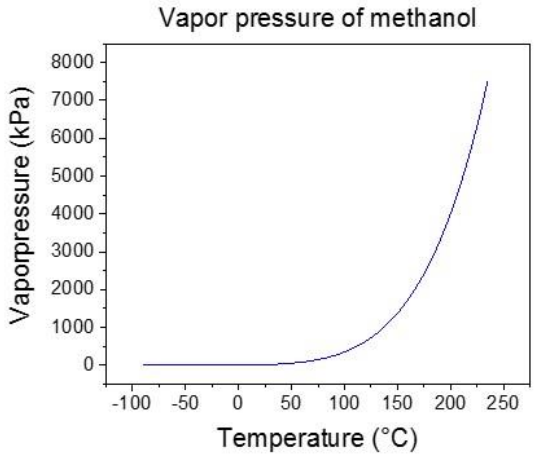

Figure 2A.23 Vapor pressure of methanol in relation to the temperature calculated by using the ANTOINE equation[52].

For a temperature range from -97.68°C (175.47 K) to 239.43°C (512.58 K) the ANTOINE equation[52] for the vapor pressure of methanol is:

$$ln(p) = -9.372816 \cdot ln(T) + \frac{-7.029198 \cdot 10^3}{T} + 7.909415 \cdot 10^1 + 7.992729 \cdot 10^{-6} \cdot T^2 \qquad (2A.8)$$

With T being the temperature in K and p being the vapor pressure in kPa. To achieve a methanol concentration of 2.3% v/v in the flow, the cooling bath was set to -8.5°C resulting in -8°C inside the bath, which was verified by a thermo couple.

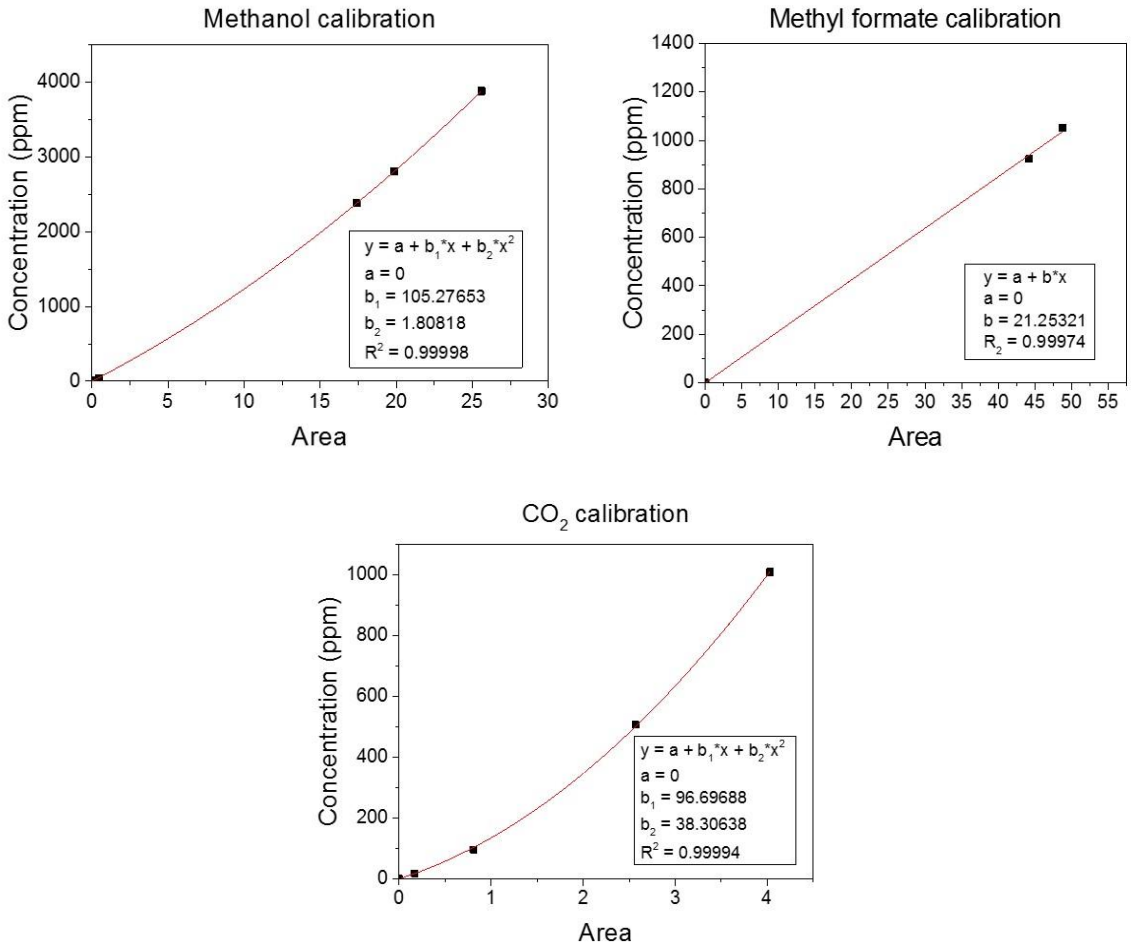

Figure 2A.24 Used calibration curves for the concentration determination of methanol, methyl formate and CO_2 during the oxidative methanol coupling.

XRD-analysis

To calculate the crystallite size the so-called SCHERRER equation was elaborated on three peaks taken from the following diffraction pattern of the sample before and after activity tests. The SCHERRER equation is described as following:

$$\tau = \frac{K \cdot \lambda}{\beta \cdot cos\theta} \qquad (2A.9)$$

In this equation τ is the mean size of the crystalline domain (in nanometers), K the dimensional shape factor (which has a typical value of 0.89 for spherical particles[62]), λ the X-ray wavelength (in this case for Cu Kα 0.15406 nm), β for the full width at half maximum of a peak (in radians)

and θ for the BRAGG angle (in degrees). The instrumental broadening was calculated and removed using a diffraction pattern collected from a NIST LaB_6 (SRM 660c) standard.

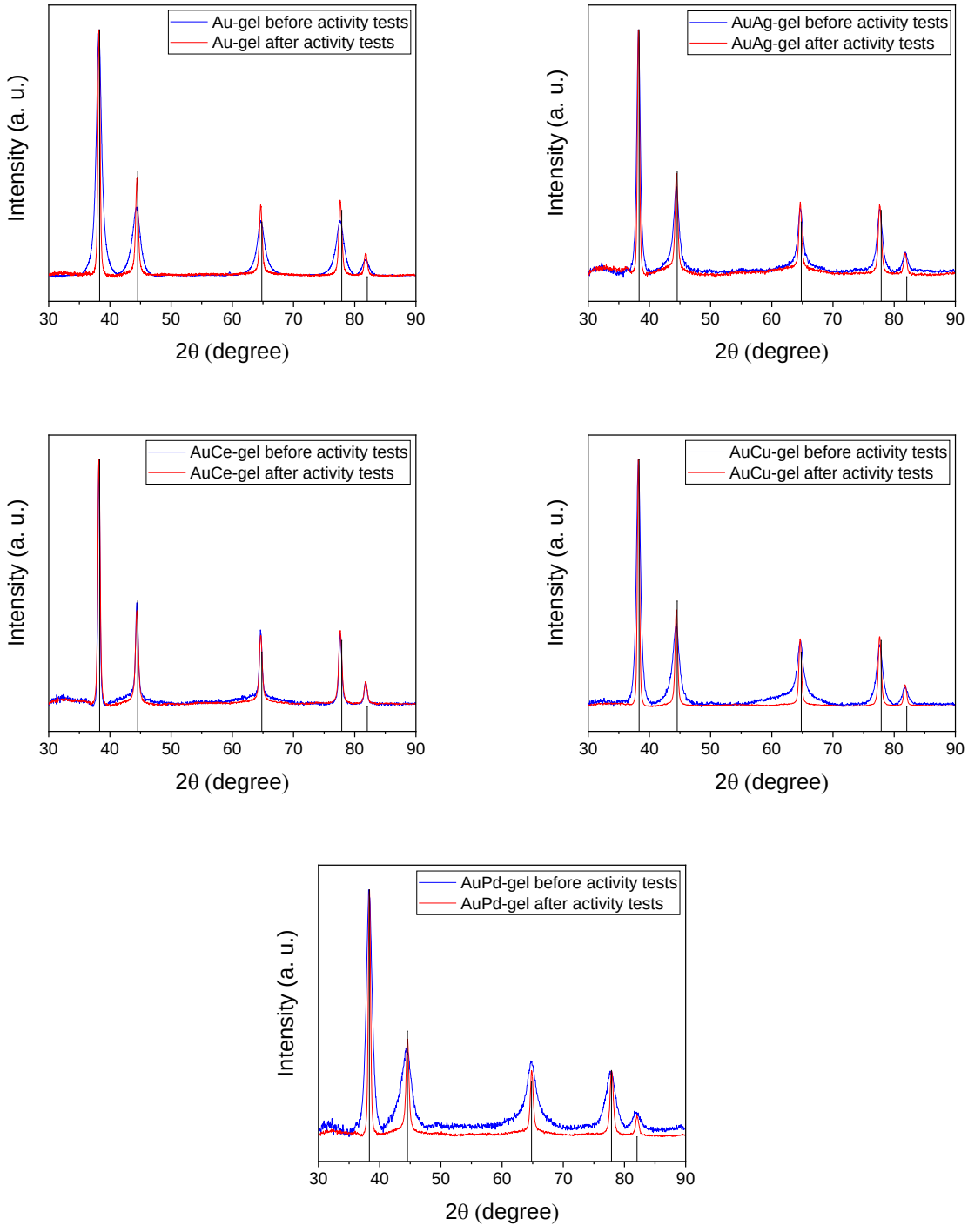

Figure 2A.25 XRD diffraction peaks for all samples before (blue line) and after (red line) activity tests compared to bulk Au diffraction pattern (black vertical lines, reference code: ICDD 96-901-1613). Sequence of samples from top to bottom: Au-gel, AuAg-gel, AuCe-gel, AuCu-gel and AuPd-gel.

In addition, the d-spacing of each sample was retrieved using the HighScore software. The following table summarizes the results of this calculation.

Table 2A.3 Calculated d-spacings for all gels before and after catalytic tests taking Au-gel as a reference at the diffraction peak 44.3 °2θ.

Metals	Before catalytic tests /Å	After catalytic tests /Å
Au-gel	1.2298 ± 0.0003 (Ref.)	
AuCu-gel	1.22968	1.22975
AuCe-gel	1.22976	1.22971
AuAg-gel	1.22953	1.22952
AuPd-gel	1.22769	1.22613

As it can be seen from **Table 2A.3** the add-metals do not show any effect on the d-spacing of the material, whereas Pd decreases the spacing significantly. This observation could be a first indication for the possibility of Pd being alloyed in the system and not decorated on the surface/in the bulk as a cation like the other metals.

Kr isotherms and the specific surface area of all gels after catalytic tests

To identify the differences in specific surface areas depending on add-metal, Kr isotherms were obtained and BET-calculations performed. The samples before the catalytic tests resulted in a desorbing rather than an adsorbing isotherm and were hence not considered at this point. This issue can be overcome by degassing the samples longer at higher temperatures, which might result in other consequences such as sintering of the sample. The following figure summarizes the results for all samples.

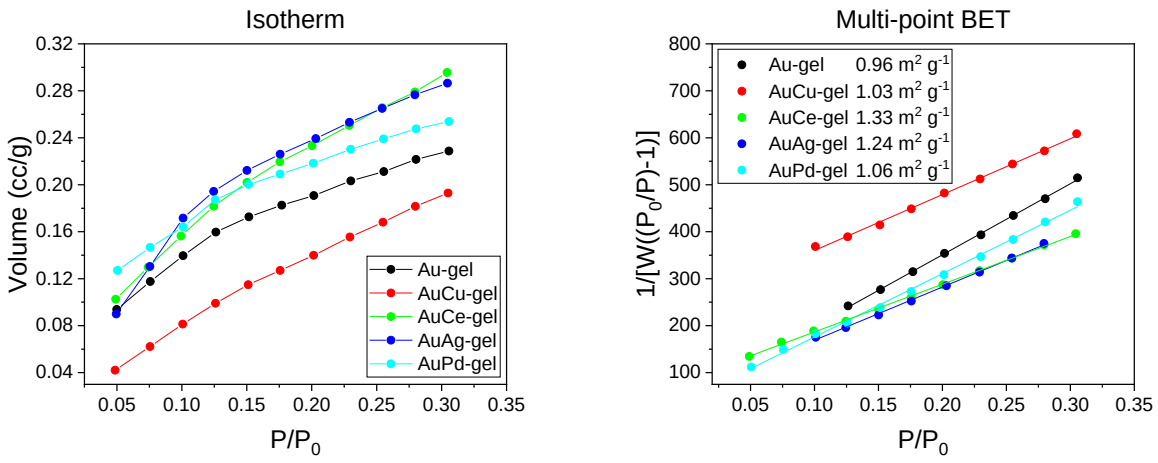

Figure 2A.26 Kr isotherms of all gels after catalytic tests (left) and corresponding BET-plots (right) with obtained specific surface areas implemented in legend.

As can be seen in **Figure 2A.26** no significant differences between samples are visible. All samples show a specific surface area of around 1 m^2 g^{-1}.

6. References

(1) Riemenschneider, W.; Bolt, H. M. Esters, Organic. *Ullmann's Encyclopedia of Industrial Chemistry*. April 30, 2005. https://doi.org/doi:10.1002/14356007.a09_565.pub2.

(2) Park, Y. C.; Shaffer, C. E. H.; Bennett, G. N. Microbial Formation of Esters. *Appl. Microbiol. Biotechnol.* **2009**, *85* (1), 13. https://doi.org/10.1007/s00253-009-2170-x.

(3) Theodorou, V.; Skobridis, K.; Tzakos, A. G.; Ragoussis, V. A Simple Method for the Alkaline Hydrolysis of Esters. *Tetrahedron Lett.* **2007**, *48* (46), 8230–8233. https://doi.org/https://doi.org/10.1016/j.tetlet.2007.09.074.

(4) Chen, H. 3 - Lignocellulose Biorefinery Feedstock Engineering; Chen, H. B. T.-L. B. E., Ed.; Woodhead Publishing, 2015; pp 37–86. https://doi.org/https://doi.org/10.1016/B978-0-08-100135-6.00003-X.

(5) Sanz, M. T.; Murga, R.; Beltrán, S.; Cabezas, J. L.; Coca, J. Autocatalyzed and Ion-Exchange-Resin-Catalyzed Esterification Kinetics of Lactic Acid with Methanol. *Ind. Eng. Chem. Res.* **2002**, *41* (3), 512–517. https://doi.org/10.1021/ie010454k.

(6) Personick, M. L.; Madix, R. J.; Friend, C. M. Selective Oxygen-Assisted Reactions of Alcohols and Amines Catalyzed by Metallic Gold: Paradigms for the Design of Catalytic Processes. *ACS Catal.* **2017**, *7* (2), 965–985. https://doi.org/10.1021/acscatal.6b02693.

(7) Duan, H.; Xu, C. Low-Temperature CO Oxidation over Unsupported Nanoporous Gold Catalysts with Active or Inert Oxide Residues. *J. Catal.* **2015**, *332*, 31–37. https://doi.org/https://doi.org/10.1016/j.jcat.2015.08.014.

(8) Moskaleva, L. V; Röhe, S.; Wittstock, A.; Zielasek, V.; Klüner, T.; Neyman, K. M.; Bäumer, M. Silver Residues as a Possible Key to a Remarkable Oxidative Catalytic Activity of Nanoporous Gold. *Phys. Chem. Chem. Phys.* **2011**, *13* (10), 4529–4539. https://doi.org/10.1039/C0CP02372H.

(9) Kameoka, S.; Tsai, A. P. CO Oxidation Over a Fine Porous Gold Catalyst Fabricated by Selective Leaching from an Ordered AuCu3 Intermetallic Compound. *Catal. Letters* **2008**, *121* (3), 337–341. https://doi.org/10.1007/s10562-007-9344-x.

(10) Lackmann, A.; Mahr, C.; Schowalter, M.; Fitzek, L.; Weissmüller, J.; Rosenauer, A.; Wittstock, A. A Comparative Study of Alcohol Oxidation over Nanoporous Gold in Gas and Liquid Phase. *J. Catal.* **2017**, *353*, 99–106. https://doi.org/10.1016/J.JCAT.2017.07.008.

(11) Kameoka, S.; Tanabe, T.; Miyamoto, K.; Tsai, A. P. Insights into the Dominant Factors of Porous Gold for CO Oxidation. *J. Chem. Phys.* **2016**, *144* (3), 034703. https://doi.org/10.1063/1.4940307.

(12) Qiu, H.-J.; Xu, H.-T.; Liu, L.; Wang, Y. Correlation of the Structure and Applications of Dealloyed Nanoporous Metals in Catalysis and Energy Conversion/Storage. *Nanoscale* **2015**, *7* (2), 386–400. https://doi.org/10.1039/C4NR05778C.

(13) Erlebacher, J.; Aziz, M. J.; Karma, A.; Dimitrov, N.; Sieradzki, K. Evolution of Nanoporosity in Dealloying. *Nature* **2001**, *410* (6827), 450–453. https://doi.org/10.1038/35068529.

(14) Piumetti, M.; Andana, T.; Bensaid, S.; Russo, N.; Fino, D.; Pirone, R. Study on the CO Oxidation over Ceria-Based Nanocatalysts. *Nanoscale Res. Lett.* **2016**, *11* (1), 165. https://doi.org/10.1186/s11671-016-1375-z.

(15) Moreno-Martell, A.; Pawelec, B.; Nava, R.; Mota, N.; Escamilla-Perea, L.; Navarro, R. M.; Fierro, J. L. G. CO Oxidation at 20 °C on Au Catalysts Supported on Mesoporous Silica: Effects of Support Structural Properties and Modifiers. *Materials* . 2018. https://doi.org/10.3390/ma11060948.

(16) Liu, X.; Tang, Y.; Shen, M.; Li, W.; Chu, S.; Shan, B.; Chen, R. Bifunctional CO Oxidation over Mn-Mullite Anchored Pt Sub-Nanoclusters via Atomic Layer Deposition. *Chem. Sci.* **2018**, *9* (9), 2469–2473. https://doi.org/10.1039/C7SC05486F.

(17) Śmiechowicz, I.; Kocemba, I.; Rogowski, J.; Czupryn, K. CO Oxidation over Pt/SnO2 Catalysts. *React. Kinet. Mech. Catal.* **2018**, *124* (2), 633–649. https://doi.org/10.1007/s11144-018-1383-3.

(18) Lu, Y.; Wang, J.; Yu, L.; Kovarik, L.; Zhang, X.; Hoffman, A. S.; Gallo, A.; Bare, S. R.; Sokaras, D.; Kroll, T.; et al. Identification of the Active Complex for CO Oxidation over Single-Atom Ir-on-MgAl2O4 Catalysts. *Nat. Catal.* **2019**, *2* (2), 149–156. https://doi.org/10.1038/s41929-018-0192-4.

(19) Soliman, N. K. Factors Affecting CO Oxidation Reaction over Nanosized Materials: A Review. *J. Mater. Res. Technol.* **2019**, *8* (2), 2395–2407. https://doi.org/10.1016/J.JMRT.2018.12.012.

(20) Schlatter, J. C.; Taylor, K. C. Platinum and Palladium Addition to Supported Rhodium Catalysts for Automotive Emission Control. *J. Catal.* **1977**, *49* (1), 42–50. https://doi.org/10.1016/0021-9517(77)90238-X.

(21) Cohn, J. G. Catalytic Converters for Exhaust Emission Control of Commercial Equipment Powered by Internal Combustion Engines. *Environ. Health Perspect.* **1975**, *10*, 159–164. https://doi.org/10.1289/ehp.7510159.

(22) Muraki, H.; Shinjoh, H.; Sobukawa, H.; Yokota, K.; Fujitani, Y. Palladium-Lanthanum Catalysts for Automotive Emission Control. *Ind. Eng. Chem. Prod. Res. Dev.* **1986**, *25* (2), 202–208. https://doi.org/10.1021/i300022a014.

(23) Thakur, P.; Thakur, P. Diesel Exhaust Control. *Adv. Mine Vent.* **2019**, 157–187. https://doi.org/10.1016/B978-0-08-100457-9.00011-0.

(24) Ertl, G. Reactions at Surfaces: From Atoms to Complexity (Nobel Lecture). *Angew. Chemie Int. Ed.* **2008**, *47* (19), 3524–3535. https://doi.org/10.1002/anie.200800480.

(25) Chemical Engineering. CATALYSIS FUNDAMENTALS https://www.chemengonline.com/catalysis-fundamentals/ (accessed Apr 6, 2020).

(26) del Río, E.; Collins, S. E.; Aguirre, A.; Chen, X.; Delgado, J. J.; Calvino, J. J.; Bernal, S. Reversible Deactivation of a Au/Ce0.62Zr0.38O2 Catalyst in CO Oxidation: A Systematic Study of CO2-Triggered Carbonate Inhibition. *J. Catal.* **2014**, *316*, 210–218. https://doi.org/10.1016/J.JCAT.2014.05.016.

(27) Xu, B.; Haubrich, J.; Freyschlag, C. G.; Madix, R. J.; Friend, C. M. Oxygen-Assisted Cross-Coupling of Methanol with Alkyl Alcohols on Metallic Gold. *Chem. Sci.* **2010**, *1* (3), 310–314. https://doi.org/10.1039/C0SC00214C.

(28) Wittstock, A.; Zielasek, V.; Biener, J.; Friend, C. M.; Bäumer, M. Nanoporous Gold Catalysts for Selective Gas-Phase Oxidative Coupling of Methanol at Low Temperature. *Science (80-.).* **2010**, *327* (5963), 319 LP – 322. https://doi.org/10.1126/science.1183591.

(29) Xu, B.; Siler, C. G. F.; Madix, R. J.; Friend, C. M. Ag/Au Mixed Sites Promote Oxidative Coupling of Methanol on the Alloy Surface. *Chem. – A Eur. J.* **2014**, *20* (16), 4646–4652. https://doi.org/10.1002/chem.201304837.

(30) Lopez, N.; Janssens, T. V. .; Clausen, B. .; Xu, Y.; Mavrikakis, M.; Bligaard, T.; Nørskov, J. . On the Origin of the Catalytic Activity of Gold Nanoparticles for Low-Temperature CO Oxidation. *J. Catal.* **2004**, *223* (1), 232–235. https://doi.org/10.1016/J.JCAT.2004.01.001.

(31) Lemire, C.; Meyer, R.; Shaikhutdinov, S.; Freund, H.-J. Do Quantum Size Effects Control CO Adsorption on Gold Nanoparticles? *Angew. Chemie Int. Ed.* **2004**, *43* (1), 118–121. https://doi.org/10.1002/anie.200352538.

(32) Mahr, C.; Kundu, P.; Lackmann, A.; Zanaga, D.; Thiel, K.; Schowalter, M.; Schwan, M.; Bals, S.; Wittstock, A.; Rosenauer, A. Quantitative Determination of Residual Silver Distribution in Nanoporous Gold and Its Influence on Structure and Catalytic Performance. *J. Catal.* **2017**, *352*, 52–58. https://doi.org/10.1016/J.JCAT.2017.05.002.

(33) Liu, W.; Herrmann, A.-K.; Bigall, N. C.; Rodriguez, P.; Wen, D.; Oezaslan, M.; Schmidt, T. J.; Gaponik, N.; Eychmüller, A. Noble Metal Aerogels—Synthesis, Characterization, and

Application as Electrocatalysts. *Acc. Chem. Res.* **2015**, *48* (2), 154–162. https://doi.org/10.1021/ar500237c.

(34) Bigall, N. C.; Herrmann, A.-K.; Vogel, M.; Rose, M.; Simon, P.; Carrillo-Cabrera, W.; Dorfs, D.; Kaskel, S.; Gaponik, N.; Eychmüller, A. Hydrogels and Aerogels from Noble Metal Nanoparticles. *Angew. Chemie Int. Ed.* **2009**, *48* (51), 9731–9734. https://doi.org/10.1002/anie.200902543.

(35) Freytag, A.; Sánchez-Paradinas, S.; Naskar, S.; Wendt, N.; Colombo, M.; Pugliese, G.; Poppe, J.; Demirci, C.; Kretschmer, I.; Bahnemann, D. W.; et al. Versatile Aerogel Fabrication by Freezing and Subsequent Freeze-Drying of Colloidal Nanoparticle Solutions. *Angew. Chemie - Int. Ed.* **2016**, *55* (3). https://doi.org/10.1002/anie.201508972.

(36) Dahman, Y.; Dahman, Y. Nanoparticles. *Nanotechnol. Funct. Mater. Eng.* **2017**, 93–119. https://doi.org/10.1016/B978-0-323-51256-5.00005-8.

(37) Zhang, K.; Zuo, W.; Wang, Z.; Liu, J.; Li, T.; Wang, B.; Yang, Z. A Simple Route to CoFe2O4 Nanoparticles with Shape and Size Control and Their Tunable Peroxidase-like Activity. *RSC Adv.* **2015**, *5* (14), 10632–10640. https://doi.org/10.1039/C4RA15675G.

(38) Nandi, A.; Majumder, R.; Nag, P.; Datta, S. K.; Saha, H.; Majumdar, S. Precursor Dependent Tailoring of Morphology and Bandgap of Zinc Oxide Nanostructures. *J. Mater. Sci. Mater. Electron.* **2017**, *28* (15), 10885–10892. https://doi.org/10.1007/s10854-017-6867-9.

(39) Kirakosyan, A.; Kim, J.; Lee, S.; Ippili, S.; Yoon, S.-G.; Choi, J. Optical Properties of Colloidal CH3NH3PbBr3 Nanocrystals by Controlled Growth of Lateral Dimension. *Cryst. Growth Des.* **2017**, *17*. https://doi.org/10.1021/acs.cgd.6b01648.

(40) Turkevich, J.; Stevenson, P. C.; Hillier, J. A Study of the Nucleation and Growth Processes in the Synthesis of Colloidal Gold. *Discuss. Faraday Soc.* **1951**, *11* (0), 55–75. https://doi.org/10.1039/DF9511100055.

(41) Mourdikoudis, S.; Liz-Marzán, L. M. Oleylamine in Nanoparticle Synthesis. *Chem. Mater.* **2013**, *25* (9), 1465–1476. https://doi.org/10.1021/cm4000476.

(42) Gillich, T.; Acikgöz, C.; Isa, L.; Schlüter, A. D.; Spencer, N. D.; Textor, M. PEG-Stabilized Core–Shell Nanoparticles: Impact of Linear versus Dendritic Polymer Shell Architecture on Colloidal Properties and the Reversibility of Temperature-Induced Aggregation. *ACS Nano* **2013**, *7* (1), 316–329. https://doi.org/10.1021/nn304045q.

(43) Goodman, C. M.; McCusker, C. D.; Yilmaz, T.; Rotello, V. M. Toxicity of Gold Nanoparticles Functionalized with Cationic and Anionic Side Chains. *Bioconjug. Chem.* **2004**, *15* (4), 897–900. https://doi.org/10.1021/bc049951i.

(44) Kimling, J.; Maier, M.; Okenve, B.; Kotaidis, V.; Ballot, H.; Plech, A. Turkevich Method for Gold Nanoparticle Synthesis Revisited. *J. Phys. Chem. B* **2006**, *110* (32), 15700–15707. https://doi.org/10.1021/jp061667w.

(45) Kikuchi, R.; Maeda, S.; Sasaki, K.; Wennerström, S.; Ozawa, Y.; Eguchi, K. Catalytic Activity of Oxide-Supported Pd Catalysts on a Honeycomb for Low-Temperature Methane Oxidation. *Appl. Catal. A Gen.* **2003**, *239* (1–2), 169–179. https://doi.org/10.1016/S0926-860X(02)00387-3.

(46) Markelonis, A. R.; Wang, J. S.; Ullrich, B.; Wai, C. M.; Brown, G. J. Nanoparticle Film Deposition Using a Simple and Fast Centrifuge Sedimentation Method. *Appl. Nanosci.* **2015**, *5* (4), 457–468. https://doi.org/10.1007/s13204-014-0338-x.

(47) Arachchige, I. U.; Brock, S. L. Sol−Gel Assembly of CdSe Nanoparticles to Form Porous Aerogel Networks. *J. Am. Chem. Soc.* **2006**, *128* (24), 7964–7971. https://doi.org/10.1021/ja061561e.

(48) Arachchige, I. U.; Brock, S. L. Highly Luminescent Quantum-Dot Monoliths. *J. Am. Chem. Soc.* **2007**, *129* (7), 1840–1841. https://doi.org/10.1021/ja066749c.

(49) Oh, H.-S.; Yang, J. H.; Costello, C. K.; Wang, Y. M.; Bare, S. R.; Kung, H. H.; Kung, M. C. Selective Catalytic Oxidation of CO: Effect of Chloride on Supported Au Catalysts. *J. Catal.* **2002**, *210* (2), 375–386. https://doi.org/10.1006/JCAT.2002.3710.

(50) Weng, H. S.; Eigenberger, G.; Butt, J. B. Catalyst Poisoning and Fixed Bed Reactor Dynamics. *Chem. Eng. Sci.* **1975**, *30* (11), 1341–1351. https://doi.org/10.1016/0009-2509(75)85063-9.

(51) Schmitz, G. What Is a Reaction Rate? *J. Chem. Educ.* **2005**, *82* (7), 1091. https://doi.org/10.1021/ed082p1091.

(52) Chemical Engineering and Materials Research Information Center Vapor Pressure of Methanol www.cheric.org/research/kdb/hcprop/showcoef.php?cmpid=817&prop=PVP (accessed Oct 22, 2019).

(53) Personick, M. L.; Zugic, B.; Biener, M. M.; Biener, J.; Madix, R. J.; Friend, C. M. Ozone-Activated Nanoporous Gold: A Stable and Storable Material for Catalytic Oxidation. *ACS Catal.* **2015**, *5* (7), 4237–4241. https://doi.org/10.1021/acscatal.5b00330.

(54) Veith, G. M.; Lupini, A. R.; Rashkeev, S.; Pennycook, S. J.; Mullins, D. R.; Schwartz, V.; Bridges, C. A.; Dudney, N. J. Thermal Stability and Catalytic Activity of Gold Nanoparticles Supported on Silica. *J. Catal.* **2009**, *262* (1), 92–101. https://doi.org/10.1016/j.jcat.2008.12.005.

(55) Chusuei, C. C.; Brookshier, M. A.; Goodman, D. W. Correlation of Relative X-Ray Photoelectron Spectroscopy Shake-up Intensity with CuO Particle Size. *Langmuir* **1999**, *15* (8), 2806–2808. https://doi.org/10.1021/la9815446.

(56) Najafishirtari, S.; Brescia, R.; Guardia, P.; Marras, S.; Manna, L.; Colombo, M. Nanoscale Transformations of Alumina-Supported AuCu Ordered Phase Nanocrystals and Their Activity in CO Oxidation. *ACS Catal.* **2015**, *5* (4), 2154–2163. https://doi.org/10.1021/cs501923x.

(57) Aguilar-Guerrero, V.; Gates, B. C. Genesis of a Highly Active Cerium Oxide-Supported Gold Catalyst for COoxidation. *Chem. Commun.* **2007**, No. 30, 3210–3212. https://doi.org/10.1039/B705562E.

(58) Venezia, A. .; Liotta, L. .; Pantaleo, G.; La Parola, V.; Deganello, G.; Beck, A.; Koppány, Z.; Frey, K.; Horváth, D.; Guczi, L. Activity of SiO2 Supported Gold-Palladium Catalysts in CO Oxidation. *Appl. Catal. A Gen.* **2003**, *251* (2), 359–368. https://doi.org/10.1016/S0926-860X(03)00343-0.

(59) Xu, J.; White, T.; Li, P.; He, C.; Yu, J.; Yuan, W.; Han, Y.-F. Biphasic Pd−Au Alloy Catalyst for Low-Temperature CO Oxidation. *J. Am. Chem. Soc.* **2010**, *132* (30), 10398–10406. https://doi.org/10.1021/ja102617r.

(60) Xiong, H.; Lester, K.; Ressler, T.; Schlögl, R.; Allard, L. F.; Datye, A. K. Metastable Pd ↔ PdO Structures During High Temperature Methane Oxidation. *Catal. Letters* **2017**, *147* (5), 1095–1103. https://doi.org/10.1007/s10562-017-2023-7.

(61) Xu, C.; Su, J.; Xu, X.; Liu, P.; Zhao, H.; Tian, F.; Ding, Y. Low Temperature CO Oxidation over Unsupported Nanoporous Gold. *J. Am. Chem. Soc.* **2007**, *129* (1), 42–43. https://doi.org/10.1021/ja0675503.

(62) Langford, J. I.; Wilson, A. J. C. Scherrer after Sixty Years: A Survey and Some New Results in the Determination of Crystallite Size. *J. Appl. Crystallogr.* **1978**, *11* (2), 102–113. https://doi.org/10.1107/S0021889878012844.

Chapter II, Part B: Pure Gold Systems

Abstract

In this work, we designed 3D self-supported porous structures made of gold nanoparticles by utilizing a bottom-up approach and investigated their application in oxidation catalysis. This bottom-up approach involved the established cryogelation technique, for which nanoparticle units are concentrated and frozen in liquid nitrogen to subsequently remove the ice-template by the freeze-drying process ultimately obtaining a 3D self-standing monolith of nanoparticles. A diverse number of techniques enabled us to characterize the catalysts to investigate the microscopic changes of the catalyst before and after tests. CO oxidation and oxidative methanol coupling were performed to compare the obtained materials to established nanoporous gold structures from a top-down method. As expected, the prepared gold sample was inactive in the CO oxidation but showed surprisingly high activities in the oxidative methanol coupling. After identifying the presence of sodium species on the surface of the catalyst using a set of analysis methods, a correlation between the presence of these species and the high activity was drawn. The removal of these sodium species by washing resulted in an inactive gold material for the oxidative methanol coupling reaction. In summary, our work indicates that presence of metal traces is required to have active porous gold catalysts in oxidation reactions.

1. Introduction

In 1906 Bone et al.[1] investigated the reaction of hydrogen and oxygen on a gold surface, which was one of the first times gold was considered as a catalyst. A number of works[2,3] followed on this pioneering attempt and the research on the captivating catalytic properties of gold began. Decades later the catalytic properties of gold were further investigated in both major fields of catalysis, homogeneous and heterogeneous catalysis. The first homogenous gold catalyst was introduced in 1976, when Thomas and co-workers reported the reaction of phenylacetylene to acetophenone by using tetrachloroauric acid[4]. Today, 30 years later, the major impact of Au(I) and (III) catalyst can be found in the field of organic synthesis, where catalysts are required to form C-C bonds[5,6] and C-X (X = O,N) bonds[7,8] for highly complex chemical compounds. Whilst the usage of gold as a catalyst in homogeneous catalysis can be considered as a young research field, gold as a heterogeneous catalyst was further developed in 1925 by oxidizing carbon monoxide (CO) over a gold surface[9]. Despite the fact that gold is rarer and more expensive compared to other metals, its usage can have advantages, such as its non-toxicity and high stability. Nowadays the application

of gold catalysts can be found in the field of emission control technologies[10,11], chemical processing of bulk and fine chemicals[12–14] and in the hydrogen production (involving fuel cell systems)[15,16]. Most of these applications imply the usage of highly active gold nanoparticles (Au NPs) of around 2 to 5 nm in size supported on a high surface area oxides, such as silica[17], ceria[18] and alumina[17]. The interfaces between the Au nanoparticles and the oxide support can provide adsorbed oxygen[19], whereas undercoordinated Au atoms can activate the dissociation of the delivered oxygen molecules[20]. In addition to the mentioned nanoparticles, many studies in literature describe the activity of Au atoms and their few atoms clusters. As an example, He et al.[21] described the activity of Au in low temperature CO oxidation arising from different sized Au nanostructures, proposing an activity hierarchy of different Au species, which finally contribute to the activity of the metal-supported catalysts.

However, to understand the elemental catalytic activity of nanoparticulate gold, the removal of the oxide support material is essential, as the support can affect the catalytic activity in a massive manner. Defect Au-sites, hydroxy-groups on the support surface and possible ionic Au-species were assigned to be the reason of the activity[22]. Hence, the development of unsupported, nanoparticulate gold material was required to further study the reasons behind the activity of nanoparticulate gold catalysts. One of these materials was the aforementioned (Chapter IIA) nanoporous gold (NPG)[23–25]. As previously described, the synthesis of this material implies a top-down approach[26] in which a gold-alloy (e. g. aluminum[27], silver[24] and copper[28]) is either chemically[25,29] or electrochemically[30,31] etched. To describe the term "top-down approach" in more detail: The alloy is considered as the "top level" which after etching finalizes in the nanoporous structures ("down level"). As already mentioned, these materials with small ligament sizes and holding metal traces from the dealloying process are capable of catalyzing different reactions, such as the carbon monoxide oxidation[28,32] and the liquid[31,33,34] and gas phase[24,25,35,36] oxidative coupling of methanol, with high conversions at low temperatures compared to supported catalysts.

Although, the reproducibility of these materials in relation to the bulk concentration of the metal traces was shown to be possible[37], higher metal trace concentrations can lead to clustering of these traces in the system, as the starting alloy is not always homogeneous[34]. Since the dealloying process is a diffusion dependent process, the system tends to reach an equilibrium in which the content of the less noble metal in the NPG cannot become zero[38]. The metal traces remaining in the porous structure appear to play the main role in the high activity of these catalysts in the oxidative coupling

of methanol and the oxidation of carbon monoxide, which still requires further clarification. The explanation found in literature for these traces being important is their ability to bind and dissociate molecular oxygen which takes part in methanol and CO oxidation reactions. However, some works in literature claim that low-coordinated gold atoms can facilitate the dissociation of molecular oxygen at step-edges[39]. Noteworthy to mention is the fact that there is an obvious correlation between the presence of metal traces (like Ag) and the activity of the catalyst. Yet, to date there is no work in literature showing a synthesis approach to obtain pure porous gold samples to clearly identify the reason for the activity of these samples.

As described before, we decided to use a bottom-up approach to tackle the challenge, utilizing the self-assembly of nanoparticles through a gelation method[40–42] to synthesize porous materials. The simple cryogelation method established by Freytag et al.[42] was used to design a complex 3D disordered structure ("upper level") built of gold nanoparticles ("bottom level")[26]. Hence, the aim of the here presented work is to synthesize pure porous gold structures, which cannot be obtained via established dealloying processes. Therefore, we were able to study the role of metal traces in the activity of porous gold structures, focusing on the oxidation of carbon monoxide and the oxidative coupling of methanol to form methyl formate.

2. Experimental Methods

Chemicals for gold sythesis

Gold(III) chloride trihydrate ($HAuCl_4 \cdot 3H_2O$), trisodium citrate dihydrate, sodium borohydride, sodium chloride and sodium hydroxide were purchased from Sigma-Aldrich. All chemicals were used as received.

Gold nanoparticles (Au NPs) and Au-gels synthesis

To obtain aqueous gold nanoparticles the aforementioned citrate reduction approach[42] at room temperature was used (see details under Experimental Methods, Chapter IIA). After concentrating the solution to the required volume ratio of 0.1 vol-%, the concentrated solution was injected in liquid nitrogen and afterwards transferred to a freeze-drier to remove the ice templates and obtain 3D self-standing nanoporous structures of pure gold (Au-gels, see **Figure 2B.1**).

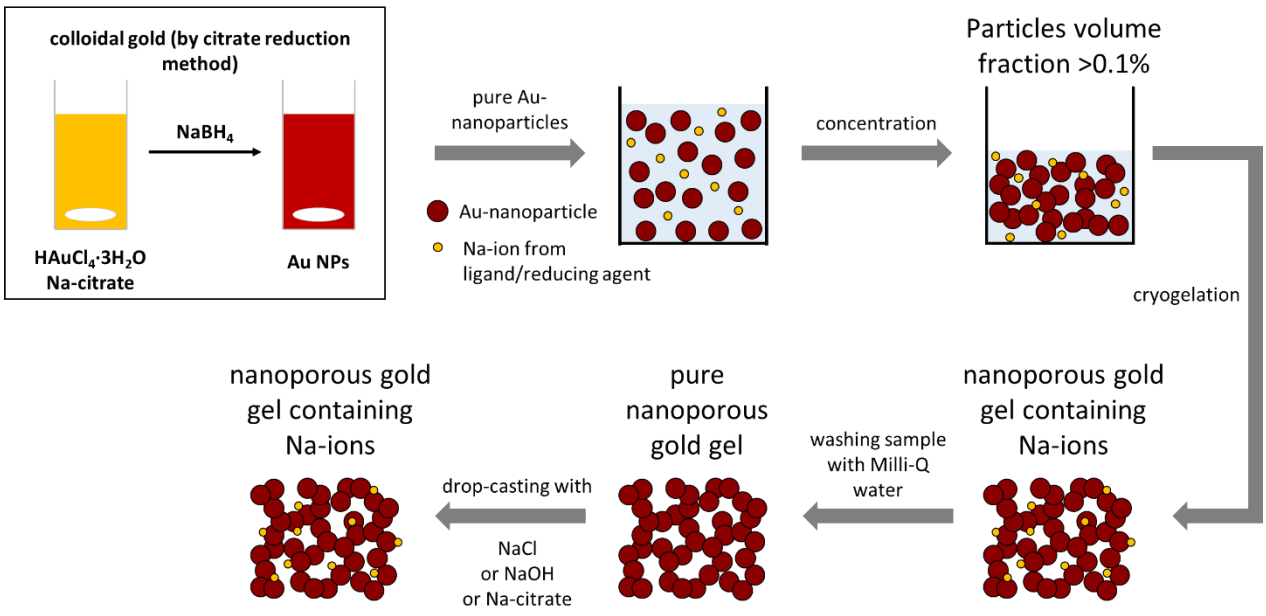

Figure 2B.1 Scheme of gel synthesis: First, the synthesis of Au NPs by citrate reduction method, then the concentration of nanoparticle solution followed by cryogelation to obtain self-standing nanoporous structures by Au NPs containing Na-ions. As a second step: washing and subsequent redecoration of samples with different Na-salts.

Washing the gels and drop-casting diverse sodium sources

By washing the gels (~20 mg) thoroughly with 100 mL Milli-Q water over a filter paper, the sodium species trapped on the surface of as-synthesized gels were reduced. To remove more sodium, the sample was let to stay in excess water, giving the sodium ions time to diffuse into the water. In addition to the washing to remove sodium traces on the sample, the role of different sodium sources in the catalytic activity were further investigated. Sodium chloride, sodium hydroxide and sodium citrate trihydrate (all purchased from Sigma-Aldrich) were dissolved in Milli-Q water and drop-cast on a beforehand washed sample. Then the sample was dried over phosphorus pentoxide (purchased from Sigma-Aldrich) inside a desiccator. Each sodium-ion solution was adjusted in the concentration to reach a final Au:Na ratio on the gel surface of 85:15 (at%), to have a relation to a freshly synthesized sample analyzed by means of XPS.

CO oxidation

To investigate the activity of the sample in the conversion of carbon monoxide (CO) to carbon dioxide (CO_2), a temperature programmed reaction in a micro reactor system was performed. The flow rate was set to 40 Ncc/min, containing 1 vol-% CO and 10 vol-% O_2 balanced with He. The temperature program was set to ramp at 5°C/min to reach 300°C with a dwell of 1 h. To cool down,

the rate was changed to -25°C/min and the outcoming gas concentrations (CO and CO_2) were analyzed using a gas analyzer (Advance Optima AO2020 Series Continuous Gas Analyzer).

Methanol coupling

To investigate the activity of the catalyst in the oxidative coupling of methanol, around 20 mg of catalyst were used. The gases were flowing at a rate of 40 Ncc/min through a cooled saturator filled with methanol. The so obtained methanol gas concentration was of around 2.3 vol-%, while oxygen was stoichiometrically balanced to 1.15 vol-% (further description to the method can be found in the Experimental Methods section of Chapter IIA). The temperature was ramped to dwells of an hour at 50, 100, 150 and 200°C and the gas outlet was analyzed using a time-resolved Fourier transform infrared spectrometer (FTIR, Spectrum Two™ by Perkin Elmer)

Transmission electron microscopy (TEM)

The synthesized gold nanoparticles were analyzed on their size distribution and shape using a transmission electron microscope (TEM, Jeol JEM-1011 with thermionic W source operated at 100 kV). The sample solution was dropped on a copper grid and subsequently used for analysis.

Elemental analysis

To verify the required volume fraction of 0.1 vol%, the concentration of the solution before and after the concentration step was analyzed using an inductively coupled plasma-optical emission spectrometer (ICP-OES, iCAP 600 series by Thermo Scientific). Before the analysis, the aqueous sample solution was dissolved in aqua regia (3:1 ratio of hydrochloric acid and nitric acid: Sigma-Aldrich, for analysis) and diluted 1:10 with water after letting it digest overnight. Finally, the solution was filtered (syringe filter, PTFE-membrane with 0.2 μm pore diameter) and analyzed.

High resolution scanning electron microscope with energy dispersive X-ray analyzer (HRSEM-EDX)

To identify the porosity of the structures an HRSEM analysis was carried out using a JEOL JSM 7500FA scanning electron microscope, equipped with a cold field emission gun (single crystal tungsten <310> emitter, ultimate resolution of 1nm) and operating at 10kV. Images were taken in backscattered electron (BSE) imaging mode using a 2-segment solid state annular detector.

To further analyze the distribution and quantification of sodium on the synthesized material, EDX analysis was performed using an Oxford X-max LN_2-free Silicon Drift Detector (SDD), with 80mm^2 of sensor active area and 129eV of energy resolution at 5.9keV (MnKα). The Extended

Pouchou and Pichoir (XPP) matrix correction algorithm included in the Oxford AZtec software was used to analyze the data. This was done by pressing and fixing the sample on an adhesive carbon tape by using a single-use spatula. To have a more accurate value for the sodium content, three different areas of the sample was analyzed via EDX.

X-ray Photoelectron Spectroscopy (XPS)

In depth investigations on the surface species was performed using X-ray photoelectron spectroscopy. The sodium to gold ratio on the surface of the catalyst was investigated and compared to EDX and ICP results. Each XPS-experiment was carried out on each sample before and after the washing and drop-casting step. The samples were once again pressed on an adhesive carbon-tape using a single-use spatula. The XPS analyses were carried out with a Kratos Axis Ultra^{DLD} spectrometer using a monochromatic Al K(alpha) source, operated at 20 mA and 15 kV. Survey scan analyses were carried out with an analysis area of 300 x 700 microns and a pass energy of 160 eV. High resolution analyses were carried out with the same analysis area at a pass energy of 20 eV on the energy region typical for Na 1s, C 1s and Au 4f peaks. Spectra were analysed using the CasaXPS software (version 2.3.17).

X-ray diffraction (XRD)

The crystallite sizes of the nanoparticles were determined by measuring X-ray diffractogram of the sample before and after catalytic tests and applying the Scherrer equation on the obtained reflexes (see detailed information in Appendix of Chapter IIA). The patterns were recorded on a Rigaku SmartLab X-Ray diffractometer equipped with a 9 kW Cu Kα rotating anode, operating at 40 kV and 150 mA. A Göbel mirror was used to convert the divergent X-ray beam into a parallel beam and to suppress the Cu Kβ radiation. The samples were measured at room temperature after pressing the gels on a quartz support using a glass substrate.

Krypton physisorption measurements

By using krypton physisorption measurements on the sample, the specific surface area was identified. The experiments were carried out at 77 K using a gas sorption analyzer (Autosorb-iQ, by Quantachrome Instruments). First, the samples were degassed for 2 h at 120 °C under vacuum conditions to remove weakly adsorbed species. After experiments were performed, specific surface areas were calculated by using the multipoint Brunauer-Emmett-Teller (BET) model, considering 8-11 equally spaced points in the P/P_0 range from 0.05 to 0.3 (P_0 is the vapour pressure of Kr at 77 K, corresponding to 2.63 Torr).

3. Results and Discussion

Macroscopic and microscopic structure of the prepared samples

Prior to the cryogelation step[42], the sample concentration analyzed by ICP-OES and the required volume ratio of 0.1 vol-% was verified. The Au NPs building units of a size around 4 nm (previously identified via TEM and can be found in Results and Discussion section of Chapter IIA) were assembled to a voluminous monolithic gel of dark-red color and golden shimmer with a low density (see **Figure 2B.2 a)**, as reported by Freytag et al[42]. SEM-imaging gave an insight to the microscopic structure of the as-synthesized material. It revealed a structure of high porosity with flakes of around 5 µm width and 10 – 50 µm length (see **Figure 2B.2 b-d**). A final disordered 3D structure was formed of these flake-like structures interconnected by wire-like structures (see arrows in **Figure 2B.2 d**). When comparing the results of these samples obtained via bottom-up approach to established NPG materials by a top-down method, significant differences can be identified. In case of NPG a homogenous bi-continuous pore structure with smaller ligament sizes of 20 - 50 nm was obtained. In contrast to these currently employed nanoporous structures[29,43], the here shown structures showed significant differences: the size of the ligaments were several hundred orders of magnitude larger than the NPG. However, the here presented materials show a plasmonic dark-red color of the nanoparticulate gold, which verifies the presence of nanoparticulate domains inside the 3D-structure. The specific surface area was determined via Kr physisorption measurements for which the Brunauer-Emmett-Teller (BET) method was used to evaluate the collected data. In comparison to NPG synthesized via top-down method (with 2-5 $m^2 g^{-1}$)[27], the here presented sample showed slightly lower surface areas of around 1 $m^2 g^{-1}$.

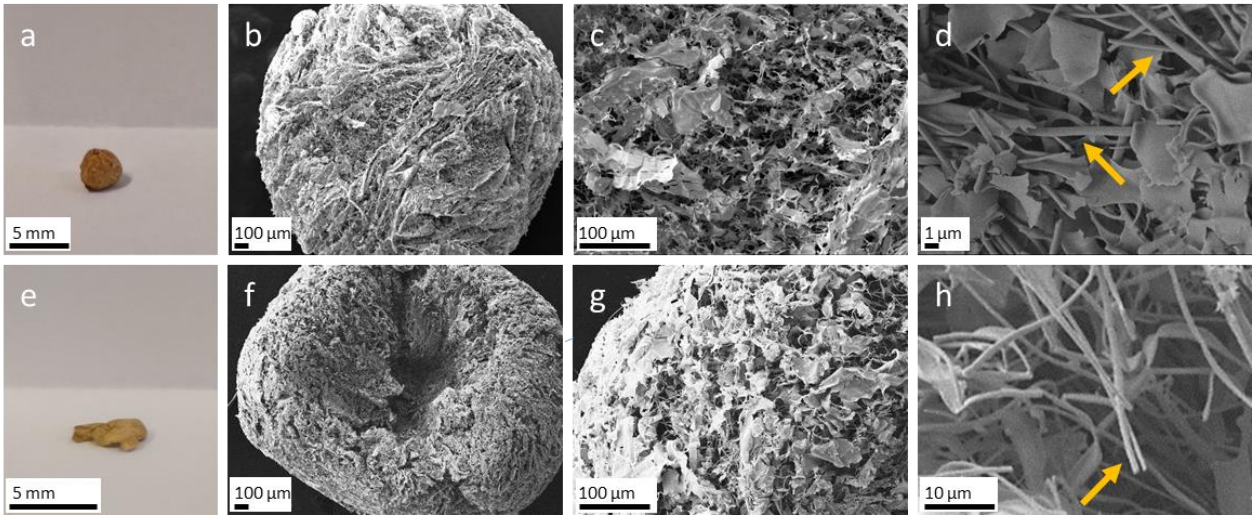

Figure 2B.2 Macroscopic (a, e) and microscopic (b-d, f-h) images of gels before (a-d) and after (e-h) exposure to catalytic conditions.

The as-synthesized materials were then exposed to reaction conditions and compared in their macroscopic and microscopic structure to the freshly prepared samples. The first impression is a loss of volume along with a change of color to golden yellow visible subsequently after exposure to high temperatures (see **Figure 2B.2 e**). This observation can be explained by the sintering of the particles occurring during the exposure to high temperatures due to the low Tammann temperature of gold of 395°C [22]. The lower melting temperature of nanoparticulate gold can be explained by the higher surface tension of the material with decreasing particle/domain sizes. The results of SEM-imaging showed a controversial result with a similar microscopic structure of the material before exposure to reaction conditions. The images show a retained flake-like structure of around several 10 µm length and width, while at the same time wire-like structures were still traceable (see **Figure 2B.2 f-h)**. These controversial results can be explained by the large ligament sizes available in the sample, pushing the sintering temperature to higher values due to lower surface tension forces. In comparison to NPG obtained via top-down method, the here presented samples seem to be stable at high temperatures, as NPG tends to show coarsening at low temperatures such as 100°C[25], due to smaller ligament sizes of around 30 nm, which can be correlated to the higher surface tensions displayed in these materials. Independently from these results, the specific surface area seemed unchanged with a result of 1 $m^2 g^{-1}$ (all isotherms and BET-plots can be taken from the Appendix section).

Finally, XRD data revealed gold being the only crystalline phase in the sample (see XRD-pattern in the Appendix section of this chapter). The Scherrer equation (as explained before in the Appendix of Chapter IIA) was used to compare the dimensions of the crystallites of the as-synthesized gold samples and of the samples after exposure to reaction conditions. The analysis revealed a crystallite size of 6 nm in a freshly synthesized sample and 20 nm after thermal exposure of the same sample, which underlines once again the sintering of the particles and explains the change of the color. The obtained sizes after thermal exposure are comparable with published works of Kameoka et al[27], whereas the group reported a crystallite size of around 20 nm for NPG developed by a top-down approach, which was determined by applying the Scherrer equation to obtained XRD patterns. However, the here shown sintering seems to affect the nanoparticulate domains but not the specific surface area as the results after thermal exposure are similar to a freshly synthesized sample.

CO oxidation

To investigate the catalytic activity of the sample, the oxidation of CO to CO_2 was performed. Preliminary results indicated a low activity for the fresh catalyst, which did not increase significantly even at higher temperatures of 300°C (see **Figure 2B.3**). After calculating the reaction rate at this temperature (0.001 $mmol_{CO}\ s^{-1}\ g_{cat}^{-1}$) and comparing the results to reported reaction rates of nanoporous gold (0.020 $mmol_{CO}\ s^{-1}\ g_{cat}^{-1}$ at 160°C[27,28]), the inactivity of this sample can be highlighted. Kameoka and co-workers[27] claimed the activity of the NPG samples in CO oxidation arriving from the presence of metal traces, such as Al, which can form oxides and increase the reactivity of the catalyst by exposing Au/AlO_x interfaces. Other authors in this topic described the activity of NPG in the oxidation of CO occurring due to low coordinated Au-atoms being present on the catalyst surface. These atoms provide higher binding energy sites for the CO adsorption and along with this, result in the observed enhanced activity of the catalyst[29,44]. In these works, the authors claimed the role of the metal trace (here Ag) is to suppress the (111)-faceting kinetics and therefore enable the presence of low coordinated Au sites.

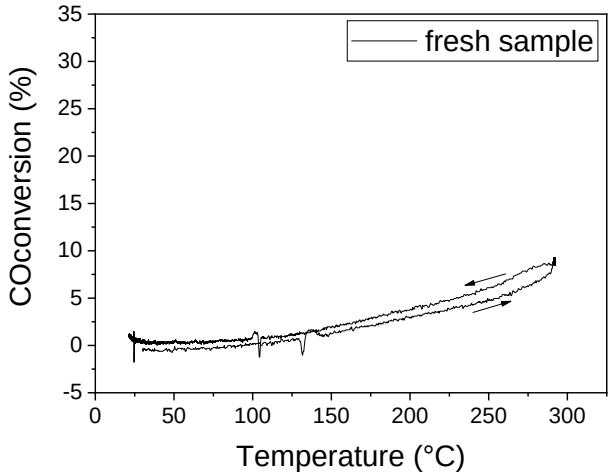

Figure 2B.3 Conversion of carbon monoxide on a fresh Au-gel sample. The reaction rate at 300°C is 0.001 $mmol_{CO}$ s^{-1} g_{cat}^{-1}.

To underline the possibility of metal traces playing a key role in the enhanced activity of the catalyst due to their oxidation and creation of Au/metal oxide interfaces, Déronzier et al.[45] demonstrated an approach in which a Au-Zr mother alloy was used to synthesize the NPG structure. In this work, the group demonstrated a way to obtain NPG structures of high purity, in which the residual Zr seemed to not be involved in the reaction.

The here shown results are comparable to the reports of Biener et al.[44], Zhang et al[46]. and Wang et al.[47], in which the catalytic activity of the NPG was ascribed to the presence of residual metal traces. In our case one possible impurity is sodium which needs further investigation. However, our results are oppositional to the interpretation of Kameoka et al.[28] , Zielasek et al.[48] and Fujita et al.[29], in which the authors ascribe the activity to low-coordinated Au-atoms to enhance the activity of the NPG in the oxidation of CO to CO_2.

Selective oxidative methanol coupling and the role of sodium

In addition to the performed experiments on the activity of the catalyst to oxidize CO, the oxidative coupling of methanol to methyl formate was carried out. A freshly synthesized sample was investigated first, resulting in a high activity for the coupling reaction with a remarkable reaction rate of 0.027 $mmol_{CH3OH}$ s^{-1} g_{cat}^{-1} at 200°C. The selectivity of the catalyst at this temperature and rate was determined via previously mentioned calculations (see Chapter IIA). With a high selectivity of 85-100% towards the desired methyl formate (see **Figure 2B.4**) the catalyst was

showing a similar behavior as previously reported results of Wittstock et al. with a reaction rate of 0.022 $mmol_{CH3OH}$ s^{-1} g_{cat}^{-1} and a selectivity of 97% at 80°C[36]. The transient data for this experiment can be found in the Appendix of this chapter.

During the synthesis of the here presented gold gels, chemicals involving sodium ions (such as sodium citrate and sodium borohydride) were used and hence the term "pure gold gel" needs to be used under these circumstances with caution. The possibility of sodium impurities on the catalyst surface could not be excluded and required further investigation in this aspect, seen as the catalyst seems to have a surprisingly high activity in oxidative methanol coupling, although the opposite was expected to occur. The nanoparticles used to form the final porous structures were obtained via citrate reduction method, which implies negatively charged citrate ligands on the surface of the particles. To have a charge balance on the surface, positive sodium ions act as counter ions for the negative citrate ligands. These sodium impurities can hence remain until the final structure is obtained on the surface of the particles and with this on the catalyst surface. It is possible that certain sodium species are capable of catalyzing this reaction[49] which implies an in depth investigation on the quantity of these sodium impurities and its correlation to the activity of the catalyst. For this reason, we decided to further investigate the role of Na presence in the catalyst. A range of different bulk and surface sensitive techniques were used to verify the presence of sodium. As a first method, ICP-OES was chosen to be performed on the colloidal solution used to design the porous catalyst. The results gave remarkably low concentrations for sodium in solution, such that the detection limit of the instrument for sodium signals was reached. Additional SEM-EDX analysis on the prepared catalyst was performed to get a better understanding on the sodium content in the bulk material. After analyzing a broad area on the sample, the results showed a very small sodium peak in the obtained spectrum (see spectrum, mapping and obtained Au:Na ratios in the Appendix of this chapter). Furthermore, this instrument reached its detection limits for sodium (0.1 wt%).

In addition to the performed bulk techniques, XPS analysis was used to identify species on the surface of the catalyst (spectra of all samples can be found in the Appendix of this chapter). The results of this experiment can be found in **Table 2B.1** and show a gold to sodium atomic ratio of 85:15. Comparing this ratio to SEM-EDX results, a conclusion that sodium species are present on the surface of the porous gold structure and not in the bulk could be drawn. It is important to mention that the quantitative analysis made by XPS did not take into account the possibility of gold

signal attenuation due to the presence of sodium containing surface layers, which can ultimately lead to overestimated sodium concentrations. The aim of this measurement was to identify the presence of sodium on the surface of the material and not in the bulk, which otherwise would have been an indication for a possible alloy of Na and Au (neglected by XRD and can be found in the Appendix of this chapter). To further identify the sodium species present on the catalyst surface, the Auger parameter was calculated using the position of the Na 1s peak and the Na KLL Auger peak. The parameter was calculated to be 2061 eV, ruling out the presence of elemental Na on this sample, as the Auger parameter would be in this case 265.9±0.3 eV[50].

In a first assumption, sodium was expected to be present in the form of Na^+-species on the gold surface (confirmed by XPS-analysis), which meant that the sodium concentration could be decreased by simply washing the catalyst material with Milli-Q water. After washing the samples as described in the Experimental Methods section of this chapter, XPS-data showed a significant decrease of the sodium concentration from 85:15 (Au:Na) before washing to 99:1 after washing (see **Table 2B.1**). After washing, a the oxidative methanol coupling test was performed, showing no activity of the catalyst independent from the temperature (see **Figure 2B.4**). This result was a first suggestion that sodium species have an influence on the catalytic activity of the porous gold systems for the oxidative methanol coupling.

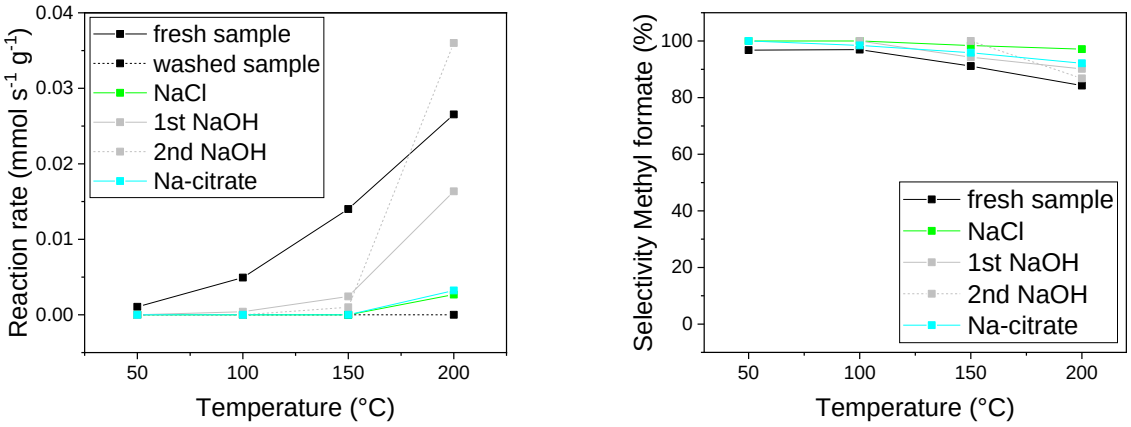

Figure 2B.4 Reaction rate normalized on mass (left) and selectivity towards methyl formate (right) for the oxidative coupling of methanol to methyl formate. The different curves indicate differently treated samples: A fresh sample (black line), a washed sample (**black dashed line**), a NaCl drop-cast sample (**green line**), repetitively NaOH drop-cast sample (**grey line and dashed grey line**) and a Na-citrate drop-cast sample (**cyan line**). All drop-castings were carried out after washing the sample thoroughly with 100 mL Milli-Q water.

In additional experiments, the influence of the sodium content on the catalytic activity of the porous structures was analyzed. Different sodium salts were used to re-deposit sodium ions on the gold surface, which was obtained by drop-casting the salt solution to obtain a fast deposition method. Sodium chloride (NaCl), sodium hydroxide (NaOH) and sodium citrate (Na-citrate) were dissolved in water and drop-cast one by one on the sample and subsequently the activity for oxidative methanol coupling was recorded (see **Figure 2B.4**).

During the first experiment, a NaCl-solution was drop-cast on the porous structure to aim for a Au:Na ratio of 85:15. XPS-analysis suggested a Au:Na ratio of 93:7, unexpectedly lower than the targeted value. These discrepancies were explained by an inhomogeneous distribution of the salt on the catalyst surface, which could lead to higher but also lower ratios than aimed for. Independently from this result, the sample was tested in the coupling reaction, which revealed a reaction rate of 0.003 $mmol_{CH3OH}\ s^{-1}\ g_{cat}^{-1}$ at 200°C. Compared to the starting value for the reaction rate of 0.027 $mmol_{CH3OH}\ s^{-1}\ g_{cat}^{-1}$, the here obtained rate was roughly ten times lower. Stable NaCl crystals on the surface can be considered responsible for the inactivity of the catalyst. The interfaces between Au and Na can be drastically decreased by larger NaCl crystallites on the surface. In addition, the chloride counter ion of this structure is known to be poisonous for catalyst in different catalytic reactions[49].

In a second experiment, the sample was washed once again to remove NaCl crystals from the surface and drop-cast once again with a NaOH-solution aiming for the same Au:Na ratio as mentioned before (85:15 atomic ratio). The result in a first experiment was 37:63 and 89:11 in a second experiment (see **Table 2B.1**). After the drop-casting test, a methanol coupling was performed on the catalyst and the activity was regained. In comparison to a washed sample, the activity was significantly higher (see **Figure 2B.4**). However, the activity of this sample was lower in comparison to a freshly synthesized sample. The reason can be found in the higher sodium content identified via XPS (**Table 2B.1)** or by the inhomogeneous distribution of the sodium on the sample surface (especially compared to the original sample) limiting the number of active interfaces. On the other hand, the second experiment resulted in a closer Au:Na ratio to the original sample, which was once again verified by XPS (see **Table 2B.1**). In this case, the reaction rate at 200°C was slightly higher than in the case of the as-synthesized sample. However, the activity of this sample did not reach the values of the fresh sample at lower temperatures (see **Figure 2B.4**). The here shown results underline the shortcomings of the chosen drop-casting technique, which

resulted in a mismatch of ratios compared to the original sample. The activity of the catalyst could not be fully recovered, when compared to a fresh sample, which can be explained by the inhomogeneity of the NaOH distribution on the sample. Yet, the results on the activity suggest a significant correlation between the sample activity in the methanol coupling and the presence of certain Na-species on the surface of the catalyst.

For the last experiment with Na-citrate, the sample was washed again and a Na-citrate solution drop-cast on the washed sample, which resulted in a surprising Au:Na ratio of 13:87 as revealed by XPS (see **Table 2B.1**). To explain the result, the presence of organic material from the citrate needs to be considered. A high content of Na-citrate on the catalyst surface could complicate the quantitative detection of gold itself. The organic part of the salt could be bulky enough to permeate the porous structure of the gels. In addition, the drop-casting method could lead to a thick Na-citrate layer covering the active sites of the catalyst. To identify the change of the Au:Na:C ratio before and after catalytic tests, XPS-measurements were performed, which revealed a ratio of 4:26:70 and 3:37:60 before and after catalytic tests, respectively (see **Table 2B.5** in the Appendix of this chapter). Firstly, the results show that the Na:Au ratio is significantly higher compared to an as-synthesized sample and secondly, that the exposure of the gold surface was significantly reduced in this experiment. Even after exposing the sample to high temperatures in the presence of oxygen, the surface situation seemed unchanged. Putting all these results together, a lower activity of this catalyst can be attributed to blocked active sites on the catalyst surface by the bulky citrate molecule or the poor Na distribution. The results confirm that organic molecules on the surface of the catalyst can be a crucial drawback for the catalytic activity and ultimately a possible drawback of this approach itself to synthesize porous gold structures, A clean surface is beneficial for the activity of a catalyst and should be aimed for.

Table 2B.1 Gold to sodium ratio on surface of sample after each treatment obtained by XPS-analysis. In comparison to the ratios, the reaction rate of each sample at 200°C normalized on the mass of used catalyst.

Sample	Au:Na ratio (atm%)	Reaction rate at 200°C ($mmol_{CH3OH}$ s^{-1} g_{cat}^{-1})
fresh sample	85:15	0.027
washed sample	99:1	0.000
NaCl	93:7	0.003
1st NaOH	37:63	0.016
2nd NaOH	89:11	0.036
Na-citrate	13:87	0.003

By analyzing the XPS-spectra in detail, measured at different points of the experiment (see timeline of experiment in Appendix of this chapter), the presence of Na-species on the catalyst surface could be correlated to the activity of the catalyst. A major focus was set on the carbon signals, as fresh samples (before catalytic activity = bct) presented a peak, indicating the presence of possible carbonate or carboxylate species on the catalyst surface.

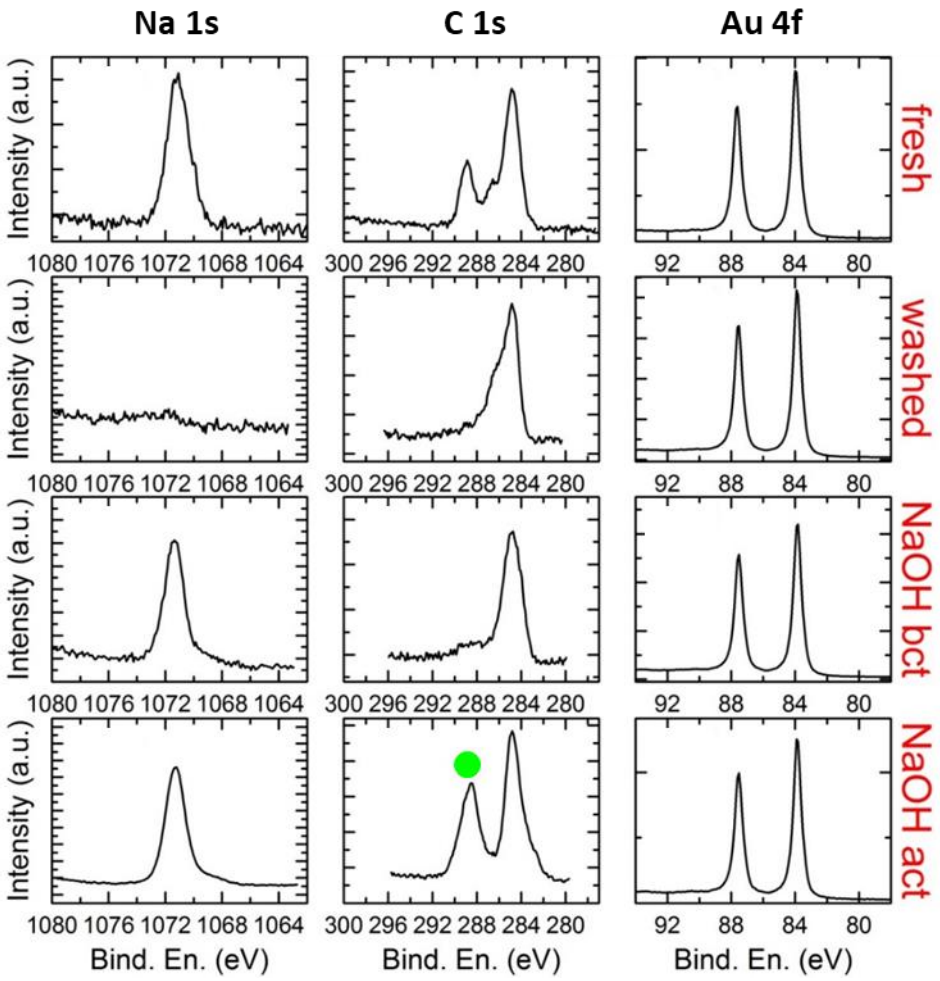

Figure 2B.5 Data on Na 1s peak (left), C 1s peak (centre) and Au 4f peak (right) for fresh sample bct, washed sample act, NaOH drop-cast sample bct and NaOH drop-cast sample act. For above spectra the C1s peak was aligned for all samples to the value 284.8 eV[50].

However, this observation was not surprising as ligands (citrates) were present on the surface of the gold particles, which reflected itself in the aforehand mentioned carbon peaks. After performing a methanol coupling reaction (in which the sample showed a high activity), the sample was washed and yet another reaction was performed, resulting in a poor activity of the catalyst. Subsequent XPS-analysis for this washed sample revealed the absence of both, sodium and the beforehand mentioned carbonate/carboxylate species found in a fresh sample (sample washed after catalytic test = act). After performing these experiments, the sample was drop-cast using a NaOH solution to regain the sodium content on the catalyst surface. Subsequently, the catalyst surface was analyzed for its surface species via XPS-analysis before (bct) and after catalytic tests (act). The results suggested, in the case of "NaOH bct", the presence of Na on the catalyst surface but the

absence of carbonate and carboxylates. In addition, the Na 1s signal was shifted compared to a fresh sample. Comparing the sample after the methanol coupling experiments, the Na 1s peak in the XPS-spectrum was back in the original position as in the case of a fresh sample and carbonates/ carboxylates were clearly identified once again. Comparing the Auger parameter for the Na-signal of a fresh sample and the NaOH drop-cast sample, a similar value of 2061 eV was observed for both. The results suggest that the observed carbonate/ carboxylate species play a key role in the catalytic coupling of methanol to methyl formate in the here shown system. The formed surface species are possible candidates for intermediates of the reaction leading to carbon dioxide and methyl formate. The results clearly indicate that the reaction mechanism can only proceed in the presence of sodium species on the surface of the catalyst. It is noteworthy to mention that the role of Na in this reaction mechanism needs to be further investigated and understood, as the mechanism seems to differ to the one suggested for NPG systems. This difference can be underlined by the fact that the here presented porous gold structure seems to be inactive in CO oxidation, whereas the metal traces in NPG seem to enhance the activity of the catalyst independent from the reaction (CO oxidation or oxidative methanol coupling).

4. Conclusion

In this work an established bottom-up method was used to synthesize porous gold structures, which were similar to the nanoporous gold from the top-down method. Analysis by means of SEM revealed a different microscopic structure of the here shown samples compared to those of NPG-systems, showing larger ligament sizes. However, the synthesized samples showed impurities (here sodium species) similar to the metal traces in the NPG. The samples obtained via cryogelation method were as expected, inactive in the oxidation of carbon monoxide but surprisingly highly active in the oxidative coupling of methanol. The inactivity in CO oxidation was explained by the absence of secondary metal traces (such as Cu, Ag and Al in NPG), whereas the high activity in methanol coupling was similar compared to nanoporous gold established by the top-down approach. The activity derived from sodium impurities on the surface of the catalyst and was detected via different bulk and surface sensitive techniques. By washing the as-synthesized samples, the sodium content on the catalyst surface was reduced significantly (verified by XPS-analysis) and pure porous gold structures were obtained, which is yet not achievable by the established top-down dealloying method. This sodium free sample was then tested in the oxidative methanol coupling showing no activity for the reaction and suggesting that the sodium holds a key role in the reaction in case of the here shown samples. Nevertheless, the activity of the catalyst

could be restored using the simple drop-casting method with a sodium hydroxide solution. XPS-analysis revealed a carbonate/carboxylate intermediate forming on the surface in the presence of sodium.

Finally, the here shown results suggest that the activity of porous gold systems obtained by the self-assembly of gold nanoparticles is strictly dependent on the presence of sodium traces on the catalyst surface, in particular in the case of the oxidative coupling of methanol. However, the comparison to nanoporous gold obtained via dealloying should be handled with care, seen that there are differences in the synthesis method, the microscopic structure and the residues present on the catalyst surface. Hence, extending these results to the nanoporous gold system would not be completely correct. The here presented approach demonstrates a well-established bottom-up method and its possible usage in future unsupported catalyst design. The cryogelation method can be extended on different particle sizes, shapes and chemical compositions paving the way to endless possibilities of catalyst development.

5. Appendix

Krypton-BET

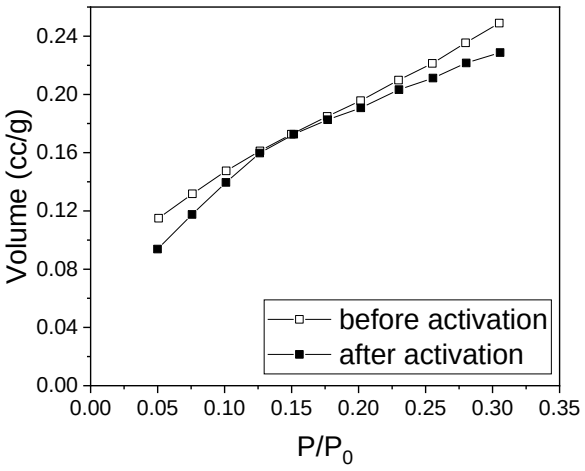

Figure 2B.6 Isotherms obtained by Kr-adsorption for a sample before (blank points) and after (filled points) activity tests.

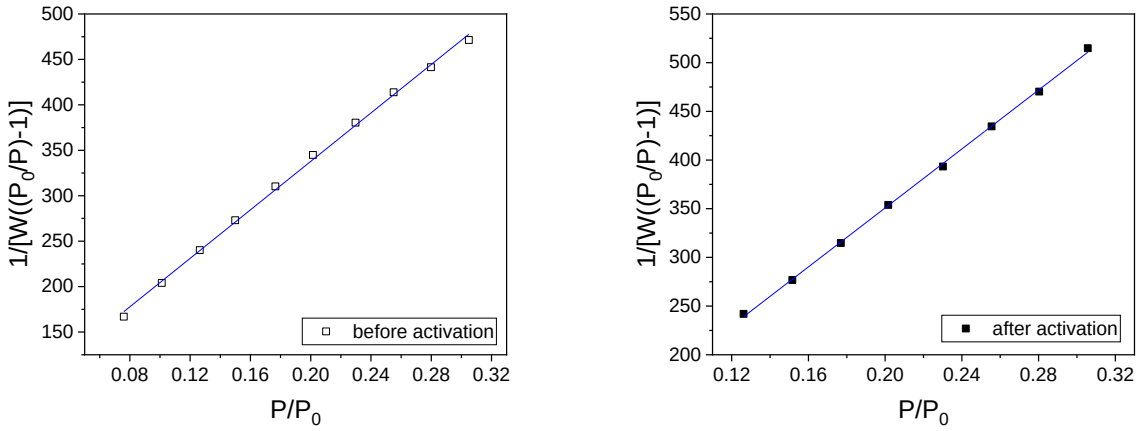

Figure 2B.7 BET-isotherms for the sample before (left) and after (right) activity tests.

XRD-analysis

To calculate the crystallite size the so-called Scherrer equation was elaborated on three peaks taken from the following diffraction pattern of the sample before and after activity tests. The obtained values are reported in **Table 2B.2**.

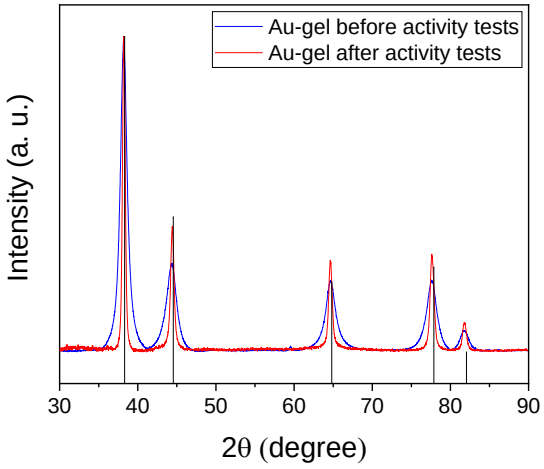

Figure 2B.8 XRD diffraction peaks for sample before (blue line) and after (red line) activity tests compared to bulk Au diffraction pattern (black vertical lines, reference code: ICDD 96-901-1613).

Table 2B.2 Peaks and corresponding crystallite size for sample before and after activity tests. Results were averaged at the end.

Peak #	**before activity tests**		**after activity tests**	
	Peak /°2θ	**Crystallite size /nm**	**Peak /°2θ**	**Crystallite size /nm**
#1	64.619	6.4	64.593	20.7
#2	77.531	6.6	77.578	20.9
#3	81.674	7.5	81.731	21.1
Average ± StDev /nm	6.8 ± 0.6		20.9 ± 0.2	

To exclude the possibility of Na-Au alloys, a pattern of $NaAu_2$ was compared to the elaborated pattern of the sample. The comparison is displayed in **Figure 2B.9** and shows no indication of the presence of such a phase in the crystallite structure of the obtained material.

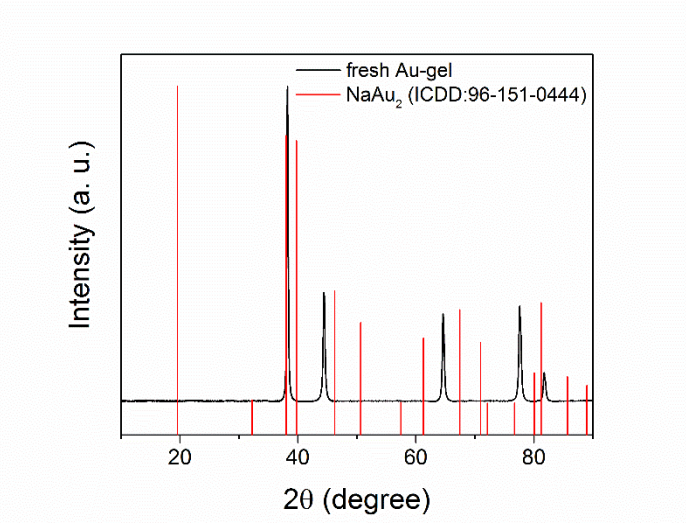

Figure 2B.9 XRD diffraction peaks for sample (black line) and $NaAu_2$ pattern from database (red vertical lines, reference code: ICDD 96-151-0444).

Transient measurement results for oxidative methanol coupling reaction

Seen that the analysis method to identify both, the incoming reactant and the outcoming reactant, needs to be precise, a third parameter provides additional accuracy. The *carbon balance* in those reactions can be described as the sum of the concentration of all molecules involving carbon (in

case of the methanol coupling reaction these molecules would be methanol, methyl formate and CO_2). The sum of all these species can be monitored throughout the experiment, to understand if there is loss of carbon molecules during the experiment due to strong adsorption on the catalyst surface, accumulation in the lines of the experimental setup or loss due to leaks. A well monitored carbon balance can give insight into how precise an experiment was performed.

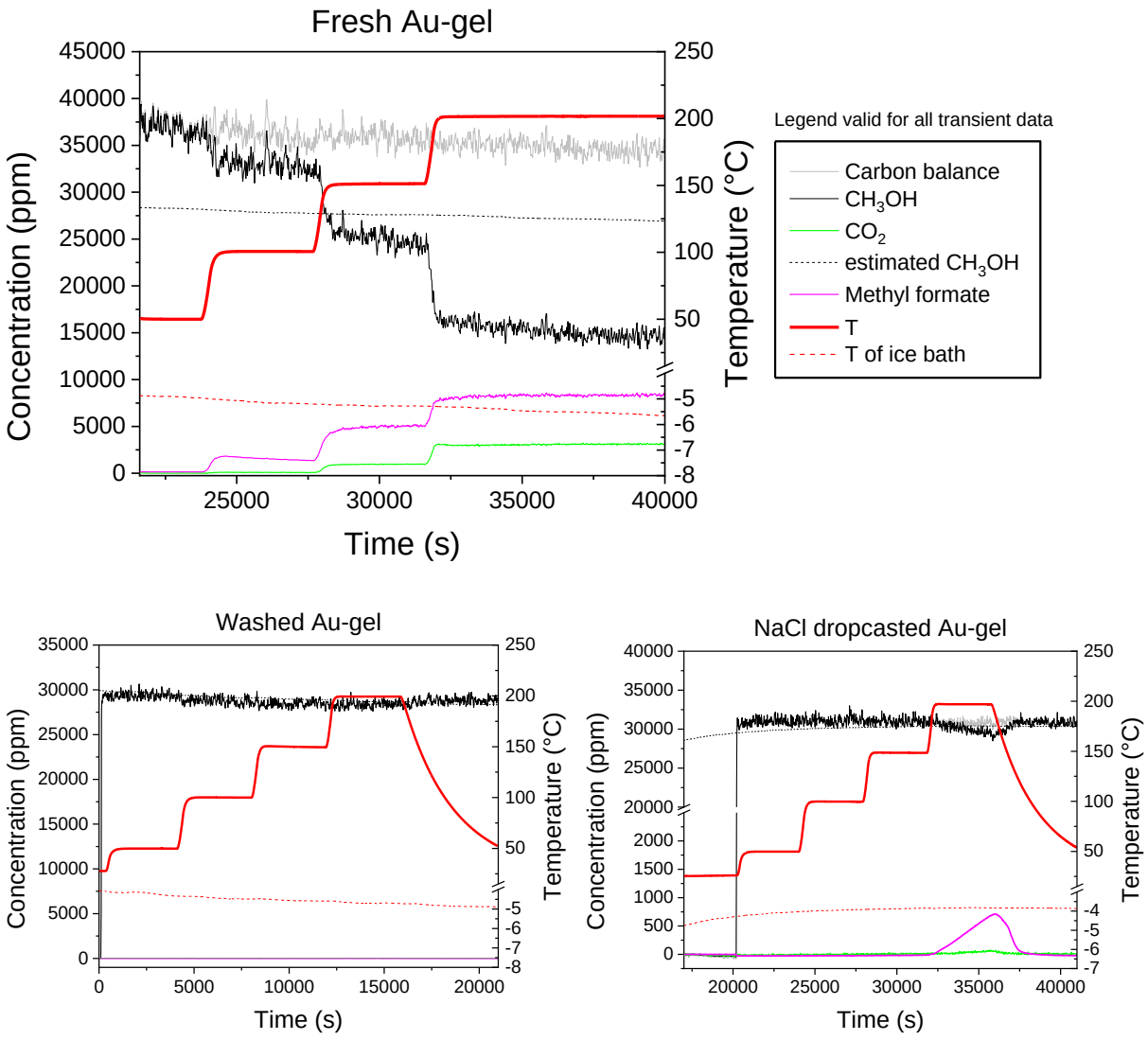

Figure 2B.10 Transient data of samples: fresh sample, washed sample and drop-cast with NaCl, respectively

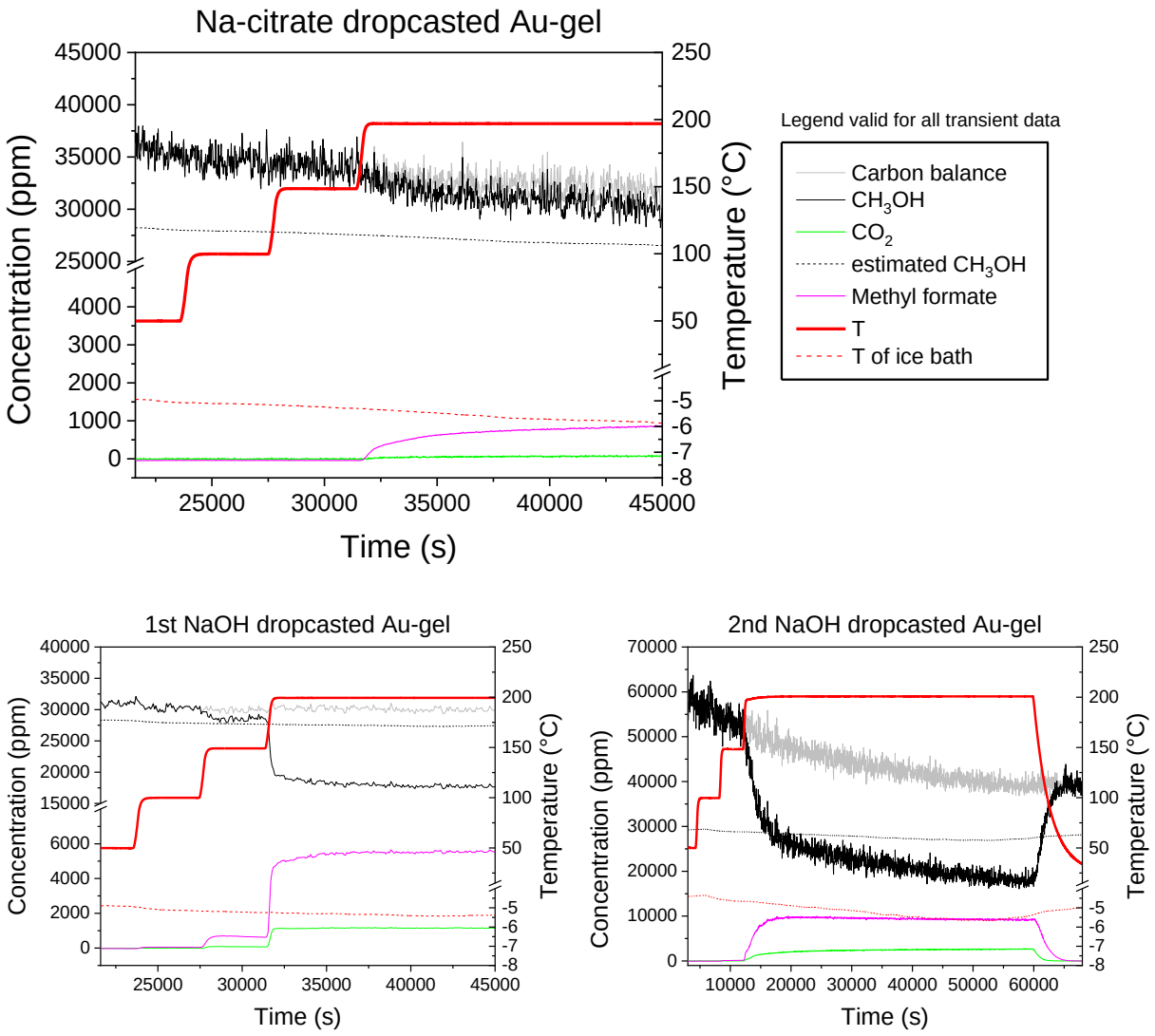

Figure 2B.11 Transient data of samples: drop-cast with Na-citrate, drop-cast 1st time with NaOH and drop-cast 2nd time with NaOH, respectively.

In **Figure 2B.10-Figure 2B.11** the carbon balance of each measurement is added. This carbon balance can differ throughout the reaction, because of temperature changes of the methanol cooling bath during time. This is particularly observed in the last image of this figure, which can be explained by the decrease of the temperature in the later period of the reaction, which consequently leads to a lower vapor pressure of methanol and finally to a lower methanol concentration in gas phase.

SEM-EDX images of gels before and after catalytic tests

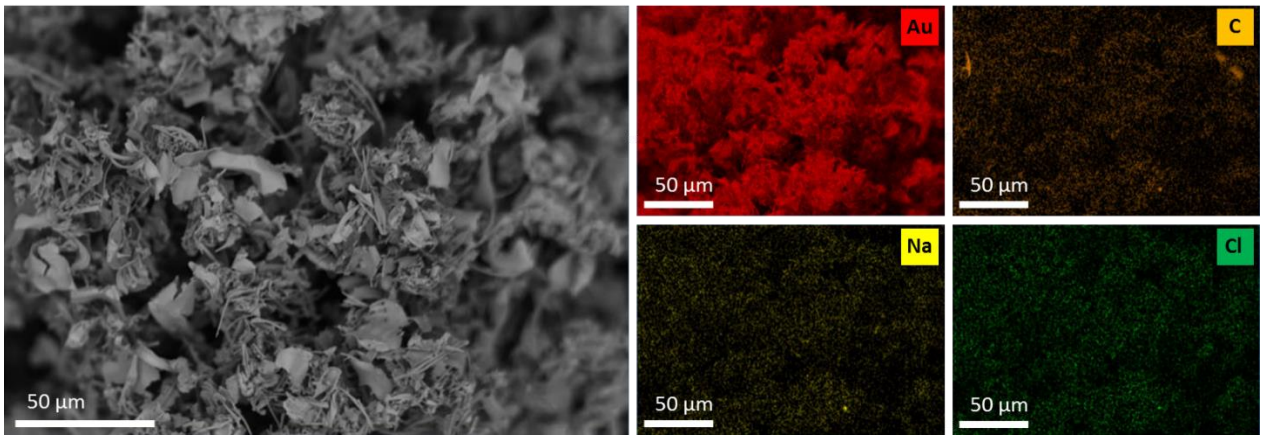

Figure 2B.12 Mapping of Au-gel before activity tests and mapped elements (Au, C, Cl and Na).

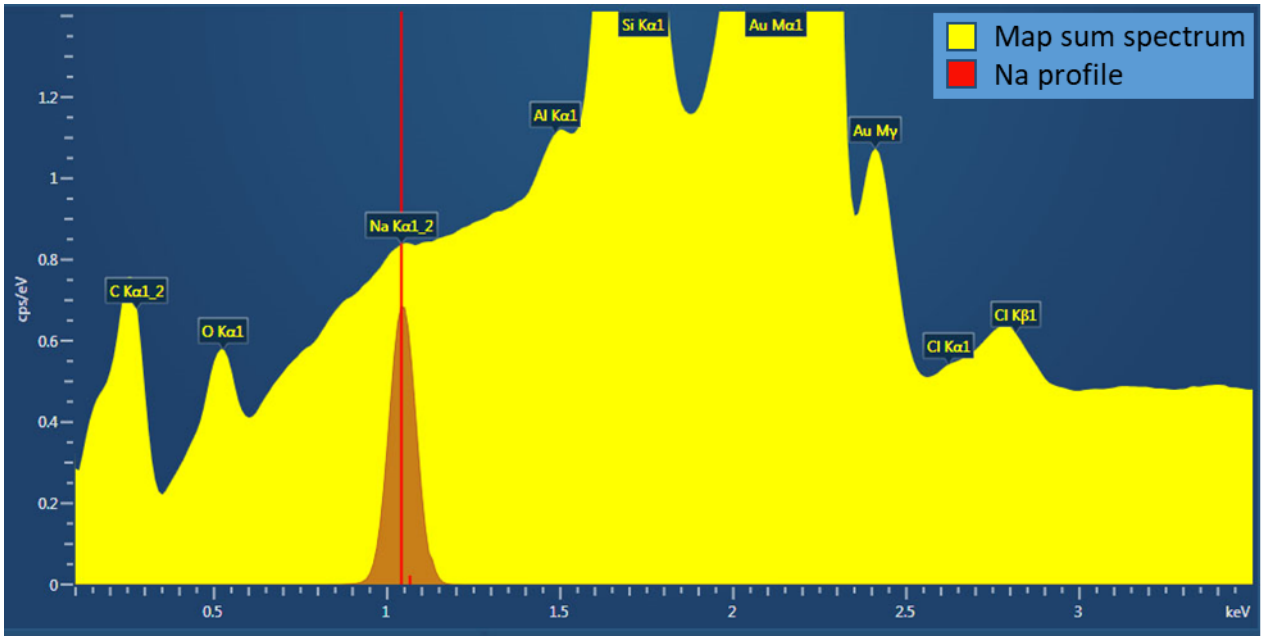

Figure 2B.13 EDX-spectrum of sample before activity tests with indicated Na profile.

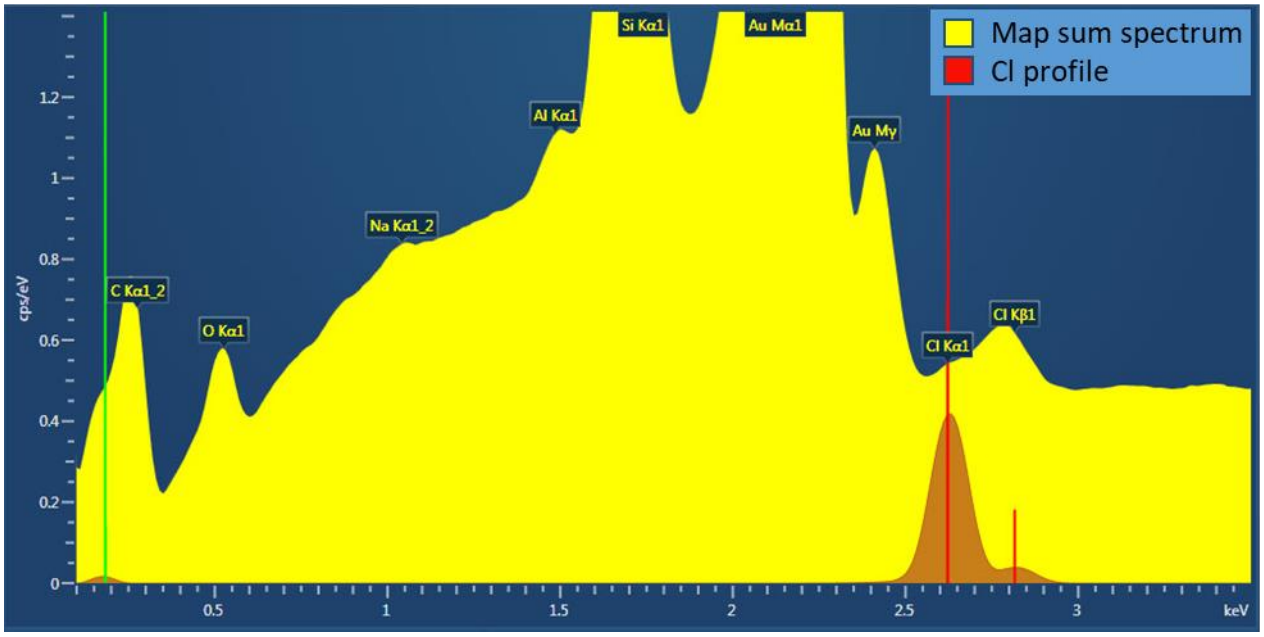

Figure 2B.14 EDX-spectrum of sample before activity tests with indicated Cl profile.

Table 2B.3 Atomic and weight ratio of Au, Na, Cl and C of sample before activity tests.

Element	Atomic%	Atomic% Sigma	Wt%	Wt% Sigma
Au	59.54	0.06	95.93	0.10
Na	0.29	0.12	0.05	0.02
Cl	0.33	0.07	0.10	0.02
C	39.85	1.02	3.92	0.10
Total	100.00		100.00	

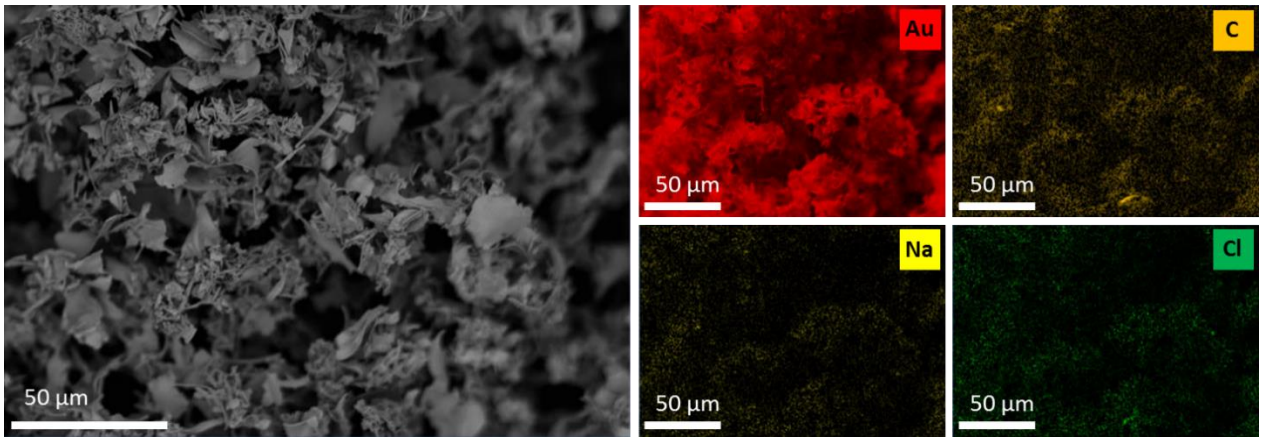

Figure 2B.15 Mapping of Au after activity tests and mapped elements (Au, C, Cl and Na).

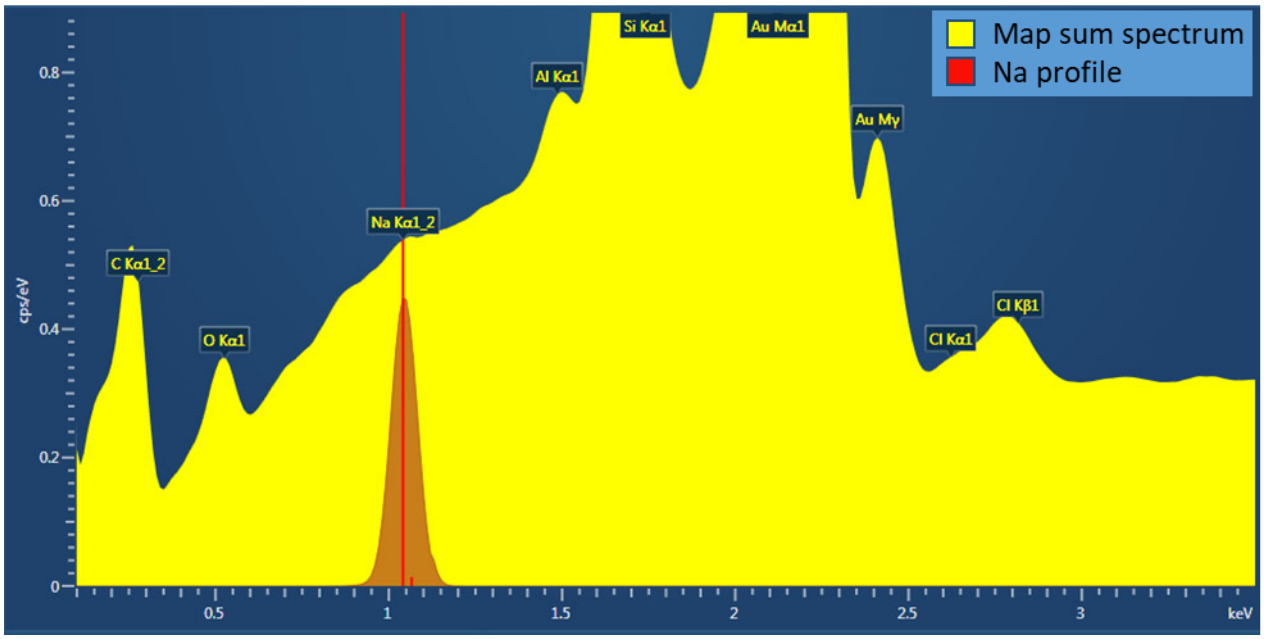

Figure 2B.16 EDX-spectrum of sample after activity tests with indicated Na profile.

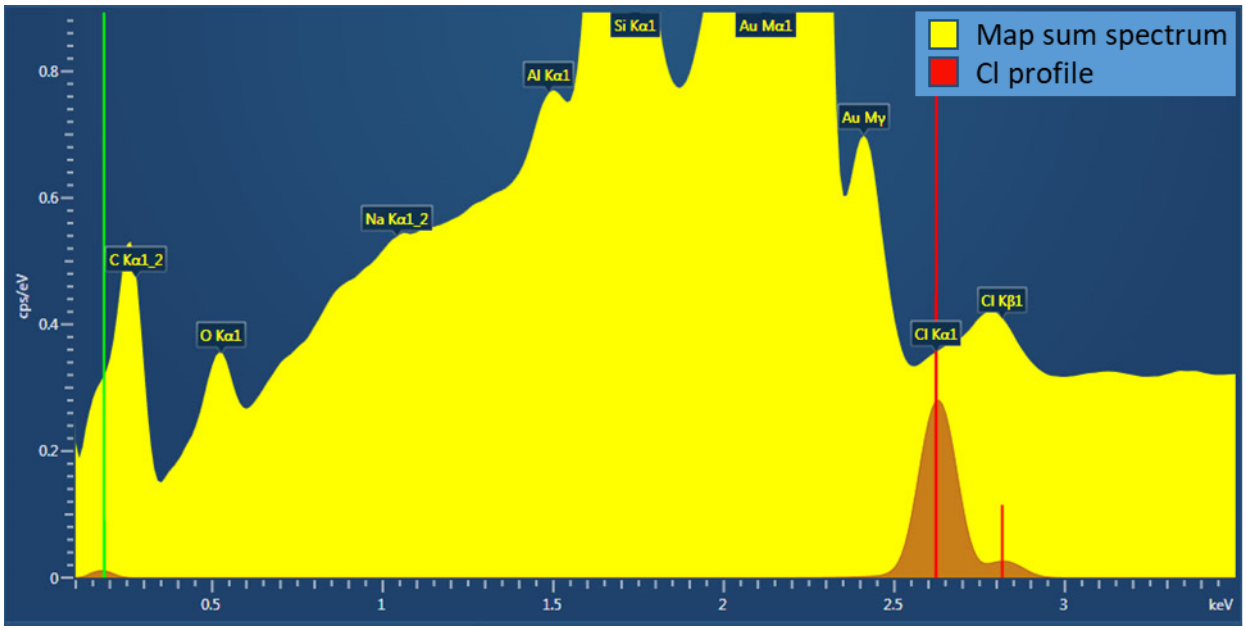

Figure 2B.17 EDX-spectrum of sample after activity tests with indicated Cl profile.

Table 2B.4 Atomic and weight ratio of Au, Na, Cl and C of sample after activity tests.

Element	Atomic%	Atomic% Sigma	Wt%	Wt% Sigma
Au	58.09	0.04	95.70	0.06
Na	0.22	0.06	0.04	0.01
Cl	0.34	0.03	0.10	0.01
C	41.35	0.60	4.15	0.06
Total	100.00		100.00	

XPS-analysis

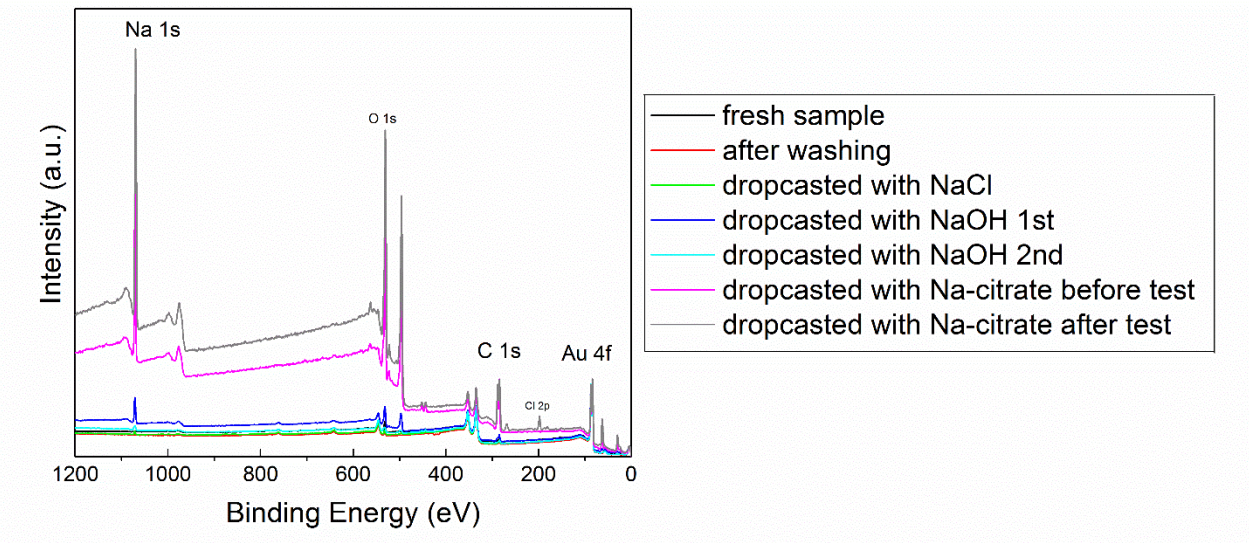

Figure 2B.18 XPS-spectra of all samples normalized on Au 4f signal.

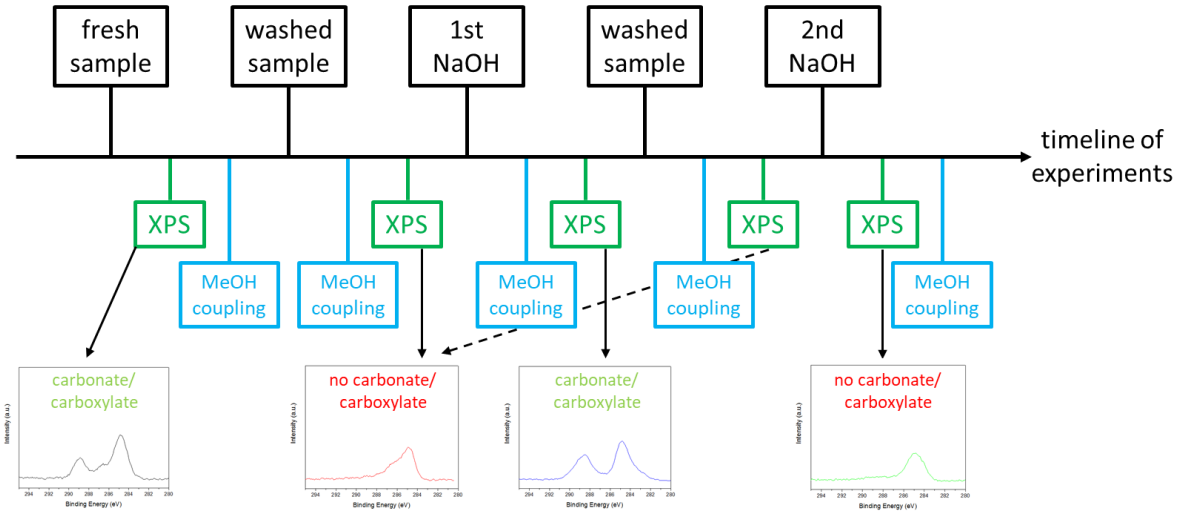

Figure 2B.19 Timeline on experiments (XPS, oxidative methanol coupling, washing and drop-casting with NaOH) performed on the sample.

Table 2B.5 Ratios of Au:Na:C determined by high resolution XPS in comparison.

Sample	Au 4f (atm%)	Na 1s (atm%)	C 1s (atm%)
washed sample	59.18	0.50	40.32
1st NaOH	14.35	26.40	59.25
2nd NaOH	53.40	6.91	39.69
Na-citrate before test	3.73	25.89	70.37
Na-citrate after test	2.90	37.48	59.61

6. References

(1) Bone, W. A.; Wheeler, R. V. The Combination of Hydrogen and Oxygen in Contact with Hot Surfaces. *Philos. Trans. R. Soc. A Math. Phys. Eng. Sci.* **1906**, *206* (402–412), 1–67. https://doi.org/10.1098/rsta.1906.0015.

(2) Chapman, D. L.; Ramsbottom, J. E.; Trotman, C. G. The Union of Hydrogen and Oxygen in Presence of Silver and Gold. *Proc. R. Soc. A Math. Phys. Eng. Sci.* **1925**, *107* (741), 92–100. https://doi.org/10.1098/rspa.1925.0007.

(3) Benton, A. F.; Elgin, J. C. THE CATALYTIC SYNTHESIS OF WATER VAPOR IN CONTACT WITH METALLIC GOLD [1]. *J. Am. Chem. Soc.* **1927**, *49* (10), 2426–2438. https://doi.org/10.1021/ja01409a012.

(4) Norman, R. O. C.; Parr, W. J. E.; Thomas, C. B. The Reactions of Alkynes, Cyclopropanes, and Benzene Derivatives with Gold(III). *J. Chem. Soc. Perkin Trans. 1* **1976**, No. 18, 1983–1987. https://doi.org/10.1039/P19760001983.

(5) Gorin, D. J.; Davis, N. R.; Toste, F. D. Gold(I)-Catalyzed Intramolecular Acetylenic Schmidt Reaction. *J. Am. Chem. Soc.* **2005**, *127* (32), 11260–11261. https://doi.org/10.1021/ja053804t.

(6) Reetz, M. T.; Sommer, K. Gold-Catalyzed Hydroarylation of Alkynes. *European J. Org. Chem.* **2003**, *2003* (18), 3485–3496. https://doi.org/10.1002/ejoc.200300260.

(7) Gasparrini, F.; Giovannoli, M.; Misiti, D.; Natile, G.; Palmieri, G.; Maresca, L. Gold(III)-Catalyzed One-Pot Synthesis of Isoxazoles from Terminal Alkynes and Nitric Acid. *J. Am. Chem. Soc.* **1993**, *115* (10), 4401–4402. https://doi.org/10.1021/ja00063a084.

(8) Fukuda, Y.; Utimoto, K. Preparation of 2,3,4,5-Tetrahydropyridines from 5-Alkynylamines Under the Catalytic Action of Gold(III) Salts. *Synthesis (Stuttg).* **1991**, *1991* (11), 975–978. https://doi.org/10.1055/s-1991-26621.

(9) Bone, W. A.; Andrew, G. W. Studies upon Catalytic Combustion. Part I. The Union of Carbon Monoxide and Oxygen in Contact with a Gold Surface. *Proc. R. Soc. A Math. Phys. Eng. Sci.* **1925**, *109* (751), 459–476. https://doi.org/10.1098/rspa.1925.0138.

(10) Pattrick, G.; van der Lingen, E.; Corti, C. W.; Holliday, R. J.; Thompson, D. T. The Potential for Use of Gold in Automotive Pollution Control Technologies: A Short Review. *Top. Catal.* **2004**, *30* (1), 273–279. https://doi.org/10.1023/B:TOCA.0000029762.14168.d8.

(11) ONOE, R.; SAKAGAMI, S.; ITO, T.; TAKEUCHI, M.; MIYOSHI, N.; SATO, A. EXHAUST GAS PURIFICATION CATALYST, 2017.

(12) Hutchings, G. J. Catalysis: A Golden Future. *Gold Bull.* **1996**, *29* (4), 123–130. https://doi.org/10.1007/BF03214746.

(13) Cunningham, A. H. D.; Zumaqué, H.; Duff, D.-G.; Völkening, S.; Wiessmeier, G. PROCESS FOR THE EPOXIDATION OF O EFINS USING GOLD- CONTAINING CATALYSTS. 2001.

(14) Landon, P.; Collier, P. J.; Papworth, A. J.; Kiely, C. J.; Hutchings, G. J. Direct Formation of Hydrogen Peroxide from H2/O2 Using a Gold Catalyst. *Chem. Commun.* **2002**, No. 18, 2058–2059. https://doi.org/10.1039/b205248m.

(15) Cameron, D.; Holliday, R.; Thompson, D. Gold's Future Role in Fuel Cell Systems. *J. Power Sources* **2003**, *118* (1), 298–303. https://doi.org/10.1016/S0378-7753(03)00074-0.

(16) Andreeva, D. Low Temperature Water Gas Shift over Gold Catalysts. *Gold Bull.* **2002**, *35* (3), 82–88. https://doi.org/10.1007/BF03214843.

(17) Rombi, E.; Cutrufello, M. G.; Monaci, R.; Cannas, C.; Gazzoli, D.; Onida, B.; Pavani, M.; Ferino, I. Gold Nanoparticles Supported on Conventional Silica as Catalysts for the Low-Temperature CO Oxidation. *J. Mol. Catal. A Chem.* **2015**, *404*, 83–91. https://doi.org/10.1016/j.molcata.2015.04.013.

(18) Wang, Z.; Fu, H.; Tian, Z.; Han, D.; Gu, F. Strong Metal–Support Interaction in Novel Core–Shell Au–CeO2 Nanostructures Induced by Different Pretreatment Atmospheres and Its

Influence on CO Oxidation. *Nanoscale* **2016**, *8* (11), 5865–5872. https://doi.org/10.1039/C5NR06929G.

(19) Bond, G. C.; Thompson, D. T. Gold-Catalysed Oxidation of Carbon Monoxide. *Gold Bull.* **2000**, *33* (2), 41–50. https://doi.org/10.1007/BF03216579.

(20) Hvolbæk, B.; Janssens, T. V. W.; Clausen, B. S.; Falsig, H.; Christensen, C. H.; Nørskov, J. K. Catalytic Activity of Au Nanoparticles. *Nano Today* **2007**, *2* (4), 14–18. https://doi.org/10.1016/S1748-0132(07)70113-5.

(21) He, Q.; Freakley, S. J.; Edwards, J. K.; Carley, A. F.; Borisevich, A. Y.; Mineo, Y.; Haruta, M.; Hutchings, G. J.; Kiely, C. J. Population and Hierarchy of Active Species in Gold Iron Oxide Catalysts for Carbon Monoxide Oxidation. *Nat. Commun.* **2016**, *7* (1), 12905. https://doi.org/10.1038/ncomms12905.

(22) Veith, G. M.; Lupini, A. R.; Rashkeev, S.; Pennycook, S. J.; Mullins, D. R.; Schwartz, V.; Bridges, C. A.; Dudney, N. J. Thermal Stability and Catalytic Activity of Gold Nanoparticles Supported on Silica. *J. Catal.* **2009**, *262* (1), 92–101. https://doi.org/10.1016/j.jcat.2008.12.005.

(23) Wittstock, A.; Biener, J.; Bäumer, M. Nanoporous Gold: A New Material for Catalytic and Sensor Applications. *Phys. Chem. Chem. Phys.* **2010**, *12* (40), 12919. https://doi.org/10.1039/c0cp00757a.

(24) Zugic, B.; Wang, L.; Heine, C.; Zakharov, D. N.; Lechner, B. A. J.; Stach, E. A.; Biener, J.; Salmeron, M.; Madix, R. J.; Friend, C. M. Dynamic Restructuring Drives Catalytic Activity on Nanoporous Gold–Silver Alloy Catalysts. *Nat. Mater.* **2016**, *16*, 558.

(25) Personick, M. L.; Zugic, B.; Biener, M. M.; Biener, J.; Madix, R. J.; Friend, C. M. Ozone-Activated Nanoporous Gold: A Stable and Storable Material for Catalytic Oxidation. *ACS Catal.* **2015**, *5* (7), 4237–4241. https://doi.org/10.1021/acscatal.5b00330.

(26) Iqbal, P.; Preece, J. A.; Mendes, P. M. Nanotechnology: The "Top-Down" and "Bottom-Up" Approaches. *Supramolecular Chemistry*. January 27, 2012. https://doi.org/doi:10.1002/9780470661345.smc195.

(27) Kameoka, S.; Tanabe, T.; Miyamoto, K.; Tsai, A. P. Insights into the Dominant Factors of Porous Gold for CO Oxidation. *J. Chem. Phys.* **2016**, *144* (3), 034703. https://doi.org/10.1063/1.4940307.

(28) Kameoka, S.; Tsai, A. P. CO Oxidation Over a Fine Porous Gold Catalyst Fabricated by Selective Leaching from an Ordered AuCu3 Intermetallic Compound. *Catal. Letters* **2008**, *121* (3), 337–341. https://doi.org/10.1007/s10562-007-9344-x.

(29) Fujita, T.; Guan, P.; McKenna, K.; Lang, X.; Hirata, A.; Zhang, L.; Tokunaga, T.; Arai, S.; Yamamoto, Y.; Tanaka, N.; et al. Atomic Origins of the High Catalytic Activity of Nanoporous Gold. *Nat. Mater.* **2012**, *11* (9), 775–780. https://doi.org/10.1038/nmat3391.

(30) Zhang, Q.; Wang, X.; Qi, Z.; Wang, Y.; Zhang, Z. A Benign Route to Fabricate Nanoporous Gold through Electrochemical Dealloying of Al–Au Alloys in a Neutral Solution. *Electrochim. Acta* **2009**, *54* (26), 6190–6198. https://doi.org/10.1016/j.electacta.2009.05.089.

(31) Lackmann, A.; Mahr, C.; Schowalter, M.; Fitzek, L.; Weissmüller, J.; Rosenauer, A.; Wittstock, A. A Comparative Study of Alcohol Oxidation over Nanoporous Gold in Gas and Liquid Phase. *J. Catal.* **2017**, *353*, 99–106. https://doi.org/10.1016/J.JCAT.2017.07.008.

(32) Xu, C.; Su, J.; Xu, X.; Liu, P.; Zhao, H.; Tian, F.; Ding, Y. Low Temperature CO Oxidation over Unsupported Nanoporous Gold. *J. Am. Chem. Soc.* **2007**, *129* (1), 42–43. https://doi.org/10.1021/ja0675503.

(33) Tanaka, S.; Minato, T.; Ito, E.; Hara, M.; Kim, Y.; Yamamoto, Y.; Asao, N. Selective Aerobic Oxidation of Methanol in the Coexistence of Amines by Nanoporous Gold Catalysts: Highly Efficient Synthesis of Formamides. *Chem. - A Eur. J.* **2013**, *19* (36), 11832–11836. https://doi.org/10.1002/chem.201302396.

(34) Mahr, C.; Kundu, P.; Lackmann, A.; Zanaga, D.; Thiel, K.; Schowalter, M.; Schwan, M.; Bals, S.; Wittstock, A.; Rosenauer, A. Quantitative Determination of Residual Silver Distribution in Nanoporous Gold and Its Influence on Structure and Catalytic Performance. *J. Catal.* **2017**, *352*, 52–58. https://doi.org/10.1016/J.JCAT.2017.05.002.

(35) Zugic, B.; Karakalos, S.; Stowers, K. J.; Biener, M. M.; Biener, J.; Madix, R. J.; Friend, C. M. Continuous Catalytic Production of Methyl Acrylates from Unsaturated Alcohols by Gold: The Strong Effect of C═C Unsaturation on Reaction Selectivity. *ACS Catal.* **2016**, *6* (3), 1833–1839. https://doi.org/10.1021/acscatal.5b02902.

(36) Wittstock, A.; Zielasek, V.; Biener, J.; Friend, C. M.; Bäumer, M. Nanoporous Gold Catalysts for Selective Gas-Phase Oxidative Coupling of Methanol at Low Temperature. *Science (80-.).* **2010**, *327* (5963), 319 LP – 322. https://doi.org/10.1126/science.1183591.

(37) Lackmann, A.; Bäumer, M.; Wittstock, G.; Wittstock, A. Independent Control over Residual Silver Content of Nanoporous Gold by Galvanodynamically Controlled Dealloying. *Nanoscale* **2018**, *10* (36), 17166–17173. https://doi.org/10.1039/C8NR03699C.

(38) Rugolo, J.; Erlebacher, J.; Sieradzki, K. Length Scales in Alloy Dissolution and Measurement of Absolute Interfacial Free Energy. *Nat. Mater.* **2006**, *5* (12), 946–949. https://doi.org/10.1038/nmat1780.

(39) Tomaschun, G.; Dononelli, W.; Li, Y.; Bäumer, M.; Klüner, T.; Moskaleva, L. V. Methanol Oxidation on the Au(3 1 0) Surface: A Theoretical Study. *J. Catal.* **2018**, *364*, 216–227. https://doi.org/10.1016/j.jcat.2018.05.020.

(40) Bigall, N. C.; Herrmann, A.-K.; Vogel, M.; Rose, M.; Simon, P.; Carrillo-Cabrera, W.; Dorfs, D.; Kaskel, S.; Gaponik, N.; Eychmüller, A. Hydrogels and Aerogels from Noble Metal Nanoparticles. *Angew. Chemie Int. Ed.* **2009**, *48* (51), 9731–9734. https://doi.org/10.1002/anie.200902543.

(41) Liu, W.; Herrmann, A.-K.; Bigall, N. C.; Rodriguez, P.; Wen, D.; Oezaslan, M.; Schmidt, T. J.; Gaponik, N.; Eychmüller, A. Noble Metal Aerogels—Synthesis, Characterization, and Application as Electrocatalysts. *Acc. Chem. Res.* **2015**, *48* (2), 154–162. https://doi.org/10.1021/ar500237c.

(42) Freytag, A.; Sánchez-Paradinas, S.; Naskar, S.; Wendt, N.; Colombo, M.; Pugliese, G.; Poppe, J.; Demirci, C.; Kretschmer, I.; Bahnemann, D. W.; et al. Versatile Aerogel Fabrication by

Freezing and Subsequent Freeze-Drying of Colloidal Nanoparticle Solutions. *Angew. Chemie - Int. Ed.* **2016**, *55* (3). https://doi.org/10.1002/anie.201508972.

(43) Takale, B. S.; Feng, X.; Lu, Y.; Bao, M.; Jin, T.; Minato, T.; Yamamoto, Y. Unsupported Nanoporous Gold Catalyst for Chemoselective Hydrogenation Reactions under Low Pressure: Effect of Residual Silver on the Reaction. *J. Am. Chem. Soc.* **2016**, *138* (32), 10356–10364. https://doi.org/10.1021/jacs.6b06569.

(44) Biener, J.; Biener, M. M.; Madix, R. J.; Friend, C. M. Nanoporous Gold: Understanding the Origin of the Reactivity of a 21st Century Catalyst Made by Pre-Columbian Technology. *ACS Catal.* **2015**, *5* (11), 6263–6270. https://doi.org/10.1021/acscatal.5b01586.

(45) Déronzier, T.; Morfin, F.; Massin, L.; Lomello, M.; Rousset, J.-L. Pure Nanoporous Gold Powder: Synthesis and Catalytic Properties. *Chem. Mater.* **2011**, *23* (24), 5287–5289. https://doi.org/10.1021/cm202105k.

(46) Zhang, X.; Ding, Y. Unsupported Nanoporous Gold for Heterogeneous Catalysis. *Catal. Sci. Technol.* **2013**, *3* (11), 2862. https://doi.org/10.1039/c3cy00241a.

(47) Wang, L.-C.; Zhong, Y.; Jin, H.; Widmann, D.; Weissmüller, J.; Behm, R. J. Catalytic Activity of Nanostructured Au: Scale Effects versus Bimetallic/Bifunctional Effects in Low-Temperature CO Oxidation on Nanoporous Au. *Beilstein J. Nanotechnol.* **2013**, *4*, 111–128. https://doi.org/10.3762/bjnano.4.13.

(48) Zielasek, V.; Jürgens, B.; Schulz, C.; Biener, J.; Biener, M. M.; Hamza, A. V.; Bäumer, M. Gold Catalysts: Nanoporous Gold Foams. *Angew. Chemie Int. Ed.* **2006**, *45* (48), 8241–8244. https://doi.org/10.1002/anie.200602484.

(49) Broqvist, P.; Molina, L. M.; Grönbeck, H.; Hammer, B. Promoting and Poisoning Effects of Na and Cl Coadsorption on CO Oxidation over MgO-Supported Au Nanoparticles. *J. Catal.* **2004**, *227* (1), 217–226. https://doi.org/10.1016/j.jcat.2004.07.009.

(50) NIST. *NIST X-Ray Photoelectron Spectroscopy Database*; Gaithersburg, 2012.

Chapter III: Total Pressure Effects on the Combustion of Methane over a Pd/Al_2O_3 Catalyst

This part of the thesis was performed at the Chalmers University of Technology, Gothenburg, Sweden in collaboration with Carl-Robert Florén and his supervisor Magnus Skoglundh[1].

Abstract

In this work a range of various kinetic parameters for the total oxidation of methane in a lean gas feed using a 0.15 wt-% Pd/Al_2O_3 catalyst was studied. A specific focus was set on the dependency of the light-off temperature, the activation energy and the reaction order on the total pressure ranging from 1 to 10 atm and the temperature from 350 to 450°C. In addition, the effect of carbon dioxide and water present in the reaction atmosphere were analyzed. Above 350°C the catalytic activity for the methane combustion can be enhanced at elevated total pressures. The reaction order for methane appears to decrease at 350°C, whereas at higher temperatures it increases with increasing total pressures. The results were compared with multiscale models to better comprehend the utility of this model in future applications. Generally, the trend of the simulations appears to follow the trend of the experimental results. At low temperatures the observed lower conversion for simulated results can be explained by blocked active sites, which are even more pronounced at higher pressures. Conversely, at high temperatures the conversion appears to be higher due to a complex interplay between fast kinetics and reduced internal mass transport resistance.

1. Introduction

Our atmosphere is composed of 78% nitrogen, 21% oxygen, 0.9% argon, 0.04% carbon dioxide and diverse range of trace gases[2]. One of these trace gases in the atmosphere is known to be methane (CH_4), which can be anthropogenically difficult to capture once emitted and hence requires the restriction of its emission in the first place. It is a known fact that methane is a powerful greenhouse gas, 25 times more powerful than carbon dioxide over a 100-year period[3], and one of the least reactive alkanes[4]. Looking at global numbers, around 50-65% of the total methane emissions results from anthropogenic activities[3]. The main emissions of methane can be found in agriculture[5,6], in oil and gas extraction[7], in waste treatment[8,9] and the combustion of fuel[3]. Due to the high impact of methane in global warming and climate change[10], great efforts should be made to reduce the emission of such gases. To tackle the emission of methane in the atmosphere, it is important to work in each of the aforementioned sectors to reduce the volumes of emitted gas. One

way to reduce the impact of methane on global warming can be a controlled emission of fuel combustion (such as natural gas combustion engines). Either alternative engines (such as electromobility) can pave a road to a greener future or the catalysts in the emission control system of combustion engines (exhaust catalysts) needs to be improved.

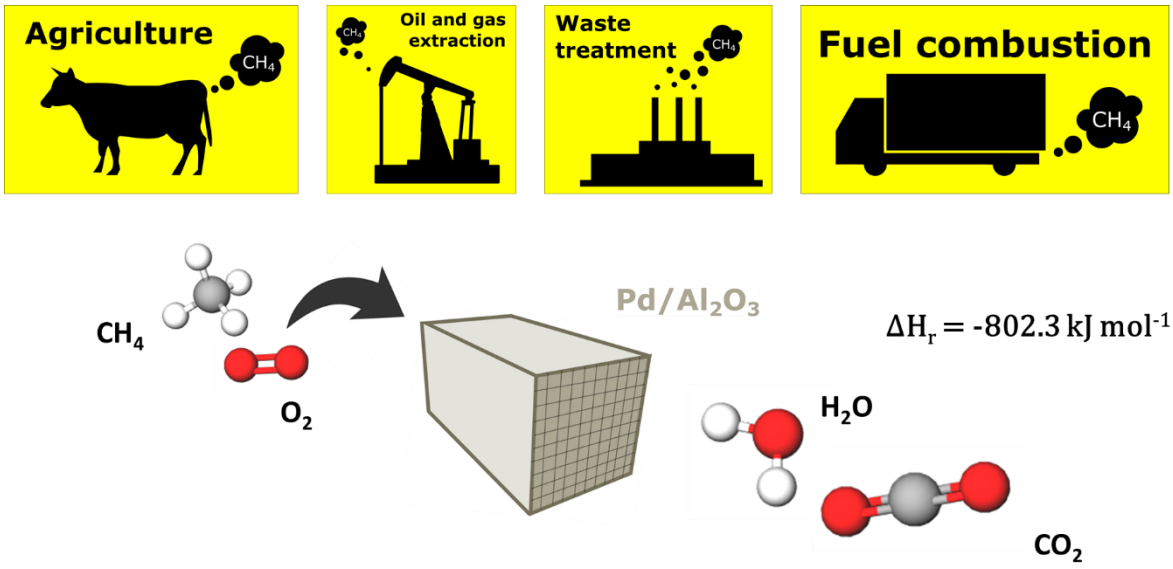

Figure 3.1 Sources of methane in different industrial fields and its conversion over a Pd/Al_2O_3 catalyst in presence of oxygen to CO_2 and water.

Methane is the main component in natural gas and has a higher hydrogen-to-carbon ratio compared to diesel and gasoline. The higher ratio results in lower emission levels of carbon dioxide per delivered unit of energy, but natural gas also benefits from lower emission levels of nitrogen oxides, sulphur oxides and particular matter compared to combustion of diesel and gasoline[11,12]. However, combustion engines are prone to have a slip of uncombusted hydrocarbons and it is essential that any methane is removed before the exhaust is released into the atmosphere[3,12]. The removal is commonly performed by catalytic converters where total combustion of methane is generally achieved over supported palladium based catalysts[13–15]. In lean conditions (oxygen excess), palladium oxide is reported to be a highly active material, whereas the PdO(101) surface has been identified as the most reactive surface for methane dissociation due to the presence of undercoordinated Pd sites[16–19].

In general, materials such as alumina (Al_2O_3), ceria (CeO_2), silica (SiO_2) and zirconia (ZrO_2) or combinations of these support materials[20–24] are utilized to deposit nanosized palladium for the

complete methane combustion reaction. In contrast to the previously mentioned support materials, supporting Pd on alumina has shown to possess a higher activity for complete methane combustion in the low temperature regime[14,15,21].

To identify highly active methane oxidation catalysts, most published experiments have been performed at atmospheric total pressures. Under these conditions, the catalysts still require high temperatures or high precious metal loadings to perform with high reaction rates[25,26], while it is known that elevated total pressures can favor catalytic reactions at lower temperatures[27,28]. One reason for the poorer performance of methane oxidation catalysts at lower temperatures is the formation of hydroxyl, carbonate and bicarbonate surface species. These species originate from the reaction itself and can block active sites of the catalyst, which can require increased temperatures to make these sites accessible for the reaction once again[29–32]. In contrast to this, several catalytic systems for hydrocarbon conversion show an increased performance at elevated total pressures and lower temperatures[27,33,34]. The same applies to the combustion of methane for power generation where the reaction rate increases with increasing total pressure[35–38]. However, the lean methane oxidation at low temperatures over a palladium-based catalyst is relevant for vehicle exhaust after-treatment systems, which is in combination with elevated total pressures, a rather limited area in literature.

The aim of this work is to study the influence of elevated total pressures on the activity of the commercially used catalyst in the conversion of methane to carbon dioxide. To do so, the catalyst has been synthesized according to already established methods, to obtain a by now acknowledged system for the reaction. In this study, different variables of the lean methane oxidation, such as light-off temperatures, activation energies and reaction orders are investigated. A major focus is set on the dependency of these variables from the applied total pressure and temperature. Furthermore, in collaboration with a PhD student from the Chalmers University of Technology (Carl Robert Florén, 2019, Gothenburg, Sweden), the results were compared to modelled values to evaluate the applicability of the model in future works.

2. Experimental Methods

Synthesis of catalyst material

A very simple method to prepare a heterogeneous catalyst is the incipient wetness impregnation method. It is by far the most standard and simple method used in industry[39,40]. Its simplicity, low cost and small amount of waste makes this technique an attractive choice. In this process a high

surface area support is impregnated with a solution containing the precursor and subsequently dried. The metal loading is controlled by the concentration of the precursor solution, or better by the metal ions in solution[40]. The role of the support surface is merely a physical support and does not influence the loading in any meaningful manner[39]. After drying the product, further treatments are performed to activate the catalyst. These activation treatments include a calcination and/or reduction of the product to obtain the final catalyst. The bottleneck of this synthesis method is to optimize the parameters (metal loading, size of the particles and distribution)[40] to acquire an efficient catalyst. Hence, the choice of precursor, its solubility in the used solvent, the counter ions present in solution due to the precursor and the concentration are crucial factors to control the aforementioned parameters[40]. In addition, the choice of the high surface area oxide used as support is important, as its porosity directs the accessibility of the active metal particles by the reactants. In this work palladium nanoparticles deposited on alumina were prepared using the incipient wetness impregnation method. The following figure shows the different steps of this procedure to synthesize the used catalyst material.

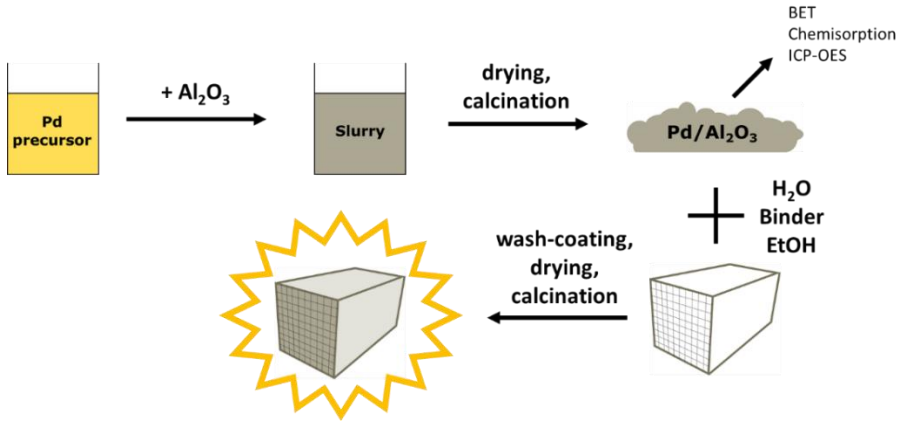

Figure 3.2 Process of catalyst synthesis for the so-called "wetness incipient impregnation" method using Pd precursor and Al_2O_3 for final deposition on a cordierite substrate.

An aqueous 10 wt.-% tetraamine (II) palladium nitrate solution (Alfa Aesar) was mixed with γ-alumina (Puralox SBa 200, Sasol) to obtain a slurry, which was instantly frozen by liquid nitrogen and freeze-dried overnight. After that, the sample was calcined in air by increasing the temperature with a rate of 5°C/min to reach 600°C for 2 h. The powder was used to wash-coat a cordierite monolith of 15 mm length and 12 mm diameter and cell density of 400 cells per square inch (cpsi). By repeatedly dipping the cordierite substrate in a slurry of 16 % catalyst powder, 4 % binder

material (Boehmite, Disperal P2, Sasol) and 80 % of a 50/50 mix of ethanol and water and subsequently drying it under a heating gun a final loading of 31 mg catalyst powder was achieved. Then, the final monolith was calcined under the aforementioned procedure for the powder itself and cooled back down to room temperature by natural convection.

Elemental analysis

Using an inductively coupled plasma-optical emission spectrometer (ICP-OES, iCAP 600 series by Thermo Scientific) the palladium loading of the catalyst powder was identified. A 3:1 mixture of hydrochloric and nitric acid was used to dissolve the sample by heating up the solution for 2 h at 100°C. Then the sample was left overnight to digest in the acid and the final solution was diluted to a ratio of 1:10 using Milli-Q water. Prior to the measurement, the solution was filtered using a syringe filter (PTFE-membrane with 0.2 µm pore diameter). In total three aliquots were measured to obtain an average loading value.

Chemisorption

Chemisorption of carbon monoxide (CO) was used to determine the dispersion of palladium on the catalyst powder and the diameter of the dispersed Pd particles. To achieve this, an approximate amount of 200 mg of sample was packed between quartz wool and degassed at 250°C for 3 h. Then, the dry weight of the sample was defined and used for the experiments. Prior to the chemisorption process, an oxidative pretreatment with 2 vol-% O_2 at 500°C for 1 h was performed and followed by a reductive pretreatment using 4 vol-% H_2 500°C for 1 h. Then the cell was cooled down to 35°C and evacuated for 1 h. The measurement was carried out at 35°C using a Micrometrics ASAP2020 instrument by stepwise increasing the CO dosage. To calculate the Pd dispersion on the powder and the hemispherical particle diameter, the ratio of adsorbed CO molecules and surface Pd atoms was assumed to be 1:2[41].

Nitrogen physisorption measurements

To determine the specific surface area (SSA) of the sample, 200 mg of catalyst powder was dried at 225°C for 3 h under a nitrogen flow to remove weakly adsorbed surface species. Then a measurement was carried out using a Micrometrics Tristar 3000 instrument. The Brunauer-Emmett-Teller (BET) model was used to calculate the SSA using five equally spaced points in the p/p_0 range from 0.05 to 0.2. In addition, the pore size distribution of the material was identified by applying the Barrett-Joyner-Halenda (BJH) method on the isotherm in a range of $0.35<p/p_0<1$.

Reactor setup

To perform the experiments an in-house built reactor setup was used. The test-bench consisted of mass flow controllers (Bronkhorst model FG-201CV), an in-line mount gauge pressure transmitter (Yokogama, model EJA530E), a stainless-steel tube (inner diameter = 15 mm, length = 480 mm) heated by electrical heating coils, a control valve (Bronkhorst F-001) and a mass spectrometer (V&F Analysetechnik, Airsense Compact) at the end of the gas outlet. The catalyst monolith was fixed in the stainless-steel tube using quartz wool. The heating coils where placed in the vicinity of the sample to reach a constant gas and reaction temperature. To measure and control the temperature, a K-type thermocouple was placed close to the catalyst material. The total pressure of the system was monitored with the pressure transmitter, which after successful communication allowed the control valve at the outlet to stabilize the total pressure to the set value. A schematic description of the setup can be found in the following scheme.

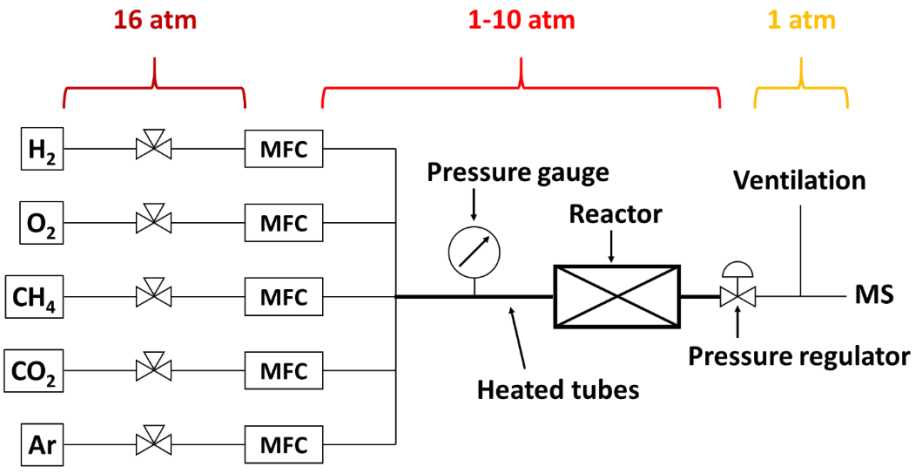

Figure 3.3 Schematic description of the experimental setup for experiments at elevated total pressures up to 10 atm.

Methane oxidation

A reductive (for 20 min at 500°C with 4 vol-% H_2) and an oxidative pretreatment (for 40 min at 500°C with 2 vol-% O_2) was carried out before every following experiment. To obtain reproducible results, each pretreatment was performed at the same total pressure of the experiment that followed up. Temperature programmed reaction (TPReaction) experiments were carried out by feeding 1000 vol-ppm CH_4 and 2 vol-% O_2 balanced with Ar to the system at a flow rate of 100 mL/min. The conversion of methane (CH_4) to carbon dioxide (CO_2) was monitored. The temperature was increased with a rate of by 2°C/min to reach a maximum temperature of 450°C, followed by a

dwell of 30 min and cooling with a rate of 2°C/min. The total pressure of the experiments was varied (1, 2, 3, 4 and 10 atm) for each experiment to reveal the dependency of the performance of the catalyst and the activation energy of the reaction on the total pressure of the system. In addition, two different experiments were performed in the presence of 10 vol-% CO_2 at 1 and 4 atm to identify the impact of CO_2 on the catalytic performance and activation energy. By considering data points between 4-10% methane conversion, the apparent activation energy for each experiment was calculated. The *activation energy* of a reaction is the energy required for a chemical reaction to proceed. This energy in heterogeneous gas-phase catalysis is dependent on many factors, such as the number of reactant collisions and the temperature of the reaction. The so-called *Arrhenius-equation*[42] describes the temperature dependency of the reaction rate as following:

$$k = A \cdot e^{-\frac{E_a}{R \cdot T}} \tag{3.1}$$

In this equation k equals the reaction rate coefficient, A the pre-exponential factor, R the ideal gas-constant and T the temperature at which the reaction rate coefficient is determined. Experimentally, the activation energy can be determined by following steps. Firstly, the Arrhenius-equation is transferred by applying the natural logarithm:

$$ln\,(k) = ln\,(A) - \frac{E_a}{R \cdot T} \tag{3.2}$$

After determining the reaction rate coefficient at the thermodynamic equilibrium at different temperatures, the natural logarithm of it can be plotted against the reciprocal temperature in Kelvin. Then a linear regression can be carried out from which the slope delivers the value of the activation energy and the intercept at the y-axis the pre-exponential factor. This relation is demonstrated in the following scheme.

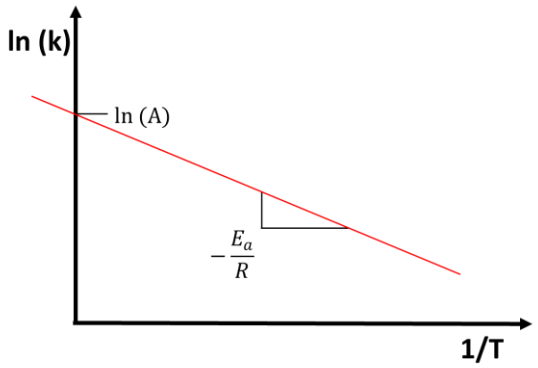

Figure 3.4 The Arrhenius-plot: After plotting the logarithm of the reaction rate constant against the reciprocal temperature, the activation energy of the reaction can be obtained from the slope of the linear regression.

Taking into account that the chemical reaction is not defined by one single elementary step, the definition of activation is adapted to an overall reaction[43]. Excluding the effect of thermodynamics, the *apparent activation energy* of a reaction can be obtained from the linear part of a plot, which can deviate from the above shown (**Figure 3.4**) straight line[43]. The linear range of such a plot is usually below ~15% of the conversion and can deliver an approximate value for the apparent activation energy.

The *reaction order* of a reaction describes the relationship between the reaction rate of a reaction and the concentration of reactants[42]. There are usually three main reaction orders the reactants can be identified by: zero, first and second order reaction[42]. In a zero-order reaction, the concentration of the reactant does not influence the reaction rate, but the presence of the reactant itself is required or otherwise no reaction will occur. A first order reaction depends only on the concentration of one reactant, even in the presence of other reactants. In a second order reaction, the rate depends on the concentration of two reactants present in the reaction atmosphere or on the square concentration of one reactant. In this work, the reaction order for methane was determined by performing a set of four measurements at three different temperatures (350, 400 and 450°C). The methane concentration was altered with 200 ppm intervals from 400 to 1600 ppm, whereas the oxygen concentration was fixed at 2 vol-% at varying pressures (1, 2, 3 and 4 atm).

Many different factors, such as catalyst poisoning by reactants[44], by traces of certain compounds in the reaction feed[45] or on the surface of the catalyst[46] but also thermal impact[47,48] can deactivate the catalyst by clogging the surface, blocking active sites or causing mechanical destabilization. To identify the effect of water on the catalytic activity in presence of elevated pressures, TPReaction experiments at 1 and 4 atm before and after treating the sample in a 10 vol-% water steam for 24 h were carried out. The process of deactivation, which was obtained by feeding water steam for 24 h, is called *degreening*. For the TPReaction experiments, 1000 vol-ppm methane and 2 vol-% O_2 were fed to the system increasing the temperature at 5°C/min to 500°C and after a 30 min dwell were cooled down at the same rate. The sequence of the experiments was as following:

1. Pretreatment (as described before), TPReaction experiment at 1 atm
2. Pretreatment, TPReaction experiment at 4 atm
3. Deactivation of the catalyst at 500°C feeding 10 vol-% gaseous water (degreening)
4. Pretreatment, TPReaction experiment at 1 atm
5. Pretreatment, TPReaction experiment at 4 atm

Multiscale modeling of methane conversion

By simulating the conversion of methane, a comparison to the experimental results could be performed. The simulations involved a previously developed 2D multiscale reactor model, which involved first-principle calculations to describe the surface kinetics inside a porous catalyst layer. In addition, mass and heat transport considerations were coupled to the previously mentioned conditions[49,50]. To describe the complete methane oxidation inside a coated monolith, a single-channel reactor model was chosen, which has been previously implemented by other groups[51,52]. A tanks-in-series method (with ten tanks) was used to separate the coated monolith, whereas the catalyst itself was subdivided into layers (in 12 layers) which resulted in axial and radial gradients. The chosen single-channel geometry represented a monolith with 400 cpsi, as used in the experiments. Further details can be obtained from published works[50,53].

All the modelling experiments where performed by Carl-Robert Florén (PhD student at Chalmers University of Technology, Gothenburg, Sweden) and are used in this report with consent of the original author to demonstrate its applicability to the experimental results obtained during the collaboration of this work.

3. Results and Discussion

Characterization of catalyst material

General properties of the Pd/Al_2O_3 catalyst, such as the specific surface area, the Pd loading, the Pd distribution and size, were determined using a various set of techniques. This knowledge was further used for the simulations performed. The nitrogen physisorption measurement revealed a specific surface area of 172 m^2/g with an average pore diameter of 0.9 nm for the synthesized catalyst powder. These results are in line with previously published works[25,54], underlining the main porosity arising from the alumina support. By assuming a bridged configuration of CO[41] adsorption onto the Pd, the dispersion of Pd on the catalyst was calculated using chemisorption measurements. The dispersion was determined to be 41% whereas the mean diameter for a hemispherical Pd-particle was 1.9 nm, which is comparable to published results[55]. To verify the loading of the catalyst, three different aliquots of the material were measured by ICP-OES. The results disclosed a 0.15% Pd-loading on alumina.

After wash-coating the here analyzed catalyst powder on a cordierite substrate, different temperature programmed reaction experiments were performed to investigate the kinetic properties of the catalyst in the conversion of methane under lean conditions.

Influence of pressure on TPR experiments and activation energies

Conversion-temperature plots at different total pressures, fixed molar flows and varying gas hourly space velocities (GHSV) were recorded to have a direct comparability and to identify the total pressure dependency of methane conversion and activation energies. **Figure 3.5** shows the cooling phase of TPReaction experiments and the simplified Arrhenius plot to identify the apparent activation energy from the slope at conversions of around 5-10%. An example on how the apparent activation energy was obtained from these plots can be found in the Appendix of this chapter.

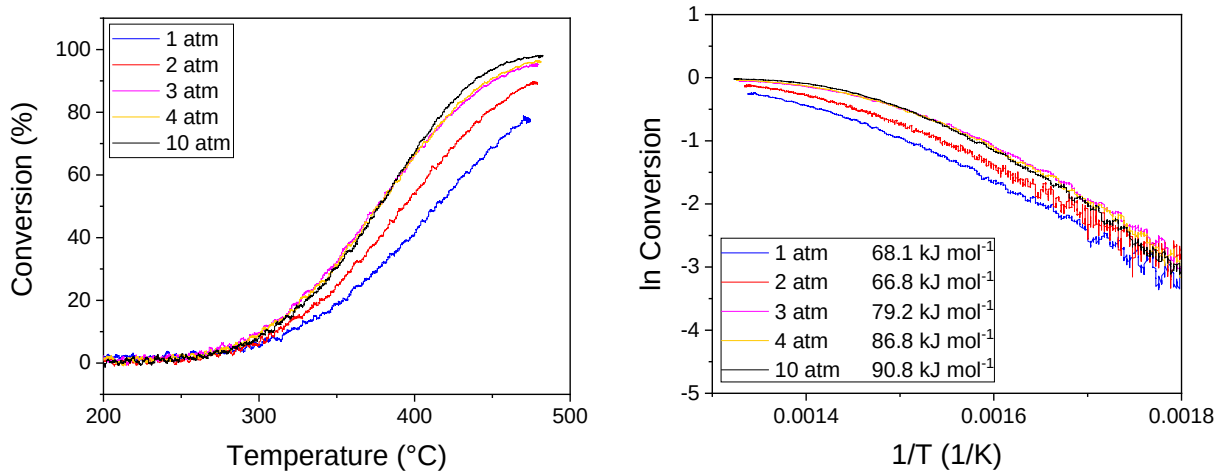

Figure 3.5 Left: Comparison of TPReaction experiments for lean methane oxidation (1000 ppm CH_4 and 2 vol-% O_2) at various total pressures (1, 2, 3, 4 and 10 atm); Right: Corresponding simplified Arrhenius-plots.

As seen in **Figure 3.5** (left), the conversion of methane was plotted against the temperature to identify the dependency of the activity to the applied total pressure to the system. It is evident that there is a positive correlation between conversion and increasing pressure. This is especially highlighted up to total pressures of 3 atm, where the conversion increases significantly with each pressure step. After 3 atm, a change of activity is barely visible. This observation can be explained by mass transport limitations occurring on the surface of the catalyst. Active sites can be blocked by intermediate species, which does not allow any further molecules to adsorb and react. Hence, a further increase in total pressure or temperature shows no significant changes in activity.

The positive effect of the pressure on the activity of the catalyst differs to the previously published work of Stotz et al.[56] in which the group observed a negative impact of the total pressure on the activity for methane conversion over a Pd/Al_2O_3 catalyst. The differences in results can derive from the experimental differences and reaction conditions. In the published work, the group performed

dry (in absence of water) and wet experiments (with varying contents of gaseous water) to investigate the influence of both total pressure and concentration of water on the activity of the catalyst. In this study we decided to keep a constant mass flow throughout the experiments and vary the gas hourly space velocity (GHSV) over the catalyst bed along with varied total pressures (GHSV was ~3,500 h^{-1} at 1 atm) while in the previously published work the authors kept a higher GHSV (60,000 h^{-1}), which was fixed. Another suggestion could be the sequence in which the experiments were performed, which can play an important role when varying the total pressure and water content simultaneously. The sequence of the experiments performed by Stotz et al. was chosen to be altering from dry to wet conditions at constant total pressure before incrementally increasing the latter. During the here presented experiments the catalyst showed generally lower activities after a treatment in gaseous water even after performing a pretreatment method as previously outlined (see later in **Figure 3.7**) and a trend on the deactivation of the catalyst with each cycle in absence of pretreatments was visible. The negative impact of water on the catalytic activity of Pd/Al_2O_3 catalyst for the oxidation of methane is a well-known fact and has been previously studied by different groups[29,31,57]. In these works, the authors claim the effect is due to adsorbed water species and hydroxyl groups on the active sites. Indeed, in this work this effect was mainly observable when the reactions were performed for a longer term without the established pretreatment method between each step. In particular, elevated total pressures seemed to impact the activity more acutely. For this reason, the established pretreatment method was chosen to be performed between each experiment, to guarantee a clean surface, which delivered reproducible results. If in addition water is added to the system, as in the case of Stotz et al., a synergistic effect is likely to occur and the water inhibition can be more pronounced[58]. Hence, an in-depth study on this effect is required and will be discussed in later in this chapter (see subsection "Influence of pressure on TPR experiments and activation energies after deactivation in water").

Figure 3.5 (right) shows the Arrhenius plots with accompanying apparent activation energies for methane conversion for each TPReaction experiment. A clear trend is seen where the apparent activation energy increases with increasing total pressure, except at 2 atm where a slightly reduced activation energy is visible. The trend of increased apparent activation energies can possibly originate from the re-adsorbed reaction products water and CO_2 which hinder the absorption of further methane molecules onto the active sites. Both water and CO_2 can form different inhibiting surface species such as carbonates, formates, adsorbed water and hydroxyl species on the catalyst surface. The mentioned surface species block or deactivate the active sites and additional energy is

needed to cleanse the surface and make the active sites accessible again[29–32]. This effect is less visible at lower pressures with around 68 kJ/mol as high pressures can push the apparent activation energy up to 90 kJ/mol, which is in range within previous studies[59].

As a next study, the obtained experimental results were compared to modelled experiments performed by a PhD student from the Chalmers University of Technology (Carl-Robert Florén, 2019) with previously described methods (see section on Experimental methods)[1]. The following figure shows the results of this comparison for TPReaction experiments.

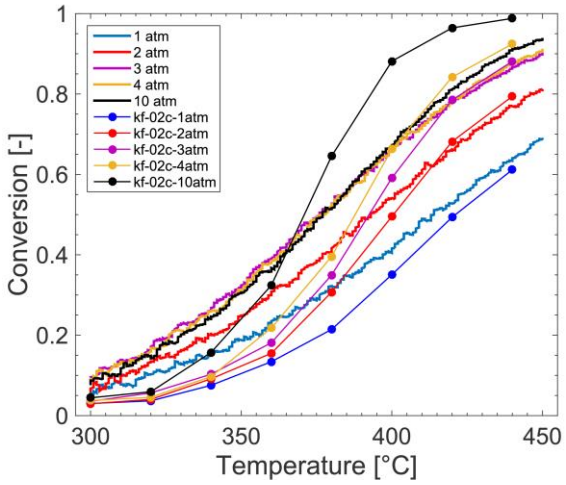

Figure 3.6 Comparison of experimental TPReaction experiments (solid lines) and modelled TPReaction experiments (dotted lines) for lean methane oxidation (1000 ppm CH_4 and 2 vol-% O_2) at various total pressures (1, 2, 3, 4 and 10 atm).[1]

To briefly compare the modelled TPReaction experiments, the experimental results were plotted alongside the modelled results in **Figure 3.6**. This figure shows that the multiscale model captures the general trend of the experiments but does not describe their exact behaviour in terms of methane conversion. In dry methane oxidation with 1000 vol-ppm CH_4 and 2 vol-% O_2, the developed multiscale model underestimates the activity at low reaction temperatures while overestimating the activity at higher reaction temperatures and total pressures. In the case of low temperatures this can be due to an overprediction of the model regarding higher coverage of active sites by adsorbates as carbonate and hydroxyl which lead to lower activities. A further simulation analysis on adsorbed species was carried out on the PdO surface and is further described in the Appendix of this chapter. The reason for the overestimated activity at high temperatures can be explained by the underestimated heat losses of the model, as it is assumed to be an adiabatic system, which loses heat only from the inlet and outlet of the reactor. In addition, mass transport limitations can occur

in the experimental reaction, which were possibly not encountered in the modelled results. Hence, for a better understanding the Weisz module for this reaction was simulated and is discussed in detail in the Appendix of this Chapter. It is crucial to remember that any support effects or structural changes of the active site are not accounted for in this model and can affect the overall catalytic activity[32]. However, it is noteworthy to mention that the model does describe the same trends of increased total pressure on catalytic activity and methane conversion.

Influence of pressure on TPR experiments and activation energies after deactivation in water

As explained before, the observations of this work in comparison to the work of Stotz et al. showed differences in the results but also in the experimental sequence. Hence, in a second experiment the effect of water steam on the catalyst activity was further investigated, to have a closer comparability to the performed experiments in the previously published work of Stotz et al[56]. To do so, the catalyst was transferred to a different reactor in which it was deactivated for 24 h in a 10 vol-% water gas stream at 500°C. The experiments where performed before (1 and 4 atm) and after this deactivation procedure. The results are compared to each other in the following figure. In addition, the simplified Arrhenius plots were compared to see the effect on the apparent activation energy of the system.

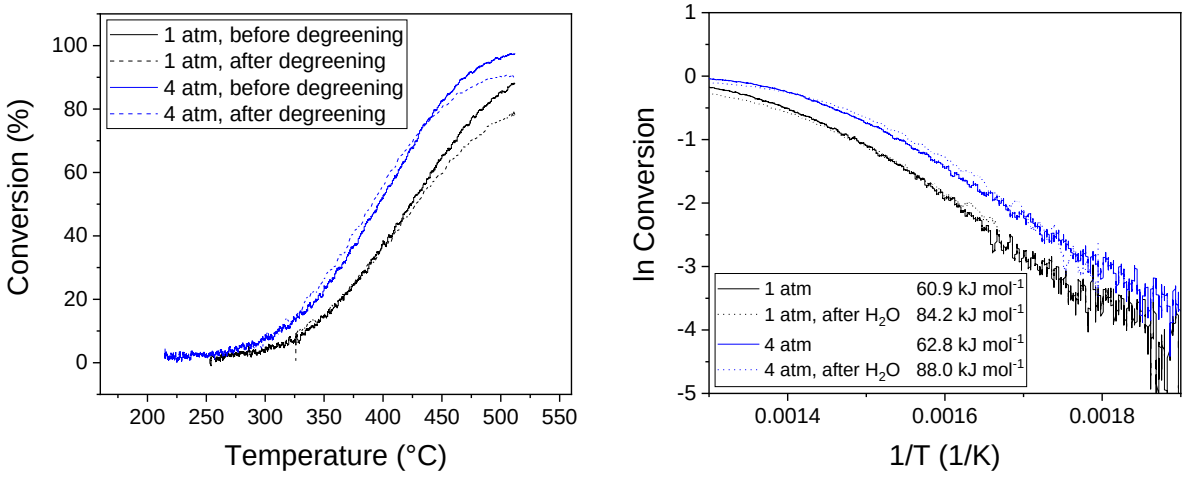

Figure 3.7 Left: Comparison of TPReaction experiments for lean methane oxidation (1000 ppm CH_4 and 2 vol-% O_2) at 1 (black lines) and 4 atm (blue lines) before (solid lines) and after (dashed lines) the degreening; Right: Corresponding simplified Arrhenius-plots.

As can be seen in **Figure 3.7** (left) the effect of the treatment with water can be mainly identified in the change in activity of the sample. The light-off temperature seems to be unchanged, whereas

the activity shows a loss of around 5-10 % at 500°C. This experiment signals the inhibitory effect of the water steam on the catalyst activity. Hence, future efforts should be made to identify the reason for this behavior.

Taking a look at the apparent activation energies under different conditions (see **Figure 3.7** right), it is remarkable that the addition of water increases the apparent activation energy, meaning higher temperature are required to reach higher reaction rates. The additional effect of the pressure is only slightly visible in presence of water (84.2 kJ mol^{-1} to 88.0 kJ mol^{-1}), which can be a slight deviation of the value. Nevertheless, these experiments show the deactivation impact of water/hydroxyl groups on the catalyst surface and can explain the different results seen in comparison to the published work of Stotz et al.

Influence of pressure on TPR experiments and activation energies in presence of CO_2

Under CO_2 rich conditions carbonate species have been shown to adsorb on the catalyst surface, which can decrease the reaction rate of the catalyst. Hence, further experiments were performed in presence of 10 vol-% CO_2. These experiments were compared to experiments in the absence of additional CO_2 (1 and 4 atm). The following figures show the results of the TPReaction experiments and the Arrhenius plots of these experiments.

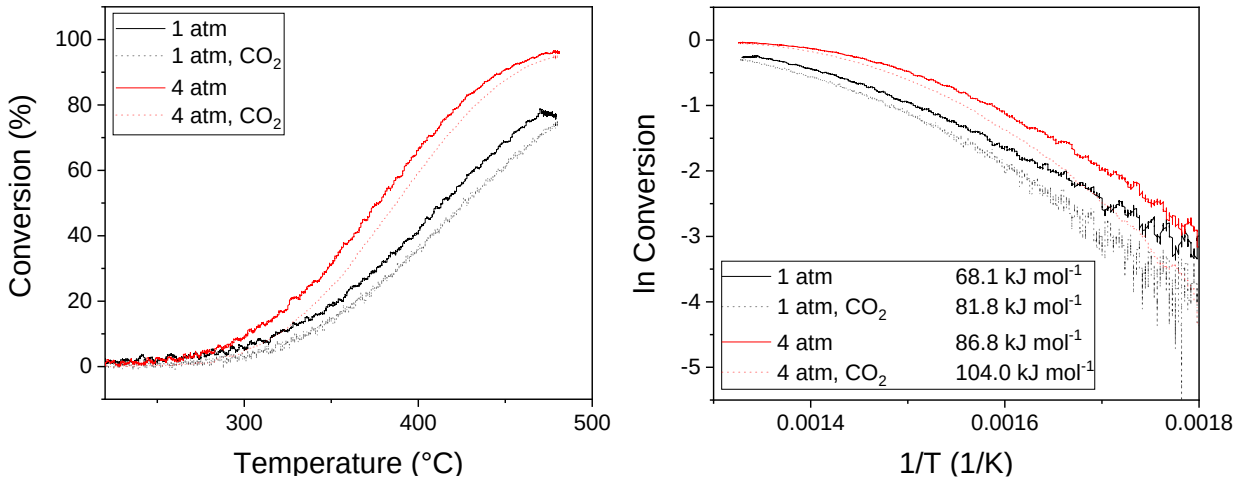

Figure 3.8 Left: Comparison of TPReaction experiments for lean methane oxidation (1000 ppm CH_4 and 2 vol-% O_2) at 1 (black lines) and 4 atm (red lines) in absence of CO_2 (solid lines) and presence of CO_2 (dashed lines); Right: Corresponding simplified Arrhenius-plots.

The general observation in **Figure 3.8** is the negative effect of the CO_2 present in the system. The conversion decreases with around 5% for all examined total pressures applied to the system and

shows a small delay in the ignition of the reaction. The formation of carbonates on the catalyst surface and the blockage of active sites by these carbonates has previously been discussed and is a well-known phenomenon[31]. In any case, it is known that carbonate and the similar formate species have been discussed by DRIFTS studies to adsorb on both the support and the active site originating from adsorbed CO or CO_2[60–67]. Hence, the identification of the changed activity of the catalyst can be dedicated to these found surface species.

In addition to the TPReaction plots, the apparent activation energies are calculated from the Arrhenius plots (see **Figure 3.8** right). The apparent activation energies were observed to increase with the presence of CO_2 in the reaction atmosphere. This effect is shown to be more pronounced at elevated total pressures, as the difference in activation energies from experiments with and without CO_2 in the feed is higher than in the case of the atmospheric pressure experiment.

Influence of pressure on reaction orders at various temperatures

Following this evaluation, steady-state measurements were carried out to obtain the reaction order for methane at varying temperatures and total pressures. The "reaction rate" of a reaction describes the consumption of reactant per unit time or the formation of the product per unit time. The "reaction order" of a reaction describes the relationship between the reaction rate of a reaction and the concentration of reactants. The reaction order defines how the reactant concentration is affecting the reaction rate. In this case, the order of the reaction of methane to CO_2 is a first order reaction, which means that the rate is only dependent on the concentration of one reactant (here methane), even in presence of other reactants (here oxygen).

The experimental values for the reaction order are shown in **Figure 3.9** at various temperatures (350, 400 and 450°C) and pressures (1, 2,3 and 4 atm).

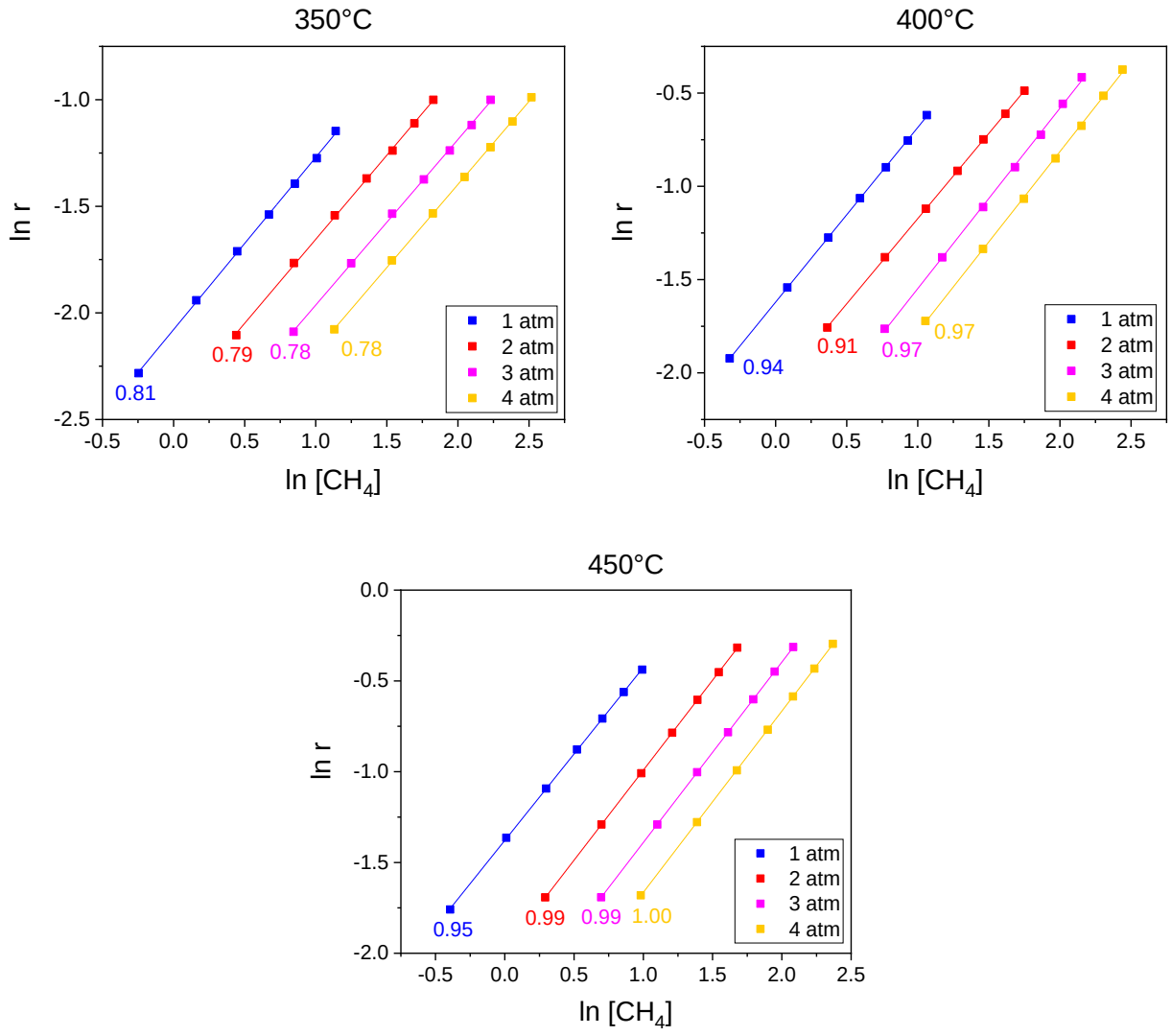

Figure 3.9 Experimental reaction orders for lean methane oxidation (400-1600 ppm CH_4 and 2 vol-% O_2) at 350°C (upper left), 400°C (upper right) and 450°C (bottom) and 1 (blue), 2 (red), 3 (purple) and 4 (yellow) atm.

From **Figure 3.9** the impact of the pressure on the reaction order and dependence on the pressure is visible. While at low temperatures (350°C) an increased total pressure seems to decrease the reaction order, at higher temperatures (above 400°C) an increased total pressure leads to an increased reaction order reaching unity (at 450°C). Generally speaking, the reaction order values are in range with published values of 0.7 to 1.1 for methane combustion reactions at varying methane concentrations[68,69], which underlines the first-order nature of the reaction itself. In general, the impact of increased total pressure on the reaction order is less pronounced at high temperatures compared to low temperatures. The lower reaction order at 350°C can arise from the coverage of

the surface with poisoning species as previously mentioned. The coverage of the most abundant surface species through the coated monolith, according to the multiscale kinetic model, are shown in the appendix of this report. At 350°C a significantly increased coverage of hydroxyl species and adsorbed water is displayed through the monolith, especially at higher total pressures. Product inhibition has previously been studied where water and carbon dioxide have a negative impact on the conversion of methane over Pd/Al_2O_3 catalyst[31,70,71], which is in good agreement with the found observations.

4. Conclusion

For this work, a well-established catalyst material for the total combustion of methane was used to investigate the total pressures effect on the oxidation of methane. In the first part of the characterization, general features of the catalyst were investigated to compare to already published works to guarantee the presence of the expected material. Nitrogen physisorption, ICP-OES and chemisorption measurements were used to verify these properties. In addition to their use in a comparison to established catalyst materials, the obtained values were used for the simulations carried out in the scope of this work.

This study indicated that the total oxidation of methane over a Pd/Al_2O_3 catalyst is affected by the total pressure of the system. Particularly at dry conditions, fixed molar flows, varying space velocities, an increased total pressure can have a positive influence on the activity of the catalyst. However, the enhanced activity obtained in conjunction with increased apparent activation energies at increasing total pressures (from 68 to 90 kJ/mol at 1 and 10 atm, respectively) underlines the requirement of increased temperatures to overcome the established energy barrier due to blocked active sites by adsorbed species. This observation was highlighted by the obtained reaction orders at three different temperatures (350°C, 400°C and 450°C). At low temperatures (350°C) the reaction order decreased with increased total pressures, whereas higher temperatures (from 400°C) lead to higher reaction orders with increased total pressures suggesting an increased reaction rate. To understand in detail the effect of adsorbed species on the surface, further experiments with CO_2 in the gas feed and a treatment with gaseous water were performed. The presence of 10 vol-% CO_2 resulted in a negative impact to the activity of the catalyst, which was even more pronounced at elevated pressures. Along with the activity, the apparent activation energy of the reaction increased significantly, which can be explained by blocked active sites by carbonates and formate species, shown by previously published Diffuse Reflectance Infrared Fourier Transform spectroscopy

(DRIFTs) results under ambient conditions[60–67]. In addition, the treatment of water showed a negative impact on the activity, even though an established pretreatment method was performed prior to each experiment. The results in presence of water in the system can explain the controversial results to the published works of Stotz et al.[56], where a negative impact of increased total pressures was recorded.

In summary, the presence of CO_2 and water in the reaction closely resembled the simulated results at low temperatures (below 370°C). At high temperatures however, the simulated results seemed to overestimate the activity due to an interplay of fast intrinsic kinetics and reduced internal mass transport resistance (further explained by Weisz modulus in Appendix). Nevertheless, the general trend between the experimental and simulated results was comparable, which underlines the utility of this model for first-principle studies to predict essential kinetic variables of a reaction.

Future studies for reactions under pressure can focus on the surface species formed during this reaction. To this end, DRIFTs can be coupled to the pressured system (already present at the labs of Chalmers University of Technology, Gothenburg, Sweden) and different reaction conditions can be probed under higher total pressure conditions. Furthermore, different catalysts and different catalytic reactions can be investigated. By this, the performance and also the reactions occurring on the surface of a catalyst can be captured from a different perspective to understand both the role of active sites and also surface species in a more controlled manner.

5. Appendix

Apparent activation energy

The apparent activation energies in this work were calculated using data points in a range of 5-10 % conversion. To do so, the natural logarithm of the conversion was plotted against the reciprocal temperature and finally a linear regression was performed in the aforementioned area. The following equation describes the relation of the slope (m) from this plot and the apparent activation energy (E_a) using the gas constant (R):

$$m = -\frac{E_a}{R} \tag{3.3}$$

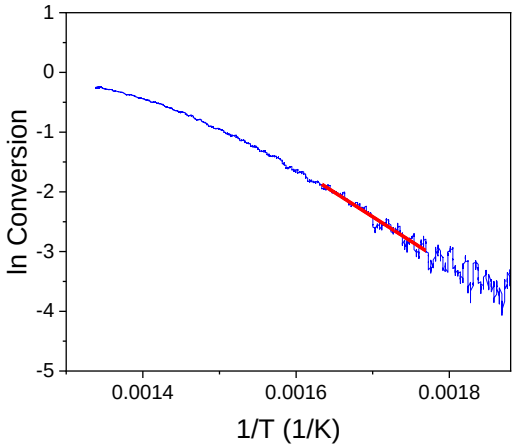

Figure 3.10 Arrhenius-plot of TPReaction experiment for lean methane oxidation (1000 ppm CH_4 and 2 vol-% O_2) at 1 atm total pressure with indicated linear regression (red line) performed in the range of 5-10% conversion.

In **Figure 3.10** the slope of the linear regression was calculated to be -8194.98 K, which allowed the following calculation using the gas constant (8.3145 J K^{-1} mol^{-1}) to arrive to the apparent activation energy:

$$E_a = -(-8194.98\ \mathrm{K}) \cdot 8.3145\ \frac{\mathrm{J}}{\mathrm{K} \cdot \mathrm{mol}} = 68\ 137.2 \frac{\mathrm{J}}{\mathrm{mol}} = 68.1 \frac{\mathrm{kJ}}{\mathrm{mol}} \qquad (3.4)$$

The Weisz-modulus

The Weisz-modulus describes internal mass diffusion limitations. By understanding the diffusion limitations of a reaction, an estimate of the reaction rate can be made. Hence in the following **Figure 3.11**, the Weisz modulus for the reaction at inlet conditions dependent on the temperatures (350 to 450°C) and pressures (1 to 10 atm) is presented. The values for the Weisz modulus were obtained using the effective diffusion from the multiscale model (standing for the temperature and total pressure changes) and the reaction rate. The used reaction rates are simulated, as above 350°C an assumption for differential conditions of experimental results cannot be made. Due to negligible external mass transport limitations, the methane concentration at the catalyst surface was approximately set equal to the inlet bulk concentration. A 30 µm thick layer of catalyst material was used to determine the Weisz-modulus.

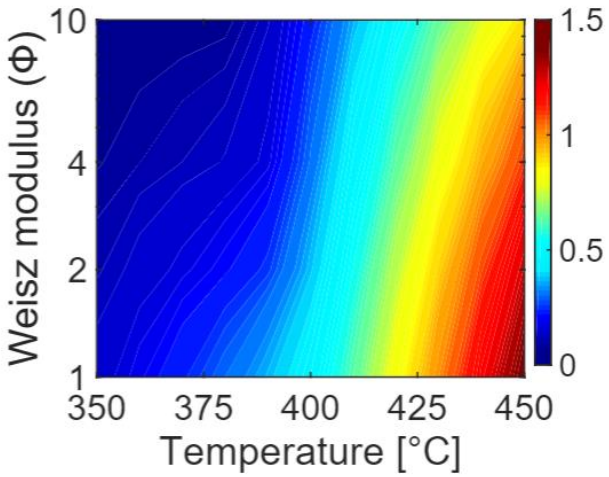

Figure 3.11 The Weisz-modulus (Φ) simulated at varying temperatures and pressures. Internal mass transport effects the experimental reaction whenever the Weisz-modulus close to or above 1 (all data provided from doctoral thesis of Carl-Robert Florén). [1]

When the pressure of the system is low and the temperatures are increased, an increased internal mass transport resistance is visible (see **Figure 3.11**). However, increasing the total pressure leads to decreased internal diffusion resistance. This effect can be explained by the greater increased surface methane concentration rather than a high reaction rate at increased total pressures. As seen here, the Weisz-modulus is low under investigated conditions (for 350 to 450°C and 1 to 10 atm, the Weisz-modulus is below 1), which means that internal mass transport will not affect the reaction rate. The results for the Weisz-modulus explain the small changes between 3 to 10 atm. The methane concentration gradient inside the porous wash-coat can be considered to be reduced, as the Weisz-modulus decreases in a correlated manner to an increased surface methane concentration. For this reason, it can be assumed that the system is influenced to a higher degree by kinetics, which ultimately means that the reaction rate of the system is dependent on a combination of kinetics and internal mass transport rates.

Surface species present on the active sites of the catalyst dependent on temperature and pressure

To explain the impact of adsorbed surface species in the activity of the catalyst dependent on the total pressure of the system (1, 2, 3, 4 and 10 atm) and temperatures (350°C, 400°C and 450°C), different adsorbates (hydroxyl, water, bicarbonate and hydrogen) and surface sites (Pd and O) were considered when the following simulations were performed.

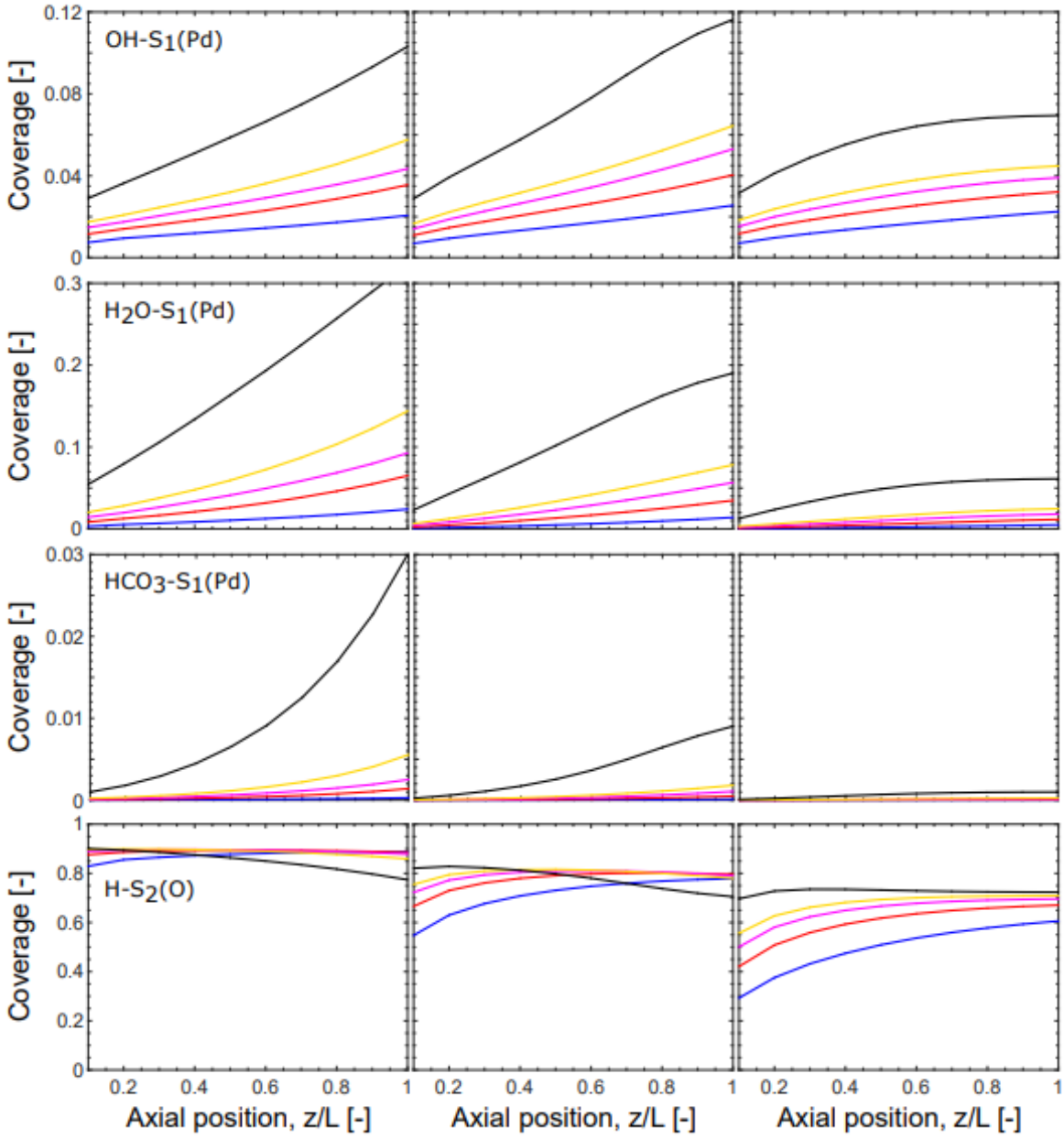

Figure 3.12 Coverage of hydroxyl (OH), water (H_2O), bicarbonate (HCO_3) and hydrogen (H) in the monolith at 350 (left column), 400 (middle column) and 450°C (right column) and 1(blue), 2 (red), 3 (purple), 4 (yellow) and 10 (black) atm. All reported surface species, except hydrogen, are adsorbed on the palladium atom (S_1(Pd)) while hydrogen is adsorbed on the oxygen atom (S_2(O)) (all data provided from doctoral thesis of Carl-Robert Florén).[1]

Generally speaking, the higher the temperature the lower the coverage of active sites by surface species can be seen. This effect is highlighted for bicarbonate species and adsorbed water at elevated temperatures. The higher the total pressure of the system, the steeper the adsorption gradient for each species appears to be, this can be explained by more frequent adsorptions

occurring on the surface of the catalyst. These results are one reason why the model shows lower activities at low temperatures but should not be considered as the only reason. The model does not take support effects into account, which can play an important role as an interface for higher reaction rates. Conversely, higher temperatures show remarkably lower coverages due to more frequent desorption events occurring on the catalyst surface. As hydroxyl species can either be formed by the dissociation of water onto S_2(O) sites or through a reaction in which CH_X(X=1-3) releases a hydrogen to the S_2(O) site, the coverage of hydroxyl species is not affected by the temperature change from 350 to 400°C in comparison to other surface species. The hydrogen adsorbed onto the S_2(O) site arrives from the break of a C-H-bond, after a CH_X (X=1-4) adsorbs on a S_1(Pd) site followed by a hydrogen dissociation.

6. References

(1) Florén, C.-R. Influence of Total Pressure on Complete Oxidation of Methane over Pd/Al2O3 Catalysts, Chalmers University of Technology, 2019.

(2) Bleam, W.; Bleam, W. Acid-Base Chemistry. *Soil Environ. Chem.* **2017**, 253–331. https://doi.org/10.1016/B978-0-12-804178-9.00006-9.

(3) United States Environmental Protection Agency. Overview of Greenhouse Gases https://www.epa.gov/ghgemissions/overview-greenhouse-gases#main-content (accessed Oct 10, 2019).

(4) Xu, Y.; Tian, Z.; Xu, Z.; Zhu, A.; Lin, L. Methane Conversion via Microwave Plasma Initiated by a Metal Initiator. *Stud. Surf. Sci. Catal.* **2001**, *136*, 75–80. https://doi.org/10.1016/S0167-2991(01)80283-4.

(5) Beef Farming Brings on Warming. *Nature* **2015**, *524* (7565), 269. https://doi.org/10.1038/524269d.

(6) Tilman, D.; Clark, M. Global Diets Link Environmental Sustainability and Human Health. *Nature* **2014**, *515* (7528), 518–522. https://doi.org/10.1038/nature13959.

(7) Saunois, M.; Bousquet, P.; Poulter, B.; Peregon, A.; Ciais, P.; Canadell, J. G.; Dlugokencky, E. J.; Etiope, G.; Bastviken, D.; Houweling, S.; et al. The Global Methane Budget 2000–2012. *Earth Syst. Sci. Data* **2016**, *8* (2), 697–751. https://doi.org/10.5194/essd-8-697-2016.

(8) Daelman, M. R. J.; van Voorthuizen, E. M.; van Dongen, U. G. J. M.; Volcke, E. I. P.; van Loosdrecht, M. C. M. Methane Emission during Municipal Wastewater Treatment. *Water Res.* **2012**, *46* (11), 3657–3670. https://doi.org/10.1016/J.WATRES.2012.04.024.

(9) Talyan, V.; Dahiya, R. P.; Anand, S.; Sreekrishnan, T. R. Quantification of Methane Emission from Municipal Solid Waste Disposal in Delhi. *Resour. Conserv. Recycl.* **2007**, *50* (3), 240–259. https://doi.org/10.1016/J.RESCONREC.2006.06.002.

(10) NASA. Global Climate Change https://climate.nasa.gov/ (accessed Oct 10, 2019).

(11) Gambino, M.; Cericola, R.; Corbo, P.; Iannaccone, S. Carbonyl Compounds and PAH Emissions From CNG Heavy-Duty Engine. *J. Eng. Gas Turbines Power* **1993**, *115* (4), 747–749. https://doi.org/10.1115/1.2906769.

(12) Kuhns, H. D.; Mazzoleni, C.; Moosmüller, H.; Nikolic, D.; Keislar, R. E.; Barber, P. W.; Li, Z.; Etyemezian, V.; Watson, J. G. Remote Sensing of PM, NO, CO and HC Emission Factors for on-Road Gasoline and Diesel Engine Vehicles in Las Vegas, NV. *Sci. Total Environ.* **2004**, *322* (1–3), 123–137. https://doi.org/10.1016/J.SCITOTENV.2003.09.013.

(13) Ciuparu, D.; Lyubovsky, M. R.; Altman, E.; Pfefferle, L. D.; Datye, A. CATALYTIC COMBUSTION OF METHANE OVER PALLADIUM-BASED CATALYSTS. *Catal. Rev.* **2002**, *44* (4), 593–649. https://doi.org/10.1081/CR-120015482.

(14) Li, Z.; Hoflund, G. B. A Review on Complete Oxidation of Methane at Low Temperatures. *J. Nat. Gas Chem.* **2003**, *12* (3), 153–160.

(15) Gélin, P.; Primet, M. Complete Oxidation of Methane at Low Temperature over Noble Metal Based Catalysts: A Review. *Appl. Catal. B Environ.* **2002**, *39* (1), 1–37. https://doi.org/10.1016/S0926-3373(02)00076-0.

(16) Martin, N. M.; Van den Bossche, M.; Hellman, A.; Grönbeck, H.; Hakanoglu, C.; Gustafson, J.; Blomberg, S.; Johansson, N.; Liu, Z.; Axnanda, S.; et al. Intrinsic Ligand Effect Governing the Catalytic Activity of Pd Oxide Thin Films. *ACS Catal.* **2014**, *4* (10), 3330–3334. https://doi.org/10.1021/cs5010163.

(17) Hellman, A.; Resta, A.; Martin, N. M.; Gustafson, J.; Trinchero, A.; Carlsson, P.-A.; Balmes, O.; Felici, R.; van Rijn, R.; Frenken, J. W. M.; et al. The Active Phase of Palladium during Methane Oxidation. *J. Phys. Chem. Lett.* **2012**, *3* (6), 678–682. https://doi.org/10.1021/jz300069s.

(18) Antony, A.; Asthagiri, A.; Weaver, J. F. Pathways and Kinetics of Methane and Ethane C–H Bond Cleavage on PdO(101). *J. Chem. Phys.* **2013**, *139* (10), 104702. https://doi.org/10.1063/1.4819909.

(19) Trinchero, A.; Hellman, A.; Grönbeck, H. Metal-Oxide Sites for Facile Methane Dissociation. *Phys. status solidi – Rapid Res. Lett.* **2014**, *8* (6), 605–609. https://doi.org/10.1002/pssr.201409090.

(20) Schmal, M.; Souza, M. M. V. M.; Alegre, V. V.; da Silva, M. A. P.; César, D. V.; Perez, C. A. C. Methane Oxidation – Effect of Support, Precursor and Pretreatment Conditions – in Situ Reaction XPS and DRIFT. *Catal. Today* **2006**, *118* (3–4), 392–401. https://doi.org/10.1016/J.CATTOD.2006.07.026.

(21) Miller, J. B.; Malatpure, M. Pd Catalysts for Total Oxidation of Methane: Support Effects. *Appl. Catal. A Gen.* **2015**, *495*, 54–62. https://doi.org/10.1016/J.APCATA.2015.01.044.

(22) Sekizawa, K.; Widjaja, H.; Maeda, S.; Ozawa, Y.; Eguchi, K. Low Temperature Oxidation of Methane over Pd Catalyst Supported on Metal Oxides. *Catal. Today* **2000**, *59* (1–2), 69–74. https://doi.org/10.1016/S0920-5861(00)00273-X.

(23) Eguchi, K.; Arai, H. Low Temperature Oxidation of Methane over Pd-Based Catalysts—Effect of Support Oxide on the Combustion Activity. *Appl. Catal. A Gen.* **2001**, *222* (1–2), 359–367. https://doi.org/10.1016/S0926-860X(01)00843-2.

(24) Kikuchi, R.; Maeda, S.; Sasaki, K.; Wennerström, S.; Ozawa, Y.; Eguchi, K. Catalytic Activity of Oxide-Supported Pd Catalysts on a Honeycomb for Low-Temperature Methane Oxidation. *Appl. Catal. A Gen.* **2003**, *239* (1–2), 169–179. https://doi.org/10.1016/S0926-860X(02)00387-3.

(25) Thevenin, P. O.; Pocoroba, E.; Pettersson, L. J.; Karhu, H.; Väyrynen, I. J.; Järås, S. G. Characterization and Activity of Supported Palladium Combustion Catalysts. *J. Catal.* **2002**, *207* (1), 139–149. https://doi.org/10.1006/JCAT.2002.3515.

(26) Epling, W. S.; Hoflund, G. B. Catalytic Oxidation of Methane over ZrO2-Supported Pd Catalysts. *J. Catal.* **1999**, *182* (1), 5–12. https://doi.org/10.1006/JCAT.1998.2341.

(27) Hartadi, Y.; Widmann, D.; Behm, R. J. Methanol Formation by CO2 Hydrogenation on Au/ZnO Catalysts – Effect of Total Pressure and Influence of CO on the Reaction Characteristics. *J. Catal.* **2016**, *333*, 238–250. https://doi.org/10.1016/J.JCAT.2015.11.002.

(28) Appl, M. Ammonia, 2. Production Processes. *Ullmann's Encyclopedia of Industrial Chemistry*. October 15, 2011. https://doi.org/doi:10.1002/14356007.o02_o11.

(29) Gholami, R.; Alyani, M.; Smith, J. K. Deactivation of Pd Catalysts by Water during Low Temperature Methane Oxidation Relevant to Natural Gas Vehicle Converters. *Catalysts* . 2015. https://doi.org/10.3390/catal5020561.

(30) Eriksson, S.; Boutonnet, M.; Järås, S. Catalytic Combustion of Methane in Steam and Carbon Dioxide-Diluted Reaction Mixtures. *Appl. Catal. A Gen.* **2006**, *312*, 95–101. https://doi.org/10.1016/J.APCATA.2006.06.032.

(31) Burch, R.; Urbano, F. J.; Loader, P. K. Methane Combustion over Palladium Catalysts: The Effect of Carbon Dioxide and Water on Activity. *Appl. Catal. A Gen.* **1995**, *123* (1), 173–184. https://doi.org/10.1016/0926-860X(94)00251-7.

(32) Willis, J. J.; Gallo, A.; Sokaras, D.; Aljama, H.; Nowak, S. H.; Goodman, E. D.; Wu, L.; Tassone, C. J.; Jaramillo, T. F.; Abild-Pedersen, F.; et al. Systematic Structure–Property Relationship Studies in Palladium-Catalyzed Methane Complete Combustion. *ACS Catal.* **2017**, *7* (11), 7810–7821. https://doi.org/10.1021/acscatal.7b02414.

(33) Piermartini, P.; Schuhmann, T.; Pfeifer, P.; Schaub, G. Water Gas Shift in Microreactors at Elevated Pressure: Platinum-Based Catalyst Systems and Pressure Effects. *Top. Catal.* **2011**, *54* (13), 967. https://doi.org/10.1007/s11244-011-9717-7.

(34) Nikitin, A. V; Dmitruk, A. S.; Arutyunov, V. S. Effect of Pressure on the Oxidative Cracking of C2—C4 Alkanes. *Russ. Chem. Bull.* **2016**, *65* (10), 2405–2410. https://doi.org/10.1007/s11172-016-1597-3.

(35) Sen, F.; Kasper, T.; Bergmann, U.; Hegner, R.; Atakan, B. Partial Oxidation of Methane at Elevated Pressures and Effects of Propene and Ethane as Additive: Experiment and Simulation. *Zeitschrift für Physikalische Chemie*. 2015, p 955. https://doi.org/10.1515/zpch-2014-0576.

(36) Reinke, M.; Mantzaras, J.; Schaeren, R.; Bombach, R.; Inauen, A.; Schenker, S. High-Pressure Catalytic Combustion of Methane over Platinum: In Situ Experiments and Detailed Numerical Predictions. *Combust. Flame* **2004**, *136* (1–2), 217–240. https://doi.org/10.1016/J.COMBUSTFLAME.2003.10.003.

(37) Barbato, P. S.; Di Benedetto, A.; Di Sarli, V.; Landi, G.; Pirone, R. High-Pressure Methane Combustion over a Perovskyte Catalyst. *Ind. Eng. Chem. Res.* **2012**, *51* (22), 7547–7558. https://doi.org/10.1021/ie201736p.

(38) Di Benedetto, A.; Landi, G.; Di Sarli, V.; Barbato, P. S.; Pirone, R.; Russo, G. Methane Catalytic Combustion under Pressure. *Catal. Today* **2012**, *197* (1), 206–213. https://doi.org/10.1016/J.CATTOD.2012.08.032.

(39) Haukka, S.; Lakomaa, E.-L.; Suntola, T. Adsorption Controlled Preparation of Heterogeneous Catalysts. *Stud. Surf. Sci. Catal.* **1999**, *120*, 715–750. https://doi.org/10.1016/S0167-2991(99)80570-9.

(40) Sietsma, J. R. A.; Jos van Dillen, A.; de Jongh, P. E.; de Jong, K. P. Application of Ordered Mesoporous Materials as Model Supports to Study Catalyst Preparation by Impregnation and Drying. *Stud. Surf. Sci. Catal.* **2006**, *162*, 95–102. https://doi.org/10.1016/S0167-2991(06)80895-5.

(41) Canton, P.; Fagherazzi, G.; Battagliarin, M.; Menegazzo, F.; Pinna, F.; Pernicone, N. Pd/CO Average Chemisorption Stoichiometry in Highly Dispersed Supported Pd/γ-Al2O3 Catalysts. *Langmuir* **2002**, *18* (17), 6530–6535. https://doi.org/10.1021/la015650a.

(42) Atkins, P.; de Paula, J. Part 3 Change. In *Atkins' Physical Chemistry*; Oxford University Press, 2014.

(43) Chorkendorff, I.; Niemantsverdriet, J. W. Kinetics. In *Concepts of Modern Catalysis and Kinetics*; 2003; pp 23–78. https://doi.org/10.1002/3527602658.ch2.

(44) Liu, J.; Lucci, F. R.; Yang, M.; Lee, S.; Marcinkowski, M. D.; Therrien, A. J.; Williams, C. T.; Sykes, E. C. H.; Flytzani-Stephanopoulos, M. Tackling CO Poisoning with Single-Atom Alloy Catalysts. *J. Am. Chem. Soc.* **2016**, *138* (20), 6396–6399. https://doi.org/10.1021/jacs.6b03339.

(45) Falcone Miller, S.; Miller, B. G. Advanced Flue Gas Cleaning Systems for Sulfur Oxides (SOx), Nitrogen Oxides (NOx) and Mercury Emissions Control in Power Plants. *Adv. Power Plant Mater. Des. Technol.* **2010**, 187–216. https://doi.org/10.1533/9781845699468.2.187.

(46) Zhu, W.; Zhang, J.; Kapteijn, F.; Makkee, M.; Moulijn, J. A. Hydrodechlorination of 1,2-Dichloropropane over Pt-Cu/C Catalysts: Coke Formation Determined by a Novel Technique-TEOM. *Stud. Surf. Sci. Catal.* **2001**, *139*, 21–28. https://doi.org/10.1016/S0167-2991(01)80176-2.

(47) Wittstock, A.; Zielasek, V.; Biener, J.; Friend, C. M.; Bäumer, M. Nanoporous Gold Catalysts for Selective Gas-Phase Oxidative Coupling of Methanol at Low Temperature. *Science (80-.).* **2010**, *327* (5963), 319 LP – 322. https://doi.org/10.1126/science.1183591.

(48) Baerns, M. Aspects of Heterogeneous Catalysis and of Its Industrial and Environmental Practice. *Ref. Modul. Chem. Mol. Sci. Chem. Eng.* **2014**. https://doi.org/10.1016/B978-0-12-409547-2.11041-8.

(49) Florén, C.-R.; Van den Bossche, M.; Creaser, D.; Grönbeck, H.; Carlsson, P.-A.; Korpi, H.; Skoglundh, M. Modelling Complete Methane Oxidation over Palladium Oxide in a Porous Catalyst Using First-Principles Surface Kinetics. *Catal. Sci. Technol.* **2018**, *8* (2), 508–520. https://doi.org/10.1039/C7CY02135F.

(50) Florén, C.-R.; Carlsson, P.-A.; Creaser, D.; Grönbeck, H.; Skoglundh, M. Multiscale Reactor Modelling of Total Pressure Effects on Complete Methane Oxidation over Pd/Al2O3. *Catal. Sci. Technol.* **2019**, *9* (12), 3055–3065. https://doi.org/10.1039/C8CY02461H.

(51) Ericson, C.; Westerberg, B.; Odenbrand, I. A State-Space Simplified SCR Catalyst Model for Real Time Applications. SAE International 2008. https://doi.org/10.4271/2008-01-0616.

(52) Creaser, D.; Karatzas, X.; Lundberg, B.; Pettersson, L. J.; Dawody, J. Modeling Study of 5 KWe-Scale Autothermal Diesel Fuel Reformer. *Appl. Catal. A Gen.* **2011**, *404* (1–2), 129–140. https://doi.org/10.1016/J.APCATA.2011.07.023.

(53) Azis, M. M.; Härelind, H.; Creaser, D. Microkinetic Modeling of H2-Assisted NO Oxidation over Ag–Al2O3. *Chem. Eng. J.* **2013**, *221*, 382–397. https://doi.org/10.1016/J.CEJ.2013.01.107.

(54) Chandra Shekar, S.; Rama Rao, K. S.; Sahle-Demessie, E. Characterization of Palladium Supported on γ-Al2O3 Catalysts in Hydrodechlorination of CCl2F2. *Appl. Catal. A Gen.* **2005**, *294* (2), 235–243. https://doi.org/10.1016/J.APCATA.2005.07.045.

(55) Kim, J.; Kelly, M. J.; Lamb, H. H.; Roberts, G. W.; Kiserow, D. J. Characterization of Palladium (Pd) on Alumina Catalysts Prepared Using Liquid Carbon Dioxide. *J. Phys. Chem. C* **2008**, *112* (28), 10446–10452. https://doi.org/10.1021/jp711495n.

(56) Stotz, H.; Maier, L.; Boubnov, A.; Gremminger, A. T.; Grunwaldt, J.-D.; Deutschmann, O. Surface Reaction Kinetics of Methane Oxidation over PdO. *J. Catal.* **2019**, *370*, 152–175. https://doi.org/10.1016/J.JCAT.2018.12.007.

(57) Choudhary, T. .; Banerjee, S.; Choudhary, V. . Catalysts for Combustion of Methane and Lower Alkanes. *Appl. Catal. A Gen.* **2002**, *234* (1–2), 1–23. https://doi.org/10.1016/S0926-860X(02)00231-4.

(58) Torkashvand, B.; Gremminger, A.; Valchera, S.; Casapu, M.; Grunwaldt, J.-D.; Deutschmann, O. The Impact of Pre-Turbine Catalyst Placement on Methane Oxidation in Lean-Burn Gas Engines: An Experimental and Numerical Study. SAE International 2017. https://doi.org/https://doi.org/10.4271/2017-01-1019.

(59) Duprat, F. Light-off Curve of Catalytic Reaction and Kinetics. *Chem. Eng. Sci.* **2002**, *57* (6), 901–911. https://doi.org/10.1016/S0009-2509(01)00409-2.

(60) Föttinger, K.; Emhofer, W.; Lennon, D.; Rupprechter, G. Adsorption and Reaction of CO on (Pd–)Al2O3 and (Pd–)ZrO2: Vibrational Spectroscopy of Carbonate Formation. *Top. Catal.* **2017**, *60* (19), 1722–1734. https://doi.org/10.1007/s11244-017-0852-7.

(61) Richard, M.; Duprez, D.; Bion, N.; Can, F. Investigation of Methane Oxidation Reactions Over a Dual-Bed Catalyst System Using 18O Labelled DRIFTS Coupling. *ChemSusChem* **2017**, *10* (1), 210–219. https://doi.org/10.1002/cssc.201601165.

(62) Jodłowski, P. J.; Jędrzejczyk, R. J.; Chlebda, D.; Gierada, M.; Łojewska, J. In Situ Spectroscopic Studies of Methane Catalytic Combustion over Co, Ce, and Pd Mixed Oxides Deposited on a Steel Surface. *J. Catal.* **2017**, *350*, 1–12. https://doi.org/10.1016/J.JCAT.2017.03.022.

(63) Wang, X.; Shi, H.; Kwak, J. H.; Szanyi, J. Mechanism of CO2 Hydrogenation on Pd/Al2O3 Catalysts: Kinetics and Transient DRIFTS-MS Studies. *ACS Catal.* **2015**, *5* (11), 6337–6349. https://doi.org/10.1021/acscatal.5b01464.

(64) Demoulin, O.; Navez, M.; Ruiz, P. Investigation of the Behaviour of a Pd/γ-Al2O3 Catalyst during Methane Combustion Reaction Using in Situ DRIFT Spectroscopy. *Appl. Catal. A Gen.* **2005**, *295* (1), 59–70. https://doi.org/10.1016/J.APCATA.2005.08.008.

(65) Almusaiteer, K.; Chuang, S. S. C. Dynamic Behavior of Adsorbed NO and CO under Transient Conditions on Pd/Al2O3. *J. Catal.* **1999**, *184* (1), 189–201. https://doi.org/10.1006/JCAT.1999.2417.

(66) Hicks, R. F.; Qi, H.; Kooh, A. B.; Fischel, L. B. Carbon Monoxide Restructuring of Palladium Crystallite Surfaces. *J. Catal.* **1990**, *124* (2), 488–502. https://doi.org/10.1016/0021-9517(90)90195-P.

(67) Baumgarten, E.; Zachos, A. Infrared Spectroscopical Investigations on the Adsorption of CO2 on Aluminas and Silica Aluminas at Elevated Temperatures. *Spectrochim. Acta Part A Mol. Spectrosc.* **1981**, *37* (2), 93–98. https://doi.org/10.1016/0584-8539(81)80093-1.

(68) Monteiro, R. .; Zemlyanov, D.; Storey, J. .; Ribeiro, F. . Turnover Rate and Reaction Orders for the Complete Oxidation of Methane on a Palladium Foil in Excess Dioxygen. *J. Catal.* **2001**, *199* (2), 291–301. https://doi.org/10.1006/JCAT.2001.3176.

(69) Zhu, G.; Han, J.; Zemlyanov, D. Y.; Ribeiro, F. H. Temperature Dependence of the Kinetics for the Complete Oxidation of Methane on Palladium and Palladium Oxide. *J. Phys. Chem. B* **2005**, *109* (6), 2331–2337. https://doi.org/10.1021/jp0488665.

(70) Sadokhina, N.; Ghasempour, F.; Auvray, X.; Smedler, G.; Nylén, U.; Olofsson, M.; Olsson, L. An Experimental and Kinetic Modelling Study for Methane Oxidation over Pd-Based Catalyst: Inhibition by Water. *Catal. Letters* **2017**, *147* (9), 2360–2371. https://doi.org/10.1007/s10562-017-2133-2.

(71) Mihai, O.; Smedler, G.; Nylén, U.; Olofsson, M.; Olsson, L. The Effect of Water on Methane Oxidation over Pd/Al2O3 under Lean, Stoichiometric and Rich Conditions. *Catal. Sci. Technol.* **2017**, *7* (14), 3084–3096. https://doi.org/10.1039/C6CY02329K.

Chapter IV: Electrocatalytic Reduction of CO_2 over Copper Catalyst

Abstract

One way to decrease greenhouse gases in the atmosphere and thus to reduce the increase of global mean surface temperature is the capture of CO_2 and reduction of it to useful products. This can be obtained electrochemically, reducing CO_2 over the surface of an electrocatalyst in an electrolyte by applying a potential to it. The aim of this work is to establish a catalyst made of Cu plates assembled out of small nanoparticles, which is combined with Au to obtain energy rich C2/C3 products (products containing two or three carbon atoms) via electrochemical reduction of CO_2. A range of samples (pure Cu, different Cu:Au ratios and pure Au) are synthesized by combining chemical deposition and electrochemical in-situ reduction methods to obtain the final porous films on a titanium substrate. The focus is set on the activity but also the selectivity of the products by tuning the catalyst composition (different Cu/Au ratios) and morphology (such as porosity).

1. Introduction

Our environment is facing a global warming crisis, in part due to a range of greenhouse gases in the atmosphere. In the last decade the emission of around 100 billion metric tons of fossil-fuel carbon sources were recorded with a steadily increasing trend[1]. The main contributor to this carbon emission is CO_2, a greenhouse gas, confirmed to cause global warming[2–5]. The reduction of CO_2 in the environment is crucial and can either be achieved via the reduction of emissions in fields where fossil-fuels are used in large quantities or by capturing the emitted CO_2. A major contribution in the last years was given by Lackner and co-workers[6], who were able to fabricate a so-called artificial tree, capable of binding the CO_2. The mechanism of this method depends on the used polymer strips which are coated with a resin that can bind the CO_2 in the ambient atmosphere. The concentration of CO_2 in the ambient atmosphere is of around 400 ppm, which is enough for the artificial trees to adsorb a large amount. Once the greenhouse gas is attached to the resins via chemical bonding, the trees are dipped in a container filled with water, which allows a moisture-induced desorption of the CO_2 into water forming carbonates and bicarbonates. By this method, the CO_2 captured from the atmosphere can be stored and further processed.

A method of processing CO_2 in such a form can be the electrochemical reduction of CO_2. This process involves the presence of CO_2 in an electrolyte allowing a catalyst at the cathode, which

once a potential is applied, to reduce the CO_2 into a diverse range of gaseous (such as carbon monoxide[7], methane[8] and ethylene[8,9]) and liquid chemical compounds (such as alcohols[10] and aldehydes[11] containing one to three carbon atoms, C1-C3), which then can be used in bulk chemical (carbon monoxide with hydrogen for Fischer-Tropsch[12] or Sabatier processes[13]) but also fuel related applications (internal combustion engines powered by methanol/ethanol[14]). However, it is crucial to consider green energy (from solar energy or wind power) as a powering source to guarantee a carbon budget with a zero net-emission of CO_2. Once the chemicals or fuels are obtained, they can be utilized, producing CO_2 as an end- or side-product, which can be brought back into the circle after capturing it from the atmosphere or directly sending the side-product of the process to an on-plant electrochemical cell. By this, an indefinite recycling of CO_2 can be carried out allowing for net zero emissions which can contribute to the regulation of CO_2 in the atmosphere. The following scheme summarizes this information in the so-called CO_2-cycle.

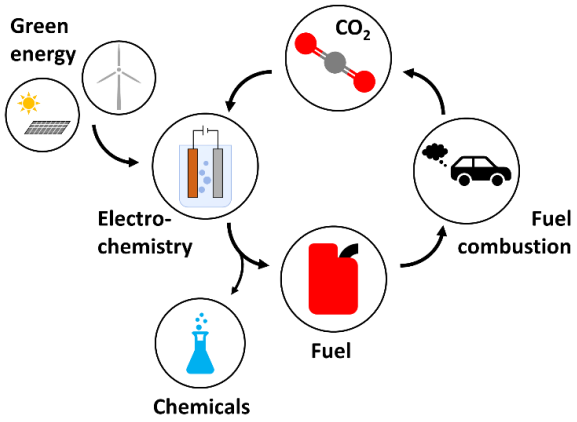

Figure 4.1 Illustration of a carbon neutral cycle involving green energy to power electrocatalytic reduction of CO_2 to form fuels for combustion to form CO_2 and close the cycle.

Recent research studies on the electrochemical reduction of CO_2 are based on the usage of different transition metal catalysts[15] (such as copper[16], gold[17,18], silver[19], and platinum[20]) as a working electrode material, of which copper has been utilized since works of Hori et al.[16] for the high activities and controllable selectivities of the formed products. Most of the time, the Cu was used as nanoparticles (NPs) or as a nanoparticulate deposition on a substrate, enabling a large surface area and high porosities, which are correlated to a high number of active sites and with this enhanced activities. In a study of Wang et al.[11] the high porosity of the Cu electrode materials was associated with the suppression of the competing hydrogen evolution reaction (HER), which

concluded in decreased HER whereas the reduction of carbon monoxide (CO, a known intermediate/final product of the CO_2 reduction[21]) could be increased. In addition, alloys of copper (with silver[9] or gold[10,22]) have been proved to enhance the activity but also the selectivity of the catalyst. In these materials, the silver/gold surface allows the reduction of CO_2 to CO molecules, which are subsequently spilled over to the copper surface during a simultaneous charge transfer from copper to silver at the interface of the domains, resulting in the sequential adsorption of the CO molecules onto the copper surface and finally leading to the coupling of these molecules to form hydrocarbons of two to three carbon atoms.

Taking this state-of-the-art knowledge into account, a simple yet effective chemical deposition approach coupled with an in-situ electrochemical reduction was used to prepare a diverse range of porous copper materials deposited on a titanium substrate. In the *chemical solution deposition (CSD) technique*[23] the precursors of the reaction are dissolved in a solvent, which, when heated, will result in the formation of the desired product[23] on a flat substrate. In the case of electrochemical reactions, a conductive substrate was chosen to deposit the material, to guarantee an electrochemical interaction of the product with the dissolved reactants. The choice of precursor and substrate defines the homogeneity of the film deposited on the substrate[24]. In addition, the interaction between precursor and substrate surface can lead to stronger or weaker attachments of the formed layer[24]. In some cases, a pretreatment to clean or roughen the surface may be necessary, which can be obtained via wet-chemical methods (acids, bases[25]) or by mechanical treatments (for example sand blast method[26]), to enhance the attachment of the films. The obtained sample can be further treated by heat or have a current/potential applied to form the final active material. This method to design metallic oxide films is very flexible, which can be further reduced to metallic materials if necessary[23,27].

The *in-situ electrochemical reduction method* can be used as a further treatment after any deposition technique on a conductive substrate[27,28]. The film (usually a metal oxide film) can be further reduced by electrochemical treatments: applying a potential to the system up to the metals standard electrode potential E^0 will lead to its reduction[27]. This standard electrode potential arises from the thermodynamics of a system, which in most cases is a well-known value. The values found in literature are calculated relative to the standard hydrogen electrode. The following table shows the standard electrode potential of selected metal reactions[29].

Table 4.1 Standard electrode potentials for selected metal reactions.

Reaction	Standard Electrode Potential E^0 /V
$Au = Au^{3+} + 3e^-$	+1.50
$Pt = Pt^{2+} + 2e^-$	+1.20
$Pd = Pd^{2+} + 2e^-$	+0.99
$Ag = Ag^{+} + e^-$	+0.80
$Cu = Cu^{2+} + 2e^-$	+0.34

The electrochemical in-situ reduction can be performed using different methods: performing cyclic voltammetry (cycling a potential range on the working electrode), chronopotentiometry (applying a constant current to the working electrode) or chronoamperometry (applying constant potential to the working electrode). Depending on the technique used, the composition of the metal oxide layer and the substrate, the reduced film can be attached to the substrate in a more stable and strong manner. When applying a constant potential to the system, the dissolution and subsequent redeposition of the metallic film is possible. This can lead to the restructuring of the film surface, which can enhance a catalysts activity due to increased porosity[27]. The in-situ reduction method can be used to reduce metal ions from the electrolyte solution and deposit these on the electrode surface[30]. The driving force in this case is the attraction of the ions by the negatively charged substrate surface. Depending on the applied potential and nature of electrolyte, this deposition can be kinetically controlled. In addition, the choice of metal salt in solution can influence the result of the deposited layer: the salt needs to be soluble in the electrolyte and must not react with it to form precipitations.

The here prepared samples ranged compositionally from pure Cu, over a combination of Cu and small amounts of Au, to pure Au. All samples were produced using the in-situ reduction method to have similar morphological structures to compare. The addition of Au to Cu-systems was chosen to identify how the interface of both domains can affect the activity and selectivity for the CO_2 reduction. The added amount of Au to the system was kept in a small range, as studies of Morales-Guio et al.[10] showed that lower Au contents on a Cu surface can reduce sintering of Au domains to result in more Au-Cu interfaces, which are recognized to be active. In addition to the bimetallic systems, pure Cu and Au samples prepared by the same technique were compared. The here chosen

experimental method possesses the ability of structuring the catalyst surface with a high level of porosity[27] allowing a higher number of active sites on the catalyst surface and increasing the selectivity towards CO_2 reduction instead of HER as shown by Wang et al.[11]

2. Experimental Methods

Chemical solution deposition of copper(II) oxide films

The here used method was adapted from a previously published work by Shinde et al.[27] with slight modifications. To deposit copper(II) oxide (CuO) on a titanium substrate, 1 mmol copper(II) chloride dihydrate ($CuCl_2 \cdot 2H_2O$, Sigma-Aldrich) was dissolved in 35 mL water, and 1.5 mL ammonia solution (30%, Sigma-Aldrich) was added, which made the color turn from turquoise to dark blue due to the formation of copper-ammine complex. Then a piece of titanium plate (1.5 x 6 cm, 0.127 mm thickness, 99.7% purity, Sigma-Aldrich) was inserted into a glass vial (40 mL vial) containing the precursor solution. Milli-Q water was added until the neck of the vial was reached (total volume of around 40 mL). The cap of the vial was fastened, and the solution was heated up in a steel block on a hot plate to 90°C for 2 h. Subsequently, the substrate was washed carefully with Milli-Q water.

Electrochemical in-situ reduction of CuO films

After the deposition, an area of 1 cm^2 of the CuO film was kept on both sides of the substrate (1 cm x 1.5 cm) by scratching off the rest of it with a scalpel. The as-prepared sample was transferred into an electrochemical cell equipped with a three-electrode system coupled with Ivium potentiostat (Compactstat). A platinum wire acted as a counter electrode, while Ag/AgCl (3.8 M KCl) was used as a reference electrode. The substrate with the CuO film was attached to a conductive clamp to act as the working electrode. All three electrodes were immersed in a 1 M sodium hydoxide electrolyte solution (NaOH,Sigma-Aldrich) paying attention that the clamp of the working electrode did not contact the electrolyte solution, but rather the whole area of the CuO film being covered in it. Then a chronopotentiometric (CP) measurement with an applied current of -5 mA for 30 min was carried out to slowly reduce CuO to Cu, followed by a 15 The washed samples were used for electrochemical CO_2 reduction studies.

In addition to pure Cu films, a small amount (0.9 and 1.8 at%) of Au was electrodeposited on the formed Cu films (samples labeled as CuAu 0.9 at% and CuAu 1.8 at%, respectively). To do so, a 1 mg mL^{-1} solution of sodium tetrachloroaurate(III) dihydrate ($NaAuCl_4 \cdot 2H_2O$ purchased from Sigma-Aldrich) was prepared, of which 83.5 µL and 167 µL were used to prepare a sample with a

gold amount of 0.9 at% and 1.8 at%, respectively. The gold precursor was added after CP measurements. Additionaly, pure Au samples were prepared by immersing a titanium plate into the electrolyte solution with an area of 1 cm^2 followed by an in-situ reduction (applied potential of -1.2 V) of the previously mentioned gold-precursor ($NaAuCl_4 \cdot 2H_2O$) in NaOH to reach an estimated gold deposition amount of 1.3 mg. The following scheme summarises both procedures used to obtain the final materials.

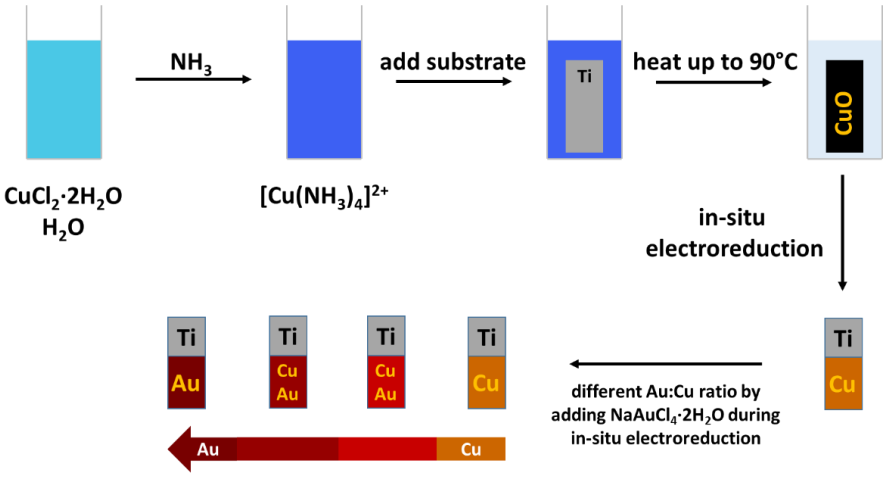

Figure 4.2 Schematic description of the sample preparation. First the chemical solution deposition (upper part) followed by the electrochemical in-situ reduction to obtain pure Cu, pure Au and different Cu:Au ratio samples.

Electrochemical CO_2 reduction

The electrochemical reduction of CO_2 over the synthesized catalyst was performed in an electrochemical two compartment H-cell purchased from Pine Research and a potentiostat from Princeton Applied Research (PARSTAT 2273). The two compartments of the glass cell were separated by a Nafion® 117 membrane (purchased from Sigma-Aldrich) to avoid formed products in the cathode compartment diffusing to the anode compartment and getting oxidized. The membrane of size ~4 x 4 cm is pretreated prior to usage in the two-compartment electrocatalytic cell. To do so, the membrane is firstly boiled in a 5% hydrogen peroxide (H_2O_2, purchased from Sigma-Aldrich) solution (80°C), then in deionized water (80°C), in a 0.05 M sulfuric acid (H_2SO_4, purchased from Sigma-Aldrich) solution (80°C) and finally again in deionized water (80°C). The electrolyte used in this reaction was a 0.1 M potassium bicarbonate ($KHCO_3$, purchased from Sigma-Aldrich) solution. To have comparable results and avoid the formation of bubbles at the reference electrode, the sample was stirred using a stirring bar at 600 rpm throughout the

experiment, keeping the reaction of the temperature at 25°C. The following scheme describes the used electrochemical two-compartment cell setup.

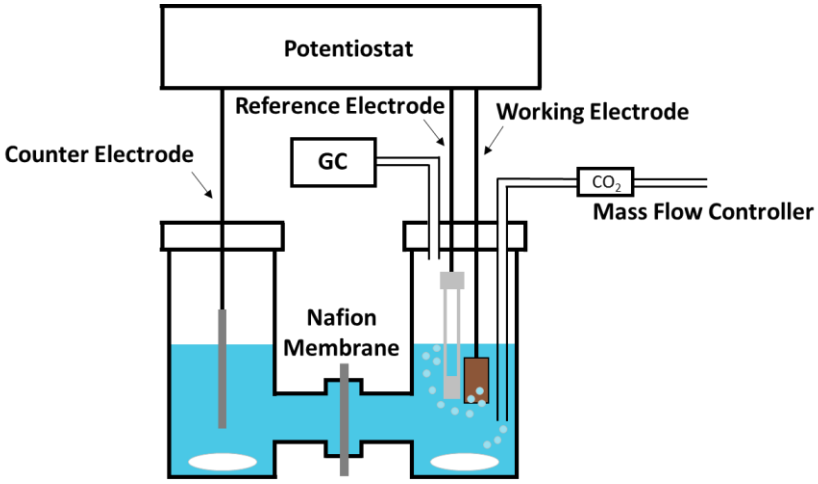

Figure 4.3 Schematic description of the used electrochemical two compartment cell for the electrochemical reduction of CO_2.

All the potentials are reported versus the reversible hydrogen electrode (RHE) scale, which were converted using the following formula: $E_{RHE} = E_{obs} + E_{Ag/AgCl} + (0.0591 \cdot pH)$, where $E_{Ag/AgCl}$ has a value of 0.199 V vs SHE.

The CVs were measured in the presence of Ar and CO_2 (after saturating the electrolyte for 30 min with each gas) at a scan rate of 10 mV sec^{-1} in a range of 0.1 to -0.6 V vs RHE. Chronoamperometric measurements to reduce CO_2 were carried out at two different potentials (-0.3 and -0.4 V vs RHE), which were chosen from the CVs in the presence of CO_2 to increase the possibility of formation of liquid products in the electrolyte. During the time of writing, the gas chromatograph to identify gaseous products was out of order, whereas the liquid products were identified using nuclear magnetic resonance spectroscopy (NMR). The used method will be described in detail in the next subsections.

The *Faradaic efficiency* of a catalyst is described by the charge delivered to a system to facilitate the electrochemical reaction to form a certain product[31]. Taking the electrochemical CO_2 reduction as an example, the following equation can be used to describe the faradaic efficiency of the catalyst:

$$FE\% = \frac{z_i \cdot n_i \cdot F}{Q} \qquad (4.1)$$

In this equation z_i describes the number of electrons necessary to form n_i moles of the product. F is the Faraday constant with 96485 C mol^{-1} and Q the total charge in Coulomb passed through the electrode during the period of electrolysis. As an example, to form formate from CO_2, the reaction requires two electrons, hence $z_{Formate}$ is 2, while the formed amount of $n_{Formate}$ moles needs to be determined by post reaction analysis methods.

Electron microscopy

Scanning electron microscopy (SEM) analysis of the samples was performed using a Helios Nanolab 600 DualBeam microscope (FEI Company) with 5 kV and 0.2 nA as measurement conditions. The sample was fixed using a carbon tape and analyzed. For the mapping of the Cu-samples with small amounts of Au (1.8 at%), additional EDX-analysis was performed.

To perform high resolution transmission electron microscopy experiments on the CuAu 1.8 at% sample, a selected area electron diffraction (SAED) analysis and energy dispersive X-ray spectroscopy (EDX) were performed on a JEOL JEM 2200FS microscope equipped with a Schottky emitter operating at 200 kV, a CEOS spherical aberration corrector for the objective lens, an in column energy filter (Omega type), and a Bruker Quantax 400 EDS system with an XFlash 5060 detector. To perform the measurements, a Nickel mesh grid was used to drop the solution after sonicating a small amount of the sample in ethanol for 3 h.

The samples were further analyzed via high angle annular dark field (HAADF) scanning TEM (STEM). Images were collected using a FEI Tecnai G2 F20 TWIN TMP with a Schottky emitter operated at 200 kV. The EDX analyses have been acquired using a Bruker XFlash 6|T30 silicon-drift detector (SDD), with 30 mm^2 effective area.

Nuclear magnetic resonance spectroscopy

Nuclear magnetic resonance spectroscopy (NMR) was performed on each electrolyte sample acquired at different potentials for each sample to identify and quantify the formed liquid products by using a Bruker AvanceIII 600 MHz spectrometer equipped with 5mm QCI cryoprobe. 5 mm disposable tubes for Sample-jet were employed, each filled with 500 µL of solution (containing 10% of D_2O for the lock engaged, purchased from Sigma-Aldrich). Before acquisition manual matching and tuning, and automatic resolution optimization were performed on each sample tubes along with a manual optimization of the 90° pulse, the offset (O1) and the power level for the pre-saturation of water signal. Then, 64 transients were accumulated at a fixed receiver gain (18), with

64K complex data points and 30 s of a relaxation delay, over a spectral width of 20.03 ppm. An exponential apodization function equivalent to 0.3 Hz was applied to the Free Induction Decays (FID) before Fourier transform. Spectra were referred to a trimethylsilyl propionate (TSP) signal set at 0.00 ppm. The pH of each solution was measured for a water-signal suppression, which was carried out on each sample manually. The quantification was performed using a PULCON external standard method compared to a standard solution of dimethyl sulfon (4.5 μM) prepared from a powder. The limit of detection for each compound was 1 μM, whereas the limit of quantification was assumed to be 10 μM.

3. Results and Discussion

To have a better comparison amongst samples, the used synthesis methods and materials were kept constant. Hence, the pure gold sample was synthesized electrochemically in-situ as with the other samples. The as-prepared samples were further analyzed via different electron microscopy methods to see structural differences and also to understand how the gold is distributed on the copper in the case of the samples obtained after in-situ reduction of Au on as-synthesized Cu films.

As a first comparison method. HR-SEM images were acquired to gain an insight in the sample's porosity and morphology. The following image shows HR-SEM images of all prepared samples.

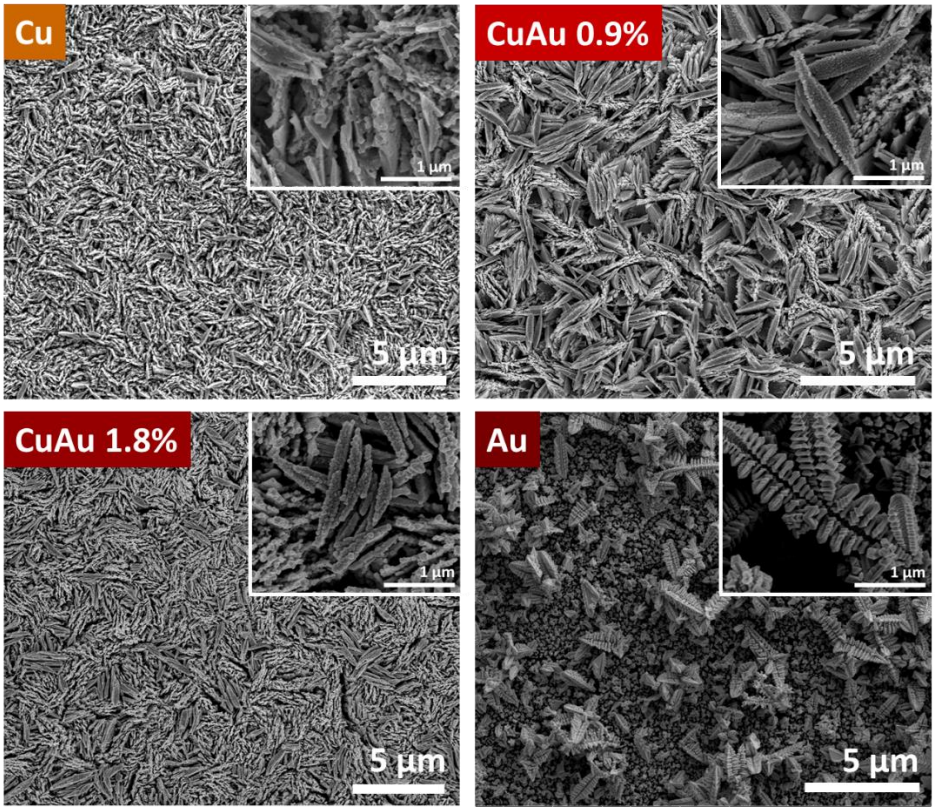

Figure 4.4 HR-SEM images of each sample (upper left: pure Cu, upper right: CuAu 0.9 at%, lower left: CuAu 1.8 at%, lower right: pure Au) with embedded higher magnification images.

As seen in **Figure 4.4**, the samples were obtained via chemical solution deposition with subsequent in-situ electrochemical reduction (for pure Cu, CuAu 0.9 at% and 1.8 at%) and displayed a slightly rougher surface compared to the pristine Cu sample. All mentioned samples are composed of sheet-like structures comparable to the published results of Shinde et al.[27] In contrast to these results, the electrochemical in-situ reduction of the gold solution resulted in a fern-like structure, which is similar to dendritic gold. Yet the difference to dendritic gold can be found in the more ordered structure of the here synthesized material. Generally, the pure gold samples were made of larger structures (around 2-4 µm in length) compared to the Cu-samples, which are composed of smaller (1 µm in length) structures.

To gain an in-depth understanding on the distribution of gold on the copper samples, the CuAu 1.8 at% sample was taken as an example and was further investigated via HR-SEM-EDX, STEM-EDX and HR-TEM-SAED mapping.

The following **Figure 4.5** shows results of the HR-SEM-EDX mapping of the CuAu 1.8 at%.

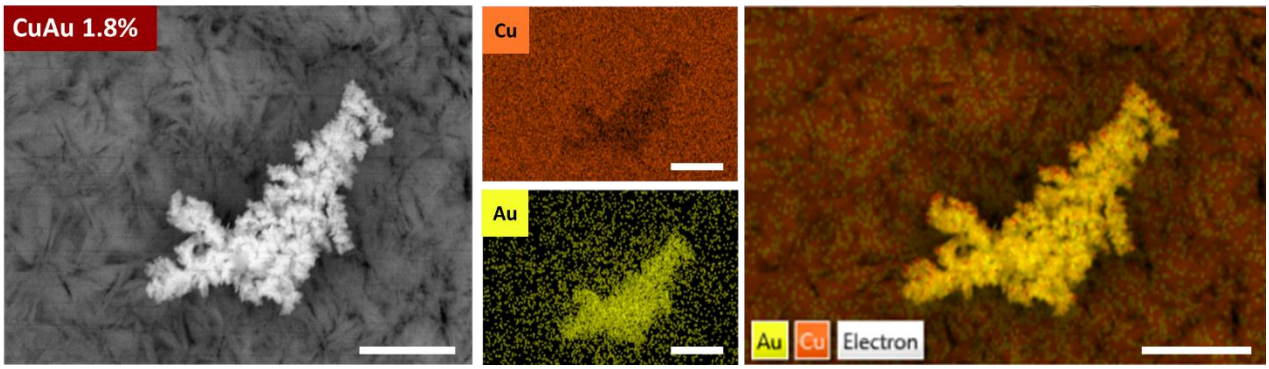

Figure 4.5 HR-SEM EDX on Cu 1.8 at% Au sample. Image of Au-dendrite on Cu sheets (left) and mapping of Cu and Au (centre) with overlapped mapping (right) (all scale bars in 1 µm).

Figure 4.5 shows the morphology of the sample, which is composed of the sheet-like Cu structures with additional dendritic formations of Au, clearly distinguishable by the overlapped mapping seen on the right-hand side of this figure. These dendritic formations differ from the pure gold sample shown before, as in that case the structures seemed more organized and larger than the here obtained dendrites by a couple of hundred nanometers. In addition, from the Au mapping in the center of **Figure 4.5** it can be assumed that additional nanosized Au is present inside the Cu sheet structures. Hence, a further investigation with STEM-EDX is required to identify smaller structures, which are not visible with the used HR-SEM-EDX technique.

The following images show the dark field image obtained using the STEM-EDX technique on the CuAu 1.8 at% sample. In addition, EDX-mapping was performed to identify elements in the structure.

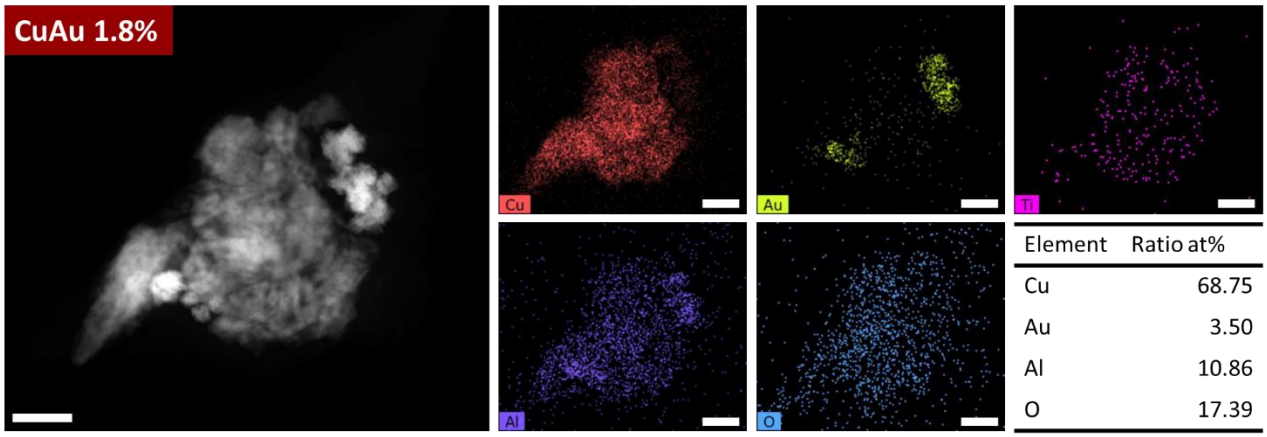

Figure 4.6 STEM-EDX mapping of CuAu 1.8 at% sample (all scale bars in 100 nm) with atomic ratios (right bottom).

As seen in the dark field image of the sample in **Figure 4.6** (left) the structure of interest was a couple of hundred nm large and showed small clusters (around 50 nm) of a brighter colored elements. EDX-mapping revealed that these clusters consist of Au (see mapping in **Figure 4.6**). The Cu:Au ratio was with 95.2:4.8, higher than expected, which can be due to the poor distribution of Au on the Cu-sample and more specifically the clustering into dendritic shapes on the catalyst surface. Surprisingly, in addition to Cu, Au, Ti and O (Ti and O from the Ti substrate capable of forming TiO_x particles on the Cu surface[27]), traces of Al were found on the sample surface (see mapping but also table on atomic ratios in **Figure 4.6**). This Al can derive from the used glassware to synthesize the material (the experiment was performed in borosilicate glass), which can be etched due to the usage of the alkaline electrolyte (1 M NaOH)[32]. Due to the porosity of the sample, the deposition of Al on the surface can be facilitated. This Al on the catalyst surface can influence the catalytic activity by forming oxides and hence requires further attention. Further analysis on the Cu-sheets (see STEM dark field image in **Figure 4.7** left), showed that the sheets were composed of smaller Cu particles.

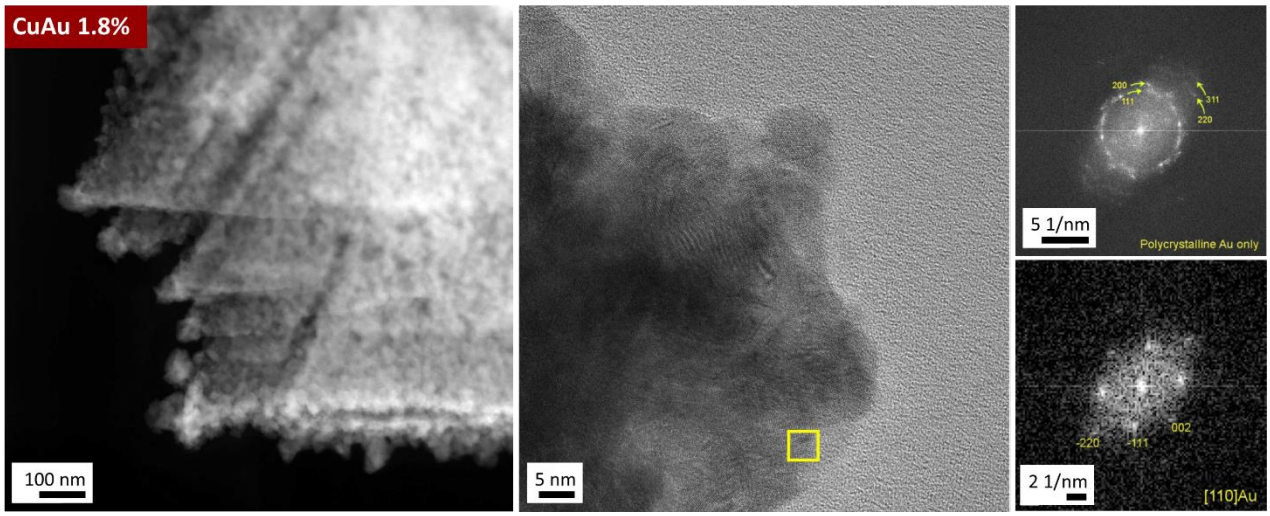

Figure 4.7 STEM dark field image (left) and HR-TEM image (centre). Yellow rectangle in HR-TEM image shows presence of Au (110) phases (right, bottom) for CuAu 1.8 at% sample. Other parts of Au clusters give polycrtysalline structures as seen in diffraction pattern (right, top).

Focusing on the clusters composed of Au nanoparticles (see central image of **Figure 4.7**), the sizes of these particles can be estimated to be around 5 nm (also confirmed by their diffraction rings on the right-hand side of **Figure 4.7**). In addition, the Au clusters show diffraction of polycrystalline Au whereas some areas show the presence of Au (110) only.

Generally speaking, the sample seems to contain large parts of Cu, Au, CuO and Cu_2O which were identified by their diffraction pattern (see **Figure 4.8**).

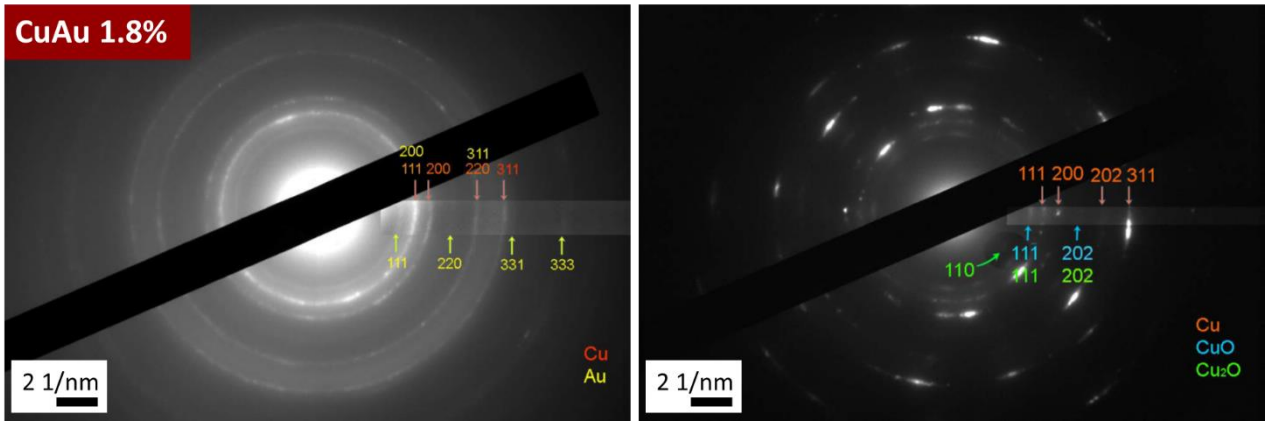

Figure 4.8 Diffracttion rings obtained via HR-TEM for CuAu 1.8 at% sample. Left: Diffraction rings for Cu and Au (corresponding to a large thick aggregate of several microns); Right: Diffraction rings of Cu, CuO and Cu_2O (corresponding to smaller aggregates and edges).

The larger aggregates gave mainly polycrystalline Cu and Au diffraction rings (left-hand side of **Figure 4.8**) whereas edges and smaller aggregates revealed mainly Cu, CuO and Cu_2O diffraction rings (right-hand side of same figure). This result signals that the surface of the material contains oxides, whereas the core is composed of metallic Cu. The oxides on the surface on the catalyst can influence the activity and selectivity of the catalyst[33–35] both positively and negatively, while at the same time the polycrystallinity[36,37] can have a positive or negative impact on the activity and selectivity, due to different mechanisms on different pathways[38–43].

After analyzing the morphology and composition of the synthesized catalysts, CO_2 reduction reactions (CO_2RR) were performed on each catalyst. Due to limited time, two potentials were chosen for the investigation (-0.3 and -0.4 V vs RHE). Prior to each experiment a CV was performed after bubbling Ar for 30 min and after bubbling CO_2 for 30 min into the electrolyte (the results can be found in the Appendix of this chapter). The following graphs show the results of the chronoamperometric measurements performed on each catalyst.

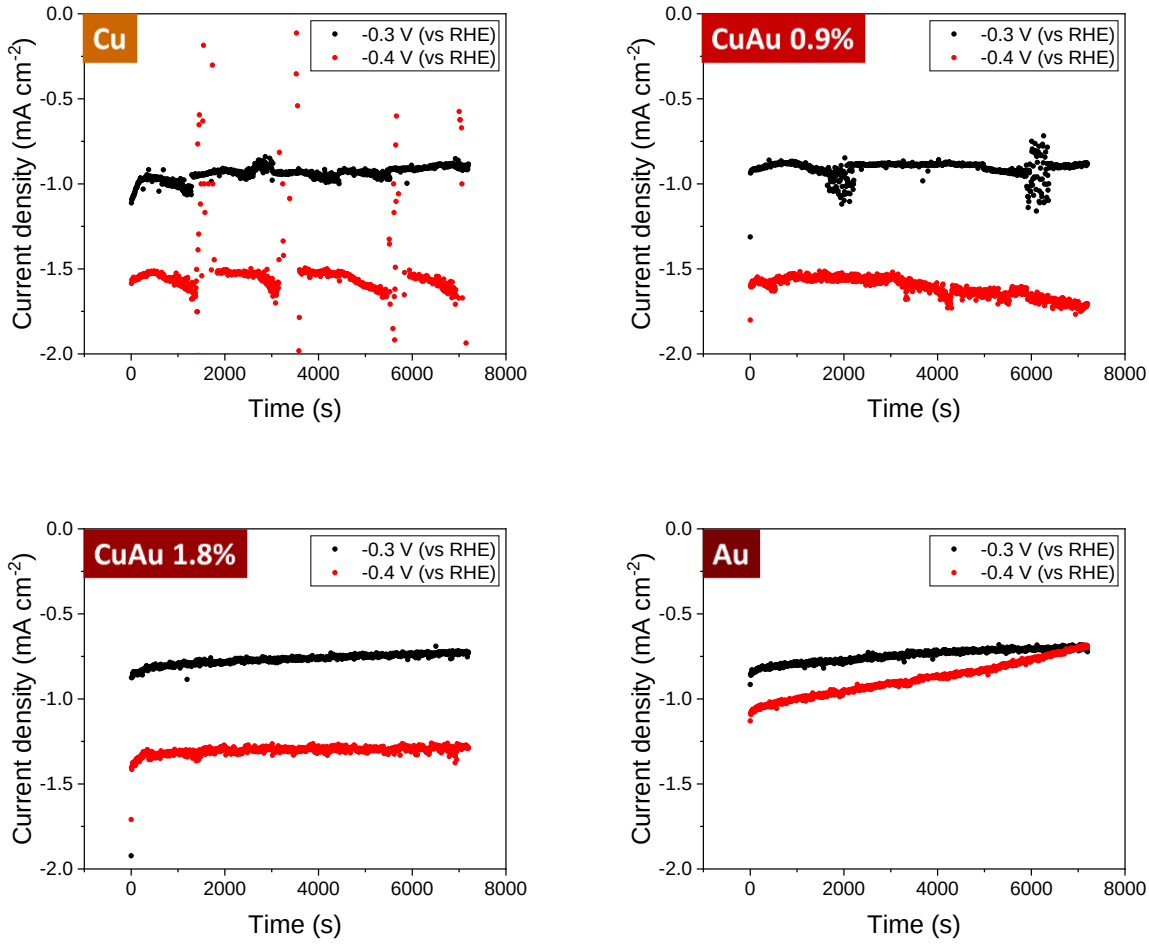

Figure 4.9 Chronoamperometric measurements for CO_2 reduction in presence of 0.1 M $KHCO_3$ at -0.3 (black dots) and -0.4 V vs RHE (red dots) for pure Cu (upper left), CuAu 0.9 at% (upper right), CuAu 1.8 at% (lower left) and pure Au sample (lower right).

The chronoamperometric results in **Figure 4.9** show comparable results in the current density for each sample. At -0.3 V vs RHE, the current density of the catalyst reaches -0.8 to -1.0 mA cm^{-2}. For an applied potential of -0.4 V vs RHE the current density varies from -1.6 mA cm^{-2} (in case of pure Cu and CuAu 0.8 at%) to -1.1 mA cm^{-2} (in case of pure Au). In addition, the pure Au sample seems to be less stable compared to the other samples, reflected by the current density (especially at -0.4 V vs RHE) where it decreases over time to the current density at a potential of -0.3 V vs RHE. The first three experiments (-0.3 and -0.4 V vs RHE for pure Cu and -0.3 V vs RHE for CuAu 0.8 at%) show a fluctuating current, which appears to repeat periodically. This effect was correlated to the presence of bubbles at the tip of the reference electrode when the stirring rate of the magnetic stirring bar was at 400 rpm. When the stirring speed

was increased (every following experiment was performed at 600 rpm) this effect disappeared. Nevertheless, the average current density was not affected in a significant manner by this effect.

As the gaseous products could not be analyzed due to the missing gas chromatograph during the time of the experiments, a focus was set on the possible formed liquid products identified and quantified via NMR analysis. Preliminary results on NMR analysis suggested the presence of different products in the liquid phase. The main compounds found in the liquid phase were formate, glycerol and ethanol. To exclude possible contaminations from the environment or the used equipment (for example due to the Nafion membrane used) a control experiment with a blank titanium substrate as a working electrode was performed and analyzed. The NMR analysis verified the absence of all previously mentioned products (see comparison of NMR spectra for one sample and blank sample in the appendix of this chapter).

The following graph shows the Faradaic efficiency (FE%) for each formed product and each sample at two different potentials.

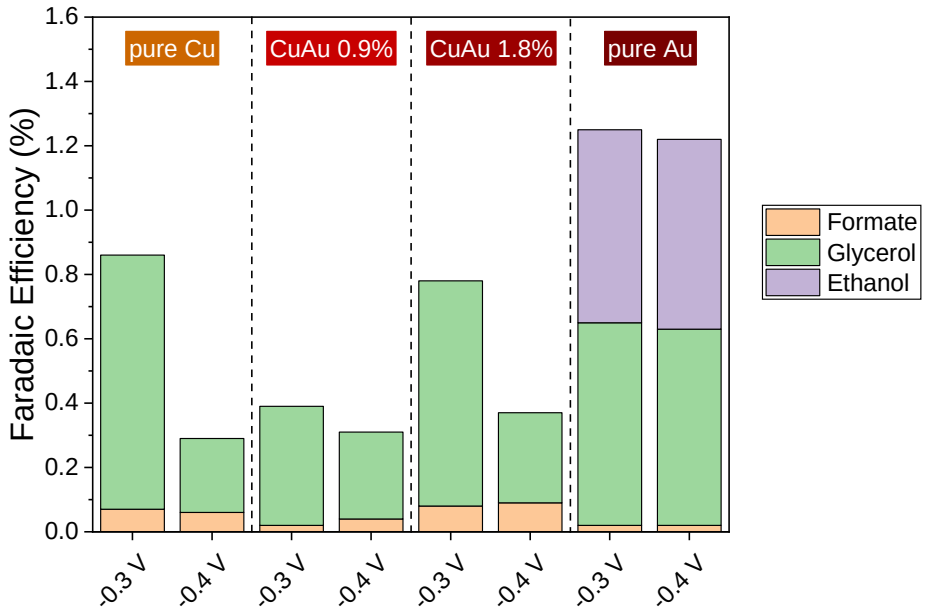

Figure 4.10 Faradaic efficiencies for all quantified products (formate, glycerol and ethanol) obtained by the samples (pure Cu, CuAu 0.9 at%, CuAu 1.8 at% and pure Au) at -0.3 V and -0.4 V. All potentials vs RHE.

As seen in **Figure 4.10**, the overall Faradaic efficiency (FE) for the formed products reaches a maximum of 1.2 % (in the case of the pure Au sample), which is considered low when compared

to published values (of at least 5% FE per formed liquid product)[10,18,44]. However, a small difference between the amount of formed liquid products can be found in both, the applied potential and the used catalyst material. When the applied potential to the system was lower (at -0.3 V vs RHE), the amount of formed liquid products was almost double in case of pure Cu and CuAu 1.8 at% when compared to the higher potential (-0.4 V vs RHE). This can be an indication that using lower potentials may lead to a further increase of the catalyst selectivity for C1-C3 liquid products. Nevertheless, in case of the other two samples (CuAu 0.9 at% and pure Au) this potential difference did not influence the number of formed products significantly. Overall, the amount of formate was negligibly low, whereas the amount of glycerol was more significant. One major difference in the results was the fact that only gold was capable of forming ethanol as a reduction product, whereas all other samples mainly formed glycerol. These results are surprising, as gold is known for the reduction of CO_2 to CO, whereas the formation of larger carbon product molecules is negligibly small[45–49]. This outcome could have derived from the peculiar morphology of the gold electrode, which requires a further analysis via a variety of physico-chemical analysis techniques. Polycrystalline materials may expose a larger number of active sites with a certain preferred orientation, which can allow the catalyst to bind formed intermediate CO molecules with a different energy than Au (111) surfaces. These results should be examined carefully, as they are in a very preliminary stage of the experiments. Further analysis at higher and lower potentials and the additional analysis of gaseous products are crucial for a better overall comparison of samples and formed products.

4. Conclusion

To conclude this work, a porous Cu-catalyst material was synthesized via a chemical deposition method followed by an electrochemical in-situ reduction. In addition, small amounts of Au (0.9 and 1.8 at%) were deposited on the present Cu surface using the same electrochemical method as stated before. Furthermore, a pure Au sample was obtained by using the electrochemical reduction method. All samples were analyzed for their morphology with a focus on the compositional structure of the CuAu 1.8 at% sample. Morphologically, the samples involving Cu were similar to each other, while the pure Au sample showed dendritically ordered structures, different from the smaller Au-dendrites identified on the CuAu samples. Diffraction patterns of different areas of the sample showed polycrystalline Cu and Au. In addition, CuO and Cu_2O was identified to be mainly present on the surface of the catalyst. HR-TEM results suggested flakes of Cu composed of small

Cu-nanoparticles of around 5-10 nm. In the case of Au, the size of the formed particles was approximately up to 5 nm large.

Each sample containing Cu gave similar results in chronoamperometric studies with low current densities of around -1.0 to -1.5 mA cm^{-2}. The pure Au sample gave similar current densities but showed a decreased current over time at higher applied potentials. When comparing the Faradaic efficiencies of the formed liquid products, which were identified and quantified using NMR spectroscopy, a similar observation was made. Samples containing copper showed a smaller Faradaic efficiency for liquid products, whereas pure Au samples showed larger amounts of formed liquid products. Interestingly, the pure Au sample formed ethanol while in the other cases this product was not identified, which was a surprising result and requires further understanding and investigation of this outcome.

The here shown results are from a preliminary study and require a further careful investigation. In general, the catalysts seem to be active in the electrochemical CO_2 reduction, which encourages further analysis and improvement of the catalysts and performed experiments. A diverse range of general characterization methods, such as X-ray powder diffraction, are required to further understand the major phases present in the catalyst. ECSA or electrochemical double-layer (ECDL) measurements can give an insight to the active surface area of the catalyst under electrochemical conditions and can be used to normalize the obtained currents for a better comparability. As the formation of titanium oxide on the catalysts surface cannot be excluded (see in works of Shinde et al.[27], but also in the STEM-EDX analysis shown before) the catalyst can be highly active for HER, which is an undesired side-product and should be suppressed to enable the catalyst to perform reduction of CO_2 to C1-C3 products. A different substrate (e.g. carbon paper) can be used to decrease the hydrogen formation and increase the formation of other gaseous and liquid products. Preliminary experiments using this substrate for the Au-deposition showed similar structures obtained on the Ti-substrate and can be found in the Appendix of this chapter (see **Figure 4.13**). In addition, the investigation on the composition of gaseous products formed during the CO_2 reduction requires the usage of a gas chromatograph. It is an important tool to analyze and verify the Faradaic efficiency of the catalysts for specific gaseous products. Furthermore, lower potentials can be applied to the system to increase the C1-C3 formation and decrease the HER. Another possible method to improve the Cu-catalyst can be the usage of a fresh CuO-film deposited on a

Ti-substrate, which can perform differently (less hydrogen production and more gaseous/liquid C1-C3 products) when compared to an in-situ electrochemically reduced sample.

5. Appendix

Cyclic voltammetry measurement of samples

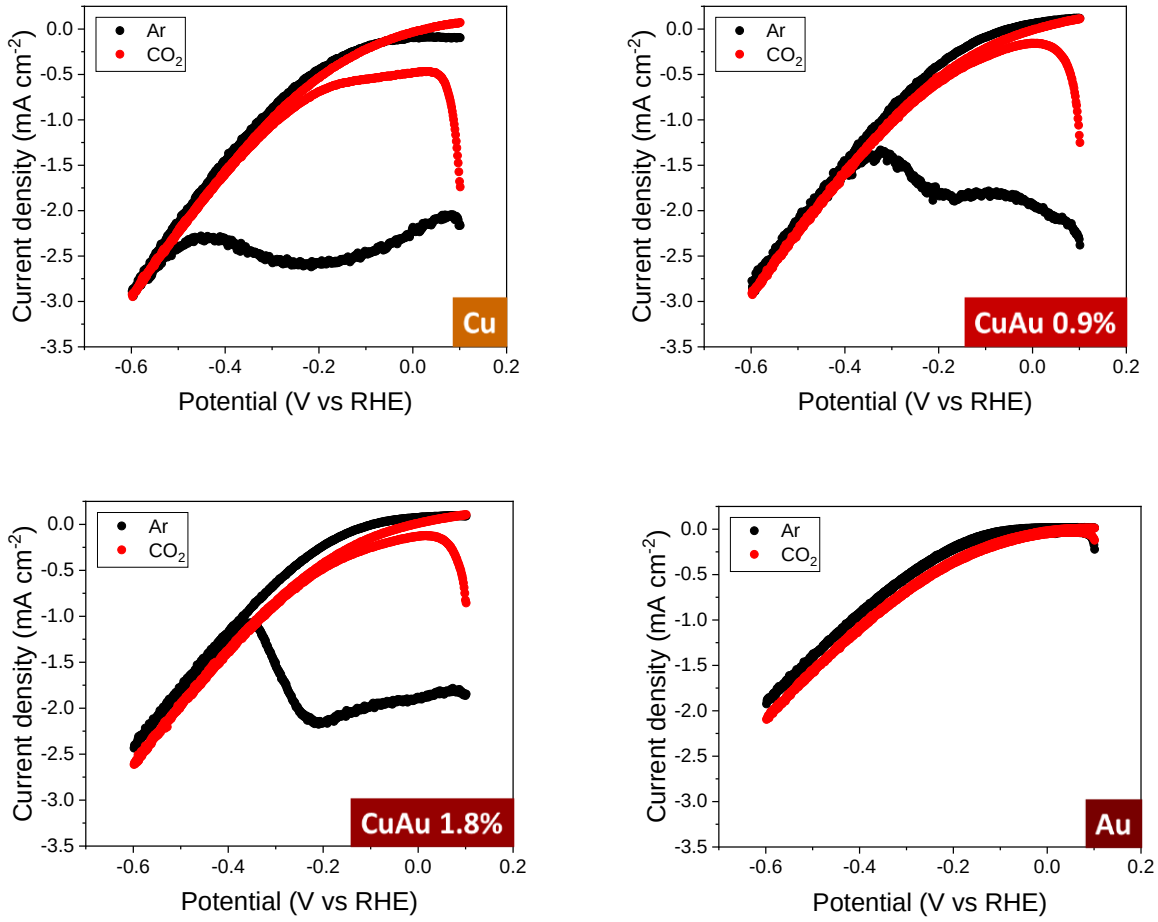

Figure 4.11 CVs of samples (pure Cu upper left, CuAu 0.9 at% upper right, CuAu 1.8 at% lower left, pure Au lower right) prior to each measurement performed in Ar (black dots) and in CO_2 (red dots).

In **Figure 4.11** the CVs in presence of Ar (black lines) and CO_2 (red lines) are presented. While in the presence of Ar the overall CVs seem not to be influenced at applied negative or positive potentials, in the presence of CO_2 significant differences can be observed when comparing the pure Au and the Cu-containing samples. Applying a negative potential to the Cu-containing samples after bubbling CO_2 for 30 min into the electrolyte shows a reduction of the oxides on the surface of up to -0.4 V vs RHE. In the case of pure Au, the reduction of the catalyst surface was not visible

due to gold being a noble metal with a higher redox potential which can lead to less or no oxides in the presence of oxidizing chemicals on the surface.

NMR spectra of liquid products

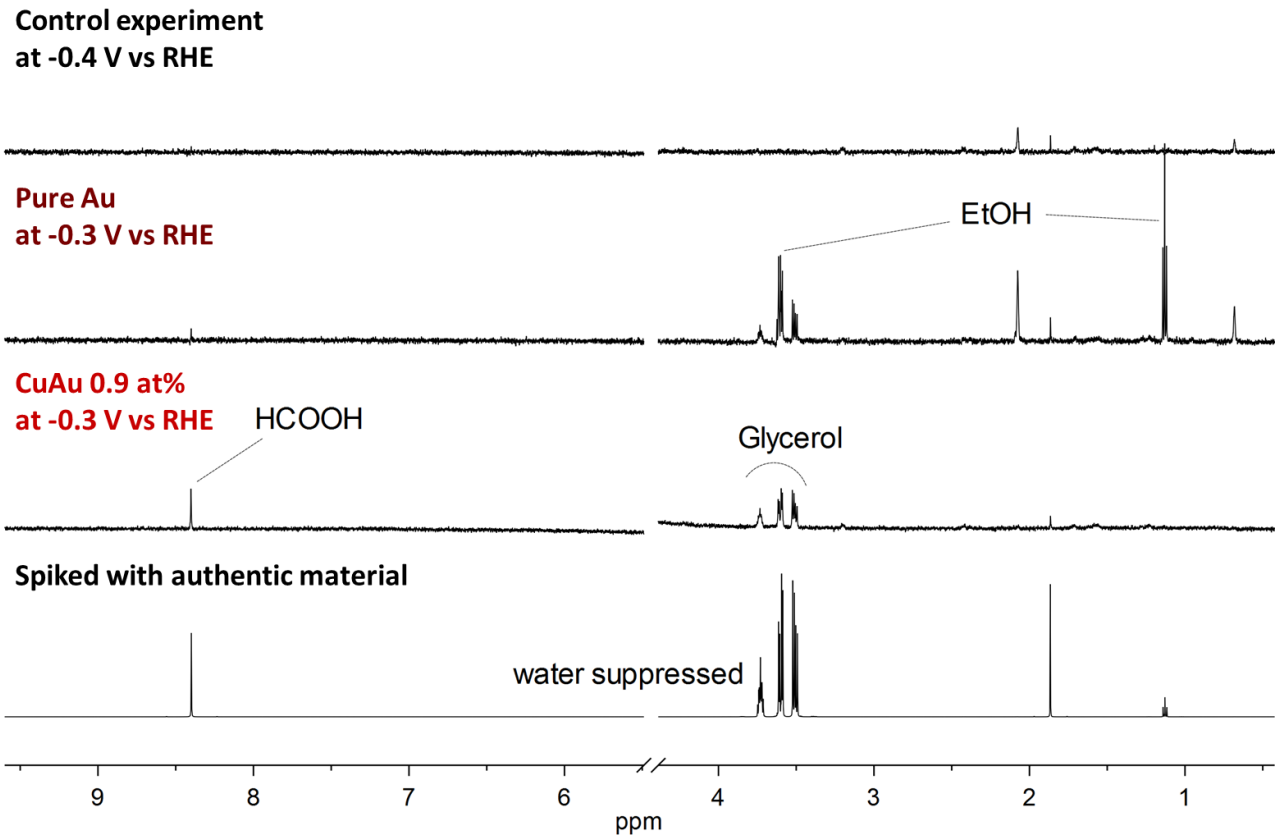

Figure 4.12 NMR spectra of the control experiment at -0.4 V vs RHE, pure Au sample at -0.3 V vs RHE, CuAu 0.9 at% at -0.3 V vs RHE and a sample spiked with authentic material (formic acid, ethanol and glycerol) from top to bottom, respectively.

NMR analyses were performed to identify formed liquid products and were compared to a control experiment to verify that the products derive from the catalyst activity and not due to contaminations. As seen in **Figure 4.12** the control experiment shows no peaks of formate, ethanol or glycerol, while those peaks can be found in both samples shown here (liquid products in electrolyte of experiment with CuAu 0.9 at% and pure Au sample). To verify the presence of the aforementioned products, the samples were spiked with additional formic acid, ethanol and glycerol and remeasured to see an increased signal rather than a different chemical shift.

Usage of carbon paper as a substrate for Au-deposition

Prior to deposition of the Au precursor on the carbon paper (Toray paper 090, substrates of 1 x 1.5 cm), a plasma treatment at 500 mTorr in O_2 atmosphere was carried out for 20 min, followed by a 12 h treatment in a 3 M H_2SO_4 solution. The carbon paper was washed thoroughly with a sequence of deionized water, ethanol and deionized water and dried in a petri glass over a heating plate. The substrate was dipped in an electrolyte solution containing 100 µL (low concentration Au) and in a second experiment with 1300 µL (high concentration Au) of a 1 mg mL^{-1} $NaAuCl_4$ solution. The microscopic structure of each sample was compared by means of HR-SEM and can be found in the following images, respectively.

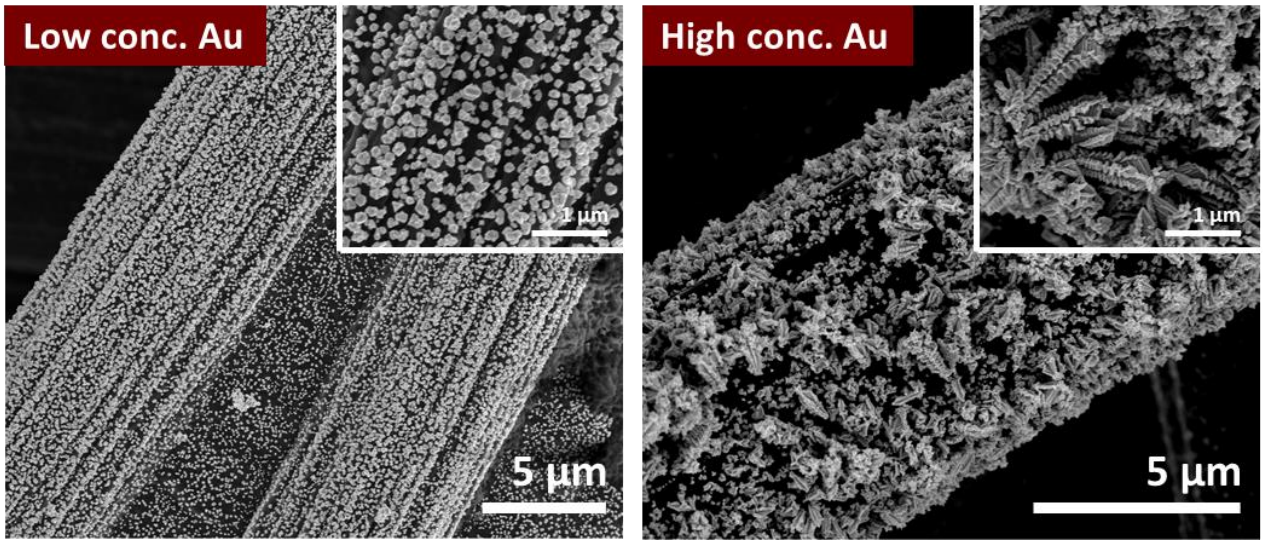

Figure 4.13 HR-SEM images of Au deposited on carbon-paper with a low concentrated precursor solution (left, 100 µL) and high concentrated precursor solution (right, 1300 µL).

As seen in **Figure 4.13** the obtained sample differs depending on the Au concentration in the electrolyte. Smaller crystals with a narrow size distribution can be obtained by using low concentration of the precursor solution, whereas larger crystals, similar to those obtained on a Ti-substrate require the usage of higher concentrated precursor-solutions. Nevertheless, this preliminary experiment shows that the method can be applied on another substrates than the Ti-substrate and is highly dependent on the precursor concentration.

6. References

(1) Annual Global Fossil-Fuel Carbon Emissions https://cdiac.ess-dive.lbl.gov/trends/emis/glo_2014.html (accessed Nov 13, 2019).

(2) SAWYER, J. S. Man-Made Carbon Dioxide and the "Greenhouse" Effect. *Nature* **1972**, *239* (5366), 23–26. https://doi.org/10.1038/239023a0.

(3) Schrag, D. P. Preparing to Capture Carbon. *Science (80-.).* **2007**, *315* (5813), 812 LP – 813. https://doi.org/10.1126/science.1137632.

(4) Friedlingstein, P.; Andrew, R. M.; Rogelj, J.; Peters, G. P.; Canadell, J. G.; Knutti, R.; Luderer, G.; Raupach, M. R.; Schaeffer, M.; van Vuuren, D. P.; et al. Persistent Growth of CO2 Emissions and Implications for Reaching Climate Targets. *Nat. Geosci.* **2014**, *7* (10), 709–715. https://doi.org/10.1038/ngeo2248.

(5) Robert, M. Running the Clock: CO2 Catalysis in the Age of Anthropocene. *ACS Energy Lett.* **2016**, *1* (1), 281–282. https://doi.org/10.1021/acsenergylett.6b00159.

(6) Wang, T.; Lackner, K. S.; Wright, A. Moisture Swing Sorbent for Carbon Dioxide Capture from Ambient Air. *Environ. Sci. Technol.* **2011**, *45* (15), 6670–6675. https://doi.org/10.1021/es201180v.

(7) Ma, M.; Djanashvili, K.; Smith, W. A. Selective Electrochemical Reduction of CO2 to CO on CuO-Derived Cu Nanowires. *Phys. Chem. Chem. Phys.* **2015**, *17* (32), 20861–20867. https://doi.org/10.1039/C5CP03559G.

(8) DeWulf, D.; Jin, T.; Bard, A. Electrochemical and Surface Studies of Carbon Dioxide Reduction to Methane and Ethylene at Copper Electrodes in Aqueous Solutions. *J. Electrochem. Soc.* **1989**, *136*, 1686–1691. https://doi.org/10.1149/1.2096993.

(9) Huang, J.; Mensi, M.; Oveisi, E.; Mantella, V.; Buonsanti, R. Structural Sensitivities in Bimetallic Catalysts for Electrochemical CO2 Reduction Revealed by Ag–Cu Nanodimers. *J. Am. Chem. Soc.* **2019**, *141* (6), 2490–2499. https://doi.org/10.1021/jacs.8b12381.

(10) Morales-Guio, C. G.; Cave, E. R.; Nitopi, S. A.; Feaster, J. T.; Wang, L.; Kuhl, K. P.; Jackson, A.; Johnson, N. C.; Abram, D. N.; Hatsukade, T.; et al. Improved CO2 Reduction Activity towards C2+ Alcohols on a Tandem Gold on Copper Electrocatalyst. *Nat. Catal.* **2018**, *1* (10), 764–771. https://doi.org/10.1038/s41929-018-0139-9.

(11) Wang, L.; Nitopi, S.; Wong, A. B.; Snider, J. L.; Nielander, A. C.; Morales-Guio, C. G.; Orazov, M.; Higgins, D. C.; Hahn, C.; Jaramillo, T. F. Electrochemically Converting Carbon Monoxide to Liquid Fuels by Directing Selectivity with Electrode Surface Area. *Nat. Catal.* **2019**, *2* (8), 702–708. https://doi.org/10.1038/s41929-019-0301-z.

(12) Schulz, H. Short History and Present Trends of Fischer–Tropsch Synthesis. *Appl. Catal. A Gen.* **1999**, *186* (1–2), 3–12. https://doi.org/10.1016/S0926-860X(99)00160-X.

(13) Speight, J. G.; Speight, J. G. Hydrocarbons from Synthesis Gas. *Handb. Ind. Hydrocarb. Process.* **2011**, 281–323. https://doi.org/10.1016/B978-0-7506-8632-7.10008-8.

(14) Bro, K.; Pedersen, P. S. Alternative Diesel Engine Fuels: An Experimental Investigation of Methanol, Ethanol, Methane and Ammonia in a D.I. Diesel Engine with Pilot Injection. SAE International 1977. https://doi.org/10.4271/770794.

(15) Kuhl, K. P.; Hatsukade, T.; Cave, E. R.; Abram, D. N.; Kibsgaard, J.; Jaramillo, T. F. Electrocatalytic Conversion of Carbon Dioxide to Methane and Methanol on Transition Metal Surfaces. *J. Am. Chem. Soc.* **2014**, *136* (40), 14107–14113. https://doi.org/10.1021/ja505791r.

(16) Hori, Y.; Kikuchi, K.; Suzuki, S. PRODUCTION OF CO AND CH4 IN ELECTROCHEMICAL REDUCTION OF CO2 AT METAL ELECTRODES IN AQUEOUS HYDROGENCARBONATE SOLUTION. *Chem. Lett.* **1985**, *14* (11), 1695–1698. https://doi.org/10.1246/cl.1985.1695.

(17) Chen, Y.; Li, C. W.; Kanan, M. W. Aqueous CO2 Reduction at Very Low Overpotential on Oxide-Derived Au Nanoparticles. *J. Am. Chem. Soc.* **2012**, *134* (49), 19969–19972. https://doi.org/10.1021/ja309317u.

(18) Shen, S.; Peng, X.; Song, L.; Qiu, Y.; Li, C.; Zhuo, L.; He, J.; Ren, J.; Liu, X.; Luo, J. Ethanol-Selectivity: AuCu Alloy Nanoparticle Embedded Cu Submicrocone Arrays for Selective Conversion of CO 2 to Ethanol (Small 37/2019) . *Small* **2019**, *15* (37), 1970193. https://doi.org/10.1002/smll.201970199.

(19) Hoshi, N.; Kato, M.; Hori, Y. Electrochemical Reduction of CO2 on Single Crystal Electrodes of Silver Ag(111), Ag(100) and Ag(110). *J. Electroanal. Chem.* **1997**, *440* (1–2), 283–286. https://doi.org/10.1016/S0022-0728(97)00447-6.

(20) Tomita, Y.; Hori, Y. Electrochemical Reduction of Carbon Dioxide at a Platinum Electrode in Acetonitrile-Water Mixtures. *Stud. Surf. Sci. Catal.* **1998**, *114*, 581–584. https://doi.org/10.1016/S0167-2991(98)80826-4.

(21) Hori, Y. Electrochemical CO2 Reduction on Metal Electrodes BT - Modern Aspects of Electrochemistry; Vayenas, C. G., White, R. E., Gamboa-Aldeco, M. E., Eds.; Springer New York: New York, NY, 2008; pp 89–189. https://doi.org/10.1007/978-0-387-49489-0_3.

(22) Tao, Z.; Wu, Z.; Yuan, X.; Wu, Y.; Wang, H. Copper–Gold Interactions Enhancing Formate Production from Electrochemical CO2 Reduction. *ACS Catal.* **2019**, 10894–10898. https://doi.org/10.1021/acscatal.9b03158.

(23) Schwartz, R. W.; Schneller, T.; Waser, R. Chemical Solution Deposition of Electronic Oxide Films. *Comptes Rendus Chim.* **2004**, *7* (5), 433–461. https://doi.org/https://doi.org/10.1016/j.crci.2004.01.007.

(24) Wördenweber, R. 4.06 - Ferroelectric Thin Layers; Bhattacharya, P., Fornari, R., Kamimura, H. B. T.-C. S. S. and T., Eds.; Elsevier: Amsterdam, 2011; pp 177–205. https://doi.org/https://doi.org/10.1016/B978-0-44-453153-7.00096-1.

(25) Casagrande, R. B.; Kunst, S. R.; Beltrami, L. V. R.; Aguzzoli, C.; Brandalise, R. N.; de Fraga Malfatti, C. Pretreatment Effect of the Pure Titanium Surface on Hybrid Coating Adhesion Based on Tetraethoxysilane and Methyltriethoxysilane. *J. Coatings Technol. Res.* **2018**, *15* (5), 1089–1106. https://doi.org/10.1007/s11998-017-0035-2.

(26) Conforto, E.; Aronsson, B.-O.; Salito, A.; Crestou, C.; Caillard, D. Rough Surfaces of Titanium and Titanium Alloys for Implants and Prostheses. *Mater. Sci. Eng. C* **2004**, *24* (5), 611–618. https://doi.org/https://doi.org/10.1016/j.msec.2004.08.004.

(27) Shinde, D. V; Dang, Z.; Petralanda, U.; Palei, M.; Wang, M.; Prato, M.; Cavalli, A.; De Trizio, L.; Manna, L. In Situ Dynamic Nanostructuring of the Cu–Ti Catalyst-Support System Promotes Hydrogen Evolution under Alkaline Conditions. *ACS Appl. Mater. Interfaces* **2018**, *10* (35), 29583–29592. https://doi.org/10.1021/acsami.8b09493.

(28) Xu, G.-R.; Ge, C.; Liu, D.; Jin, L.; Li, Y.-C.; Zhang, T.-H.; Rahman, M. M.; Li, X.-B.; Kim, W. In-Situ Electrochemical Deposition of Dendritic Cu-Cu2S Nanocomposites onto Glassy Carbon Electrode for Sensitive and Non-Enzymatic Detection of Glucose. *J. Electroanal. Chem.* **2019**, *847*, 113177. https://doi.org/https://doi.org/10.1016/j.jelechem.2019.05.059.

(29) Ashby, M. F.; Jones, D. R. H.; Ashby, M. F.; Jones, D. R. H. Wet Corrosion of Materials. *Eng. Mater. 1* **2012**, 385–400. https://doi.org/10.1016/B978-0-08-096665-6.00026-X.

(30) Antoine, O.; Durand, R. In Situ Electrochemical Deposition of Pt Nanoparticles on Carbon and inside Nafion. *Electrochem. SOLID STATE Lett.* **2001**, *4* (5), A55–A58. https://doi.org/10.1149/1.1361233.

(31) Görlin, M.; Chernev, P.; Ferreira de Araújo, J.; Reier, T.; Dresp, S.; Paul, B.; Krähnert, R.; Dau, H.; Strasser, P. Oxygen Evolution Reaction Dynamics, Faradaic Charge Efficiency, and the Active Metal Redox States of Ni–Fe Oxide Water Splitting Electrocatalysts. *J. Am. Chem. Soc.* **2016**, *138* (17), 5603–5614. https://doi.org/10.1021/jacs.6b00332.

(32) Gasteiger, H. A.; Frederick, W. J.; Streisel, R. C. Solubility of Aluminosilicates in Alkaline Solutions and a Thermodynamic Equilibrium Model. *Ind. Eng. Chem. Res.* **1992**, *31* (4), 1183–1190. https://doi.org/10.1021/ie00004a031.

(33) Li, C. W.; Kanan, M. W. CO2 Reduction at Low Overpotential on Cu Electrodes Resulting from the Reduction of Thick Cu2O Films. *J. Am. Chem. Soc.* **2012**, *134* (17), 7231–7234. https://doi.org/10.1021/ja3010978.

(34) Dutta, A.; Rahaman, M.; Luedi, N. C.; Mohos, M.; Broekmann, P. Morphology Matters: Tuning the Product Distribution of CO2 Electroreduction on Oxide-Derived Cu Foam Catalysts. *ACS Catal.* **2016**, *6* (6), 3804–3814. https://doi.org/10.1021/acscatal.6b00770.

(35) Mandal, L.; Yang, K. R.; Motapothula, M. R.; Ren, D.; Lobaccaro, P.; Patra, A.; Sherburne, M.; Batista, V. S.; Yeo, B. S.; Ager, J. W.; et al. Investigating the Role of Copper Oxide in Electrochemical CO2 Reduction in Real Time. *ACS Appl. Mater. Interfaces* **2018**, *10* (10), 8574–8584. https://doi.org/10.1021/acsami.7b15418.

(36) Hahn, C.; Hatsukade, T.; Kim, Y.-G.; Vailionis, A.; Baricuatro, J. H.; Higgins, D. C.; Nitopi, S. A.; Soriaga, M. P.; Jaramillo, T. F. Engineering Cu Surfaces for the Electrocatalytic Conversion of CO₂: Controlling Selectivity toward Oxygenates and Hydrocarbons. *Proc. Natl. Acad. Sci.* **2017**, *114* (23), 5918 LP – 5923. https://doi.org/10.1073/pnas.1618935114.

(37) Schouten, K. J. P.; Qin, Z.; Pérez Gallent, E.; Koper, M. T. M. Two Pathways for the Formation of Ethylene in CO Reduction on Single-Crystal Copper Electrodes. *J. Am. Chem. Soc.* **2012**, *134* (24), 9864–9867. https://doi.org/10.1021/ja302668n.

(38) Calle-Vallejo, F.; Koper, M. T. M. Theoretical Considerations on the Electroreduction of CO to C2 Species on Cu(100) Electrodes. *Angew. Chemie Int. Ed.* **2013**, *52* (28), 7282–7285. https://doi.org/10.1002/anie.201301470.

(39) Montoya, J. H.; Peterson, A. A.; Nørskov, J. K. Insights into C□C Coupling in CO2 Electroreduction on Copper Electrodes. *ChemCatChem* **2013**, *5* (3), 737–742. https://doi.org/10.1002/cctc.201200564.

(40) Luo, W.; Nie, X.; Janik, M. J.; Asthagiri, A. Facet Dependence of CO2 Reduction Paths on Cu Electrodes. *ACS Catal.* **2016**, *6* (1), 219–229. https://doi.org/10.1021/acscatal.5b01967.

(41) Goodpaster, J. D.; Bell, A. T.; Head-Gordon, M. Identification of Possible Pathways for C–C Bond Formation during Electrochemical Reduction of CO2: New Theoretical Insights from an Improved Electrochemical Model. *J. Phys. Chem. Lett.* **2016**, *7* (8), 1471–1477. https://doi.org/10.1021/acs.jpclett.6b00358.

(42) Xiao, H.; Cheng, T.; Goddard, W. A. Atomistic Mechanisms Underlying Selectivities in C1 and C2 Products from Electrochemical Reduction of CO on Cu(111). *J. Am. Chem. Soc.* **2017**, *139* (1), 130–136. https://doi.org/10.1021/jacs.6b06846.

(43) Garza, A. J.; Bell, A. T.; Head-Gordon, M. Mechanism of CO2 Reduction at Copper Surfaces: Pathways to C2 Products. *ACS Catal.* **2018**, *8* (2), 1490–1499. https://doi.org/10.1021/acscatal.7b03477.

(44) Loiudice, A.; Lobaccaro, P.; Kamali, E. A.; Thao, T.; Huang, B. H.; Ager, J. W.; Buonsanti, R. Tailoring Copper Nanocrystals towards C2 Products in Electrochemical CO2 Reduction. *Angew. Chemie Int. Ed.* **2016**, *55* (19), 5789–5792. https://doi.org/10.1002/anie.201601582.

(45) Cave, E. R.; Montoya, J. H.; Kuhl, K. P.; Abram, D. N.; Hatsukade, T.; Shi, C.; Hahn, C.; Nørskov, J. K.; Jaramillo, T. F. Electrochemical CO2 Reduction on Au Surfaces: Mechanistic Aspects Regarding the Formation of Major and Minor Products. *Phys. Chem. Chem. Phys.* **2017**, *19* (24), 15856–15863. https://doi.org/10.1039/C7CP02855E.

(46) Zhao, S.; Jin, R.; Jin, R. Opportunities and Challenges in CO2 Reduction by Gold- and Silver-Based Electrocatalysts: From Bulk Metals to Nanoparticles and Atomically Precise Nanoclusters. *ACS Energy Lett.* **2018**, *3* (2), 452–462. https://doi.org/10.1021/acsenergylett.7b01104.

(47) Welch, A. J.; DuChene, J. S.; Tagliabue, G.; Davoyan, A.; Cheng, W.-H.; Atwater, H. A. Nanoporous Gold as a Highly Selective and Active Carbon Dioxide Reduction Catalyst. *ACS Appl. Energy Mater.* **2019**, *2* (1), 164–170. https://doi.org/10.1021/acsaem.8b01570.

(48) Cao, Z.; Zacate, S. B.; Sun, X.; Liu, J.; Hale, E. M.; Carson, W. P.; Tyndall, S. B.; Xu, J.; Liu, X.; Liu, X.; et al. Tuning Gold Nanoparticles with Chelating Ligands for Highly Efficient Electrocatalytic CO2 Reduction. *Angew. Chemie* **2018**, *130* (39), 12857–12861. https://doi.org/10.1002/ange.201805696.

(49) Hori, Y.; Murata, A.; Kikuchi, K.; Suzuki, S. Electrochemical Reduction of Carbon Dioxides to Carbon Monoxide at a Gold Electrode in Aqueous Potassium Hydrogen Carbonate. *J. Chem. Soc. Chem. Commun.* **1987**, No. 10, 728–729. https://doi.org/10.1039/C39870000728.

Chapter V: Summary and Perspectives

In this PhD thesis, different catalytic approaches were used to reduce the emission and presence of greenhouse gases in the environment, which at a larger scale can help to tackle the global need of reducing these gases to decrease their impact on global warming. Utilizing metallic nanoparticles or nanoparticulate structures enabled us to employ these materials as catalysts for different heterogenous catalytic reactions, involving gas-phase and electrocatalysis.

1. Porous Gold Catalysts from a Bottom-Up Approach for Oxidation Reactions

The first project focused on the selectivity of catalytic reactions, which can be found in the bulk synthesis of products in industrial applications. As an example, the focus was set on the oxidative coupling of methanol to methyl formate over a gold catalyst, which involves carbon dioxide as a side-product, depending on the selectivity of the used catalyst. We used the very simple cryogelation approach to aim for a nanoporous gold structure via a bottom-up method, which resulted in porous gold structures, also called gels. In addition, we were able to show a simple way to decorate these porous structures with different add-metals (Ag, Ce, Cu and Pd) by simply dissolving the metal salts in the colloidal gold solution followed by cryogelation of the colloidal solutions to form the gels. Depending on the add-metal, different catalytic activities and selectivities were observed, which was explained using different surface and bulk analysis techniques based on the nature of the decorated metal (as an oxide or chloride) and its environment (clustering of the add-metal or a good distribution). In the second part of this project, sodium ions were found on the surface of the pre-assumed pure gold catalyst, which allowed the formation of intermediate species (such as carbonates or formates) in its presence, leading to unexpectedly high activities for the “pure gold sample”. Its absence instead led to inactivity of the catalyst, hence underlining the necessity of the add-metal to a pure gold system to obtain a highly active catalyst for the oxidative coupling of methanol to methyl formate.

In the future, the here used synthesis method (cryogelation) can be further extended to acquire many different porous catalysts, using a diverse range of building units, varying in size, shape and composition (e.g. bimetallic particles, use of chemically different nanoparticles), to verify their activity in different catalytic reactions and investigate the dependency of the activity or selectivity of a reaction on the previously mentioned properties of the building units of the catalyst.

2. Total Pressure Effects on the Combustion of Methane on a Pd/Al_2O_3 Catalyst

In this project, a well-established palladium catalyst was used to focus on the lean oxidation of methane at elevated total pressures to reduce the emission of methane due to slips in combustion engines, which consume natural gas as a powering source. After characterizing the synthesized material on its general properties and comparing those results to published values, the powder was wash-coated on a cordierite monolith. The catalyst was investigated on its activity in an in-house built reactor set-up, analyzing different kinetic properties (light-off temperature, activation energy and reaction order) of the reaction for the dependency on temperature (350 to 450°C) and total pressures (1 to 10 atm) of the system. A clear positive impact of increased total pressures on the activity of the catalyst (light-off temperature was reduced) was visible. However, due to adsorbed surface species occurring during the reaction, the activation energies increased with increasing pressures, signaling the necessity of higher temperatures to activate the catalyst. In agreement with that, at low temperatures the reaction orders for the methane concentration seemed to decrease with increased pressures, underlining the presence of blocked active sites with increased pressures, whereas at higher temperatures the opposite results for the reaction order were recorded. These results were additionally confirmed performing experiments in the presence of water and carbon dioxide, which effected the activity and activation energies of the reaction with increasing total pressures in negatively. The experimental results were compared and confirmed by simulated results, performed in collaboration with the Chalmers University of Technology (Gothenburg, Sweden) signaling the utility of this first-principles model in future applications for a diverse range of catalysts and catalytic reactions.

To further analyze the impact of surface species on the catalyst surface during the total combustion of methane at elevated pressures, in-situ surface spectroscopy techniques, such as DRIFTs analysis, can be used to identify intermediate steps occurring on the surface. This method would result in an overall better understanding of the reaction, active sites and surface species itself.

3. Electrocatalytic Reduction of CO_2 over Copper Catalyst

The last project dealt with the electrochemical reduction of CO_2 over copper- and gold-based catalysts to form valuable carbon products. Using chemical deposition methods followed by an electrochemical in-situ reduction in the absence or presence of a gold-salt in the electrolyte, the catalyst materials were obtained. Four types of catalyst material (pure Cu, Cu with 0.9 and 1.8 at% of Au and pure Au) were studied for their morphology, composition and catalytic

activity/selectivity in CO_2 reduction. From a morphological point of view all samples containing Cu were similar, consistently showing Cu flakes made of small Cu nanoparticles giving the required porosity of the catalyst for higher surface areas and by that, a higher number of active sites. Pure Au samples on the other hand, showed dendric, ordered structures, which differed in size and shape from the Au-dendrites (made of small Au particles) formed on the bimetallic samples. The bimetallic sample containing 1.8 at% of gold was further analyzed on its composition and phase structure. Polycrystalline Cu and Au phases and phases of CuO and Cu_2O were identified to be present. Catalytic experiments at two different potentials (-0.3 and -0.4 V vs RHE) revealed a low current density for each catalyst (up to -1.5 mA cm^{-2}, while different liquid products (formate, ethanol and glycerol) were formed in small amounts during the reaction. Interestingly, the pure Au sample formed ethanol during the reaction, which was an unexpected result for this material.

The here shown results are preliminary and require further investigation and optimization of the designed catalyst and experiment. The main objective would be to use gas chromatography for the identification and quantification of the gaseous products to cover all possible formed products of the reaction. Furthermore, more general characterizations, such as surface area measurements via ECSA or ECDL and XRD-measurements, should be carried out for a better comparability of the catalyst material. In addition, the used substrate can be exchanged to a more inert one, such as porous carbon paper, to avoid influence of the substrate in the reaction (such as titanium oxide particles enhancing HER). CuO-films should be considered as a possible catalyst material, as it might increase the activity or selectivity for certain C1-C3 products.

Brief Summary of this Thesis

Introduction

Scientists worldwide agree that for a sustainable future on planet Earth, it is important to stay below the limit of a 1.5°C increase in global mean surface temperature. This value is measured relative to temperatures from when the industrial revolution started (around 1880)[1]. It is the limit from which there is no return to preindustrial values, at which consequences such as extreme weather/temperatures and climate feedback loops will increase in frequency and unpredictability[2–4]. At this point natural catastrophes are more prevalent than before, more extreme temperatures are more common[2], and ecosystems decease due to anthropogenic activities. Hence, it is not only the task of governments worldwide to take action and prevent this value from being reached but also the objective of scientists worldwide to find new technologies and methods to prevent the unpredictable from occurring.

The term greenhouse-effect derives from the function of a greenhouse: A greenhouse is usually built in countries where the temperatures are normally too cold or the weather too rainy to grow plants. The function of a greenhouse is to keep the heat coming from sunlight inside the house, as the sunlight can enter the house, while the glass or plastic walls of the house retain part of the sunlight, causing the greenhouse to warm up. The very same effect can be found on a much grander scale with the earth: In this case, greenhouse gases are capable of retaining incident sunlight within the earth's atmosphere[5] and as a result, global surface temperatures increase over time. Some of these greenhouse gases are naturally transformed and absorbed by different ecosystems, returning back into the energetic cycle, whereas other gases remain longer in atmosphere and constantly contribute to the increase in overall temperature of our atmosphere[1,5].

These gases that cause the atmosphere to heat up are called greenhouse gases and different greenhouse gases have different impacts on global warming. The most commonly known greenhouse gas is CO_2, which is principally formed during the combustion of fossil fuels. As the quantities emitted of this gas are large, it is used as a standard unit of measurement against which the global warming potential (GWP) of other gases are compared to[5]. Another important greenhouse gas is methane (CH_4) which can be found largely in the agricultural and waste management sectors. For example, the GWP of methane relative to CO_2 is around 28-36 over 100 years[5].

To remain below the indicated limit of an overall global surface temperature increase of 1.5°C, different actions can be taken using catalysis to aid in reaching this goal. One very simple and straightforward way to do so is to reduce, or better to avoid, the emission of greenhouse gases. It is no secret that burning fossil fuels has the greatest impact on the emission of greenhouse gases (CO_2 but also CH_4)[5]. Another large contribution derives from industrial processes, where CO_2 can be found as a side-product of different reactions for bulk chemical synthesis[6]. For example, the production of methyl formate can be obtained by oxidatively coupling two methanol molecules to form the final product[7,8]. One side-product obtained during this reaction is CO_2. Hence, it is required to design a catalyst in such a way, that the selectivity of the reaction is shifted towards the more desired methyl formate to reduce CO_2 emission. This reaction in particular was investigated over an unsupported gold catalyst in the first project of this thesis.

As methane has a higher GWP compared to CO_2, the emission has to be reduced drastically. In the transportation sector, where fossil fuels are used to generate energy for vehicles, the slip of uncombusted methane into the atmosphere is possible (especially when natural gas is used to power the engine)[9–11]. A catalyst in these sectors is required to reduce the methane slip by decreasing the activation energy of the combustion reaction and obtain the less harmful CO_2[5]. This parameter was studied in the second project of this thesis, where the total pressure and temperature influence of the methane combustion was examined over a palladium catalyst.

Another method is to capture the CO_2 formed during industrial processes and use it as a carbon source to synthesize useful chemicals, which can be used again as a fuel or to further obtain fine chemicals[12–14]. On the condition green energy (energy which does not emit CO_2) is used to power the reaction, a closed circle of CO_2 capture and emission can be obtained[12]. The third and last project tries to tackle this task by electrochemically reducing CO_2 over a copper and gold catalysts to form C1 (hydrocarbon containing one carbon atom) to C3 (hydrocarbon containing three carbon atoms) hydrocarbons over copper and gold catalysts. The following scheme shows the relations between the three different projects, which close the circle of CO_2 production and consumption by catalytic oxidation and reduction reactions over different metal catalysts using heterogeneous catalysis (gas-phase and electrocatalysis).

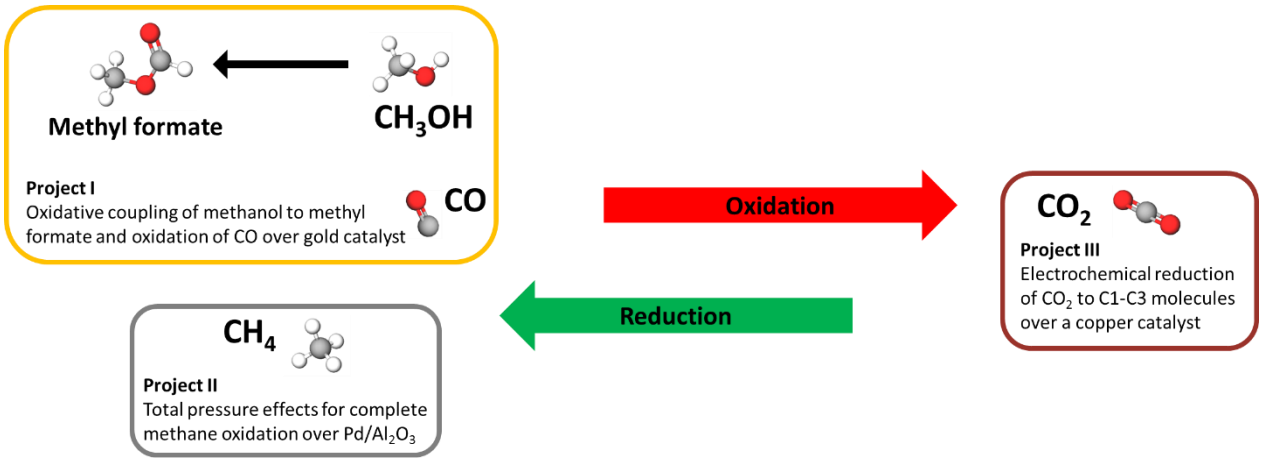

Figure 5.1 Summary and relation of the three topics of heterogenous catalysis investigated in this thesis.

In this PhD thesis, different catalytic approaches were used to reduce the emission and presence of greenhouse gases in the environment, which at a larger scale can help to tackle the global need of reducing these gases to decrease their impact on global warming. Using metallic nanoparticles or nanoparticulate structures enabled us to use these materials as catalysts for different heterogenous catalytic reactions, involving gas-phase and electrocatalysis. Finally, reduction and oxidation reactions with these catalysts can be used to close the carbon cycle and result in a final net-zero carbon emission.

Project I: Porous Gold Catalysts from a Bottom-Up Approach for Oxidation Reactions

The capability of gold to catalyze oxidative reactions has led to an increasing interest in gold (Au) catalysts, which has resulted in the development of new nanostructured materials in the past years[15]. One material established in the last few decades is the so-called nanoporous gold (NPG). This material is synthesized by the chemical or electrochemical etching of gold-alloys that were a priori formed with different miscible metals. The so obtained porous structure with small ligament sizes, capable of holding metal traces from the dealloying process, is able to catalyze different reactions with enhanced activities at low temperatures compared to corresponding supported catalysts[16,17]. One reaction of interest is the oxidative methanol coupling in gas phase over gold catalysts, in which two methanol molecules are coupled by using oxygen over the gold surface[18].

The initiating step of the oxidative methanol coupling is the adsorption of oxygen on the catalyst surface followed by the formation of methoxy groups from the methanol feed and the simultaneous condensation of water. The rate-limiting step in this reaction is considered to be the β-H-

elimination of the methoxy-group to form formaldehyde. This formaldehyde can undergo two different reaction paths: Firstly, a formaldehyde molecule can react with other methoxy-species to become a hemiacetal alcoholate on the surface which finally desorbs to form the products methyl formate and water. Secondly, the formaldehyde can be further oxidized on the surface to formate which finally combusts to carbon dioxide and water. This step occurs in the presence of higher oxygen concentrations in which CO_2 is an undesirable side-product[18]. Related to this, the selectivity for the coupling products appears to decrease with increasing metal trace content[8]. Controversially to these results, in the works of Lackmann et al.[19] low coordinated surface sites of gold were identified to be active for the coupling of methanol.

Despite these fascinating catalytic functions, the synthesis method of these materials has many drawbacks, such as the limitation of the chemical composition of the final product or the restriction of control over pore sizes. Furthermore, no published works can explain if actual pure nanoporous structures are able to catalyze the reaction to prove if the metal traces in the NPG synthesized by the top-bottom approach play a crucial role in the oxidative methanol coupling reaction. In addition, the reproducibility of this approach is not high, as the starting point of the alloy is not always homogenous and the formation of clusters during the dealloying process[20] leads to a poor distribution of the metal traces. For these reasons, the development of a new method for the synthesis of nanoporous structures is desirable, which allows for the choice of composition and amount of metal trace in the system, permitting these effects on the activity to be investigated in detail.

In our work we chose a bottom-up approach to tackle this challenge, exploiting the self-assembly of nanoscale units (i.e. metallic nanoparticles) through the cryogelation method[21] to synthesize nanoporous materials. Freytag et al. showed in their work a simple method to build 3D disordered porous structures (i.e. cryogels) by freeze-drying of different metallic nanoparticles (NPs)[21]. The aim of this work was thus to obtain nanoporous metal structures with morphologically and chemically controlled properties as the building units, which is not achievable through the more established dealloying process. With this approach, the role of the metal traces in the oxidative methanol coupling will be studied and clarified in further detail.

After obtaining porous gold catalysts by the aforementioned bottom-up method, their activity for carbon monoxide oxidation and selective oxidative coupling of methanol was investigated. In addition, we were able to show a simple way to decorate these porous structures with different add-

metals (Ag, Ce, Cu and Pd) by adding the metal salts to the colloidal gold solution used during the cryogelation to obtain the gels. Depending on the add-metal, different catalytic activities and selectivities were observed, which was explained using different surface and bulk analysis techniques, by the nature of the decorated metal (as an oxide of chloride) and its environment (clustering of the add-metal or well distribution). In the second part of this project, sodium ions were found on the surface of the pre-assumed pure gold catalyst, which allowed the formation of intermediate species (such as carbonates or formates) in its presence, leading to unexpectedly high activities for the "pure gold sample". Its absence instead led to inactivity of the catalyst, hence underlining the necessity of the add-metal to a pure gold system to obtain a highly active catalyst for the oxidative coupling of methanol to methyl formate.

Project II: Total Pressure Effects on the Combustion of Methane over a Pd/Al_2O_3 Catalyst

Our atmosphere is composed of 78% nitrogen, 21% oxygen, 0.9% argon, 0.04% carbon dioxide and diverse other gases[22]. One of these gases in the atmosphere is known to be methane, which can be anthropologically difficult to capture once emitted and hence requires the restriction of its emission in the first place. The main emissions of methane can be found in agriculture, in oil and gas extraction, in waste treatment and the combustion of fuel[5]. There is a necessity to reduce the emission of methane in all these sectors, whereas the focus in this chapter is set to the fuel combustion (such as natural gas combustion engines) itself. Either the usage of an alternative engine (such as electromobility) would be required or the catalytic combustion in combustion engines needs to be improved.

Methane is the main component in natural gas and has a higher hydrogen-to-carbon ratio compared to diesel and gasoline. However, combustion engines using natural gas are prone to have a slip of uncombusted fuel and it is essential that any methane is removed before the exhaust is released into the atmosphere since methane is a highly potent greenhouse gas[5]. The removal is commonly performed by catalytic converters where total combustion of methane is generally achieved over supported palladium based catalysts[23].

To identify highly active methane oxidation catalysts, most published experiments have been performed at atmospheric total pressures. Under these conditions, the catalysts still require high temperatures or high precious metal loadings to perform with high rates[24,25], while it is known that elevated total pressures can favor catalytic reactions at lower temperatures[26,27]. One reason for the poorer performance of methane oxidation catalysts at lower temperatures is the formation of

hydroxyl, carbonate and bicarbonate surface species. These species originate from the reaction itself and can block active sites of the catalyst, which can require increased temperatures to make these sites accessible for the reaction again[28]. The lean methane oxidation at low temperatures is relevant for vehicle exhaust after-treatment systems, which in combination with elevated total pressures is a rather poorly studied area in the literature.

The aim of this work was to study the influence of elevated total pressures on the activity of the commercially used catalyst in the conversion of methane to carbon dioxide. To do so, the catalyst was synthesized according to already established methods, to obtain a by now acknowledged catalyst for the reaction. In this study, different variables of a chemical reaction, such as light-off temperatures, activation energies and reaction orders, were investigated independently to different pressures and temperatures to understand the relation between those variables from reaction conditions. Furthermore, in collaboration with a PhD student from the Chalmers University of Technology (Gothenburg, Sweden), the results were compared to modelled values to evaluate the applicability of the model in future works.

After characterizing the synthesized material on its general properties and comparing those results to published values, we used the powder to wash-coat a cordierite monolith with it. The catalyst was investigated for its activity in an in-house built reactor set-up, analyzing different kinetic properties (light-off temperature, activation energy and reaction order) of the reaction for their dependency on temperature (350 to 450°C) and total pressures (1 to 10 atm) of the system. A clear positive impact of increased total pressures on the activity of the catalyst (light-off temperature was reduced) was visible. However, due to adsorbed surface species occurring during the reaction, the activation energies increased with increasing pressures, signaling the necessity of higher temperatures to activate the catalyst. In agreement with that, at low temperatures the reaction orders for the methane concentration seemed to decrease with increased pressures, underlining the presence of blocked active sites with increased pressures, whereas at higher temperatures opposite results for the reaction order were recorded. These results were additionally confirmed when performing experiments in the presence of water and carbon dioxide, which affected the activity and activation energies of the reaction with increasing total pressures in a negative manner. The experimental results were compared and confirmed by simulated results, performed in collaboration with the Chalmers University of Technology (Gothenburg, Sweden) signaling the

utility of this first-principle model in future applications for a diverse range of catalysts and catalytic reactions.

Project III: Electrocatalytic Reduction of CO_2 over Copper Catalyst

The reduction of CO_2 in the environment is crucial and can either be achieved via the reduction of emissions in fields where fossil-fuels are used in large quantities or via capturing the emitted CO_2. A method of processing captured CO_2 can be the electrochemical reduction of CO_2. This process involves the CO_2 being present in an electrolyte allowing a catalyst at the cathode, which once a potential is applied, to reduce the CO_2 into a diverse range of gaseous and liquid chemical compounds. These products can contain one to three carbon atoms (C1-C3), which then can be used in bulk chemical but also fuel related applications. However, it is crucial to consider green energy (from solar energy or wind power) as a powering source to guarantee a carbon budget with a zero net-emission of CO_2. Once the chemicals or fuels are obtained, they can be utilized, producing CO_2 as an end- or side-product, which can be brought back into the carbon circle after capturing it from the atmosphere or directly leading the side-product of the process to an on-plant electrochemical cell. By this, an indefinite recycling of CO_2 can be carried out allowing for net-zero emissions which can contribute to the regulation of CO_2 concentrations in the atmosphere.

Recent research studies on the electrochemical reduction of CO_2 are based on the usage of different transition metal catalysts[29] as a working electrode material, of which copper has been utilized since works of Hori et al.[30] for the high activities and controllable selectivities of the formed products. Most of the time, the Cu was used as nanoparticles (NPs) or as nanosized materials deposited on a substrate, enabling a large surface area and high porosities, which are correlated to a high number of active sites and with this also enhanced activities. In a study of Wang et al.[31] the high porosity of the Cu electrode materials was associated with the suppression of the competing hydrogen evolution reaction (HER). The study showed hydrogen evolution was decreased whereas the reduction of carbon monoxide (CO, a known intermediate/final product of the CO_2 reduction[32]) could be increased. In addition, alloys of copper (with silver[33] or gold[12,34]) have proved to enhance the activity but also the selectivity of the catalyst. In these materials, the silver/gold surface allows the reduction of CO_2 to CO molecules, which are subsequently spilled over to the copper surface during a simultaneous charge transfer from copper to silver/gold at the interface of the domains. This results in the sequential adsorption of the CO molecules onto the copper surface and finally leading to the coupling of these molecules to form hydrocarbons of two to three carbon atoms.

Taking this state-of-the-art knowledge into account, a simple yet effective chemical deposition approach coupled with an in-situ electrochemical reduction was used to prepare a diverse range of porous copper materials deposited on a titanium substrate. The prepared samples compositionally ranged from pure Cu, over a combination of Cu and small amounts of Au, to pure Au. All samples were produced using the in-situ reduction method to have similar morphological structures to compare. The addition of Au to Cu-systems was chosen to identify how the interface of both domains can affect the activity and selectivity for the CO_2 reduction. The added amount of Au to the system was kept in a small range, as studies of Morales-Guio et al.[12] showed that lower Au contents on a Cu surface can reduce sintering. Consequently, more Au-Cu interfaces can be accessible, which are known to be active. In addition to the bimetallic systems, pure Cu and Au samples prepared by the same technique were compared. The here chosen experimental method possesses the ability of structuring the catalyst surface with a high level of porosity[35], allowing a higher number of active sites on the catalyst surface and increasing the selectivity towards CO_2 reduction as shown by Wang et al.[31]

Four types of catalyst material (pure Cu, Cu with 0.9 and 1.8 at% of Au and pure Au) were studied on their morphology, composition and catalytic activity/selectivity in CO_2 reduction. From a morphologic point of view all samples containing Cu were similar, consistently showing Cu flakes made of small Cu nanoparticles giving the required porosity of the catalyst for higher surface areas and by that a higher number of active sites. On the other hand, pure Au samples showed dendric, ordered structures, which differed in size and shape from the Au-dendrites (made of small Au particles) formed on the bimetallic samples. The bimetallic sample containing 1.8 at% of gold was further analyzed on its composition and phase structure. Polycrystalline Cu and Au phases and phases of CuO and Cu_2O were identified to be present. Catalytic experiments at two different potentials (-0.3 and -0.4 V vs RHE) revealed a low current density for each catalyst (up to -1.5 mA cm^{-2}), while different products (formate, ethanol and glycerol) were formed in small amounts during the reaction. Interestingly, the pure Au sample formed ethanol during the reaction, which was an unexpected result for this material. The presented results are preliminary and require further investigation and optimization on behalf of the catalysts and experimental procedure.

References

(1) NASA. GISS Surface Temperature Analysis (GISTEMP v4) https://data.giss.nasa.gov/gistemp/ (accessed Apr 6, 2020).

(2) Power, S. B.; Delage, F. P. D. Setting and Smashing Extreme Temperature Records over the Coming Century. *Nat. Clim. Chang.* **2019**, *9* (7), 529–534. https://doi.org/10.1038/s41558-019-0498-5.

(3) Jones, N. The Polar Bear Struggle. *Nat. Clim. Chang.* **2011**, *1* (9), 433. https://doi.org/10.1038/nclimate1306.

(4) McClanahan, T. R.; Darling, E. S.; Maina, J. M.; Muthiga, N. A.; 'agata, S. D.; Jupiter, S. D.; Arthur, R.; Wilson, S. K.; Mangubhai, S.; Nand, Y.; et al. Temperature Patterns and Mechanisms Influencing Coral Bleaching during the 2016 El Niño. *Nat. Clim. Chang.* **2019**. https://doi.org/10.1038/s41558-019-0576-8.

(5) United States Environmental Protection Agency. Overview of Greenhouse Gases https://www.epa.gov/ghgemissions/overview-greenhouse-gases#main-content (accessed Oct 10, 2019).

(6) Speight, J. G.; Speight, J. G. Hydrocarbons from Synthesis Gas. *Handb. Ind. Hydrocarb. Process.* **2011**, 281–323. https://doi.org/10.1016/B978-0-7506-8632-7.10008-8.

(7) Rao, V. M.; Shankar, V. High Activity Copper Catalyst for One-Step Conversion of Methanol to Methyl Formate at Low Temperature. *J. Chem. Technol. Biotechnol.* **1988**, *42* (3), 183–196. https://doi.org/10.1002/jctb.280420303.

(8) Wittstock, A.; Zielasek, V.; Biener, J.; Friend, C. M.; Bäumer, M. Nanoporous Gold Catalysts for Selective Gas-Phase Oxidative Coupling of Methanol at Low Temperature. *Science (80-.).* **2010**, *327* (5963), 319 LP – 322. https://doi.org/10.1126/science.1183591.

(9) Thakur, P.; Thakur, P. Diesel Exhaust Control. *Adv. Mine Vent.* **2019**, 157–187. https://doi.org/10.1016/B978-0-08-100457-9.00011-0.

(10) Schlatter, J. C.; Taylor, K. C. Platinum and Palladium Addition to Supported Rhodium Catalysts for Automotive Emission Control. *J. Catal.* **1977**, *49* (1), 42–50. https://doi.org/10.1016/0021-9517(77)90238-X.

(11) Cohn, J. G. Catalytic Converters for Exhaust Emission Control of Commercial Equipment Powered by Internal Combustion Engines. *Environ. Health Perspect.* **1975**, *10*, 159–164. https://doi.org/10.1289/ehp.7510159.

(12) Morales-Guio, C. G.; Cave, E. R.; Nitopi, S. A.; Feaster, J. T.; Wang, L.; Kuhl, K. P.; Jackson, A.; Johnson, N. C.; Abram, D. N.; Hatsukade, T.; et al. Improved CO2 Reduction Activity towards C2+ Alcohols on a Tandem Gold on Copper Electrocatalyst. *Nat. Catal.* **2018**, *1* (10), 764–771. https://doi.org/10.1038/s41929-018-0139-9.

(13) Clark, E. L.; Hahn, C.; Jaramillo, T. F.; Bell, A. T. Electrochemical CO2 Reduction over Compressively Strained CuAg Surface Alloys with Enhanced Multi-Carbon Oxygenate Selectivity. *J. Am. Chem. Soc.* **2017**, *139* (44), 15848–15857. https://doi.org/10.1021/jacs.7b08607.

(14) Zhuang, T.-T.; Pang, Y.; Liang, Z.-Q.; Wang, Z.; Li, Y.; Tan, C.-S.; Li, J.; Dinh, C. T.; De Luna, P.; Hsieh, P.-L.; et al. Copper Nanocavities Confine Intermediates for Efficient Electrosynthesis of C3 Alcohol Fuels from Carbon Monoxide. *Nat. Catal.* **2018**, *1* (12), 946–951. https://doi.org/10.1038/s41929-018-0168-4.

(15) Personick, M. L.; Madix, R. J.; Friend, C. M. Selective Oxygen-Assisted Reactions of Alcohols and Amines Catalyzed by Metallic Gold: Paradigms for the Design of Catalytic Processes. *ACS Catal.* **2017**, *7* (2), 965–985. https://doi.org/10.1021/acscatal.6b02693.

(16) Qiu, H.-J.; Xu, H.-T.; Liu, L.; Wang, Y. Correlation of the Structure and Applications of Dealloyed Nanoporous Metals in Catalysis and Energy Conversion/Storage. *Nanoscale* **2015**, *7* (2), 386–400. https://doi.org/10.1039/C4NR05778C.

(17) Erlebacher, J.; Aziz, M. J.; Karma, A.; Dimitrov, N.; Sieradzki, K. Evolution of Nanoporosity in Dealloying. *Nature* **2001**, *410* (6827), 450–453. https://doi.org/10.1038/35068529.

(18) Xu, B.; Haubrich, J.; Freyschlag, C. G.; Madix, R. J.; Friend, C. M. Oxygen-Assisted Cross-Coupling of Methanol with Alkyl Alcohols on Metallic Gold. *Chem. Sci.* **2010**, *1* (3), 310–314. https://doi.org/10.1039/C0SC00214C.

(19) Lackmann, A.; Mahr, C.; Schowalter, M.; Fitzek, L.; Weissmüller, J.; Rosenauer, A.; Wittstock, A. A Comparative Study of Alcohol Oxidation over Nanoporous Gold in Gas and Liquid Phase. *J. Catal.* **2017**, *353*, 99–106. https://doi.org/10.1016/J.JCAT.2017.07.008.

(20) Mahr, C.; Kundu, P.; Lackmann, A.; Zanaga, D.; Thiel, K.; Schowalter, M.; Schwan, M.; Bals, S.; Wittstock, A.; Rosenauer, A. Quantitative Determination of Residual Silver Distribution in Nanoporous Gold and Its Influence on Structure and Catalytic Performance. *J. Catal.* **2017**, *352*, 52–58. https://doi.org/10.1016/J.JCAT.2017.05.002.

(21) Freytag, A.; Sánchez-Paradinas, S.; Naskar, S.; Wendt, N.; Colombo, M.; Pugliese, G.; Poppe, J.; Demirci, C.; Kretschmer, I.; Bahnemann, D. W.; et al. Versatile Aerogel Fabrication by Freezing and Subsequent Freeze-Drying of Colloidal Nanoparticle Solutions. *Angew. Chemie - Int. Ed.* **2016**, *55* (3). https://doi.org/10.1002/anie.201508972.

(22) Bleam, W.; Bleam, W. Acid-Base Chemistry. *Soil Environ. Chem.* **2017**, 253–331. https://doi.org/10.1016/B978-0-12-804178-9.00006-9.

(23) Gélin, P.; Primet, M. Complete Oxidation of Methane at Low Temperature over Noble Metal Based Catalysts: A Review. *Appl. Catal. B Environ.* **2002**, *39* (1), 1–37. https://doi.org/10.1016/S0926-3373(02)00076-0.

(24) Thevenin, P. O.; Pocoroba, E.; Pettersson, L. J.; Karhu, H.; Väyrynen, I. J.; Järås, S. G. Characterization and Activity of Supported Palladium Combustion Catalysts. *J. Catal.* **2002**, *207* (1), 139–149. https://doi.org/10.1006/JCAT.2002.3515.

(25) Epling, W. S.; Hoflund, G. B. Catalytic Oxidation of Methane over ZrO2-Supported Pd Catalysts. *J. Catal.* **1999**, *182* (1), 5–12. https://doi.org/10.1006/JCAT.1998.2341.

(26) Hartadi, Y.; Widmann, D.; Behm, R. J. Methanol Formation by CO2 Hydrogenation on Au/ZnO Catalysts – Effect of Total Pressure and Influence of CO on the Reaction Characteristics. *J. Catal.* **2016**, *333*, 238–250. https://doi.org/10.1016/J.JCAT.2015.11.002.

(27) Appl, M. Ammonia, 2. Production Processes. *Ullmann's Encyclopedia of Industrial Chemistry*. October 15, 2011. https://doi.org/doi:10.1002/14356007.o02_o11.

(28) Willis, J. J.; Gallo, A.; Sokaras, D.; Aljama, H.; Nowak, S. H.; Goodman, E. D.; Wu, L.; Tassone, C. J.; Jaramillo, T. F.; Abild-Pedersen, F.; et al. Systematic Structure–Property

Relationship Studies in Palladium-Catalyzed Methane Complete Combustion. *ACS Catal.* **2017**, *7* (11), 7810–7821. https://doi.org/10.1021/acscatal.7b02414.

(29) Kuhl, K. P.; Hatsukade, T.; Cave, E. R.; Abram, D. N.; Kibsgaard, J.; Jaramillo, T. F. Electrocatalytic Conversion of Carbon Dioxide to Methane and Methanol on Transition Metal Surfaces. *J. Am. Chem. Soc.* **2014**, *136* (40), 14107–14113. https://doi.org/10.1021/ja505791r.

(30) Hori, Y.; Kikuchi, K.; Suzuki, S. PRODUCTION OF CO AND CH4 IN ELECTROCHEMICAL REDUCTION OF CO2 AT METAL ELECTRODES IN AQUEOUS HYDROGENCARBONATE SOLUTION. *Chem. Lett.* **1985**, *14* (11), 1695–1698. https://doi.org/10.1246/cl.1985.1695.

(31) Wang, L.; Nitopi, S.; Wong, A. B.; Snider, J. L.; Nielander, A. C.; Morales-Guio, C. G.; Orazov, M.; Higgins, D. C.; Hahn, C.; Jaramillo, T. F. Electrochemically Converting Carbon Monoxide to Liquid Fuels by Directing Selectivity with Electrode Surface Area. *Nat. Catal.* **2019**, *2* (8), 702–708. https://doi.org/10.1038/s41929-019-0301-z.

(32) Hori, Y. Electrochemical CO2 Reduction on Metal Electrodes BT - Modern Aspects of Electrochemistry; Vayenas, C. G., White, R. E., Gamboa-Aldeco, M. E., Eds.; Springer New York: New York, NY, 2008; pp 89–189. https://doi.org/10.1007/978-0-387-49489-0_3.

(33) Huang, J.; Mensi, M.; Oveisi, E.; Mantella, V.; Buonsanti, R. Structural Sensitivities in Bimetallic Catalysts for Electrochemical CO2 Reduction Revealed by Ag–Cu Nanodimers. *J. Am. Chem. Soc.* **2019**, *141* (6), 2490–2499. https://doi.org/10.1021/jacs.8b12381.

(34) Tao, Z.; Wu, Z.; Yuan, X.; Wu, Y.; Wang, H. Copper–Gold Interactions Enhancing Formate Production from Electrochemical CO2 Reduction. *ACS Catal.* **2019**, 10894–10898. https://doi.org/10.1021/acscatal.9b03158.

(35) Shinde, D. V; Dang, Z.; Petralanda, U.; Palei, M.; Wang, M.; Prato, M.; Cavalli, A.; De Trizio, L.; Manna, L. In Situ Dynamic Nanostructuring of the Cu–Ti Catalyst-Support System Promotes Hydrogen Evolution under Alkaline Conditions. *ACS Appl. Mater. Interfaces* **2018**, *10* (35), 29583–29592. https://doi.org/10.1021/acsami.8b09493.

List of Figures

Chapter I

Chapter IIA

Figure 2A.11 AuCe-gel synthesized according second approach before (left) and after (right) catalytic tests (at 300°C for 1 h in 1 vol-% CO and 10 vol-% O_2 atmosphere).

Figure 2A.12 AuAg-gel synthesized according second approach before (left) and after (right) catalytic tests (at 300°C for 1 h in 1 vol-% CO and 10 vol-% O_2 atmosphere).

Figure 2A.13 AuPd-gel synthesized according second approach before (left) and after (right) catalytic tests (at 300°C for 1 h in 1 vol-% CO and 10 vol-% O_2 atmosphere).

Figure 2A.14 Semi-Quantitative XPS-investigations on oxidation state before (top) and after (bottom) reaction conditions (at 300°C for 1 h in 1 vol-% CO and 10 vol-% O_2 atmosphere, followed by oxidative methanol coupling at 200°C for 1 h in 2.3 vol-% MeOH and 1.15 vol% O_2).

Figure 2A.15 HRSEM-EDX image on AuAg-gel before reaction conditions; left: Image used for mapping, right: Mapping with Au, Ag, Cl and Na.

Figure 2A.16 SEM-image of AgCl-crystals on the gel before reaction conditions.

Figure 2A.17 HAADF-STEM-EDX image on AuCu-gel (left) and the correlated mapping of Au (center) and Cu (right) before reaction conditions.

Figure 2A.18 HAADF-STEM-EDX image on AuCu-gel (left) and the correlated mapping of Au, Ce and O (center) and overlayed mapping (right) after reaction conditions (at 300°C for 1 h in 1 vol-% CO and 10 vol-% O_2 atmosphere).

Figure 2A.19 HRSEM-EDX image on AuPd-gel before reaction conditions; left: Image used for mapping, right: Mapping with Au, Pd, O and Cl.

Figure 2A.20 CO-oxidation: Comparison on catalytic activity for all synthesized gels. The used sample weight in each case was 20 mg.

Figure 2A.21 CO-oxidation: Comparison on catalytic activity for AuCe-gel after two identical cycles.

Figure 2A.22 Comparison of all catalyst for oxidative coupling of methanol; Left: Comparison on reaction rate, Right: Comparison on selectivity towards methyl formate.

Figure 2A.23 Vapor pressure of methanol in relation to the temperature calculated by using the ANTOINE equation.

Figure 2A.24 Used calibration curves for the concentration determination of methanol, methyl formate and CO_2 during the oxidative methanol coupling.

Figure 2A.25 XRD diffraction peaks for all samples before (blue line) and after (red line) activity tests compared to bulk Au diffraction pattern (black vertical lines, reference code: ICDD 96-901-1613). Sequence of samples from top to bottom: Au-gel, AuAg-gel, AuCe-gel, AuCu-gel and AuPd-gel.

Figure 2A.26 Kr isotherms of all gels after catalytic tests (left) and corresponding BET-plots (right) with obtained specific surface areas implemented in legend.

Chapter IIB

Figure 2B.1 Scheme of gel synthesis: First, the synthesis of Au NPs by citrate reduction method, then the concentration of nanoparticle solution followed by cryogelation to obtain self-standing nanoporous structures by Au NPs containing Na-ions. As a second step: washing and subsequent redecoration of samples with different Na-salts.

Figure 2B.2 Macroscopic (a, e) and microscopic (b-d, f-h) images of gels before (a-d) and after (e-h) exposure to catalytic conditions.

Figure 2B.3 Conversion of carbon monoxide on a fresh Au-gel sample. The reaction rate at 300°C is 0.001 $mmol_{CO}\ s^{-1}\ g_{cat}^{-1}$.

Figure 2B.4 Reaction rate normalized on mass (left) and selectivity towards methyl formate (right) for the oxidative coupling of methanol to methyl formate. The different curves indicate differently treated samples: A fresh sample (black line), a washed sample (**black dashed line**), a NaCl drop-cast sample (**green line**), repetitively NaOH drop-cast sample (**grey line and dashed grey line**) and a Na-citrate drop-cast sample (**cyan line**). All drop-castings were carried out after washing the sample thoroughly with 100 mL Milli-Q water.

Figure 2B.5 Data on Na 1s peak (left), C 1s peak (centre) and Au 4f peak (right) for fresh sample bct, washed sample act, NaOH drop-cast sample bct and NaOH drop-cast sample act. For above spectra the C1s peak was aligned for all samples to the value 284.8 eV.

Figure 2B.6 Isotherms obtained by Kr-adsorption for a sample before (blank points) and after (filled points) activity tests.

Figure 2B.7 BET-isotherms for the sample before (left) and after (right) activity tests.

Figure 2B.8 XRD diffraction peaks for sample before (blue line) and after (red line) activity tests compared to bulk Au diffraction pattern (black vertical lines, reference code: ICDD 96-901-1613).

Figure 2B.9 XRD diffraction peaks for sample (black line) and $NaAu_2$ pattern from database (red vertical lines, reference code: ICDD 96-151-0444).

Figure 2B.10 Transient data of samples: fresh sample, washed sample and drop-cast with NaCl, respectively

Figure 2B.11 Transient data of samples: drop-cast with Na-citrate, drop-cast 1^{st} time with NaOH and drop-cast 2^{nd} time with NaOH, respectively.

Figure 2B.12 Mapping of Au-gel before activity tests and mapped elements (Au, C, Cl and Na).

Figure 2B.13 EDX-spectrum of sample before activity tests with indicated Na profile.

Figure 2B.14 EDX-spectrum of sample before activity tests with indicated Cl profile.

Figure 2B.15 Mapping of Au after activity tests and mapped elements (Au, C, Cl and Na).

Figure 2B.16 EDX-spectrum of sample after activity tests with indicated Na profile.

Figure 2B.17 EDX-spectrum of sample after activity tests with indicated Cl profile.

Figure 2B.18 XPS-spectra of all samples normalized on Au 4f signal.

Figure 2B.19 Timeline on experiments (XPS, oxidative methanol coupling, washing and drop-casting with NaOH) performed on the sample.

Chapter III

Figure 3.1 Sources of methane in different industrial fields and its conversion over a Pd/Al_2O_3 catalyst in presence of oxygen to CO_2 and water.

Figure 3.2 Process of catalyst synthesis for the so-called "wetness incipient impregnation" method using Pd precursor and Al_2O_3 for final deposition on a cordierite substrate.

Figure 3.3 Schematic description of the experimental setup for experiments at elevated total pressures up to 10 atm.

Figure 3.4 The Arrhenius-plot: After plotting the logarithm of the reaction rate constant against the reciprocal temperature, the activation energy of the reaction can be obtained from the slope of the linear regression.

Figure 3.5 Left: Comparison of TPReaction experiments for lean methane oxidation (1000 ppm CH_4 and 2 vol-% O_2) at various total pressures (1, 2, 3, 4 and 10 atm); Right: Corresponding simplified Arrhenius-plots.

Figure 3.6 Comparison of experimental TPReaction experiments (solid lines) and modelled TPReaction experiments (dotted lines) for lean methane oxidation (1000 ppm CH_4 and 2 vol-% O_2) at various total pressures (1, 2, 3, 4 and 10 atm).

Figure 3.7 Left: Comparison of TPReaction experiments for lean methane oxidation (1000 ppm CH_4 and 2 vol-% O_2) at 1 (black lines) and 4 atm (blue lines) before (solid lines) and after (dashed lines) the degreening; Right: Corresponding simplified Arrhenius-plots.

Figure 3.8 Left: Comparison of TPReaction experiments for lean methane oxidation (1000 ppm CH_4 and 2 vol-% O_2) at 1 (black lines) and 4 atm (red lines) in absence of CO_2 (solid lines) and presence of CO_2 (dashed lines); Right: Corresponding simplified Arrhenius-plots.

Figure 3.9 Experimental reaction orders for lean methane oxidation (400-1600 ppm CH_4 and 2 vol-% O_2) at 350°C (upper left), 400°C (upper right) and 450°C (bottom) and 1 (blue), 2 (red), 3 (purple) and 4 (yellow) atm.

Figure 3.10 Arrhenius-plot of TPReaction experiment for lean methane oxidation (1000 ppm CH_4 and 2 vol-% O_2) at 1 atm total pressure with indicated linear regression (red line) performed in the range of 5-10% conversion.

Figure 3.11 The Weisz-modulus (Φ) simulated at varying temperatures and pressures. Internal mass transport effects the experimental reaction whenever the Weisz-modulus close to or above 1.

Figure 3.12 Coverage of hydroxyl (OH), water (H_2O), bicarbonate (HCO_3) and hydrogen (H) in the monolith at 350 (left column), 400 (middle column) and 450°C (right column) and 1(blue), 2

(red), 3 (purple), 4 (yellow) and 10 (black) atm. All reported surface species, except hydrogen, are adsorbed on the palladium atom (S_1(Pd)) while hydrogen is adsorbed on the oxygen atom (S_2(O)).

Chapter IV

Figure 4.1 Illustration of a carbon neutral cycle involving green energy to power electrocatalytic reduction of CO_2 to form fuels for combustion to form CO_2 and close the cycle.

Figure 4.2 Schematic description of the sample preparation. First the chemical solution deposition (upper part) followed by the electrochemical in-situ reduction to obtain pure Cu, pure Au and different Cu:Au ratio samples.

Figure 4.3 Schematic description of the used electrochemical two compartment cell for the electrochemical reduction of CO_2.

Figure 4.4 HR-SEM images of each sample (upper left: pure Cu, upper right: CuAu 0.9 at%, lower left: CuAu 1.8 at%, lower right: pure Au) with embedded higher magnification images.

Figure 4.5 HR-SEM EDX on Cu 1.8 at% Au sample. Image of Au-dendrite on Cu sheets (left) and mapping of Cu and Au (centre) with overlapped mapping (right) (all scale bars in 1 µm).

Figure 4.6 STEM-EDX mapping of CuAu 1.8 at% sample (all scale bars in 100 nm) with atomic ratios (right bottom).

Figure 4.7 STEM dark field image (left) and HR-TEM image (centre). Yellow rectangle in HR-TEM image shows presence of Au (110) phases (right, bottom) for CuAu 1.8 at% sample. Other parts of Au clusters give polycrtysalline structures as seen in diffraction pattern (right, top).

Figure 4.8 Diffracttion rings obtained via HR-TEM for CuAu 1.8 at% sample. Left: Diffraction rings for Cu and Au (corresponding to a large thick aggregate of several microns); Right: Diffraction rings of Cu, CuO and Cu_2O (corresponding to smaller aggregates and edges).

Figure 4.9 Chronoamperometric measurements for CO_2 reduction in presence of 0.1 M $KHCO_3$ at -0.3 (black dots) and -0.4 V vs RHE (red dots) for pure Cu (upper left), CuAu 0.9 at% (upper right), CuAu 1.8 at% (lower left) and pure Au sample (lower right).

Figure 4.10 Faradaic efficiencies for all quantified products (formate, glycerol and ethanol) obtained by the samples (pure Cu, CuAu 0.9 at%, CuAu 1.8 at% and pure Au) at -0.3 V and -0.4 V. All potentials vs RHE.

Figure 4.11 CVs of samples (pure Cu upper left, CuAu 0.9 at% upper right, CuAu 1.8 at% lower left, pure Au lower right) prior to each measurement performed in Ar (black dots) and in CO_2 (red dots).

Figure 4.12 NMR spectra of the control experiment at -0.4 V vs RHE, pure Au sample at -0.3 V vs RHE, CuAu 0.9 at% at -0.3 V vs RHE and a sample spiked with authentic material (formic acid, ethanol and glycerol) from top to bottom, respectively.

Figure 4.13 HR-SEM images of Au deposited on carbon-paper with a low concentrated precursor solution (left, 100 µL) and high concentrated precursor solution (right, 1300 µL).

Brief Summary of this Thesis

Figure 5.1 Summary and relation of the three topics of heterogenous catalysis investigated in this thesis.

List of Tables

Chapter IIA

Chapter IIB

Chapter IV

Acknowledgements

Writing these final lines of my thesis, I think back to the time when I was so certain of never starting a PhD. Yet I am here at this institute, away from my home country of Germany, in this beautiful country of Italy, which I called home now for three years. For sure it has not been easy to leave home, family and friends to commit to a three-year experience abroad, which made me reach my limits at times yet has given me so many experiences in return. This and so much more would have never been possible if not for the key people involved in my life, and I am grateful for everything professional and personal I learned in these years.

The first person to thank is my supervisor, PI and the reason I joined the group, Prof. Liberato Manna, for giving me this opportunity to work and share the knowledge in this international group of professional co-workers within a high-class laboratory. Deciding to leave Germany and starting a career in his group made me believe in myself for all the scientific works I was performing and opened the door of academia which I was not even considering before I arrived here. Thank you, Libero, for this great impact on my future career and life.

Next, I would like to thank Dr. Massimo Colombo, for teaching me all the knowledge I had missed out on during my undergrad studies and shaping me professionally. Thank you for this great experience and all the knowledge you shared with me.

I would like to thank Dr. Dipak Shinde, for being such a great and patient teacher, when I was just starting my last project in the half year before the submission of my thesis. Electrocatalysis, I thought, would be so complicated and practically impossible to learn in such a short period of time. Yet you showed me with mountains of patience how similar it has always been to thermocatalysis and you made me enjoy and feel excited about science again. Thank you so much for your impact.

Then, I would like thank Prof. Magnus Skoglundh, for allowing me to join his lab at Chalmers University of Technology in Gothenburg, Sweden and learn more about chemical engineering and Swedish traditions. The joint project that we started with Carl Robert Florén (I guess you will be an official Dr. by now), has given me so much experience in the engineering part of my thesis, which broadened my horizon of knowledge even further. Thank you all at Chalmers for these amazing six months I have shared with you.

A big thank you to the technicians of our labs (Simone Nitti, Giammarino Pugliese, Francesco De Donato, Filippo Drago and Gabriele La Rosa), all the co-workers and obviously the administrative

staff (Iulia Monolache), who made life in the lab but also in the office so much easier, both from a professional but also personal perspective. Thank you all for this great experience.

I would like to thank my friends, Lea Pasquale, Mengjiao Wang and Tathiana Kokumai who have always been there with me through the difficult times. However, the great moments we shared when we travelled or laughed like chickens are the strongest memories on my mind. Thank you, girls, for all your love and patience.

A special thanks to the love of my life and partner in crime, Fausto Fanin, who actually proof-read this thesis. You made me realize how glad I am for making the decision to come to Genova, which allowed me to find you. I love you, my sweet and I hope to share many more years with you in my life. Thank you for your patience with me, even though it was and is very difficult at times.

I want to thank my family, for allowing me to pursue my career whichever way I wanted to and for always standing behind me. I know, Baba, it was not easy being the only one to support the family, but I am so grateful and proud to be your daughter and I hope that one day I can give you back at least a fraction of all that you have done for me. Sizleri çok seviyorum, canım ailem.

Finally, I would like to thank the person who ultimately inspired me to study chemistry: My high school chemistry teacher Mr. Manfred Mischnick, for being such a patient and dedicated teacher. I want to thank you for being such an inspiration in my life, with all the experiments we performed in class, which showed me the fun side of chemistry. I wish for all future kids in school to meet a teacher like you, who inspires them to do what they love to do.

So, this is it, all the memories and friendships I made will always stay with me. I learned to love Genova, even though it was difficult at the beginning. Now leaving it will be the next difficult step in my life, but I am sure, no matter what, Genova will always be home to me.